

Setup and Characterization of the Multi-Conjugate Adaptive Optics System for the Solar Telescope GREGOR

Dissertation zur Erlangung des Doktorgrades
der Fakultät für Mathematik und Physik
der Albert-Ludwigs-Universität Freiburg im Breisgau

Eingereicht von
Dirk Schmidt

im November 2012

Betreut durch
Professor Dr. Oskar von der Lühe



Contents

1 Motivation	13
1.1 Astronomy and Earth's Atmosphere	13
1.2 Observations of the Sun with adaptive optics	15
2 A short course on adaptive optics	17
2.1 The Principle of Adaptive Optics	17
2.1.1 Schemes of adaptive optics	20
2.2 Modeling of optical imaging and imaging quality	25
2.2.1 A model of ideal imaging	25
2.2.2 Angular resolution and imaging quality of ideal and imperfect telescopes	28
2.3 Imaging through atmospheric turbulence	30
2.3.1 Statistical model of atmospheric turbulence	31
2.3.2 Modeling wavefronts with Zernike polynomials	33
2.3.3 Temporal characteristics of atmospheric turbulence	37
2.3.4 Angular anisoplanatism – the need for MCAO	39
2.4 Wavefront modulators	41
2.4.1 Types of deformable mirrors	41
2.4.2 Wavefront modulation with deformable mirrors	43
2.4.3 Image stabilization with tip-tilt mirrors	44
2.5 Hartmann-Shack wavefront sensors	45
2.5.1 Image shift estimation	46
2.5.2 Zonal patterns	49
2.6 Wavefront reconstruction and tomography for multi-conjugate adaptive optics	49
2.6.1 Wavefront reconstruction from Hartmann-Shack shift measurements .	49
2.6.2 Wavefront tomography	51
2.6.3 Wide-field Hartmann-Shack wavefront sensor	53
2.7 Adaptive optics control loop	56
2.7.1 PID Controller	57
2.7.2 Modal basis sets	59
3 The Multi-conjugate Adaptive Optics System of GREGOR	61
3.1 GREGOR – Europe's largest solar telescope	61
3.2 Optical design of GREGOR with MCAO	62
3.3 Key components of GREGOR's MCAO	65
3.3.1 Adaptive mirrors	65
3.3.2 Wavefront sensors	72

Contents

3.3.3	Control computer	74
3.4	Position of the On-axis wavefront sensor in GREGOR MCAO	74
3.4.1	Dynamic misregistration caused by high-altitude DMs	74
3.4.2	Non-linear interaction	75
3.4.3	Atmospheric power of pupil distortion	77
4	The Kiepenheuer-Institute Adaptive Optics System – KAOS Evo 2	79
4.1	Introduction	79
4.2	The essentials of KAOS Evo 2	82
4.2.1	The KAOS control loop	82
4.2.2	Calibration	90
5	The Testbed of GREGOR’s MCAO system	93
5.1	Introductory remarks	93
5.2	Configuration of the MCAO testbed	95
5.2.1	Illumination	95
5.2.2	Turbulence generation	97
5.2.3	Science focus camera	98
5.3	System tests	98
5.3.1	Tip-tilt systems	98
5.3.2	Deformable mirrors	102
5.3.3	Frame grabbers and camera synchronization	106
5.3.4	Control loop timing	107
6	MCAO Testruns	109
6.1	General remarks on the test runs	109
6.1.1	Failure of deformable mirrors	109
6.1.2	Unstable optical alignment due to thermal expansion	109
6.2	Evaluation tools and measures of the MCAO effectivity	110
6.2.1	Plain images in the science focus	111
6.2.2	Image distortion in the science focus	111
6.2.3	Wavefront modes in the guide directions and wavefront slopes	114
6.2.4	Wavefront error reconstructed by the KAOS software	119
6.3	Tested scenarios and results	120
6.3.1	MCAO control with $DM_{0\text{km}}$ and $DM_{8\text{km}}$	120
6.3.2	Comparison of Karhunen-Loève modes and Lai modes	131
6.3.3	MCAO control with DM_0 km, DM_8 km and DM_{25} km	135
6.3.4	Unperformed tests	142
7	Summary	149
7.1	GREGOR MCAO system and the testbed	149
7.2	MCAO Performance	149
7.3	Outlook	150

A Technical data of GREGOR's adaptive optics systems	153
A.1 Optical design of the MCAO	153
A.2 Deformable mirrors	154
A.3 High-voltage electronics system	156
A.4 Tip-tilt mirrors	159
A.5 Wavefront sensors	160
A.6 Control computer	161
B Wavefront modes used for OKO PDMs	163
C Design tips for Hartmann-Shack Wavefront Sensors for extended fields	171

Danksagung

*«You never win alone.
Once you start believing
something different,
you start loosing.»*

(Mika Häkkinen)

Ohne die Unterstützung zahlreicher Personen wäre GREGOR's MCAO-System nicht Wirklichkeit geworden, und ohne das Vertrauen, welches die entscheidenden Personen in mich gesetzt haben, wäre GREGOR's MCAO nicht *meine* Doktorarbeit geworden.

Aus Respekt vor dem Persönlichkeitsrecht der gedankten Personen wurden die Namen aus diesem on-line Dokument entfernt.

Abriss

Das Thema dieser Dissertation ist eine multikonjugierte adaptive Optik für ein Sonnenteleskop zur optischen Korrektur der Bildverschlechterung aufgrund erdatmosphärischer Turbulenz. Ein solches System mit drei verformbaren Spiegeln wurde für das Sonnenteleskop GREGOR aufgebaut.

Das Besondere einer adaptiven Optik im Vergleich zu nachträglicher, digitaler Bildverbesserung ist bereits durch ihren Namen ausgezeichnet. Eine adaptive Optik korrigiert die Bildunschärfe optisch bevor das eigentliche Bild, das von wissenschaftlichem Belang ist, entsteht. Die Korrektur erfolgt durch ein optisches Bauteil — dies ist in der Regel ein verformbarer Spiegel — welches sich rasch dem momentanen optischen Fehler, der zur Bildunschärfe führt, anpasst und diesen korrigiert. Das auf diese Weise korrigierte Bild kann spektroskopisch untersucht werden, was mit digital verbesserten Bildern nicht möglich ist. Der Begriff *adaptiv* ist von dem Lateinischen Wort *adaptare* übernommen, welches *anpassen, passend herrichten* bedeutet. Adaptive Optik wurde bereits 1953 von Horace W. Babcock vorgeschlagen, es dauerte jedoch bis in die 1990er Jahre hinein, bis die ersten Systeme für astronomische Teleskope realisiert werden konnten. Seit ungefähr der Jahrtausendwende wurde adaptive Optik für die Beobachtung der Sonne im sichtbaren Licht etabliert und ist heute nicht mehr wegzudenken.

Aufgrund ihrer Nähe zur Erde können auf der Sonne selbst kleinskalige Strukturen beobachtet werden, während Strukturen auf entfernten Sternen selbst mithilfe interferometrischer Methoden oder auch mit überwältigend großen Teleskopen nur ansatzweise aufgelöst werden können. Da sich viele wissenschaftliche Fragen der Sonnenphysik auf diese kleinskaligen Strukturen beziehen, ist adaptive Optik für die Sonnenforschung von noch größerer Bedeutung als für die Astrophysik im allgemeinen, die genügend "Ausweichfragen" bietet. Oftmals wird die Sonne auch als Prototyp anderer Sterne im Universum angesehen, weswegen das Erlangen eines immer detaillierteren Verständnisses der Sonne besonders bedeutsam ist.

Die heutigen adaptiven Optiken, die sich im Alltagsgebrauch an den großen Sonnenteleskopen befinden, sind in der Lage, das Bild der Sonne in einem Ausschnitt von etwa 10 Bogensekunden zu korrigieren. Dies entspricht in etwa dem 180. Teil des Sonnen-durchmessers. Um den korrigierten Ausschnitt zu vergrößern, hat Jacques M. Beckers in den späten 1980er Jahren eine Erweiterung angedacht, die unter dem Begriff *multikonjugierte adaptive Optik* bekannt wurde. Beckers sah vor, mit mehreren verformbaren Spiegeln die turbulenten Störungen in einem größeren Volumen zu korrigieren als es mit einem solchen Spiegel der Fall ist. Erst wenige Jahre vor dem Beginn dieser Arbeit wurde dieses Prinzip an Sonnenteleskopen erstmals experimentell demonstriert und zwar noch bevor es für nacht-astronomische Beobachtungen gelang.

Die Arbeit, über welche diese Schrift berichtet, umfasste den Aufbau, die Inbetriebnahme und die Charakterisierung einer multikonjugierten adaptiven Optik für das neue Deutsche Sonnenteleskop GREGOR, deren ursprüngliches Konzept in das Jahr 2006 zurückreicht. Dieses System, welches die Versechsfachung des korrigierten Bildfeldes verspricht, befindet sich derzeit im Freiburger Labor des Kiepenheuer-Instituts und soll 2013 in das GREGOR Teleskop, welches das größte Europäische Sonnenteleskop ist und sich auf Teneriffa befindet, eingebaut werden.

Abstract

The topic of the present dissertation is a multi-conjugate adaptive optics system for a solar telescope to correct image blur due to turbulence in Earth's atmosphere. Such a system with three deformable mirrors was set up for the solar telescope GREGOR. The specialty of adaptive optics compared to digital, post-facto reconstruction techniques is reflected in its name. An adaptive optics corrects the image blur optically before the scientifically observed image is formed. This correction is carried out by an optical element, usually a deformable mirror, which is rapidly adjusted to the instantaneous optical error in such a way that the image blur is compensated. The image that is corrected in this manner can be spectroscopically analyzed. This is not possible with digitally reconstructed images. Horace W. Babcock came up with the idea of adaptive optics already in 1953, but it should take another four decades until the first systems could be realized at astronomical telescopes. Since round about the turn of the millennium, adaptive optics has been established for solar observations in the visible light regime.

Because the Sun being close to Earth, small-scale solar structures can be observed whereas structures of distant stars can only be resolved rudimentary even with interferometric methods or overwhelmingly large telescopes. Adaptive optics is especially important for solar research because many scientific questions in solar physics are related to these small-scale structures, whereas astrophysics in general still offers a good amount of "low-resolution" questions. Understanding the Sun in more and more detail is outstandingly interesting inasmuch the Sun is often regarded as a prototype of other stars in the universe.

Today's adaptive optics systems, which are routinely used at the large solar telescopes, are able to correct the image of the Sun in a section of about 10 arcsecond, which is about 1/180 of the solar diameter. In order to widen the correction over a larger field, Jacques M. Beckers contemplated an extension in the late 1980s that became famous under the name *multi-conjugate adaptive optics*. Beckers envisioned the use of multiple deformable mirrors which would compensate for turbulent flows in the atmosphere in a larger volume than this is the case when a single deformable mirror is utilized. This principle was demonstrated first at solar telescopes and before it was demonstrated at nighttime telescopes only a few years before the beginning of this thesis.

The work presented in this thesis involved the setup, commissioning and characterization of a multi-conjugate adaptive optics system for the new German solar telescope GREGOR in a testbed. This system, which promises to enlarge the corrected field of view by a factor of six, is currently located in the lab of the Kiepenheuer-Institut in Freiburg and is to be integrated into the GREGOR telescope, which is the largest European solar telescope and located on Tenerife, in 2013.

Structure of this thesis

The first chapter is characterized by an enjoyable tour through the trouble Earth's atmosphere brings into astronomy and ends with the momentousness of adaptive optics. Be even readers outside of the subject area motivated and encouraged to continue with the second chapter, which first introduces the basic concepts of adaptive optics in an attractive way before it starts to get physical by explaining the theory behind. Chapter 3 is dedicated to the features of the multi-conjugate adaptive optics system of GREGOR from the optical and hardware point of view. Chapter 4 concentrates on the control software and algorithms that are used. The testbed of this system and its verification is reported on in chapter 5 whereas its effectiveness of compensating for hot-air turbulence is presented in the sixth chapter.

Enjoy this fascinating work and technology!

1 Motivation

1.1 Astronomy and Earth's Atmosphere



Figure 1.1: Daytime and nighttime views of the sky above the Teide volcano on Tenerife from the Izana observatory. The blue color of the daytime sky is sunlight scattered by Earth's atmosphere and outshines the dim starlight. Clouds impede any visual observations of extra-terrestrial objects.

Imagine we want to observe a star, let's say Vega. Although Vega might be above horizon all day long at our site, we cannot see it all the time. Earth's atmosphere limits our observation opportunity. About half of the day, the intense sun light is scattered by the atmosphere, giving a beautiful blue sky on a nice day. The scattered sun light outshines the dim star light of Vega. On a cloudy or rainy day, when we can't even see the Sun, we cannot observe Vega either. Earth's atmosphere, however, not only limits our observation time, it also narrows the information we can get about the star because the atmosphere is not transparent for all kinds of light and electro-magnetic radiation. For example, at the blue end of the visible light regime, the atmosphere blocks ultra-violet radiation. While this is essential for life

1 Motivation

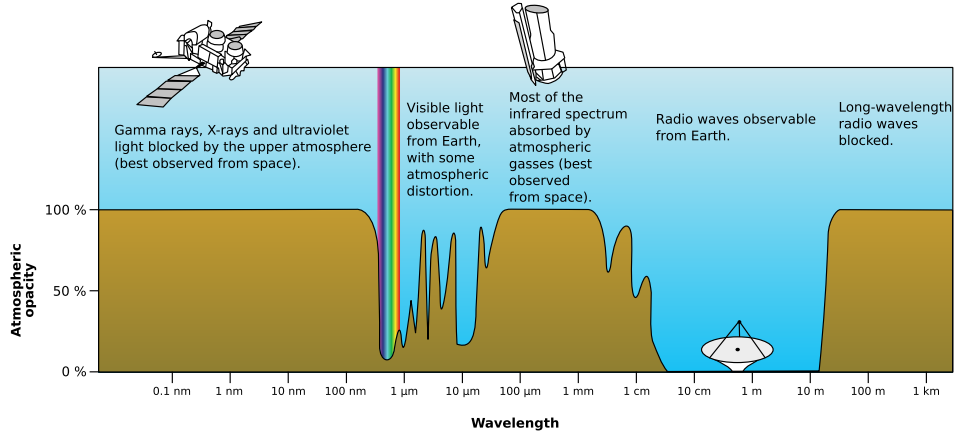


Figure 1.2: Electro-magnetic transmittance of Earth's atmosphere (NASA artwork).

on Earth in general, it complicates your life if you want to be an ultra-violet astronomer. In the thermal infrared regime, the atmosphere is also not transparent. Although infrared radiation from outer space does not harm life on Earth, the transmittance barriers in this regime is again indispensable for life because the atmosphere prevents most thermal energy escaping from Earth. Water would not be liquid—and this is the basis of all life—on Earth but frozen without the thermal infrared insulation of the atmosphere. Figure 1.2 shows the electromagnetic transmittance of the Earth's atmosphere.

Let's continue our imaginary Vega observation at a clear, dark and starry night. Once we located Vega on the sky and look at it by naked eye, we see it twinkling. But Vega itself does not twinkle, it is the atmosphere duping you. As Isaak Newton wrote in 1718 in his book Opticks: «*For the Air through which we look upon the Stars, is in a perpetual Tremor; as may be seen [...] by the twinkling of the fix'd Stars. But these Stars do not twinkle[...]*» . In fact, the atmosphere is turbulent as you might have experienced physically if you ever flew with an airplane. However not only airplane passengers may have a bumpy ride but also the light coming from Vega. If we observe Vega magnified through a large telescope, another consequence of the turbulent air reveals: the image of Vega jumps around and gets blurred randomly. The optical impact of the turbulent atmosphere on images of astronomical objects is called *astronomical seeing*.

Having traveled for 25 years through empty space on straight line, the light coming from Vega is either blocked or seriously distorted on its final kilometers in the atmosphere of the Earth (fig. 1.3). Not only images of stars like Vega but of all objects outside the atmosphere—in particular the Sun, our closest star—suffer from seeing. This is unavoidable, but as we will see it can be compensated with a modern technology called *adaptive optics* (AO).

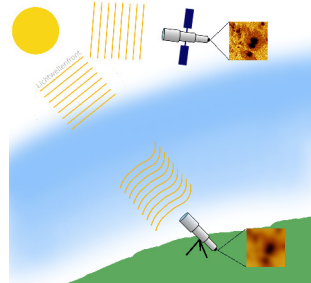


Figure 1.3: Earth's atmosphere blurs not only the image of Vega but also of the image of the Sun by distorting the light wavefront.

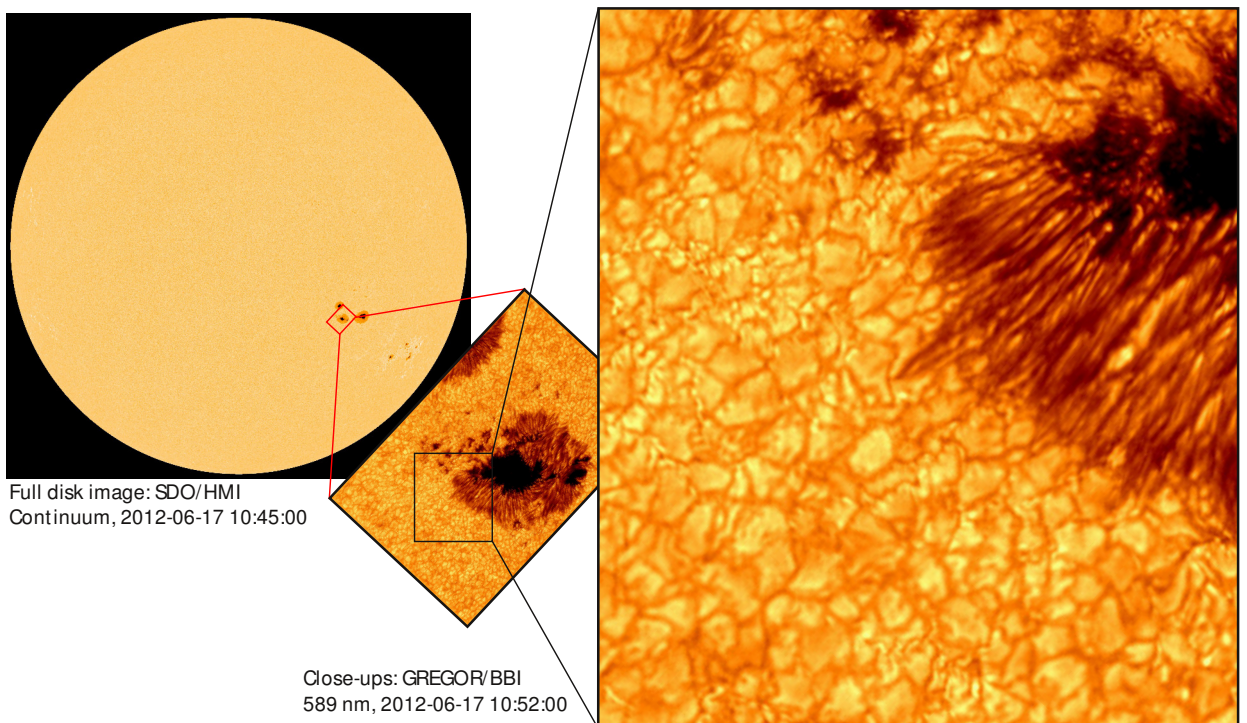


Figure 1.4: The Sun in the visible light regime. The full disk, low resolution image was taken from NASA's spacecraft Solar Dynamics Observatory (SDO). The high-resolution close-up images were taken almost simultaneously at the GREGOR telescope with the use of adaptive optics by T. Berkefeld, D. Schmidt, O. von der Lühe, R. Geißler, and A. Feller. Speckle reconstruction was applied to the close-ups by O. von der Lühe. The larger close-up is about 70×110 arcseconds wide. Solar granulation and a sunspot are shown. The umbra (the dark core) of the spot and the penumbral filaments can be clearly seen.

1.2 Observations of the Sun with adaptive optics

Observing the Sun in the visible light regime with a telescope of about 7–10 cm in diameter reveals a granular structure (figure 1.4). This is the photosphere from which the vast majority of the energy that has been released in the core of the Sun is radiated away. The photosphere is only about 300 km thick, which is about 0.06% of the solar radius, and is about 6000°C hot. The granules are cells of convective plasma. The hotter and thus rising plasma is concentrated in the bright center of a granule. The plasma cools down as it rises and flows down in the darker boundary of the granule. Granules are several hundreds kilometers large and last for a couple of minutes. Granulation is often descriptively compared with boiling water. Other prominent structures in the photosphere, which are caused by strong magnetic fields, are sunspots. Large sunspots can be discovered by the eye (wear protective glasses!). Granulation and sunspots are just two examples of features that are visible in the photosphere of the Sun. Observations thereof with higher and higher resolution are needed to extend the physical understanding of the Sun. As long as space based observatories are at least a factor of ten more expensive than ground based facilities, adaptive optics is indispensable to push solar science.

2 A short course on adaptive optics

«Mit jeder Welle kam ein Traum.
Träume gehen vorüber.

...
Jetzt kommt sie langsam auf dich zu.

...
Das ist die perfekte Welle!»

(Juli, "Perfekte Welle")

This chapter recapitulates the most important aspects of adaptive optics and shall provide readers outside the subject area with an idea of the concepts and challenges arising in the field of astronomical adaptive optics, in particular solar adaptive optics. Due to the nature of this chapter, its content is based on various sources. My understanding of and my writing about adaptive optics was in particular influenced by the textbooks of Hardy (1998), Tyson (1991), Roddier (2004), by the online tutorial of Tokovinin*, by the living review of Rimmeli and Marino (2011) and by educational presentation slides provided online by the *Center for Adaptive Optics*[†].

2.1 The Principle of Adaptive Optics

Retrieving the maximum angular information (image detail) about an astronomical object out of the light portion that reaches a ground-based telescope by compensating the turbulence effects physically is the scope of adaptive optics in astronomy. In the domain of adaptive optics, light is usually modeled with the means of wave optics which will be touched in section 2.2. The most important term in adaptive optics is *wavefront aberration*. A wavefront is the surface of points having the same phase of the electro-magnetic light wave. That is, the light in all points of this surface was emitted by the source at the same instant. When light from a distant object like the Sun or a star reaches Earth's atmosphere, its wavefront can be considered to be flat. The wavefront aberration is the difference of phase from a reference surface like a sphere or a flat as shown in figure 2.1. However, the terms wavefront aberration and wavefront will be used synonymously for the rest of this thesis, i. e. the aberration shall refer to a flat surface.

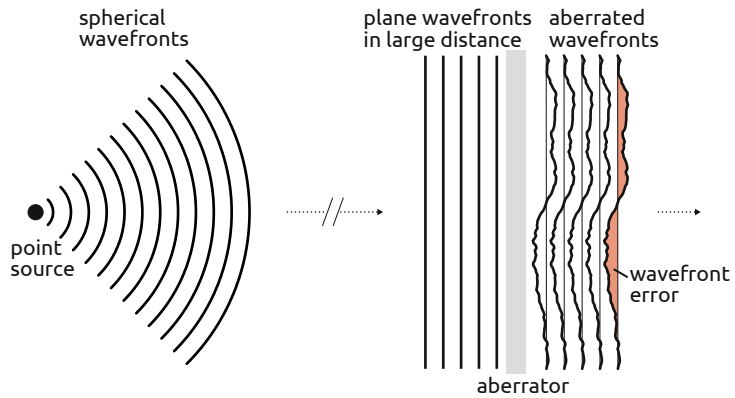
The aberration caused by atmospheric turbulence and seen by a telescope is not static but rapidly changing thousands of times a second. As a consequence, a ground-based telescope

*<http://www.ctio.noao.edu/~atokovin/tutorial/>

[†]<http://cfao.ucolick.org>

2 A short course on adaptive optics

Figure 2.1: Graphical explanation of the term *wavefront error*.
A point source is emitting spherical waves. Their curvature drops with distance. Thus, the wavefront can be considered as plane in a large distance. The wavefront error is the deviation from this plane.



with fixed optics delivers a blurred image of the object. Schlieren above hot roads in the summer or above the flame of a candle is the very same effect of turbulent airflows.

Adaptive optics, first suggested by Babcock (1953), addresses this kind of image degradation by flattening the distorted wavefront within the imaging telescope. Flattening the wavefront, also called *phase conjugation*, is typically done by reflecting the light with *deformable mirrors* which adapt to the incident wavefront such that the reflected wavefront is flat. This is the case when the shape of the wavefront is embossed on the deformable mirror with half of its amplitude (fig. 2.2). The flattened wavefront is then fed into scientific instruments to analyze the information about the observed object carried by the light. This principle is shown in figure 2.3.

Devices that are used to flatten the wavefront are generally called *wavefront compensators* or *wavefront modulators*. In order to adapt such a device to the wavefront, a device which registers the wavefront is required. Such a device is called *wavefront sensor*. A *control computer* is used to reconstruct the wavefront modulator commands from the wavefront sensor measurements in a *control loop*. These are the three basic components of an adaptive optics system.

Adaptive optics perform physical compensation of optical turbulence in real-time and before the astronomical image is delivered to arbitrary scientific instruments, like in particular light-spectrometers. There exists a number of numerical image restoring post-processing algorithms like speckle interferometry, phase diversity, deconvolution approaches and lucky imaging. However, their output is high-resolution digital information which cannot be fed back into optical analyzers. Computational image restoration methods often need already good image quality in order to extract even more detailed image information. For this reason, adaptive optics and post-processing are often used complementary for high-resolution imaging.

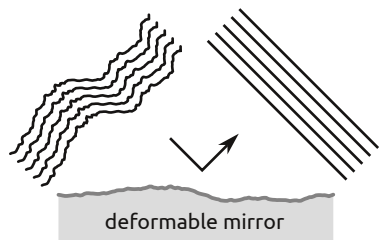


Figure 2.2: Wavefront flattening with a deformable mirror.

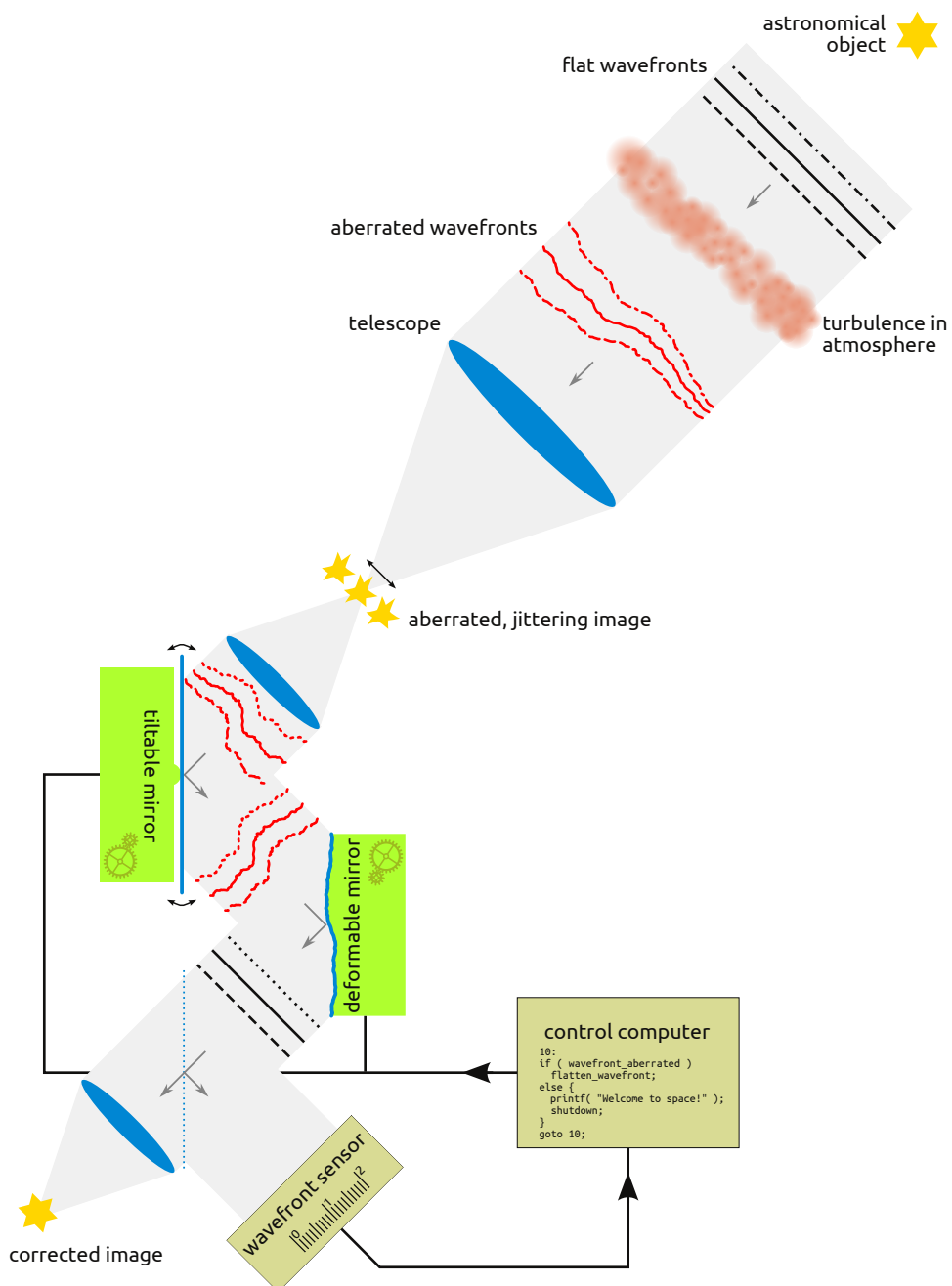
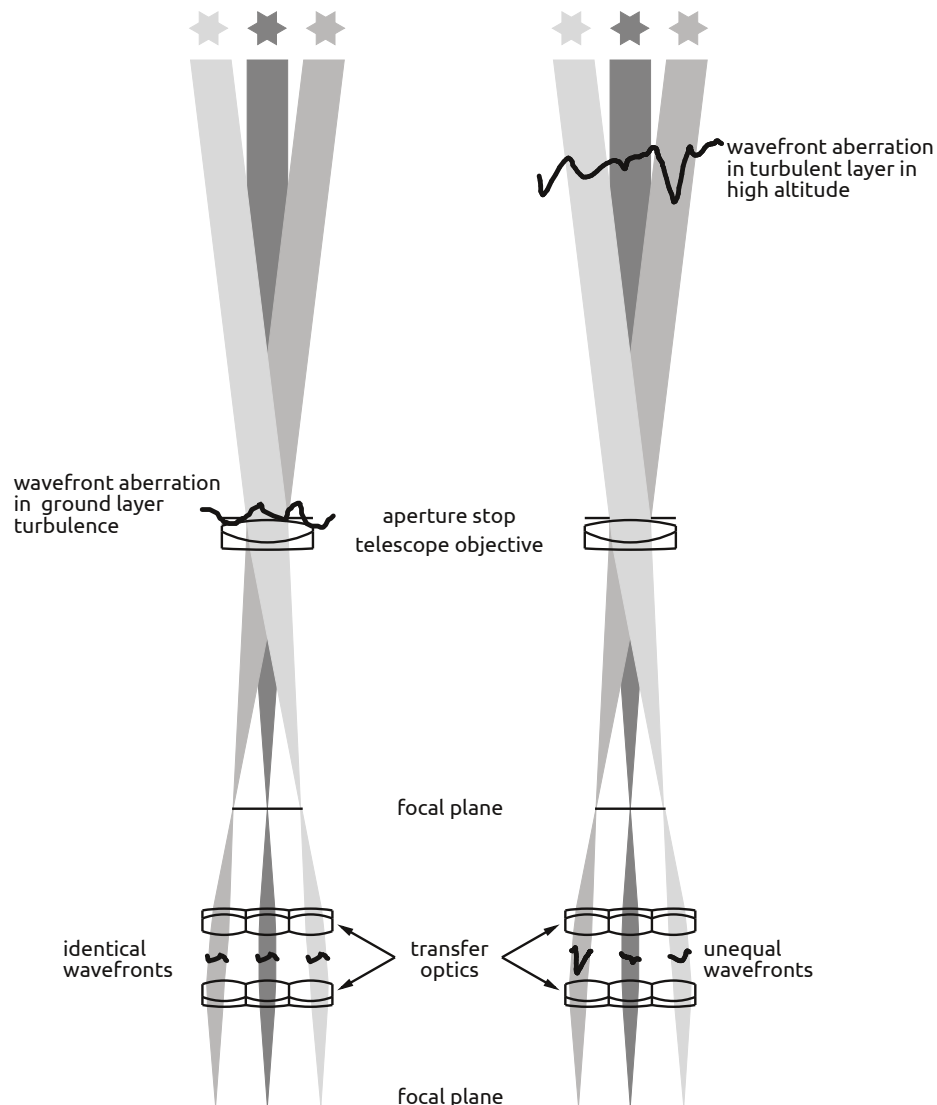


Figure 2.3: Scheme of a generic astronomical adaptive optics system. An aberrated wavefront enters the telescope and the image of the observed object is degraded and dancing around randomly. The image motion is corrected with a tilttable mirror and the wavefront is flattened with a deformable mirror. The corrected image is analyzed with scientific instruments (not shown). A control computer adapts the mirrors according to the measurement of a wavefront sensor .

2.1.1 Schemes of adaptive optics

Adaptive optics is the general term in astronomy for equipments that physically compensate fast optical aberrations due to atmospheric turbulence in real time. Turbulence in Earth's atmosphere is distributed over a wide range from ground to the tropopause in about 15 km altitude. The turbulence strength varies greatly with height, and there occur distinct layers with strong turbulence. Aircraft pilots exploit this fact sometimes to keep out of turbulence by changing the altitude by some hundreds of meters instead of flying around turbulent areas. The vertical turbulence distribution is the origin of the variety of adaptive optics schemes existing. If turbulence would be located exclusively close to the telescope aperture, the wavefront error would be independent of the viewing direction (fig. 2.4). However, if this is not the case, the wavefront error depends on the viewing direction. This effect is referred to as *anisoplanatism* of the atmosphere and is the most challenging problem in adaptive optics.



A single turbulent layer could be perfectly compensated by placing a wavefront modulator into the image plane (the conjugate plane) of the turbulent layer in the telescope, as shown in figure 2.5. Even at good telescope sites, however, atmospheric turbulence is not limited to a single layer. Thus, an adaptive optics scheme with one wavefront modulator will only be able to perfectly compensate for turbulence in one direction.

There exists a number of acronyms describing various schemes of adaptive optics; most frequently used are: single-conjugate (SCAO), ground-layer (GLAO), multi-object (MOAO), and multi-conjugate adaptive optics (MCAO). The acronym NOAO is also known in astronomy. However, this is in general not an oblique paraphrase for the absence of an adaptive optics system but is more commonly associated with the United States *National Optical Astronomy Observatory*. In the following, the listed schemes are discussed briefly with emphasis on phase conjugation, abstracting away from the problem of wavefront sensing. Wavefront modulators and wavefront sensors are covered by sections 2.4 and 2.5.

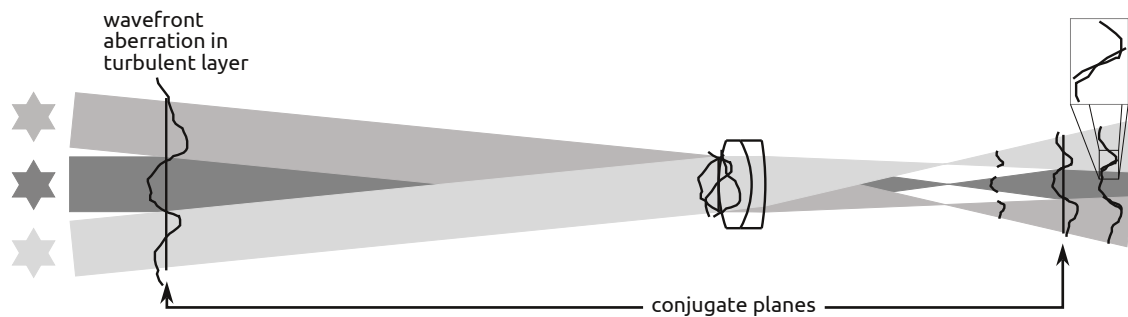


Figure 2.5: Illustration of wavefront conjugation in conjugate (=image) planes. The wavefront aberration introduced by a turbulent layer over an extended field of view can be compensated in the image plane of this layer. In this plane, the wavefront aberration is consistently reproduced. In any other plane, wavefront aberrations of different directions do not stitch uniquely and, thus, could not be compensated perfectly.

2.1.1.1 Single-conjugate adaptive optics

Single-conjugate is the simplest form of an adaptive optics system and describes Babcock's original idea. It features a single wavefront modulator for phase conjugation as sketched in figure 2.6. The modulator is typically positioned conjugate to the telescope aperture, i. e. in a pupil plane, or close to it. Wavefront aberrations that have accumulated along the optical axis are measured by a wavefront sensor and are compensated by the modulator. The turbulence compensation is only effective for a small angle of some arcseconds due to anisoplanatism of the atmospheric turbulence.

Single conjugate systems were the first operational adaptive optics and are now a mature technology. For this reason,

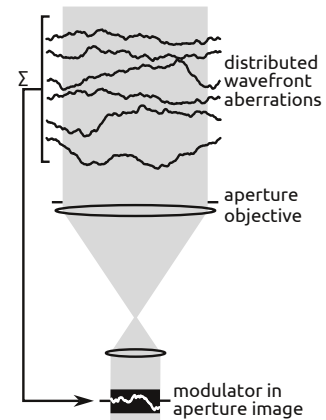


Figure 2.6: Single conjugate adaptive optics scheme.

single-conjugate systems are often referred to as *conventional* or *classical adaptive optics* (CAO). The first system, which was named ADONIS, was made available to astronomers by the European Southern Observatory (ESO) in 1993 at the 3.6-meter telescope in La Silla, Chile. From that time on, most major nighttime telescopes have been equipped with this kind of adaptive optics. The Dunn Solar Telescope became the first solar telescope with routinely operating adaptive optics in 1999. Now, adaptive optics is indispensable for solar research, and the most productive ground-based telescopes focussing on high angular resolution, the Dunn Solar Telescope (DST), the German Vacuum Tower Telescope (VTT), the Swedish Solar Telescope (SST) and the New Solar Telescope (NST) feature adaptive optics systems.

2.1.1.2 Multi-object adaptive optics

Multi-object adaptive optics is addressed to simultaneous observations of a small number of science objects. A wave-front modulator (or a section of a large modulator) is dedicated to each object. Multi-object adaptive optics can be considered as multiple single conjugate systems compensating the accumulated aberrations for different directions separately. Thus, turbulence can be compensated for objects spread over a wide field of view. However, the compensation performance is not uniform over the field. For this reason, multi-object AO is not pursued for solar adaptive optics. The red-shift of galaxies and the cosmological expansion is an observation scenario as well as spectroscopy of individual stars. Multi-object AO systems are foreseen for future extremely large telescopes and are currently studied by various groups.

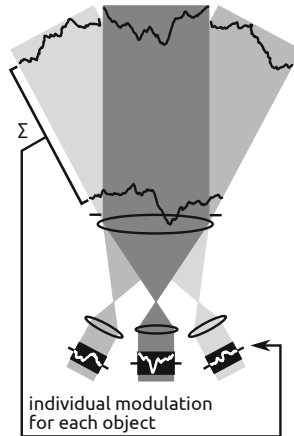


Figure 2.7: Multi-object adaptive optics scheme.

2.1.1.3 Multi-conjugate adaptive optics

The multi-conjugate adaptive optics (MCAO) scheme is targeted to seeing compensation that is uniform over an extended field (some ten arcseconds for solar observations) by compensating turbulence in three dimensions. Strong turbulence is usually concentrated in a few prominent layers. In MCAO systems, one wavefront modulator is dedicated to each of the most prominent layers (fig. 2.8). The modulators are placed into the conjugate planes of the corresponding layers. Turbulence between these layers is not effectively compensated. Thus, the peak compensation performance will be less compared to single-conjugate systems if there is significant turbulence between the compensated layers. However, Tokovinin et al. (2001) demonstrated theoretically that the quality of turbulence compensation with two modulators is practically independent of the conjugate plane of the high-altitude modulator. Because optical imaging is symmetric, i. e. light rays can be traced forwards and backwards, the sequence of wavefront modulators must be the reverse sequence of turbulent layers in order to obtain corrected groups. This involves additional reimaging optics forming

intermediate images as shown in figure 2.8. However, if turbulence in two high-altitude layers is weak, the order of their conjugate modulators may be interchanged to simplify the optical setup(Berkefeld et al., 2006).

The concept of MCAO was proposed by Beckers (1988a,b). It has been pursued for both solar and stellar observations. The first successful on-sky demonstration was performed in 2004 at the solar Vacuum Tower Telescope(Berkefeld et al., 2005) and at the Dunn Solar Telescope(Langlois et al., 2004). ESO succeeded with the MAD (Multi-Conjugate Adaptive Optics Demonstrator) project at the Very Large Telescope (VLT) using natural guide stars for wavefront sensing(Marchetti et al., 2007). All three systems used two wavefront modulators. An MCAO system with laser guide stars is currently commissioned at the Gemini South telescope. This system is designed—like the MCAO system this thesis is about—to use three wavefront modulators. Due to issues with one modulator, the first MCAO observations at Gemini South were carried out with two modulators(Rigaut et al., 2012).

MCAO is considered to be an important technology for future observations of the Sun with upcoming telescopes: The new German solar telescope *GREGOR* is planned to be the first solar telescope with an integrated MCAO system that is able to serve all scientific post-focus instruments with an extended compensated field of view. The setup of this MCAO system in a laboratory testbed and its characterization is presented in this document. The *New Solar Telescope (NST)* is to be upgraded with an MCAO system in 2013 that is closely related to GREGOR’s MCAO. The *Advanced Technology Solar Telescope (ATST)*, which is currently being built, is planned with MCAO in mind, and MCAO is an integral feature in the design study of the *European Solar Telescope (EST)*.

There are two different approaches for sensing the three-dimensional wavefront error. In the first approach, multiple wavefront sensors measure the aberrations that have summed up along various guide directions. The wavefront error introduced in a particular layer can be estimated from these measurements by tomographic algorithms which will be discussed in section 2.6.2. This approach is referred to as *guide star oriented MCAO* in night-time astronomy. In the second approach, multiple wavefront sensors are deployed which are—like the wavefront modulators—dedicated to the aberrations in a single layer instead of the accumulated error in one direction. This is called *layer oriented MCAO*. Special kinds of wavefront sensors which are able to discriminate the wavefront by distance from the telescope are needed for this approach.

2.1.1.4 Ground-layer adaptive optics

If turbulence is mainly concentrated in a layer near ground and if high-altitude turbulence is much weaker, a light version of MCAO without wavefront modulators conjugate to higher altitudes is an option to achieve a large uniformly compensated field of view. This scheme is a special kind of single-conjugate AO. However, the wavefront modulator adapts only to aberrations introduced in its conjugate layer—the ground-layer—rather than to accumulated wavefront errors. Again, there is a trade-off between uniformity and peak performance of the turbulence compensation. Ground-layer AO was proposed by Rigaut (2002) and is considered to be an attractive option for solar research by Rimmele et al. (2010), because turbulence near ground is exceptionally strong during daytime observations.

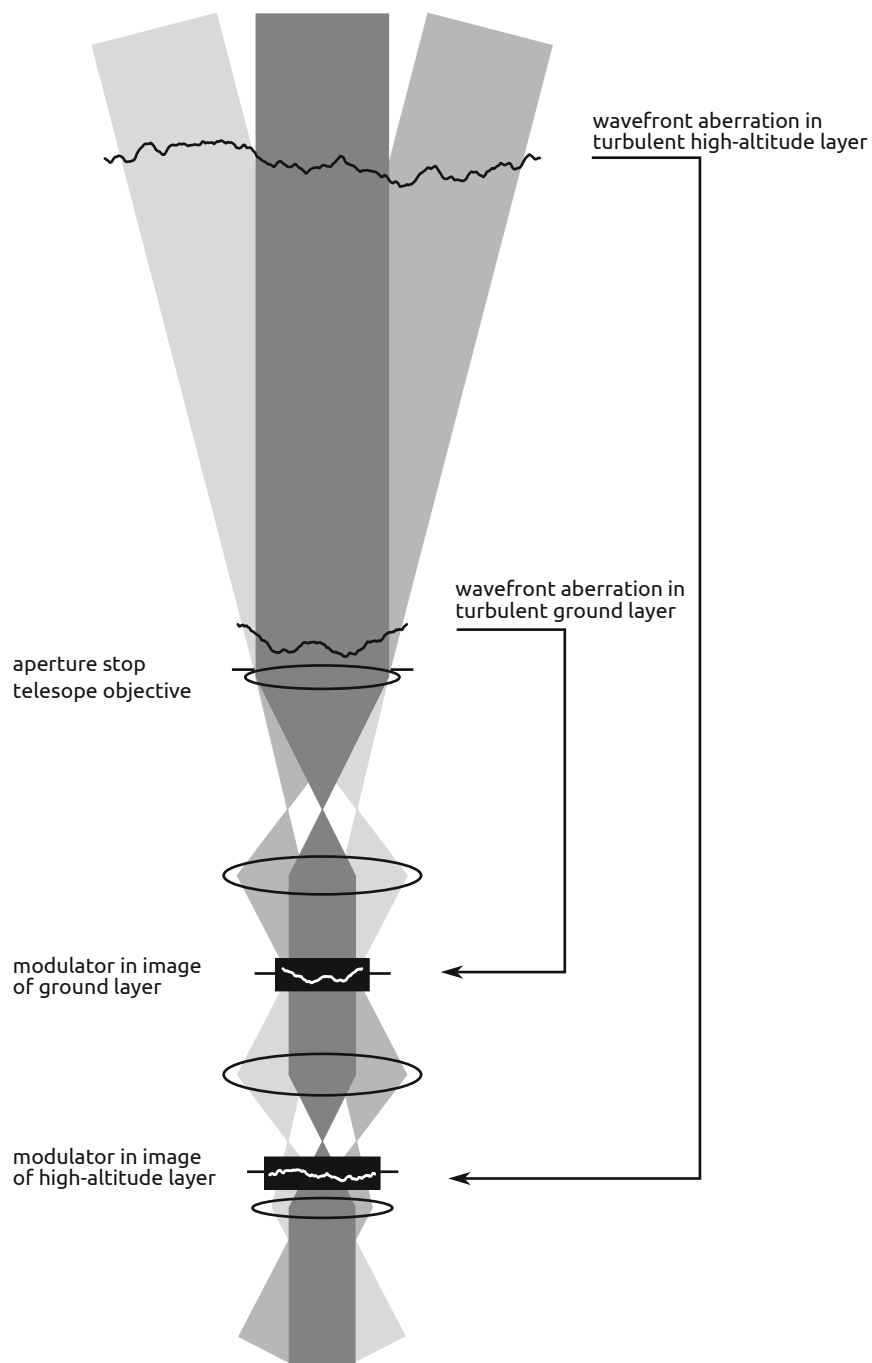


Figure 2.8: Multi-conjugate adaptive optics scheme. Turbulent layers in high altitude and close to the ground and compensated in their respective image planes. The ideal order of compensation, which is the inverse of the turbulent layers, is established by additional relay optics in this sketch.

2.2 Modeling of optical imaging and imaging quality

Pupils in optical systems An important term in optics is *pupil*. A pupil is any image of the aperture stop of an optical system. That is, the aperture stop, which is the stop that limits the light beam diameter, and the pupils are optically conjugate. In astronomical telescopes, the aperture stop is typically either the rim of the primary or the rim of the secondary mirror.

2.2.1 A model of ideal imaging

In order to compensate optical imaging for turbulent disturbances, it is necessary to understand the formation of an image. The theory of *Fourier optics* which describes the propagation of light based on its electro-magnetic wave-nature is an adequate and practical model for the scope of adaptive optics. Fourier optics does not include polarization because it only considers the magnitude of the electro-magnetic field vector but not its direction. Although the light's polarization bears great information on the light source, and therefore is of great astronomical interest, it is irrelevant for understanding image formation and optical aberrations.

The magnitude of the electric field strength of a monochromatic light-wave at a point \vec{x} in space at the instant t can be expressed by the real-valued quantity

$$E(\vec{x}, t) = \Re \left\{ a(\vec{x}) e^{-i\phi(\vec{x})} \cdot e^{i\omega t} \right\}. \quad (2.1)$$

The term $\phi(\vec{x})$ is called *phase* and is the object of adaptive optics. The parameter ω depicts the angular velocity which reflects the wavelength $\lambda = 2\pi/\omega$. The magnitude $E(\vec{x}, t)$ separates in space and time. The stationary term

$$u(\vec{x}) := a(\vec{x}) e^{i\phi(\vec{x})} \quad (2.2)$$

which includes the real-valued amplitude $a(\vec{x})$ and the phase $\phi(\vec{x})$ is called *complex amplitude*. It bears all information of special interest for imaging. The rapid fixed oscillation of $E(\vec{x}, t)$ expressed by $e^{i\omega t}$ is not particular exciting and is therefore often omitted.

The point \vec{x} in space is usually described in Cartesian ($\vec{x} = (x, y, z)$) or cylindrical coordinates ($\vec{x} = (r, \theta, z)$) in which the z -axis is typically put on the optical axis of the imaging system. Thus, the complex amplitude $u(\vec{x})$ is handled as a two-dimensional function, e. g. $u_i(x, y)$, in the normal plane intersecting the optical axis at z_i .

Jack D. Gaskill illustrated the concepts of diffraction, Fourier optics and imaging systems in great detail in his very excellent textbook *Linear Systems, Fourier Transforms, and Optics* (Gaskill, 1978) based on the Fresnel-Huygens principle and approximations of the Rayleigh-Sommerfeld diffraction integral which describes the propagation of the electric field through space.

The point of direct interest for this thesis is imaging of incoherently radiating light sources, which shall be accentuated in the next paragraphs. The image of an object in this context is the irradiance distribution raised by the object in the image plane of an imaging system. The irradiance is the squared modulus of the electric field amplitude, i. e. $I(x, y) = |u(x, y)|^2$.

The physical dimension of irradiance is power per area. The irradiance incident in the image plane of an imaging system can be modeled by

$$I_{\text{image}}(x, y) = l \Omega \cdot I_{\text{object}} \left(\frac{x}{m}, \frac{y}{m} \right) * \text{PSF}(x, y), \quad (2.3)$$

where I_{object} is the irradiance of the object in the object plane. The variables x and y are Cartesian coordinates perpendicular to the optical axis. Their physical dimension is length. The constant l represents the loss of light due to reflection and absorption within the imaging system. Hence, it is $0 \leq l \leq 1$. Ω is the solid angle subtended by the entrance pupil of the system as seen from the object. The imaging character of the system is described by the *point spread function* $\text{PSF}(x, y)$. The symbol $*$ denotes the two-dimensional convolution which effectively smears its operands. The scaling factor m is the magnification of the image given by $m = f / (f - \delta z)$, where δz is the distance between the object and the first principal plane of the system (the center in the case of a single thin lens) and f its focal length. For sake of readability, equation (2.3) is printed without explicit dependence on wavelength, however, l , I_{object} , PSF and hence I_{image} share the parameter λ . The core of this section is:

Optical imaging of an incoherent radiating object results in a dimmed, scaled copy that is smeared out by the point spread function of the imaging system.

2.2.1.1 The point spread function

The point spread function is the irradiance distribution in the image plane due to a single point source with unit radiance. The idea of the incoherent imaging equation (2.3) is: each point of the object raises a point spread function like irradiance at its corresponding position in the image plane—dependent of the other object points. The magnitude of such a point image corresponds to the irradiance of the source point. Finally, the collective irradiance distribution caused by all points of the object is the sum of the individual single point irradiances. As a consequence, the image cannot exhibit smaller structures than included in the point spread function despite the fact that the object is considered to be covered continuously with an infinite number of point sources.

The figure of the point spread function is solely determined by diffraction due to the finite aperture and by wavefront aberrations present in the imaging system. The geometric size of the point spread function figure is affected by the effective focal length of the system and by the distance of the object. The point spread function is a mathematical construct because there is no real point source. However, the irradiance pattern caused by a star in a focussed telescope is a good practical example. The point spread function of a simplified telescope imaging a star into its focal plane can be calculated by

$$\text{PSF}(x, y) = \frac{1}{[\lambda f]^2 \cdot A} \left| \mathcal{F}\{p(x, y)\} \Big|_{\begin{subarray}{l} \xi = x/(\lambda f) \\ \eta = y/(\lambda f) \end{subarray}} \right|^2, \quad (2.4)$$

where $p(x, y)$ is the *complex amplitude transmission* and A the area of the aperture stop. This equation is valid for a telescope with a single focussing element (e. g. a lens) that also

constitutes the aperture stop. If this is not the case, ξ , η and A need to be scaled by additional factors derived from the given configuration. In general, the complex amplitude transmission $t(x, y)$ of an optical element is defined by the ratio of the amplitudes directly in front ('-') and behind ('+') an element, i. e.

$$t(x, y) := \frac{u^+(x, y)}{u^-(x, y)}. \quad (2.5)$$

Note that the transmission function in equation (2.4) only refers to the aperture stop and to wavefront errors. The imaging effect of the lens—free of aberrations—is already included in the Fourier transform. Consequently, it is

$$p(x, y) = a(x, y) e^{i\phi(x, y)}, \quad (2.6)$$

where $0 \leq a(x, y) \leq 1$ represents the aperture. $\phi(x, y)$ is the wavefront error in the aperture plane which may be composed of both instrumental and atmospheric aberrations. As long as the wavefront error $\phi(x, y)$ is linear in x and y (inclined plane), the figure of the point spread function is only affected by the aperture $a(x, y)$. A linear wavefront error, usually referred to as *tip-tilt*, simply shifts the point spread function due to the shifting property of the Fourier transform which reads

$$\mathcal{F}\{e^{i2\pi\xi_0 x} f(x)\} = F(\xi - \xi_0). \quad (2.7)$$

Hence, equations (2.4) and (2.6) constitute the importance of a flat wavefront for diffraction limited imaging.

2.2.1.2 Limits of this model

Two basic assumptions enter the derivation of equation (2.3):

1. The imaging system is shift-invariant.
2. The source is a highly diffuse radiator, i. e. the radiance ($\text{W}/\text{m}^2/\text{sr}$) is independent of the viewing angle.

An imaging system is shift-invariant, also referred to as being *isoplanatic*, if there is no difference in image structure of a given object, no matter if the object is centered on the optical axis or not. That is, the point spread function is assumed to be identical for all object points—*independent of their positions in the object plane*. Coma, for example, is a typical aberration of lenses effective for object points offside the optical axis (fig. 2.9). The real image of an extended object gets gradually blurred with the distance to the center. This effect cannot be modeled with equation (2.3). Image distortions can also not be produced by this equation. Without exercising the derivation of equation (2.3), the reader may be convinced by the presence of the convolution. The convolution is a global smoothing operation, it does not rescale locally. Image distortion can be considered as tip-tilt error that depends non-uniformly on the direction of the source point in field of view.

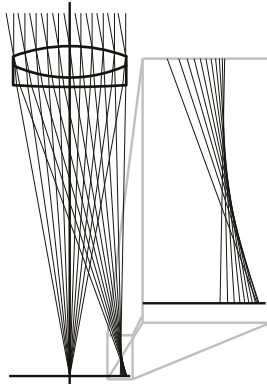


Figure 2.9: Example of anisoplanatic imaging. Parallel light rays that are inclined to the optical axis of the lens do not intersect in a point of the image plane.

The two assumptions above are always fulfilled within a limited angular range for which equation (2.3) is applicable. Numerical models of imaging larger, *anisoplanatic* angular fields can be implemented by breaking imaging down to small isoplanatic patches and combining them afterwards.

Imaging through Earth's turbulent atmosphere is generally not shift-invariant. This effect is called *angular anisoplanatism* of the atmosphere and is the challenge of multi-conjugate adaptive optics (MCAO).

2.2.2 Angular resolution and imaging quality of ideal and imperfect telescopes

The point spread function of a telescope free of aberrations, i. e. diffraction limited, with a clear circular aperture is

$$\text{PSF}_{\odot}(r) = \left[\frac{J_1\left(\pi D \frac{r}{\lambda f}\right)}{D \frac{r}{\lambda f}} \right]^2, \quad (2.8)$$

where r is the radial image plane coordinate, J_1 is the Bessel function of first kind. The imaging system is characterized by the aperture diameter D and the focal length f . The optical wavelength of the light considered is represented by λ . The spatial coordinate r can be translated to the angular distance α of the object to the optical axis of the imaging system using the paraxial approximation $\alpha = r/f$. Equation (2.8) is referred to as *Airy disc*[‡] and is plotted in figure 2.10. Its first root appears at the radius $r_{\min} = 1.22 f \lambda/D$ and accordingly at the angle $\alpha_{\min} = 1.22 \lambda/D$.

A common but somewhat arbitrary definition of the diffraction limited resolution of an imaging system is given by the *Rayleigh criterion*[§]. Accordingly, two equally bright point sources are considered as being resolvable if their positions coincide with each others first

[‡]named after George Biddell Airy (1801-1892), English mathematician and astronomer

[§]named after John Strutt, 3rd Baron Rayleigh (1842-1919), English physicist

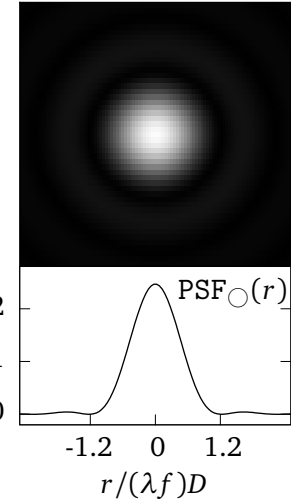


Figure 2.10: Airy disc.

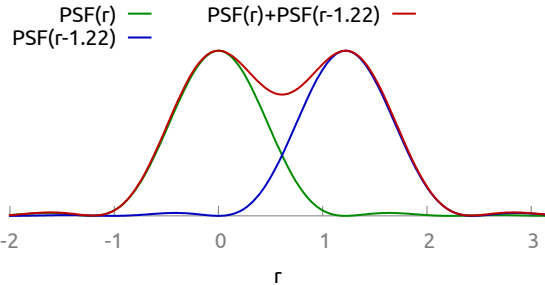


Figure 2.11: Illustration of the Rayleigh criterion.

roots (fig. 2.11), that is if the condition

$$\delta\alpha > 1.22 \lambda/D . \quad (2.9)$$

is satisfied where $\delta\alpha$ is the angular separation of the point sources measured in radians. In practice, the resolution limit is usually smaller—depending on the signal-to-noise ratio of the detector in use—and the factor 1.22 is often omitted or replaced by smaller values. The core of this section shall be:

The larger the aperture, the higher is the angular resolution of an ideal telescope at a given wavelength.

2.2.2.1 The Strehl ratio

The quality of imperfect imaging is often related to diffraction limited imaging. A figure of merit is the *Strehl ratio*[¶] which is defined by the ratio of the peak intensities of the aberrated and the diffraction limited point images, i. e.

$$S := \frac{\max(I_{\text{aberrated}})}{\max(I_{\text{ideal}})} \leq 1 . \quad (2.10)$$

The Strehl ratio disregards the image shift since it only refers to the peak intensities regardless of their positions. If $\phi(\rho, \theta)$ represents the wavefront error measured in radians of the imperfect system specified within the unit circle, i. e. $0 \leq \rho \leq 1$ and $0 \leq \theta \leq 2\pi$, and if both

[¶]named after Karl Strehl (1864-1940), German physicist and mathematician

average offset and slope have been removed from $\phi(\rho, \theta)$, the Strehl ratio can be calculated by

$$S = \frac{1}{\pi^2} \left| \int_0^1 \int_0^{2\pi} e^{i\phi(\rho, \theta)} \rho \, d\theta \, d\rho \right|^2. \quad (2.11)$$

This integral is usually simplified in the field of adaptive optics to

$$S \approx e^{-\sigma_\phi^2}, \quad (2.12)$$

where σ_ϕ^2 is the variance of the wavefront aberration within the aperture. This approximation, which is sometimes referred to as *extended Marechal approximation*, is valid up to about $\sigma_\phi = 2$ rad. According to Marechal, a system should be considered to be diffraction limited, if $S > 0.8$, and correspondingly $\sigma_\phi < 2\pi/14$ rad.

2.3 Imaging through atmospheric turbulence

The instantaneous distortion of an incident light wavefront from outer space caused by an optically turbulent layer in the atmosphere at height h can be modeled by

$$\phi(x, y; t) = \frac{2\pi}{\lambda} \int_h^{h+\delta h} n_\lambda(x, y, z; t) dz, \quad (2.13)$$

where $n_\lambda(x, y, z; t)$ is the instantaneous refractive index for the wavelength λ . The thickness of the turbulent layer is denoted δh . This is the *geometric approach* that neglects diffraction effects, which is adequate for the geometric sizes typically involved if the turbulence is not too strong. It is assumed, in addition, that $n_\lambda(x, y, z; t)$ is constant within the very short propagation time ($< 1 \mu s$) of the light wave through the turbulent layer. In fact, the refractive index fluctuates significantly on the scale of milliseconds. Airflows in Earth's atmosphere are almost always turbulent. The turbulence strength, however, varies greatly with height. Strong turbulence is often concentrated in a few layers. The thickness of turbulent layers is typically hundreds of meters. Capturing optical images of astronomical objects typically involves camera exposure times T which exceed by far the fluctuation time scale of milliseconds. Consequently, the image quality is affected by a statistical ensemble of wavefronts $\{\phi(x, y; t)\}_{t \in T}$ and not just by a single random realization.

The *Fried parameter* r_0 is a widely used measure of the spatial strength of turbulence effects on optical imaging. It denotes the maximum diameter of an imaginary telescope whose resolution limit would be just determined by diffraction and not by atmospheric degradation. This situation is known as *seeing limit*. A small value of r_0 corresponds to strong turbulence. The Fried parameter may change substantially within seconds. In the visible light regime, it is typically in the order of decimeters during night and in the order of 5–20 cm during day. Daytime seeing is stronger because the energy input of the sun light is fueling the

turbulence—in particular at the ground, in which the vast majority of the solar flux is absorbed. Thus, the advantage of larger telescopes without seeing compensation is limited to greater light-collecting area allowing shorter exposure times or increased signal-to-noise ratio and it does not include sharper images.

Turbulent airflows—whose dynamic forces you may experience on airplane flights—themselves would not impact the propagation of light, not until air masses with different temperatures are mixed. The optical index of refraction of air is sensitive to the air's temperature. Thus, a wavefront gets significantly crumpled while traveling through a region with small air bubbles with differences in temperatures in the order of 1°C . Although the index of refraction also depends on the air pressure, fluctuations of pressure relax with the speed of sound and thus are negligible compared to temperature fluctuations.

2.3.1 Statistical model of atmospheric turbulence

The fluctuations of temperature in the atmosphere and hence of the refractive index are dominated by the fluctuations of speed of airflows. In 1941, Andrei N. Kolmogorov came up with a model of turbulence occurring in flows of incompressible fluids. His model is also applicable to air because the viscosity of gases at pressures from about 0.1–10 bars is independent of the gas pressure. Kolmogorov's model is the base of today's understanding of atmospheric turbulence in the field of adaptive optics.

The vast majority of the energy of the turbulent motions in the atmosphere was entered by the light of the Sun. In Kolmogorov's model, this energy input causes large scale disturbances, often called *eddies*, which break down in a cascade to smaller and smaller structures. This effect can be visually observed when cold milk is poured into hot beverages. When the ratio of inertial forces and viscous forces falls below a certain level, the energy of air mass flow is dissipated into frictional heat and turbulence dies away. The spatial scale L_0 of the input disturbances is called *outer scale* and ranges from tens to hundreds of meters. The scale l_0 in which energy of turbulent motion is dissipated into heat is called *inner scale* and is in the range of millimeters. Turbulence is assumed to be isotropic, homogeneous and stationary.

2.3.1.1 The structure function – a measure of fluctuation strengths

The random variables appearing in atmospheric turbulence modeling, for example temperature, are not necessarily stationary but may show changing mean values within the interval under consideration. The variance is not a good measure of the strength of fluctuation of such a random variable because it does not distinguish between fast fluctuations (the random process under consideration) and slow changes (superimposed / underling processes). The structure function

$$D_f(\tau) := \langle [f(t + \tau) - f(t)]^2 \rangle_t, \quad (2.14)$$

which was introduced by Kolmogorov, is a useful measure of the fluctuation of a non-stationary random variable $f(t)$ over intervals in the order of τ and smaller. The physical quantity of t can be both time and space within the present context.

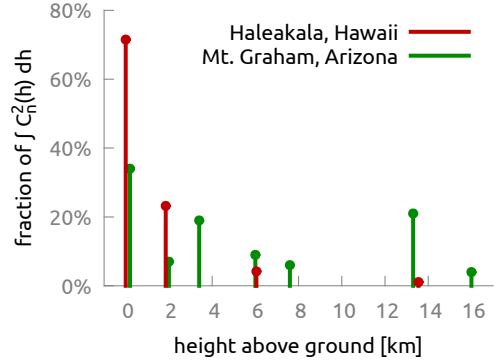


Figure 2.12: Example of a discrete $C_n^2(h)$ profile estimation as used by Marino for AO system simulations (Rimmele and Marino, 2011); data is based on work by Rimmele et al. (2006) and Milton et al. (2003)

2.3.1.2 Optical phase fluctuations

Tatarski (1961) derived the spatial power spectrum of refractive index variations

$$F_n(\kappa) = 0.033 C_n^2 \kappa^{-11/3} \quad \text{with } \kappa = \frac{2\pi}{l} \text{ and } L_0 > l > l_0 \quad (2.15)$$

from Kolmogorov's mechanical turbulence model. In the derivation of this equation, the relation $\delta n = 7.9 \cdot 10^{-6} p/T^2 \delta T$ between the refractivity fluctuation δn and the temperature fluctuation of δT is used. The air pressure is represented by p . It is assumed additionally that the scale of temperature fluctuations and of velocity fluctuations, occurring when air with different temperatures gets mixed, are the same. The parameter C_n^2 , which is referred to as *refractive index structure parameter*, is a measure of the strength of the optical turbulence. It depends on the air temperature and pressure as well as on the energy dissipation rate per mass. C_n^2 varies greatly with height, hence it is actually $C_n^2(h)$ (fig. 2.12). There is a number of theoretical models for $C_n^2(h)$ profiles, but measured profiles are more authentic and are usually considered for the design of adaptive optics systems. However, the $C_n^2(h)$ profile at a given site is not stable but may vary during the year and from day to night.

The *phase structure function* represents the mean quadratic difference of phase of two separate points. It can be written as

$$D_\phi(r) = 6.88 \left[\frac{r}{r_0} \right]^{5/3} \text{ rad}^2 \quad (2.16)$$

according to Fried (1965), where r is the distance of the two points. Again, this expression is valid between L_0 and l_0 . The proportionality constant 6.88, which can be more precisely evaluated through $2 [24/5 \Gamma(6/5)]^{5/6}$, follows from the definition of r_0 , referred to as *Fried parameter*, to be «[the] diameter of a heterodyne collector for which distortion effects begin to seriously limit performance». Fried also showed that the mean squared wavefront error (including tilt but without piston) is $\Delta_\phi \approx 1.030 \text{ rad}^2$ within the diameter r_0 (sec. 2.3.2.2). The formal definition of the Fried parameter is

$$r_0 := \left[0.423 k^2 \frac{1}{\cos(\beta)} \int_h C_n^2(h) dh \right]^{-3/5}, \quad (2.17)$$

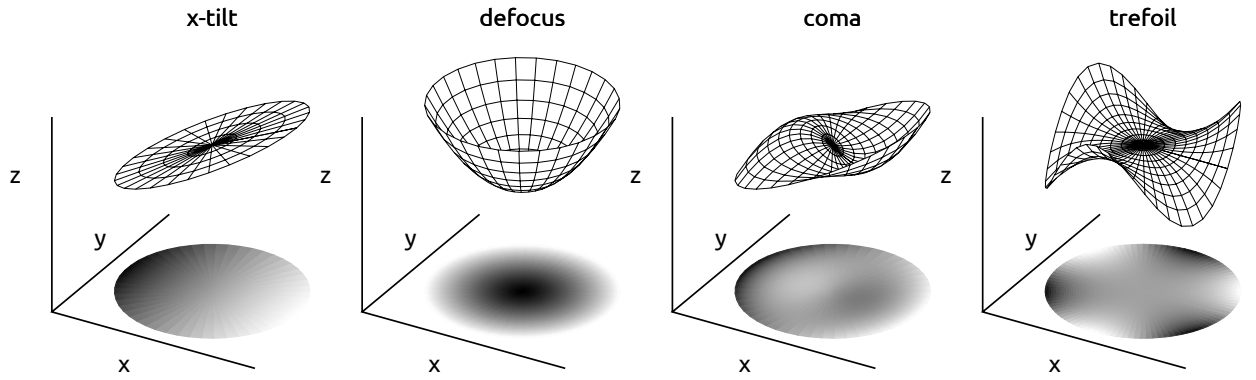


Figure 2.13: Wavefronts of four basic optical aberrations.

where β is the angle of the observing direction to zenith and $k = 2\pi/\lambda$.
The power spectrum of the phase fluctuations is

$$\Phi_\phi(k) = 0.023 r_0^{-5/3} \kappa^{-11/3}. \quad (2.18)$$

Integrating this yields the mean square wavefront error Δ_ϕ in square radians within the diameter r_0

$$\Delta_\phi = \int \Phi_\phi(\kappa) d^2\kappa. \quad (2.19)$$

2.3.2 Modeling wavefronts with Zernike polynomials

Instantaneous atmospheric wavefronts are random but smooth and in the scope of imaging they are always considered within a limited area only. Any Wavefront ϕ within a circular region of radius R can be represented by an infinite series of *Zernike polynomials*^{||} $Z_j(\rho, \theta)$, i. e.

$$\phi(R\rho, \theta) = \sum_{j=1}^{\infty} a_j Z_j(\rho, \theta). \quad (2.20)$$

$0 \leq \rho \leq 1$ and $0 \leq \theta \leq 2\pi$ are the polar coordinates of the unit circle. Zernike polynomials offer an orthogonal set of basis modes, and they are widely used in optics to model wavefronts in circular apertures because the lower orders are identical to typical aberrations of imperfect optical systems. Zernike polynomials, which will also be referred to as *Zernike modes* in this document, are characterized and ordered by the radial frequency n and by the azimuthal frequency m . Modes 1 through 11 are listed in table 2.1. The general definition including

^{||}named after Frits Zernike (1888-1966), Dutch physicist and Nobel prize laureate 1953

the normalization introduced by Noll (1976) reads

$$Z_j(\rho, \theta) := Z_n^m(\rho, \theta) := \sqrt{n+1} R_n^m(\rho) \cdot \begin{cases} \sqrt{2} \cos(m\theta) & , \text{ if } m > 0 \\ 1 & , \text{ if } m = 0 \\ \sqrt{2} \sin(m\theta) & , \text{ if } m < 0 \end{cases} \quad (2.21)$$

where ρ and θ are the polar coordinates of the unit circle and

$$R_n^m(\rho) := \sum_{l=0}^{[n-m]/2} \frac{[-1]^l [n-l]}{l! [\frac{n+m}{2}-l]! [\frac{n-m}{2}+l]!} \rho^{n-2l} \quad (2.22)$$

for $n \in \mathbb{N}$ with

$$m = -n, \dots, 0, \dots, n \quad \text{and} \quad (n-m) \text{ even.} \quad (2.23)$$

Noll defined a relation of frequencies n and m to the single index j in his essay by a set of literal ordering instructions. A mathematical expression for translating the Noll index j into n and m was found by von der Lühe (unpublished) which reads:

$$n = \text{fix}\left(-0.5 + \sqrt{2.0j - 7/4}\right) \quad (2.24)$$

$$m = -1^k \cdot k \quad (2.25)$$

with

$$k = j - \frac{n[n+1]}{2} + 1 + \text{rem}\left(j - \text{rem}\left(\frac{n[n+1]}{2} + 1, 2\right) + \text{rem}(n, 2), 2\right) \quad (2.26)$$

The operator expression $\text{fix}(x)$ rounds x towards zero, e. g. $\text{fix}(-\pi) = -3$ and $\text{fix}(\pi) = 3$. The expression $\text{rem}(n, 2)$ represents the remainder of the integer devision $n/2$, e. g. $\text{rem}(7, 2) = 1$. These terms coincide with the corresponding functions of Matlab / GNU Octave. The expansion of an arbitrary wavefront $\phi_0(R\rho, \theta)$ into Zernike coefficients a_j is given by

$$a_j = \frac{1}{\pi} \int_0^1 \int_0^{2\pi} \phi_0(R\rho, \theta) Z_j(\rho, \theta) \rho d\theta d\rho \quad (2.27)$$

$$= \frac{1}{\pi R^2} \int_0^R \int_0^{2\pi} \phi_0(r, \theta) Z_j(r/R, \theta) r d\theta dr. \quad (2.28)$$

The normalization factors $\sqrt{n+1}$ and $\sqrt{n+1}\sqrt{2}$ in equation (2.21) were introduced by Noll. The advantage of Noll's normalization is the unity of the mean square of his modified polynomials, i. e.

$$\frac{1}{\pi} \int_0^1 \int_0^{2\pi} [Z_j(\rho, \theta)]^2 \rho d\theta d\rho = 1 \quad \text{for } j \geq 2. \quad (2.29)$$

Table 2.1: The first 11 Zernike polynomials.

j	n	m	$Z_n^m(\rho, \theta)$	optical meaning
1	0	0	1	piston
2	1	+1	$2\rho \cos(\theta)$	x -tilt
3	1	-1	$2\rho \sin(\theta)$	y -tilt
4	2	0	$\sqrt{3}[2\rho^2 - 1]$	defocus
5	2	-2	$\sqrt{6}\rho^2 \sin(2\theta)$	astigmatism
6	2	+2	$\sqrt{6}\rho^2 \cos(2\theta)$	astigmatism
7	3	-1	$\sqrt{8}[3\rho^2 - 2\rho] \sin(\theta)$	coma
8	3	+1	$\sqrt{8}[3\rho^2 - 2\rho] \cos(\theta)$	coma
9	3	-3	$\sqrt{8}\rho^3 \sin(3\theta)$	trefoil, 0
10	3	+3	$\sqrt{8}\rho^3 \cos(3\theta)$	trefoil, 30
11	4	0	$\sqrt{5}[6\rho^4 - 6\rho^2 + 1]$	spherical aberration

Hence, the mean squared error of the wavefront $\phi(R\rho, \theta) = \sum_{j=2}^{\infty} a_j Z_j(\rho, \theta)$ is given by

$$\Delta_\phi := \frac{1}{\pi} \int_0^1 \int_0^{2\pi} [\phi(R\rho, \theta)]^2 \rho \, d\theta \, d\rho = \sum_{j=2}^{\infty} a_j^2. \quad (2.30)$$

2.3.2.1 Statistics of Zernike coefficients of atmospheric wavefronts

An instantaneous atmospheric wavefront $\phi(R\rho, \theta)$ can be described by a random set of coefficients $\{a_j\}$ according to the expansion integral in equation (2.27). Besides showing that the derivative in Cartesian coordinates of Zernike mode Z_j is a linear combination of Zernike modes lower than j , Noll also elaborated on the statistics of the random coefficients for an ensemble of atmospheric wavefronts in his famous essay (Noll, 1976). Accordingly, the coefficients $\{a_j\}$ with $j \geq 2$ of a wavefront ensemble undergone Kolmogorov turbulence can be considered to be Gaussian random variables with zero mean, i. e.

$$\langle a_j \rangle = 0. \quad (2.31)$$

However, the coefficients are not statistically independent, and Noll derived an analytical expression for their covariance, which shall not be repeated here. The covariance of two coefficients a_{j_1} and a_{j_2} is zero if and only if their azimuthal frequencies m_1 and m_2 are different. Due to the power law of the phase fluctuation (eq. (2.18)), the variance $\langle a_j^2 \rangle$ of the Zernike coefficients of atmospheric wavefronts drops as the radial frequency m increases as shown in figure 2.14. The piston mode Z_1 is not effective to optical aberration and its variance in Kolmogorov turbulence is infinity.

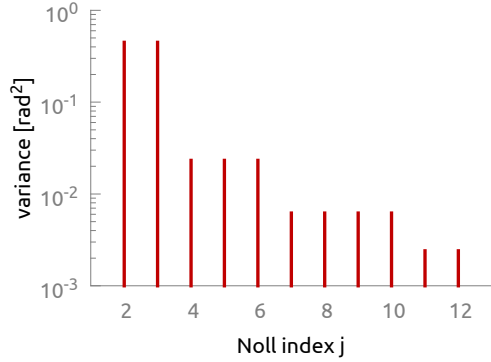


Figure 2.14: Variance of low order Zernike coefficients of atmospheric wavefronts within the diameter r_0 .

2.3.2.2 Compensation of atmospheric wavefronts with Zernike modes

The decreasing statistical contribution of high-order Zernike modes to atmospheric wavefronts implies that compensating low order Zernike modes is most effective. Separating the Zernike expansion of the wavefront in equation (2.20) into low and high-order modes yields

$$\phi(R\rho, \theta) = \underbrace{\sum_{j=1}^J a_j Z_j(\rho, \theta)}_{=: \phi_J(R\rho, \theta)} + \sum_{j=J+1}^{\infty} a_j Z_j(\rho, \theta). \quad (2.32)$$

The mean-square residual error after removing the first J Zernike mode from a wavefront sample $\phi(R\rho, \theta)$ is then

$$\Delta_J := \frac{1}{\pi} \int_0^{2\pi} \int_0^1 \langle [\phi(R\rho, \theta) - \phi_J(R\rho, \theta)]^2 \rangle \rho \, d\theta \, d\rho, \quad (2.33)$$

and is only determined by fluctuations of a_j with $j > J$. The combination of equations (2.31)–(2.33) results in

$$\Delta_J = \langle [\phi(R\rho, \theta)]^2 \rangle - \sum_{j=1}^J \langle |a_j|^2 \rangle. \quad (2.34)$$

Noll approximated this by

$$\Delta_J = A_J \left[\frac{d}{r_0} \right]^{5/3} \text{rad}^2, \quad (2.35)$$

where $d = 2R$ is the diameter of the considered area and r_0 is the Fried parameter. The first 12 parameters A_J are specified by

$$\begin{aligned} A_1 &= 1.030 & A_2 &= 0.582 & A_3 &= 0.134 & A_4 &= 0.111 \\ A_5 &= 0.088 & A_6 &= 0.065 & A_7 &= 0.059 & A_8 &= 0.053 \\ A_9 &= 0.046 & A_{10} &= 0.040 & A_{11} &= 0.037 & A_{12} &= 0.034 \end{aligned} \quad (2.36)$$

and for higher orders they can be calculated by

$$A_J \approx 0.2944 J^{-\sqrt{3}/2} \text{ rad}^2, \text{ for } J > 10. \quad (2.37)$$

The residual wavefront error of uncompensated turbulence without the piston term Z_1 is $\Delta_1 = 1.03 [d/r_0]^{5/3} \text{ rad}^2$. By perfectly compensating the first 10 modes, the residual error is reduced to about 4%.

The error of atmospheric wavefront distortion on account of wavefront tilt is

$$\Delta_1 - \Delta_3 = 0.896 \left[\frac{D}{r_0} \right]^{5/3} \text{ rad}^2. \quad (2.38)$$

The angle of arrival α is the direction in which a star is seen by the telescope. Its fluctuation in a single axis can be expressed by the variance

$$\sigma_\alpha^2 = 0.182 \left[\frac{D}{r_0} \right]^{\frac{5}{3}} \left[\frac{\lambda}{D} \right]^2 = 0.182 \lambda^2 D^{-1/3} r_0^{-5/3} \text{ rad}^2. \quad (2.39)$$

Note that, in equation (2.39), *rad* represents a geometric angle and not the phase error of the wavefront. Almost 90% of atmospheric wavefront error is attributed to random image motion which is represented by the linear modes Z_2 and Z_3 . Consequently, image stabilization is the most effective and most important task in turbulence compensation. Numerical examples of angle of arrival fluctuation for typical daytime seeing ($r_0 = 0.1 \text{ m}$) and nighttime seeing ($r_0 = 0.5 \text{ m}$) for various telescope diameters D at $\lambda = 500 \text{ nm}$ are given in table 2.2.

Table 2.2: Examples of angle of arrival fluctuations.

$D \text{ [m]}$	$r_0 \text{ [m]}$	$\sigma_\alpha [\text{"}]$
0.7	0.1	0.32
0.7	0.5	0.08
1.5	0.1	0.28
1.5	0.5	0.07
4	0.1	0.24
4	0.5	0.06
10	0.1	0.20
10	0.5	0.05
42	0.5	0.04

2.3.3 Temporal characteristics of atmospheric turbulence

So far, the introduction to atmospheric turbulence only considered spatial effects. Being to correct seeing with adaptive optics, knowing the temporal characteristics of the wavefront is as important as knowing their spatial attributes. The spatial statistics discussed above apply on both areal and temporal wavefront ensembles. The velocities within the turbulence,

however, are typically much slower than the wind speed. It is common practice in the field of adaptive optics (at least for small telescopes) to regard the turbulence structure (i. e. the refractive index distribution) as "frozen" whilst being translated by wind across the telescope aperture. If the wind speed is \vec{v} , the wavefront at position \vec{x} at the instant $t + \Delta t$ can be estimated by

$$\phi(\vec{x}; t + \Delta t) = \phi(\vec{x} - \vec{v} \Delta t; t). \quad (2.40)$$

This is known as Geoffrey I. Taylor's *frozen flow hypothesis*. A spatio-temporal phase structure function $D_\phi(x, t)$ can be formulated taking Taylor's hypothesis into account. In analogy to the Fried parameter which quantifies the spatial coherence length of turbulence, a coherence time τ_0 can be defined to be the difference of time for which the spatio-temporal structure function $D(0, \tau_0) = 1 \text{ rad}^2$. This yields to

$$\tau_0 = 0.314 \frac{r_0}{\bar{V}}, \quad (2.41)$$

where

$$\bar{V} := \left[\frac{\int_0^\infty |\vec{v}(h)|^{5/3} C_n^2(h) dh}{\int_0^\infty C_n^2(h) dh} \right]^{3/5} \quad (2.42)$$

is the wind speed average which is weighted with the turbulence strength distribution. Typical values of \bar{V} range from 10–30 m/s resulting in τ_0 in the order of 3–10 ms for $r_0 = 10 \text{ cm}$. Greenwood (1977) showed that the minimum 3-dB-bandwidth** of the adaptive optics control system that is required to compensate for atmospheric turbulence is

$$f_G = \left[0.102 \kappa^2 \sec(\xi) \int_0^\infty C_n^2(h) v(h)^{5/3} dh \right]^{3/5}. \quad (2.43)$$

and that the residual mean squared wavefront error scales with the actual bandwidth $f_{3 \text{ dB}}$ of a control system according to

$$\Delta_{\text{bandwidth}}^2 = \left[\frac{f_G}{f_{3 \text{ dB}}} \right]^{5/3}. \quad (2.44)$$

Fried (1990) showed that the *Greenwood frequency* f_G is related to the coherence time through

$$f_G \approx \frac{0.134}{\tau_0} = 0.427 \frac{\bar{V}}{r_0}. \quad (2.45)$$

The Greenwood frequency is typically in the order of 100 Hz.

**The 3-dB-bandwidth, also 3-dB-cutoff-frequency, is the frequency of the error signal at which the damping falls below 3 dB, i. e. when less than 50 % of the spectral power is eliminated.

2.3.3.1 Temporal power spectra of Zernike coefficients

The power spectrum $W_{a_j}(\nu)$ of Zernike coefficient a_j of atmospheric wavefronts as a function of temporal frequency ν is

$$W_{a_j}(\nu) \propto \begin{cases} \nu^{-2/3} & , \text{ if } \nu < \nu_c \text{ and } j \in \{2, 3\} \\ \nu^0 & , \text{ if } \nu < \nu_c \text{ and } j \geq 4 \\ \nu^{-17/3} & , \text{ if } \nu > \nu_c \end{cases}, \quad (2.46)$$

as shown by Conan et al. (1995) by combining Taylor's frozen flow hypothesis with Kolmogorov's spatial turbulence. The cut-off frequency ν_c can be estimated by

$$\nu_c \approx 0.3 [n+1] \frac{\bar{V}}{d}, \quad (2.47)$$

where d is the aperture diameter and n is the radial frequency corresponding to the Noll index j . The averaged wind speed \bar{V} was defined in equation (2.42). The cut-off frequency for turbulence induced image motion (linear wavefront errors, i.e. $n = 1$), for a 1.5 m aperture is typically in the order of 5–15 Hz. Exemplified spectra are plotted in figure 2.15.

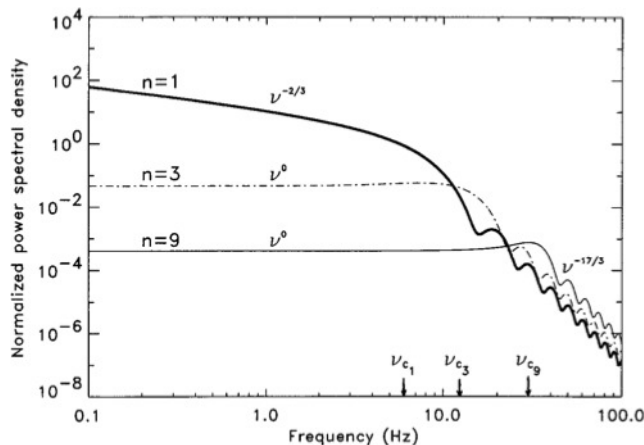


Figure 2.15: Zernike polynomial mean temporal power spectra in a given radial degree n for $n = 1, 3, 9$. The spectra are normalized to the turbulence variance of one polynomial of the considered radial degree; $\bar{V}/d = 10$ Hz. The asymptotic power laws and the cutoff frequencies are indicated. (Graphic and caption taken from Conan et al. (1995))

2.3.4 Angular anisoplanatism – the need for MCAO

This section discusses the feature of atmospheric turbulence that motivates the demand of astronomers not only for adaptive optics but for multi-conjugate adaptive optics. Optical imaging (as discussed on page 27) is called *isoplanatic* if the wavefronts emerging from all points of the object are identical when being focussed to the image plane. Imaging through the turbulent atmosphere is not isoplanatic because turbulence is present within a wide range of heights. If turbulence were limited to the ground layer, the wavefront error would be independent of the viewing angle (fig. 2.4). Such a wavefront could be flattened by a single adaptive mirror. However, as soon there is a turbulent layer above the telescope the

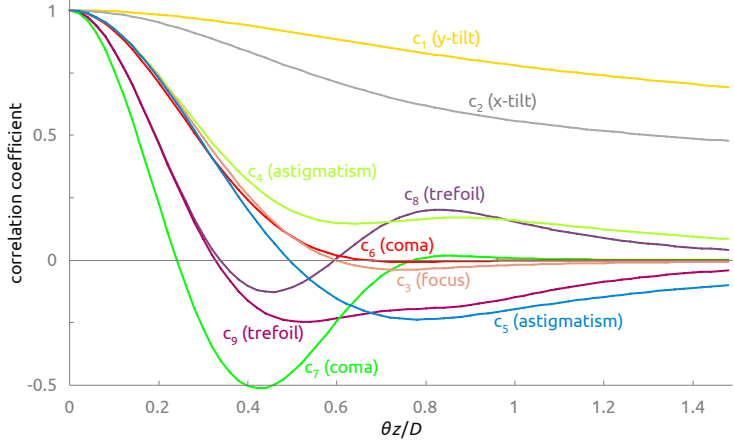


Figure 2.16: Correlation of Zernike coefficients seen in a telescope with diameter D in two directions as a function of the angular difference θ for a turbulent layer in the height z . The angle θ is oriented in the x -direction. (Reproduced from Berkefeld (1998))

wavefronts for different directions inevitably decorrelate. The correlation of the Zernike coefficients seen in different viewing directions for Kolmogorov-like wavefronts in a turbulent layer is plotted in figure 2.16. The correlation functions for the x - and y -tilt differ, because the viewing directions are separated in x -direction and hence symmetry is broken. The same is true for the other modes with $m \neq 0$. The Strehl ratio as a function of the field angle for a modeled single conjugate adaptive optics system is shown in figure 2.17.

The mean square wavefront difference of two directions separated by the angle θ can be written as

$$\Delta_\theta := \frac{1}{\pi} \int_{\text{aperture}} \left\langle [\phi_{\theta_1} - \phi_{\theta_1 + \theta}]^2 \right\rangle d^2r \quad (2.48)$$

The *isoplanatic angle* θ_0 is defined to be the angle for which $\Delta_\theta = 1 \text{ rad}^2$. It can be calculated by

$$\theta_0 = 0.314 \cos(\xi) \frac{r_0}{h}, \quad (2.49)$$

where

$$\bar{h} := \left[\frac{\int_0^\infty C_n^2(h) h^{5/3} dh}{\int_0^\infty C_n^2(h) dh} \right]^{3/5} \quad (2.50)$$

is the average turbulence height weighted with the $C_n^2(h)$ -profile. The mean-square wavefront difference of two directions increases with their angular separation θ as

$$\Delta_\theta = \left[\frac{\theta}{\theta_0} \right]^{5/3} \text{ rad}^2. \quad (2.51)$$

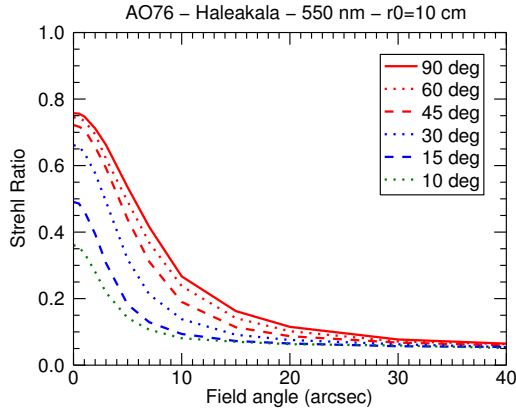


Figure 2.17: Exemplary plot of Strehl ratio vs. field angle. Plotted data represents the typical situation for a solar telescope at a good site with a single conjugate adaptive optics system (numerically modeled). Curves for various elevations of the Sun are shown (90 deg=zenith). The simulated turbulence strength is indicated by $r_0 = 10$ cm. Courtesy of Jose Marino (NSO). Imaging is nearly diffraction limited in the center of the field (0 arcsec). Full-width half-maximum is less than 8 arcsec.

The field of view with diameter θ_0 is referred to as *isoplanatic patch*. This is the field for which a single-conjugate adaptive optics is most effective. The isoplanatic angle is typically less than 10 arcseconds for solar observations in the visible light regime. This angle can be small compared to extensions of scientifically interesting solar regions such as sunspots which can extend over more than 100 arcseconds.

2.4 Wavefront modulators

Deformable mirrors are the main type of wavefront modulators used in adaptive optics of astronomical telescopes. The shape of the reflective surface of deformable mirrors can be controlled quickly by means of *actuators*. The resulting wavefront deformation is twice the mechanical surface shape of the mirror. The required stroke required to compensate for atmospheric turbulence can be calculated from the phase structure function (eq. (2.16)) and is typically in the order of a couple of micrometers. An alternative technology for wavefront modulation is provided by liquid crystals whose refractive index can be controlled by electrical fields. Transmissive devices with constant refractivity but controllable surfaces could also be used as wavefront modulators. However, transmissive optics are usually prone to dispersion whereas reflective optics are not. Deformable mirrors have been established as an adequate approach for astronomical adaptive optics. However, deformable mirrors are two-dimensional devices and as such they cannot provide continuous wavefront modulation in three dimensions, as it might be desirable for "ultimate adaptive optics" which would compensate for the whole turbulent volume in the field of view.

2.4.1 Types of deformable mirrors

Most deformable mirrors are made of a thin, continuous, reflective face plate which is bent by numerous electrically controlled actuators. In the early years of adaptive optics, some devices were also composed of push- and tiltable mirror segments. Actuators are realized by either piezo-electric, by electro-static (micro-electro-mechanical systems, MEMS), or by magnetic forces (voice coils). Today, deformable mirrors are available as off-the-

shelf or customized products from specialized companies, and development is ongoing. A comprehensive overview of up to date deformable mirror technologies and vendors was recently prepared by Madec (2012).

Deformable mirrors are much smaller than telescope apertures. The main advantage of smaller face plates, except of eased feasibility, is their increased resonance frequency (similar to the strings of a harp) and the lower moments of inertia, resulting in less forces and powers required and faster devices. The actual size of a deformable mirror is mostly determined by the mirror type and the number of actuators. Thus, the light beam inside in the telescope needs to be scaled to an appropriate footprint.

This section shall introduce the two main mirror types that are currently in operation at solar telescopes and which are used in the GREGOR MCAO testbed. Both types use the reverse piezo-electric effect of certain ceramics: An electric field is applied to the piezo ceramics which is oriented parallel to the internal polarization of the material. If the ceramic is unstressed, it changes its length l_{\parallel} measured parallel to the electric field by

$$\delta l_{\parallel} = E d_{3,3} l_{\parallel} \quad (2.52)$$

and its length l_{\perp} perpendicular to the field by

$$\delta l_{\perp} = E d_{3,1} l_{\perp} \quad (2.53)$$

for limited field strengths E . The material parameters $d_{3,3}$ for the *longitudinal effect* and $d_{3,1}$ for the *transversal effect* are named *strain constants*. Lead zirconate titanate (PZT) is a piezo ceramic which is widely used for actuators. The strain constants for such materials according to *Physikinstrumente* are $d_{3,3} \approx 250\text{--}550 \text{ pm/V}$ and $d_{3,1} \approx -0.5 d_{3,3}$. The maximum field strength is about 1–2 kV/mm in polarization direction. Fields up to about 300 V/mm may be applied in opposite direction for short times only. An alternative material that is used for deformable mirrors is lead magnesium niobate (PMN).

2.4.1.1 Discrete piezo actuator mirrors

The reflective face plate is made of glass and is up to a few millimeters thick. The actuators are piezo ceramic bars which are bonded to the flexible face plate on one side and to the stiff base plate on the other side, as sketched in figure 2.19. The actuators can push and pull the face plate punctually by applying electrical voltages of some hundreds volts.

The actuators in deformable mirrors may either use the transversal or the longitudinal piezo-electric effect as shown in figure 2.18. Actuators based on the transversal effect are long slats, and the voltage is applied to electrodes at the sides. The company *Flexible Optical B.V.* provides mirrors based this effect. The longitudinal effect is exploited by stacking a number of thin piezo disks with alternating polarization which are separated by electrodes. Mirrors using this effect are provided, for example, by *CILAS* and by *AOA Xinetics*.

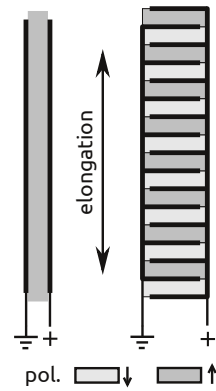


Figure 2.18: Cross-section of piezo actuators using the transversal (left) and the longitudinal effect (right). Gray levels indicate the polarization of the piezos.

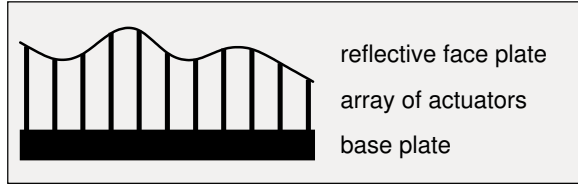


Figure 2.19: Cross-section of a deformable mirror with discrete piezo actuators (deflection is not to scale).

2.4.1.2 Bimorph mirrors

Bimorph mirrors can be made of two large, equally polarized piezo-ceramic disks which are separated by a thin electrode layer which forms the actuators as shown in figure 2.20. Additional electrode layers are attached to the outside faces of the piezo disk. One surface has optical quality and is reflectively coated. The piezo disks are thin compared to the actuator size, so that applying a voltage mostly results in lateral elongation of the piezo material between the electrodes due to the transversal piezo effect. However, since the electrode voltage is oppositely applied to the piezo ceramics in the top and bottom disk, the piezo material surrounding an actuator electrode expands in one disk while contracting in the other disk. The consequence is a local curvature of the layer composite because the disks are equally stiff. Since the transversal piezo effect is exploited in bimorph mirrors, the actuator stroke is determined by the lateral size of the actuator. Actuators of bimorph mirrors are much larger than discrete piezo actuators. The bending forces in bimorph mirrors are produced in the bimorph composite itself and a reaction structure like a massive base plate or ring is not required. The bimorph plate can be supported rather simply. The name *bimorph* refers to the Greek word *morphe* for shape and to the fact that two piezo disks are used. Bimorph mirrors are available, for example, from *Night N Opt* and *CILAS*.

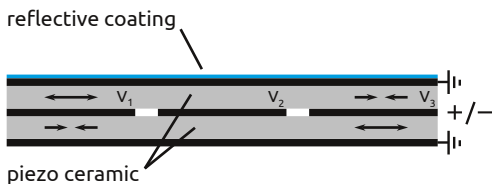


Figure 2.20: Cross-section of a bimorph mirror. Three actuator electrodes are sketched in between two piezo disks. The top disk expands locally while the bottom disk contracts (or vice versa) and a local curvature is produced when voltages are applied to the electrodes.

2.4.2 Wavefront modulation with deformable mirrors

Reflecting a wavefront at a deformable mirror yields the wavefront modulation

$$\psi(x, y) = 2 \cdot \text{mechanical surface shape} \cdot 2\pi/\lambda \text{ rad}. \quad (2.54)$$

The *influence function* $\psi_i(x, y)$ of actuator i is the wavefront modulation when a unit voltage is applied. Deformable mirrors with piezo actuators are linear within the operating range, i. e. the wavefront modulation $\Psi(x, y)$ when an arbitrary voltage v_i is applied to the i^{th} of all N actuators of the mirror can be calculated by the linear combination

$$\Psi(x, y) = \sum_{i=1}^N v_i \psi_i(x, y). \quad (2.55)$$

Non-linearities like hysteresis and creep are present, but they are compensated by the closed control loop which iteratively minimizes the residual error.

Influence functions of discrete piezo mirrors can be roughly estimated by Gauss functions in order to construct a simple (numerical) model of the mirror. Influence functions are practically orthogonal in the sense that no influence function can be reproduced by using other actuators. Thus, it is possible to fit the mirror to an arbitrary wavefront $\phi(x, y)$ by orthogonally projecting it onto the influence functions, i. e. applying the voltage

$$v'_i = \iint_{\text{aperture}} \phi(x, y) \psi_i(x, y) dx dy \quad (2.56)$$

to the i -th actuator. This results in the wavefront modulation

$$\Psi_{\text{fit}}(x, y) = \sum_{i=1}^N v'_i \psi_i(x, y). \quad (2.57)$$

2.4.2.1 Fitting error

A deformable mirror features a finite number of actuators and its influence functions are spatially extended. Consequently, a deformable mirror cannot adapt perfectly to an arbitrary shape, and in particular it cannot resemble higher spatial frequencies than given by the actuator spacing. The average spatial fitting error of a deformable mirror with unlimited stroke to atmospheric wavefronts is

$$\Delta_{\text{fit, turb}} = a_F \left[\frac{d}{r_0} \right]^{5/3} \text{rad}^2, \quad (2.58)$$

where d is the actuator spacing projected to the telescope aperture. The fitting parameter a_F depends on the kind of deformable mirror. For continuous face plate mirrors, $a_F \approx 0.3$ is often used as a generic value.

2.4.3 Image stabilization with tip-tilt mirrors

Linear wavefront errors, i. e. image motion, amount to about 90% of the atmospheric wavefront error (sec. 2.3.2.2). In order to relax the stroke requirement of deformable mirrors, it is common practice to relieve deformable mirrors from image stabilization by dedicating a separate tiltable mirror to this task. Such a device is referred to as *tracking*, *steering* or *tip-tilt mirror* and it is placed into a pupil image or nearby.

The required tilt range of a tip-tilt mirror can be deduced from the angle of arrival variance σ_α^2 printed in equation (2.39). Tip-tilt mirrors used for beam stabilization are much smaller than the telescope aperture for same reason as deformable mirrors. The wavefront tilt angle in a down scaled pupil image with diameter d is magnified by the factor D/d , where D is the aperture diameter of the telescope. As a consequence of the law of reflection, the mirror only needs to be tilted by half of the incident angle in order to compensate the deflection of

the beam. Considering these aspects and requiring a $6\sigma_\alpha$ range to cover 99.9997% of the fluctuations yields the tilt angle range

$$\alpha = \pm 3 \frac{D}{d} \sigma_\alpha . \quad (2.59)$$

This results in $\alpha = \pm 122 \mu\text{rad}$ for $D = 1.5 \text{ m}$, $d = 5 \text{ cm}$, $r_0 = 10 \text{ cm}$ and $\lambda = 500 \text{ nm}$, as an example.

2.5 Hartmann-Shack wavefront sensors

The idea of optical wavefront sensing in general is to convert the wavefront information into irradiance patterns that can be detected by cameras or other kinds of photo-sensors. The phase of light waves cannot be measured directly: The electromagnetic field of a light wave with $\lambda = 500\text{nm}$ oscillates with $f = c/\lambda = 600 \text{ THz}$. There is no detector which is fast enough to sample such a signal.

The most famous wavefront sensor type is the *Hartmann-Shack wavefront sensor*^{††}, which is sketched in figure 2.21. It allows for detecting the wavefront tilt within separate zones of the telescope aperture, called *subapertures*. This is achieved by propagating the wavefront through an array of identical lenses that is placed into a pupil image of the telescope. Each lens forms an image of the object in the focal plane which is recorded by a CMOS camera for instance. The images are shifted away from the optical axis according to the wavefront tilt that is present in the area of the lens. If the object is a star, the image is simply a spot. However, if the object is extended, the image is extended as well and the field of view must

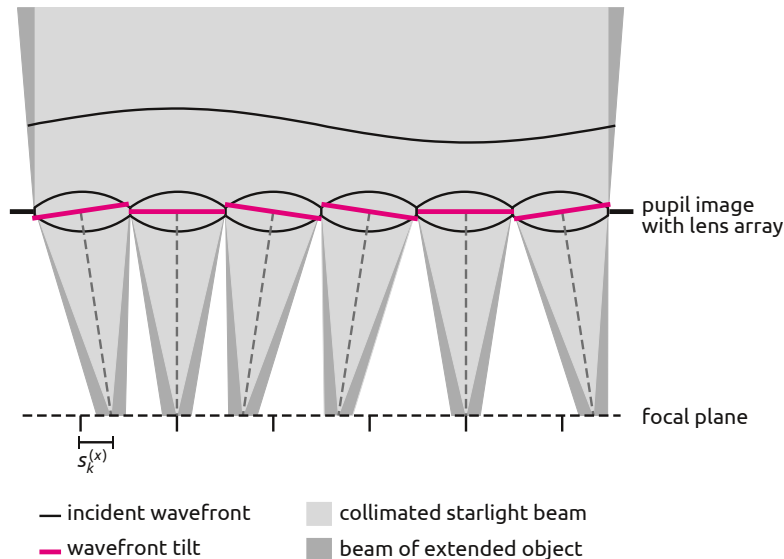


Figure 2.21: Principle of a Hartmann-Shack wavefront sensor.

^{††}named after Johannes Franz Hartmann (1865-1936), German physicist and astronomer, and Ronald V. Shack

be limited in advance in order to avoid overlapping images of neighboring lenses. Further, it is necessary that the wavefront is the same for all image points, i. e. the field of view must not be larger than the isoplanatic angle θ_0 , in order to speak of one wavefront when observing extended objects.

The image shift $s_k^{(x)}$ in the direction of x in the k^{th} subaperture is proportional to the wavefront tilt in x , i. e.

$$s_k^{(x)} = f \frac{\lambda}{2\pi} \left\langle \frac{\partial \phi(x, y)}{\partial x} \right\rangle_k , \quad (2.60)$$

where $\langle \dots \rangle_k$ denotes the average over area of subaperture k . The proportionality constant f is the effective focal length of the subaperture focus. The image shift in y -direction can be expressed in a similar manner. The absolute phase in the zones remains undetected. Thus, a smooth wavefront needs to be reconstructed from the slope informations. Wavefront reconstruction and 3d-tomography is covered by section 2.6.

For use in astronomical telescopes, the lens array is placed into a scaled image plane of the aperture. The physical lens sizes are typically in the order of millimeters and less. Such *micro-lens arrays* are fabricable in a single piece. The actual size of the microlenses may be chosen for practical purpose (be referred to appendix C for design rules following from the subaperture layout, the aperture diameter and the field of view). The microlens size with respect to the pupil, the *subaperture size*, or rather the number of subapertures marks the sampling of the wavefront slope. The subapertures must be large enough to limit diffraction blurring of the subaperture images when observing extended objects because a minimum amount of image structure is required to estimate the shifts. On the other hand, subapertures must not be too large in order to avoid image blur due to non-linear atmospheric aberrations (focus and above) within the subaperture area. Exposure times of the used cameras are in the order of 100 μs which is fast enough to freeze the wavefront (refer to eq. (2.47)) and to avoid motion blur due to fluctuating atmospheric wavefront tilt in the subapertures. Subaperture sizes for high-order wavefront sensing in the visible light regime for solar applications range from about 7–15 cm.

The measurement error due to the finite spatial sampling of the wavefront with the subapertures is referred to as *aliasing error* because high frequencies "alias" into low order frequencies. This error can be estimated (Rimmele and Marino, 2011) for the subaperture size d by

$$\Delta_{\text{alias}} = 0.08 \left[\frac{d}{r_0} \right]^{5/3} \text{rad}^2 . \quad (2.61)$$

2.5.1 Image shift estimation

If the observed object is a star, the image positions in the focal plane of the micro-lens array can be defined by the centroids of the star images. A detector with at least 2×2 pixels is required for each subaperture to compute the centroids. However, extended objects like the surface of the Sun do generally not show any localized structure that could be used for centroid tracking. Von der Lühe proposed a tracking method for low-contrast objects based

on cross-correlation(von der Lühe, 1983). Accordingly, the mutual shift (δ_x, δ_y) of two otherwise identical images $I_1(x, y)$ and $I_2(x, y)$ can be estimated by finding the maximum of their cross-correlation function

$$(I_1 * I_2)(x, y) := \iint I_1^*(x', y') I_2(x' + x, y' + y) dx' dy' \quad (2.62)$$

i. e. solving: $\max((I_1 * I_2)(x, y)) = (I_1 * I_2)(\delta_x, \delta_y)$. The coordinate systems (x', y') of I_1 and I_2 are centered on the optical axis of their corresponding subapertures. Instead of computing the double integral in equation (2.62), the convolution theorem may be exploited yielding

$$I_1 * I_2 = \mathcal{F}^{-1} \{ \mathcal{F} \{ I_1 \} \cdot \mathcal{F} \{ I_2 \} \}. \quad (2.63)$$

Discrete Fourier transforms can be performed very efficiently with sophisticated algorithms(Frigo and Johnson, 2005). Alternative correlation algorithms were lately evaluated by Löfdahl (2010).

Since only the differential image shift can be found, correlating the subaperture images of a single camera frame with each other would not identify the overall wavefront tilt. Thus, the initial image of one subaperture needs to be selected as reference and all subaperture images need to be correlated with the reference henceforth. The reference image needs to be updated regularly as the object structure evolves. Although correlating subaperture images of subsequent camera frames with their own initial images could also be used to estimate the overall tilt, this scenario would only allow to measure deviations from the (random) initial wavefront but not the absolute, instantaneous wavefront.^{**} Section 4.2.1.2 describes the corresponding algorithm of the control software KAOS which is used for the MCAO of GREGOR.

The field of view must contain sufficient structure and the detector must provide an adequate number of pixels in order to resolve the image structure for use with correlation techniques. Hartmann-Shack wavefront sensors for solar applications typically use a ca. $10'' \times 10''$ (5-6 solar granules) wide field of view, sampled with about 20×20 pixels per subaperture. This field of view is slightly larger than the typical isoplanatic angle, yielding an additional measurement error source.

2.5.1.1 Measurement error

The error of the wavefront tilt measurement in a subaperture of a correlation based Hartmann-Shack sensor was elaborated by Michau et al. (1992). The variance of the measurement error in one dimension can be estimated by

$$\sigma_x^2 = \frac{5 m^2 \sigma_b^2}{4 n_r^2 \sigma_i^2} \lambda^2, \quad (2.64)$$

^{**}At this point it also seems worth noting that the absolute overall wavefront tilt cannot be defined with a *correlating* Hartmann-Shack sensor. The initial image position in the reference subaperture is random and is not interconnected to the overall tilt. Thus, if no special care is taken, the image compensated by an adaptive optics system usually jumps when switching on the control loop because it assigns the initial tilt of the reference subaperture to zero for the whole wavefront.

where m is the width of the correlation peak of the autocorrelation of the reference image ("width" might mean the FWHM but this is not explained in the original work) and n_r is the width of the reference image in pixels, σ_i^2 is the variance of the image irradiance structure, and σ_b^2 is the background noise variance. The following assumptions were made for this estimation: 1.) the reference image and the cross-correlated image are identical but mutually shifted (i. e. anisoplanatism is not considered). 2.) the image is sampled according to the Nyquist theorem. 3.) the background noise (photon and detector noise) is constant over the image. 4.) the cross-correlation function is gaussian. 5.) the centroid was calculated after half maximum thresholding of the cross-correlation peak.

Expanding equation (2.64) by the square of the mean image irradiance $\langle I \rangle$ yields

$$\sigma_x^2 = \frac{5}{4} \frac{m^2}{n_r^2} \frac{\langle I \rangle^2}{\sigma_i^2} \frac{\sigma_b^2}{\langle I \rangle^2} \lambda^2. \quad (2.65)$$

The ratio $\sigma_i/\langle I \rangle$ is known as *rms image contrast* and is about 1–4% for solar granulation in the focus of a Hartmann-Shack sensor microlens. The occurrence of the image contrast in the measurement error represents the trade-off between diffraction and atmospheric blurring in choosing the subaperture size. The dependence of the measurement error on the width of the (auto)correlation peak expresses the importance of a slim correlation peak. The correlation peak width is affected by the image structure, which is blurred by diffraction and aberration. $\langle I \rangle/\sigma_b$ is the signal-to-noise ratio of the exposure. The intense sunlight allows for exposures such that the signal $\langle I \rangle$ is close to the saturation level of the detector even for narrow wavelength ranges. The saturation level in units of photo-electrons is known as *full well depth*. Current CMOS cameras used for solar Hartmann-Shack sensors can collect 30 000–200 000 electrons per pixel. The noise of an exposure is composed of the Poisson-noise of the incident photon number, also called *shot noise* and of the read-out-noise of the detector (thermal excitation, quantization error). The read-out-noise is negligible compared to shot noise, hence the background noise restricts to $\sigma_b = \sqrt{N_{e^-}}$, where N_{e^-} is the number of photo-electrons accumulated in a pixel during the exposure. Thus, the signal-to-noise ratio of the exposure is given by

$$\frac{\langle I \rangle}{\sigma_b} = \frac{N_{e^-}}{\sqrt{N_{e^-}}} = \sqrt{N_{e^-}}. \quad (2.66)$$

The effect of anisoplanatism in the subaperture images is that the subsequent images differ from the initial reference image—beyond being shifted—because they get distorted, harming the correlation. Wöger and Rimmele (2009) pointed out that anisoplanatism increases the shift measurement error significantly and has to be added as additional noise. Accordingly, the measurement error can be assumed to be $\sigma_x \approx 30 \dots 40$ nm for typical solar observations scenarios.

2.5.2 Zonal patterns

The subapertures are usually arranged in either square or hexagonal layout. To sense and control the wavefront most effectively, the layout of the subapertures and the arrangement of the deformable mirror's actuators must be matched. A popular arrangement for Hartmann-Shack sensors and deformable mirrors with discrete actuators is the *Fried geometry* in which an actuator is put in each corner of square subapertures as shown in figure 2.22. This way, pushing an actuator results in the greatest image shifts in the corresponding subapertures. However, the Fried geometry is prone to *waffle mode*, i. e. alternating actuator deflections (fig. 2.23), which can not be sensed. Apart from degrading the wavefront, waffle mode mechanically stresses deformable mirrors and wastes the actuator signal range. It must be avoided logically that the deformable mirror can form waffle modes.

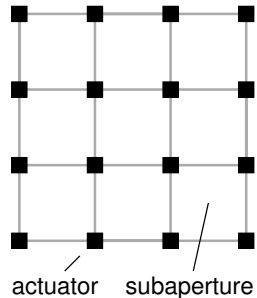


Figure 2.22: Top view of the Fried geometry.

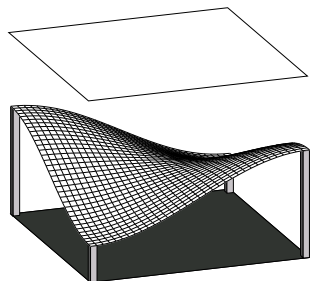


Figure 2.23: Waffle mode. The actuators of a deformable mirror in the corners of a subaperture are driven diagonally symmetrical. The wavefront tilt within this subaperture is zero, thus the Hartmann-Shack sensor is not able to detect this actuator signal pattern.

2.6 Wavefront reconstruction and tomography for multi-conjugate adaptive optics

2.6.1 Wavefront reconstruction from Hartmann-Shack shift measurements

Wavefront reconstruction is the process of finding a continuous wavefront that fits to the measured wavefront slopes. The piston term of the original wavefront is lost in the derivation performed by the Hartmann-Shack sensor. Neither can it be reconstructed, nor is it relevant for the application on hand.

There are two approaches, the *modal* and the *zonal reconstruction*, to this problem which both end up in similar sets of linear equations that need to be inverted. Modal reconstruction seeks for the wavefront expansion in a given modal basis, whereas zonal reconstruction is aimed at the phase in the sampling points. The main mathematics of both reconstructions are similar. Modal reconstruction is outlined in the following because this approach is used in the GREGOR AO system. Zonal reconstruction is therefore not repeated herein and the interested reader is referred to one of the textbooks mentioned at the beginning of this chapter.

2.6.1.1 Modal reconstruction

Let an arbitrary wavefront $\phi(x, y)$ be represented by the first N Zernike polynomials, i. e.

$$\phi(x, y) = \sum_{j=1}^N a_j Z_j(x, y), \quad (2.67)$$

as discussed in section 2.3.2. Then, the shifts of Hartmann-Shack subaperture images in x -direction according to equation (2.60) result in

$$s_i^{(x)} = f \frac{\lambda}{2\pi} \sum_{j=2}^N a_j \left\langle \frac{\partial}{\partial x} Z_j(x, y) \right\rangle_i, \quad (2.68)$$

for $i = 1, \dots, M$, where M is the number of subapertures. Summation starts from $j = 2$ because $Z_1(x, y)$ is the constant piston term which does not contribute to the image shift. Equation (2.68) is a set of linear equations which can be written in vector-matrix notation as

$$\begin{pmatrix} s_1^{(x)} \\ \vdots \\ s_M^{(x)} \\ s_1^{(y)} \\ \vdots \\ s_M^{(y)} \end{pmatrix} := \vec{s} = f \frac{\lambda}{2\pi} \cdot \underbrace{\begin{pmatrix} \left\langle \frac{\partial Z_2(x, y)}{\partial x} \right\rangle_1 & \dots & \left\langle \frac{\partial Z_N(x, y)}{\partial x} \right\rangle_1 \\ \vdots & \ddots & \vdots \\ \left\langle \frac{\partial Z_2(x, y)}{\partial x} \right\rangle_M & \dots & \left\langle \frac{\partial Z_N(x, y)}{\partial x} \right\rangle_M \\ \left\langle \frac{\partial Z_2(x, y)}{\partial y} \right\rangle_1 & \dots & \left\langle \frac{\partial Z_N(x, y)}{\partial y} \right\rangle_1 \\ \vdots & \ddots & \vdots \\ \left\langle \frac{\partial Z_2(x, y)}{\partial y} \right\rangle_M & \dots & \left\langle \frac{\partial Z_N(x, y)}{\partial y} \right\rangle_M \end{pmatrix}}_{:= \mathbf{I}_{Z \rightarrow S}} \underbrace{\begin{pmatrix} a_2 \\ \vdots \\ a_N \end{pmatrix}}_{:= \vec{z}} \quad (2.69)$$

where $\vec{s} \in \mathbb{R}^{2M}$ is the *shifts-vector*, $\vec{z} \in \mathbb{R}^{N-1}$ is the *Zernike-vector* and $\mathbf{I}_{Z \rightarrow S} \in \mathbb{R}^{2M \times (N-1)}$ is the *interaction matrix* which converts the wavefront's Zernike coefficients into subaperture image shifts. Instead of Zernike polynomials any appropriate basis functions may be used.

As long as the matrix $\mathbf{I}_{Z \rightarrow S}$ is square, i. e. $2M = N - 1$, and not singular, the wavefront coefficients could be reconstructed by pre-multiplying equation (2.69) with the *reconstruction matrix* $\mathbf{R}_{S \rightarrow Z} := \mathbf{I}_{Z \rightarrow S}^{-1}$ yielding

$$\vec{z} = \mathbf{R}_{S \rightarrow Z} \vec{s}. \quad (2.70)$$

However, the interaction matrix of a Hartmann-Shack sensor is usually not invertible, because there are modes that are badly sensed or not even sensed at all. Such modes should be removed from the matrix before the following inversion is performed.

2.6.1.2 Matrix inversion with singular value decomposition

In order to find a solution of the inverse problem $\vec{s} \rightarrow \vec{z}$, the singular value decomposition of matrices provides a powerful and widely used method for computing the *pseudo-inverse* of a matrix.

Any matrix $\mathbf{A} \in \mathbb{R}^{m \times n}$ with $m \geq n$ can be written by the product of three matrices:

$$\mathbf{A} = \mathbf{U} \begin{pmatrix} w_1 & & \\ & \ddots & \\ & & w_n \end{pmatrix} \mathbf{V}^T \quad (2.71)$$

The matrix $\mathbf{U} \in \mathbb{R}^{m \times n}$ and the transpose matrix \mathbf{V}^T of a square matrix $\mathbf{V} \in \mathbb{R}^{n \times n}$ feature the orthogonality properties

$$\mathbf{U}^T \mathbf{U} = \mathbf{V}^T \mathbf{V} = \mathbf{V} \mathbf{V}^T = \mathbf{I}. \quad (2.72)$$

$\text{Diag}(w_1, \dots, w_n)$ is a diagonal matrix containing the singular values w_i of \mathbf{A} which are ordered such that $w_1 \geq w_2 \geq \dots \geq w_n \geq 0$.

The singular value decomposition can be computed numerically and corresponding functions are available in numerical software packages like GNU Scientific Library, GNU Octave, Numerical Recipes, LAPACK et cetera. Be referred to the documentation of these packages for discussion of the algorithms.

The pseudo-inverse of \mathbf{A} is

$$\mathbf{A}^+ = \mathbf{V} \begin{pmatrix} 1/w_1 & & \\ & \ddots & \\ & & 1/w_n \end{pmatrix} \mathbf{U}^T. \quad (2.73)$$

If $w_n \neq 0$, i. e. the rank of \mathbf{A} equals n , then

$$\vec{z} = \mathbf{A}^+ \vec{s} \quad (2.74)$$

is a unique least-squares solution of $\mathbf{A}^+ \vec{s} = \mathbf{A}^+ \mathbf{A} \vec{z} = \vec{z}$. If w_i is zero or a very small numerical number, mode i can be ignored by replacing $1/w_i$ with 0 and equation (2.73) yields a practically unique least-squares solution of the inverse problem. Thus, the diagonal matrix $\text{Diag}(1/w_1, \dots, 1/w_n)$ can be used to introduce a gain factor to individual modes and as a modal filter to reject badly sensed modes. However, modes known to be problematic better do not enter the inversion.

2.6.2 Wavefront tomography

The Hartmann-Shack sensor with a field of view limited to the isoplanatic angle can be used to reconstruct the wavefront aberrations which have accumulated in the observation direction. Using multiple such sensors allows reconstructing the wavefront in three dimensions. This process is often referred to as *wavefront tomography*.

In figure 2.24, as an example, the axes $\alpha_1, \alpha_2, \alpha_3$ of three Hartmann-Shack sensors are shown. The sensors are pointing at different directions and they independently detect the accumulated wavefronts of the penetrated volumes which are represented by cylinders. Wavefront aberrations have been introduced by two turbulent layers in distance h_1 and h_2 . The three beams cross the layers at different lateral positions and cut out distinct sections

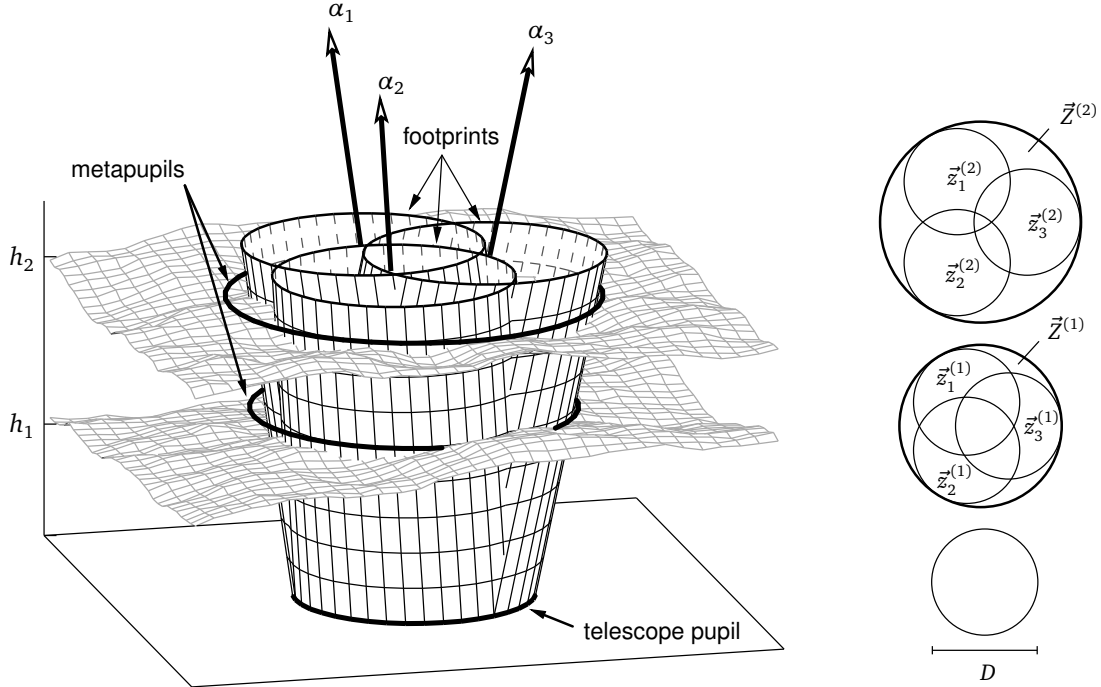


Figure 2.24: Wavefront tomography.

(known as *footprints*) from the wavefront. The circumcircles of the penetrated sections (the footprint of the total field of view) are called *metapupils*. In modal tomography, the modal expansion of the wavefront within the metapupils is sought (Ragazzoni et al., 1999). Let us assume to know the accumulated wavefronts from M sensors, and let \vec{z}_α be the vector of Zernike coefficients of the wavefront accumulated in the direction of wavefront sensor α , i. e.

$$\vec{z}_\alpha = \sum_{l=1}^L \vec{z}_\alpha^{(l)}, \quad (2.75)$$

for $\alpha = 1, \dots, M$ and with $\vec{z}_\alpha^{(l)}$ denoting the Zernike expansion vector of the wavefront section within the footprint of the beam in direction α in the layer l . The wavefront within the whole metapupil in layer l shall be represented by $\vec{Z}^{(l)}$. The circular areas corresponding to the expansions $\vec{z}_\alpha^{(l)}$ and $\vec{Z}^{(l)}$ are indicated on the right side of figure 2.24. The length of the vectors, i. e. the number of considered Zernike polynomials, may be chosen $J < \infty$ for both $\vec{Z}^{(l)}$ and $\vec{z}_\alpha^{(l)}$. Being allowed to limit $\vec{z}_\alpha^{(l)}$ to the same length as $\vec{Z}^{(l)}$ seems to be intuitive because J reflects the maximum spatial frequency with respect to the Zernike circle. Thus, Zernike polynomial Z_J defined in a subcircle corresponds to even higher absolute frequencies. The justification of limiting the vectors to same length was shown mathematically by Ragazzoni et al. (1999). Accordingly, it is possible to define a matrix $\mathbf{A}_\alpha^{(l)} \in \mathbb{R}^{J \times J}$ that converts metapupil expansion into subcircle expansion, i. e.

$$\vec{z}_\alpha^{(l)} = \mathbf{A}_\alpha^{(l)} \vec{Z}^{(l)}. \quad (2.76)$$

This equation describes the contribution of the layer l to the measurement of wavefront sensor pointing in direction α . Taking all L layers and all M wavefront sensors into account yields again a linear set of equations which can be written in as

$$\begin{pmatrix} \vec{z}_1 \\ \vdots \\ \vec{z}_M \end{pmatrix} = \begin{pmatrix} \mathbf{A}_1^{(1)} & \dots & \mathbf{A}_1^{(L)} \\ \vdots & \ddots & \vdots \\ \mathbf{A}_M^{(1)} & \dots & \mathbf{A}_M^{(L)} \end{pmatrix} \begin{pmatrix} \vec{Z}^{(1)} \\ \vdots \\ \vec{Z}^{(L)} \end{pmatrix} \quad (2.77)$$

or rather in compact form as

$$\vec{z} = \mathbf{A} \vec{Z}. \quad (2.78)$$

The number of wavefront sensors is usually larger than the number of turbulent layers, i.e. $M > L$, in order to avoid a significant amount of metapupil area that is not covered by any wavefront sensor. As discussed in the previous section, equation (2.78) can be inverted in order to reconstruct the wavefronts in the metapupils \vec{Z} from the accumulated single-direction wavefronts \vec{z} .

2.6.3 Wide-field Hartmann-Shack wavefront sensor

During daytime observations, strong turbulence occurs close to the ground whereas high-altitude turbulence is much weaker. Consequently, wavefront aberrations in high-altitudes are limited to lower spatial frequencies. For this reason, wavefront sensors used for solar MCAO can be separated into two kinds which shall be referred to as *on-axis* and *multi-direction wavefront sensors* within this thesis. An on-axis sensor features small subapertures for high spatial wavefront sampling and is dedicated to a narrow field of view centered around the optical axis of the telescope. Off-axis sensors point to various directions off the optical axis and can use larger, i.e. less, subapertures. In order to facilitate the optical design and to save cameras and beam splitters, off-axis sensors can be merged into one unit which is sometimes called *wide field Hartmann Shack wavefront sensor*. The term "the multi-direction wavefront sensor (Multi-Dir-WFS, MD-WFS)" will always stand for a wide-field Hartmann-Shack sensor unit for the rest of this thesis. This term is preferred in order to stress that this sensor is used to register the integral wavefront aberrations in multiple directions spread over the field of view rather than registering field averaged aberrations as it would be the case in a ground-layer AO system. The principle of such a device is visualized in figures 2.26 and 2.25. A single microlens array which is designed (appendix C) for a wide field of view is used rather than multiple narrow field microlens arrays. However, the wide field images are not used to estimate the wavefront tilt over the whole field of view. Instead, the wide field images are divided into narrow subregions, and the image shift and hence the wavefront slope is tracked in these regions. Combining the correspondent slopes of all subapertures in each direction results in the same information that separate narrow field sensors would deliver that observe the same subregions.

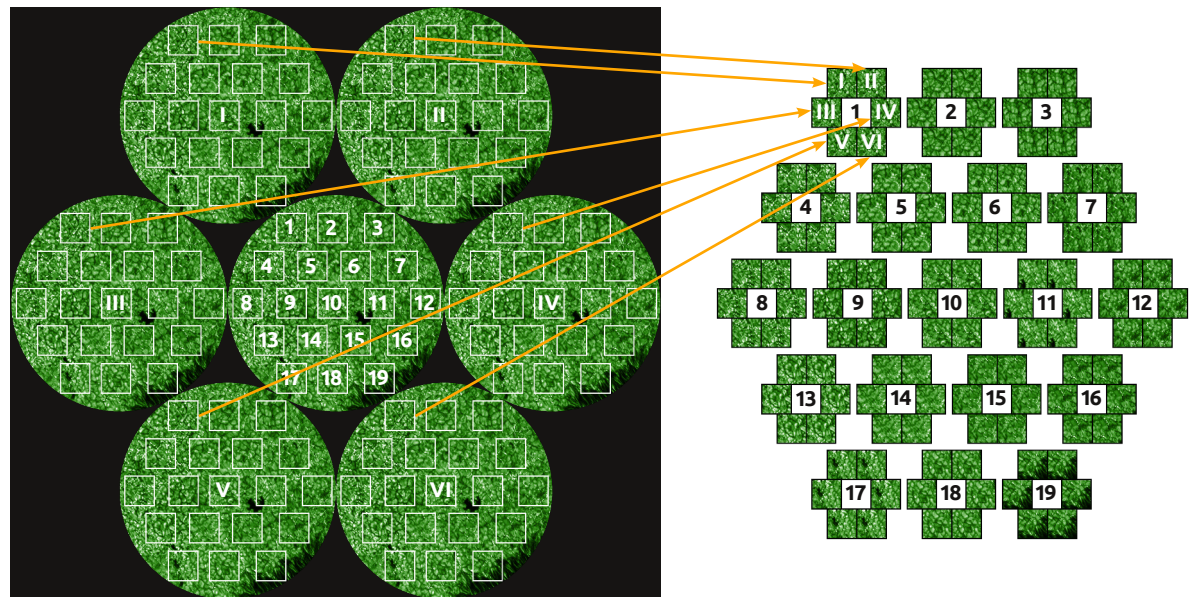


Figure 2.25: Illustration of multi-direction wavefront sensing in GREGOR's MCAO.

Left: Image plane of the microlens array of the multi-direction sensor featuring 7 subaperture images showing solar granulation. The real central subaperture image is obstructed by GREGOR's secondary mirror and is not being used. 19 subfields of each subaperture image are considered.

Right: Recombination (indicated by arrows) of correspondent subfields to unfold 19 Hartmann-Shack sensors with each 6 subapertures pointing to different directions. The correspondent subfields are then correlated.

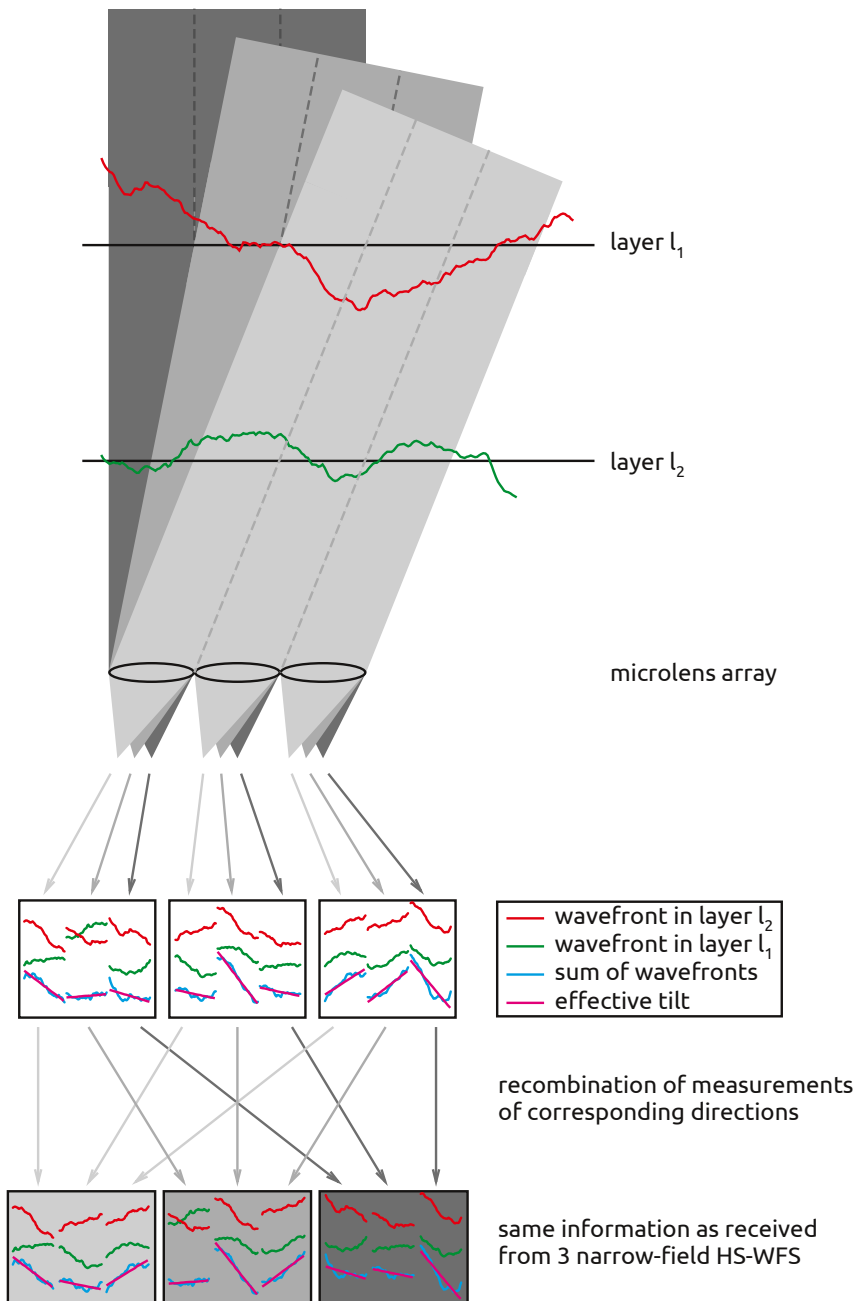


Figure 2.26: Principle of a wide-field Hartmann-Shack sensor for multi-direction wavefront sensing. The local shift of narrow subfields within the wide field is measured and correspondent subfield shifts are combined as if they were taken with individual narrow field wavefront sensor units.

2.7 Adaptive optics control loop

The wavefront modulators and the wavefront sensors of an adaptive optics system are combined in a control loop in which the modulators are driven depending on the sensors input such that the wavefront error is compensated. This section shall concentrate on *negative feedback loops*, which are often also called *closed control loops*. In such a configuration, the wavefront sensor follows the wavefront modulator in the optical path as shown in figure 2.27. Hence, the wavefront sensor is able to register the effect of the modulation and it only needs to sense small deviations from the reference once the control loop has been established. Figure 2.27 shows a single-input single-output system which is not only good for explanation but also is how a single wavefront mode is controlled in the control software of GREGOR's MCAO system. That is, one controller is dedicated to each wavefront mode.

An advantage of a feedback loop is that strict linearity (or in general a very accurate model) of the involved components (sensor, modulator including electronics etc.) is not as vital as it is for non-feedback controls. As long as the feedback control loop knows how to build the wavefront modes' shapes and their signs, the required amplitudes to compensate the incident wavefront are found iteratively as the loop continues. (The procedure of teaching the control loop how to build the wavefront modes is referred to as *calibration* and is described for the control software of GREGOR in section 4.2.2.) However, the system oscillates if the control loop adjusts the modulation amplitudes too fast. In control theory, the components of control process are usually described by their transfer functions that are given by the Laplace transform of their impulse responses in the case of continuous systems or by z-transforms in the case of time-discrete systems. This formalism is a generalization of the Fourier formalism in imaging and also considers the system components to be linear and time invariant. Recapitulating control theory basics is beyond the scope of this chapter and only the PID controller shall be introduced in a few words.

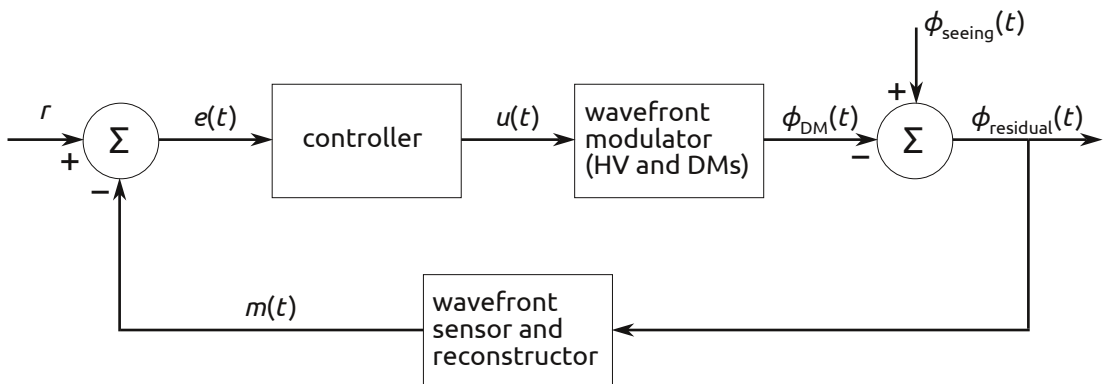


Figure 2.27: Block diagram of a simplified negative feedback control loop of an adaptive optics system with the seeing induced disturbance ϕ_{seeing}

2.7.1 PID Controller

A controller is the "mechanism" of a control system that sets the modulator depending on the input error signal. A famous controller which is widely used in closed-loop control systems is the PID controller. This controller considers the instantaneous error as well as its history and the instantaneous rate of its change. If the error signal that enters the controller is

$$e(t) = r - m(t), \quad (2.79)$$

the PID controller's output is expressed by

$$u(t) = K_p e(t) + \frac{K_p}{T_i} \int_0^t e(\tau) d\tau + K_p T_d \frac{d}{dt} e(t). \quad (2.80)$$

This equation is made of three terms after which the controller is named:

1. the proportional term $K_p e(t)$
2. the integral term $K_p / T_i \int_0^t e(\tau) d\tau$
3. and the derivative term $K_p T_d \frac{d}{dt} e(t)$

Equation (2.80) represents a continuous PID controller. However, today's adaptive optics systems are digital control systems with time-discrete sampling and modulation. For a discrete control process with sampling interval Δt , the following substitutions can be made to emulate the behavior of the continuous controller:

$$e(t) \rightarrow e_n, \quad \int_0^t e(\tau) d\tau \rightarrow \sum_{i=0}^n e_i \Delta t, \quad \frac{d}{dt} e(t) \rightarrow \frac{e_n - e_{n-1}}{\Delta t} \quad (2.81)$$

Thus, the discrete controller output can be written as

$$u_n = K e_n + \frac{K}{T_i} \sum_{i=0}^n e_i \Delta t + K T_d \frac{e_n - e_{n-1}}{\Delta t}. \quad (2.82)$$

An algorithm to implement this equation in a computer program can be found from the difference

$$u_n - u_{n-i} = K(e_n - e_{n-1}) + K \frac{\Delta t}{T_i} \left(\sum_{i=0}^n e_i - \sum_{j=0}^{n-1} e_j \right) + K \frac{T_d}{\Delta t} ((e_n - e_{n-1}) - (e_{n-1} - e_{n-2})). \quad (2.83)$$

Simplifying the sums and rearranging yields the controller iteration directive

$$u_n = u_{n-1} + K(e_n - e_{n-1}) + K \frac{\Delta t}{T_i} e_n + K \frac{T_d}{\Delta t} (e_n - 2e_{n-1} + e_{n-2}). \quad (2.84)$$

This directive is sometimes named *velocity algorithm* because it refers to the previous output u_{n-1} and not the initial output u_0 .

The control software of GREGOR's adaptive optics systems adds a *leaky integrator* to the controller output such that

$$\check{u}_n = \check{u}_{n-1} + K(e_n - e_{n-1}) + K \frac{\Delta t}{T_i} e_n + K \frac{T_d}{\Delta t} (e_n - 2e_{n-1} + e_{n-2}) + \gamma (\check{u}_{n-1} - \check{u}_{n-2}) \quad (2.85)$$

with γ smaller but close to one. The leaky integrator avoids that wavefront modes that cannot be sensed effectively (e. g. piston or waffle) build up in the controller output.

PID parameter tuning A heuristic procedure of tuning the PI or PID control parameters in closed loop was suggested by Ziegler and Nichols (1942). Accordingly, the integral and derivative terms are deactivated and the proportional gain K is set to a low (safe) value. Then the control loop without any external disturbances is closed and K is slowly increased until a stable oscillation is reached. This gain is the *ultimate gain* K_u and the oscillation period is P_u . Ziegler and Nichols offered a set of formulas to calculate K , T_i and T_d from K_u and P_u . However, for GREGOR's adaptive optics system, we use the formulas of Tyreus and Luyben (1992) as listed in table 2.3 to find the control parameters.

Table 2.3: Tyreus-Leuben PI(D) control parameter tuning.

	K	T_i	T_d
PI controller	$K_u/3.2$	$2.2 P_u$	
PID controller	$K_u/2.2$	$2.2 P_u$	$P_u/6.3$

2.7.1.1 Misregistration

In a real telescope, the alignment of the deformable mirror with respect to the wavefront sensor is not stable but may change over time. That is, the actuators of the deformable mirrors are not imaged onto the same points in the subapertures (i. e. the microlenses of the Hartmann-Shack sensor) for all times. A changing alignment invalidates the interaction matrix between the wavefront sensor and the deformable mirror that was gained from the calibration process. This leads to a misinterpretation of the mirror actuations from the wavefront sensor measurements. In the adaptive optics community, this effect is widely referred to as *misregistration*. The lateral alignment tolerance between the microlens array of the Hartmann-Shack sensor and the deformable mirror is often agreed to be about 10% of the grid spacing until the wavefront compensation performance degrades seriously. The effect of an additional deformable mirror between the pupil plane deformable mirror and the wavefront sensor, as is it could be the case in an MCAO system, is touched in section 3.4.1.

2.7.2 Modal basis sets

Using Zernike modes as introduced in section 2.3.2 to model optical aberrations is very famous. However, Zernike modes are not the ideal basis for atmospheric wavefront modeling. The properties of such an ideal basis $\{M_i\}$ are:

$$\phi(R\vec{r}) = \sum_{n=1}^{\infty} a_n M_n(\vec{r}) \quad (\text{completeness}) \quad (2.86)$$

$$\int_{\text{AP}} M_k(\vec{r}) M_l(\vec{r}) d\vec{r} = A \cdot \delta_{kl} \quad (\text{orthogonality}) \quad (2.87)$$

$$\langle a_i a_j \rangle = \lambda_{ij}^2 \delta_{ij} \quad (\text{statistical independence}) \quad (2.88)$$

Integrations are performed over the aperture (AP)—which might feature obstructions. The unobstructed area is denoted by A . If equations (2.86) and (2.87) are satisfied, the weight a_i of mode M_i in a wavefront ϕ can be calculated by

$$a_i = \frac{1}{A} \int_{\text{AP}} \phi(\vec{r}) M_i(\vec{r}/R) d\vec{r}. \quad (2.89)$$

Zernike modes are not statistically independent (eq. (2.88)) for Kolmogorov-like wavefronts as shown by Noll (1976), and Zernike modes are only orthogonal (eq. (2.87)) for circular apertures without central obstruction. However, most telescopes feature a central obstruction due to the secondary mirror.

Karhunen-Loève modes A modal basis $\{M_i\}$ that satisfies not only orthogonality on annular apertures but also is statistical independent for a given random process can be found by solving the Karhunen-Loève integral equation

$$\int_{\text{AP}} \text{covar}(\phi(\vec{r}_1), \phi(\vec{r}_2)) M_i(\vec{r}_1/R) d\vec{r}_1 = A \cdot \lambda_i^2 M_i(\vec{r}_2) \quad (2.90)$$

as pointed out by Fried (unpublished). The spatial covariance of the wavefront can be derived from the phase structure function (eq. (2.16)) if isotropy of the turbulence is assumed. The resulting modes, which were calculated by (Wang and Markey, 1978) for Kolmogorov turbulence and compared to Zernike modes, are referred to as *Karhunen-Loève modes* in the field of adaptive optics. A numerical solution of equation (2.90) for annular apertures was provided by Cannon (1996). The solution is beyond the scope of the author of this document. Karhunen-Loève modes used in the context of this thesis were computed with a program written by Markus Kasper (then MPIA) several years ago. Zernike modes are much less efficient for compensating atmospheric wavefronts. Lane and Tallon (1992) showed that,

2 A short course on adaptive optics

among other examples, compensating atmospheric wavefronts in a circular aperture with the first 133 Karhunen-Loève modes yields the same mean wavefront error as with the first 246 Zernike modes.

Karhunen-Loève modes are Eigenmodes of the statistical process that enters equation (2.90). However, Karhunen-Loève modes do not respect the geometries of the actual wavefront reconstruction, like actuator influence functions and subaperture layout, involved in an adaptive optics system.

Lai modes Lai (1998) and Lai et al. (2000) suggested a modal basis which not only takes the statistical covariance of the wavefront error into account but also the geometric covariance of the influence functions of the deformable mirror. He derives optimal modes in the sense that they allow for compensating turbulence to a given precision with the minimum number of modes. In order to set up these modes, he finds «the mode that the deformable mirror can produce that, if it was perfectly removed from the wavefront, would remove the maximum amount of phase variance». Then, the next such modes is sought. The computation of this mode set, which will be referred to as *Lai modes* in this document, shall also not be repeated herein. Lai provided the Kiepenheuer-Institut with an IDL program to compute the modes which was used in the context of the thesis at hand.

3 The Multi-conjugate Adaptive Optics System of GREGOR

«Den Fokus legt man immer auf das, wo man hinguckt.»

(Angela Merkel)

3.1 GREGOR – Europe’s largest solar telescope

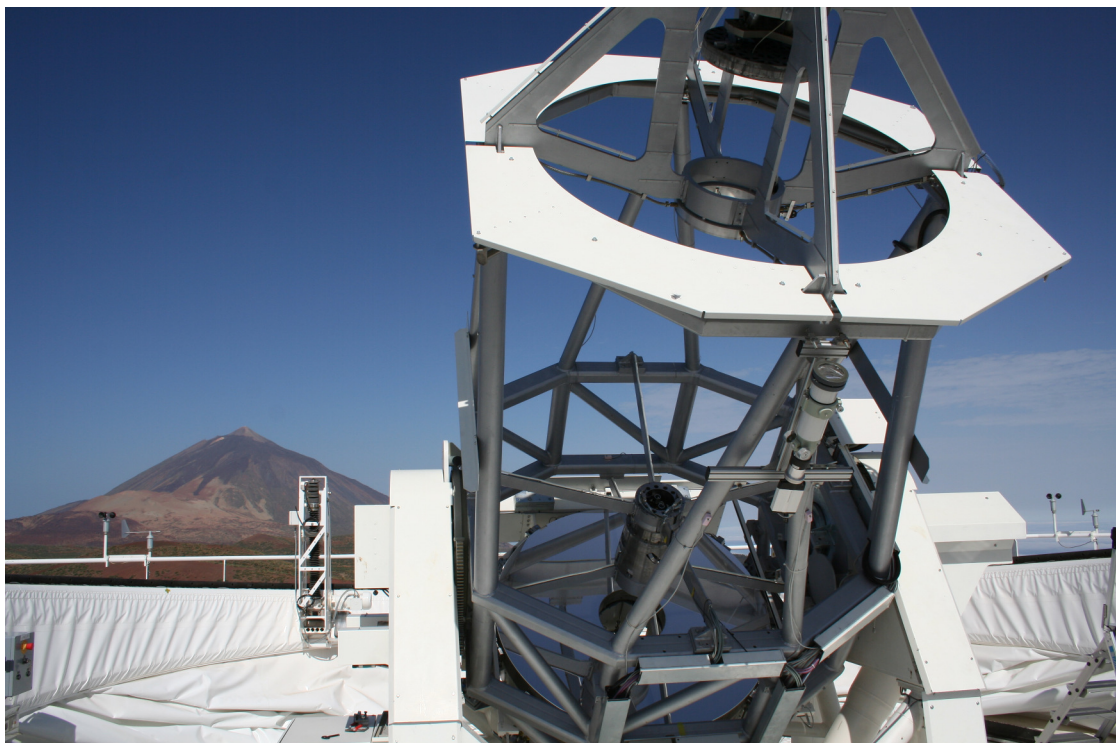


Figure 3.1: The GREGOR telescope pointing at the Sun shortly after the integration of the 1.5-meter primary mirror in 2011.

GREGOR is the name of the new German solar telescope located in the Teide Observatory on Tenerife at 2400 meters altitude (fig. 3.1). With its 1.5-meter aperture, GREGOR is targeted at observations in the visible and near-infrared light regime of the Sun with highest angular resolution so far. Beyond that, the telescope shall be used for observations of night-sky and solar-system objects. GREGOR was built and is operated by a German consortium including

3 The Multi-conjugate Adaptive Optics System of GREGOR

the Leibniz-Institut für Astrophysik Potsdam (AIP), the Institut für Astrophysik Göttingen (IAG) and the Max-Planck-Institut für Sonnensystemforschung (MPS) under the leadership of the Kiepenheuer-Institut für Sonnenphysik (KIS). The Instituto de Astrofísica de Canarias (IAC) and the Astronomical Institute of the Academy of Sciences of the Czech Republic contributed to the GREGOR project. The telescope, whose primary mirror is made of ZERODUR, saw first light in May 2011 and is in science verification phase while this thesis is being prepared. GREGOR replaced the 40-years-old 45-cm *Gregory Coudé Telescope (GCT)* which was located in the same building, which is next to the second German solar telescope in the observatory, the *Vacuum Tower Telescope (VTT)*. Another optical solar telescope in the 1.5-meter class, the *New Solar Telescope (NST)*, is concurrently commissioned by the USA in the Big Bear Lake in California. Major optical solar telescopes presently in scientific operation offer 0.7 up to 1 m apertures. Until the advent of the funded 4-meter *Advanced Technology Solar Telescope (ATST)*, the proposed Indian 2-meter telescope and drafted the 4-meter European Solar Telescope (EST), both 1.5-meter-class telescopes are expected to unveil unseen and predicted features of the Sun and will be major science facilities for the solar community in the present decade and beyond. GREGOR is currently equipped with a number of instruments for imaging, polarimetric as well as spectroscopic analysis of the sunlight, namely the *GREGOR Fabry-Perot Interferometer (GFPI)* (Puschmann et al., 2011), the *GREGOR Infrared Spectrograph (GRIS)* (Collados et al., 2008) and the *Broad-Band Imager (BBI)* (von der Lühe, 2011). In order to reach the angular resolution potential of the 1.5-meter aperture at all, an adaptive optics system is an integral gadget of GREGOR (Berkefeld et al., 2012). This system serves each post-focus instrument with an image of the Sun that has been partially compensated for optical aberrations due to atmospheric turbulence, and it also controls the active optics devices to reduce slowly varying and static aberrations over a wider range than the deformable mirror could do. In particular, GREGOR shall be the first telescope featuring a permanently installed MCAO system as an integral part of the telescope, which can be easily operated by the observer. It is this system which was set up in this thesis.

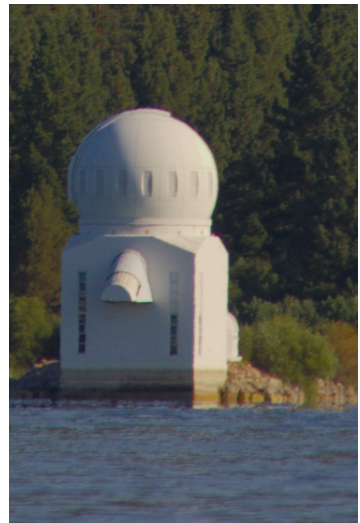


Figure 3.2: The *New Solar Telescope* in Big Bear Lake (California) at the end of a 150-meter catwalk in 2009.

3.2 Optical design of GREGOR with MCAO

The optical design of GREGOR including MCAO is sketched in figure 3.3. GREGOR is a double Gregory* system with an actively cooled 1.5-meter primary mirror M_1 . That is, a real image of the sun is formed in the primary focus F_1 between the parabolic primary mirror M_1 and the elliptic secondary mirror M_2 as well as in the secondary focus F_2 between M_2 and the elliptic tertiary mirror M_3 . The mirrors M_1 through M_3 feature positive focal

*named after the Scottish astronomer James Gregory (1638-1675)

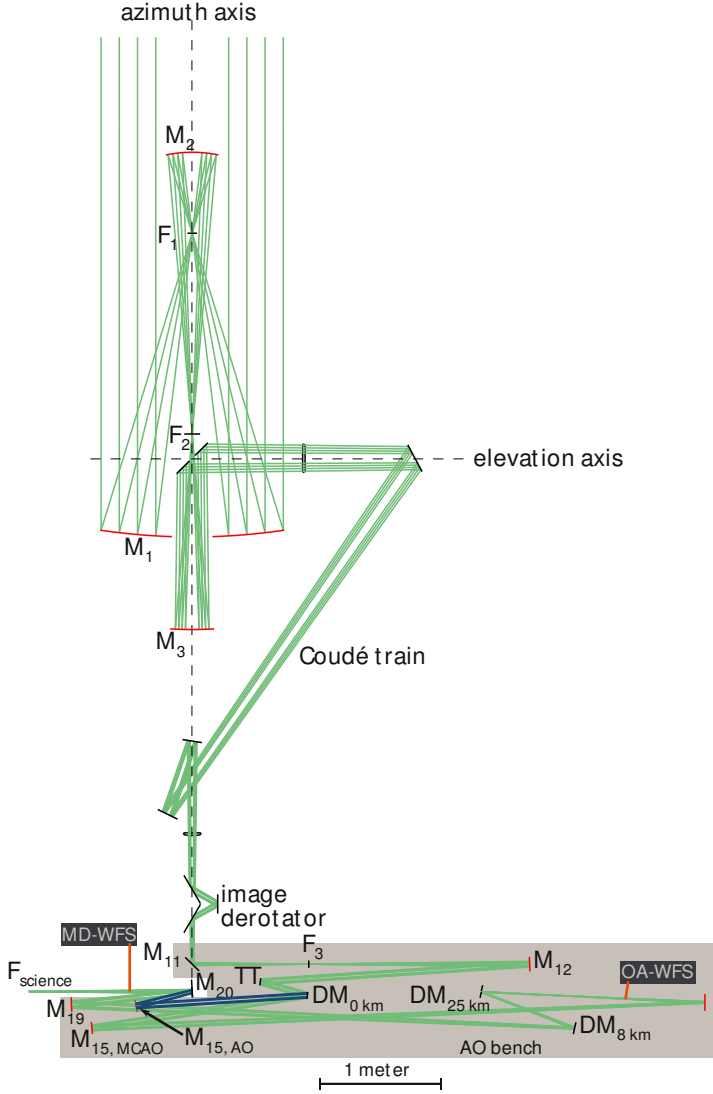


Figure 3.3: Optical layout of the GREGOR telescope including AO and MCAO path. The MCAO can be bypassed by inserting $M_{15, \text{AO}}$ that directs the light to M_{20} as indicated by blue rays. The complete adaptive optics train can be bypassed by removing M_{11} , and tilting M_{20} to 45° . Red-drawn mirrors are curved, all others are flat. The orange lines indicate where the light for the on-axis and multi-direction wavefront sensors (OA-WFS/MD-WFS) is split off.

lengths. M_3 forms an image with the final magnification and which is directed via a coudé train to a fixed position referred to as F_3 . The benefit of the double Gregory configuration compared to a Cassegrain telescope is the availability of the real images in the primary and secondary foci which is useful for solar applications. In GREGOR's primary focus F_1 , an inclined reflective and actively cooled field stop (not shown fig. 3.3) reduces the thermal load (and hence mirror seeing) on subsequent optics by reflecting most of the sunlight into the sky and transmitting only a sector of about 1% of the Sun's image. A calibration unit (also not shown) for polarimetric observations is located in the secondary focus F_2 . An image derotator is foreseen to compensate for image rotation due to the alt-azimuthal mount of the telescope.

The multi-conjugate adaptive optics follows the fixed coudé focus F_3 . The MCAO path reproduces the coudé focus in the final science focus F_{science} . Mirror M_{20} is rotatable around

3 The Multi-conjugate Adaptive Optics System of GREGOR

the azimuth axis in order to distribute the light to either GFPI and GRIS or BBI. The MCAO path can be short-cut if solely conventional adaptive optics is desired. The base line of the optical design of GREGOR's MCAO was described by Berkefeld et al. (2006). The turbulence distribution measurement at the telescope's site made by Fuensalida et al. (2004) was used to decide about the number and the conjugate position of deformable mirrors: GREGOR's MCAO shall compensate for two turbulent layers in 5 and 15 km height above the telescope. Seeing of solar observations is typically best in the morning and in the afternoon when the elevation of the Sun is low. When the Sun's elevation grows, seeing gets typically worse, and diffraction limited imaging is harder to reach with adaptive optics or may be even impossible. For this reason, GREGOR's MCAO was designed for a zenith angle of the Sun of 50°. The altitudes 5 and 15 km correspond to 8 and 25 km distances on the line of sight at this elevation. Thus, two deformable mirrors $DM_{8\text{ km}}$ and $DM_{25\text{ km}}$ are placed into the conjugate planes of these distances in addition to the deformable mirror $DM_{0\text{ km}}$ which is conjugate to the pupil in 0 km distance. The field of view over which GREGOR's MCAO shall compensate for turbulence is 60''. The deformable mirrors $DM_{8\text{ km}}$ and $DM_{25\text{ km}}$ should compensate for about 110–120 degrees of freedom. The multi-direction wavefront sensor with six 50-centimeter subapertures was foreseen to use 37 directions in order to cover the turbulence in 25 km well over the 60'' wide field of view. However, the current configuration uses 19 guide directions. Details on the actual deformable mirrors and wavefront sensors follow in the next section. Originally, it was planned to place both the multi-direction wavefront sensor and the on-axis wavefront sensor behind all deformable mirrors. However, the on-axis sensor was moved upstream to $DM_{8\text{ km}}$ and $DM_{25\text{ km}}$ for the reason explained in section 3.4.1.

Spatial constrains (e.g. limited space, fixed points of interest), image scale as well as typical beam diameters for adequate deformable mirrors with some dozens of actuators lead to the layout as illustrated in figure 3.1. Angles of incidence were decreased since the last draft published by Berkefeld et al. (2006) for reduced instrumental polarization. Starting at the coudé focus F_3 , the collimating mirror M_{12} follows and creates a 48 mm image of the telescope's pupil on a tip-tilt mirror which is used for image stabilization. The deformable mirror $DM_{0\text{ km}}$, which is dedicated to high-order on-axis wavefront correction, of the conventional adaptive optics is next. The combination of the two positive mirrors M_{15} and M_{16} reimages the focus such that the footprint of the 60'' wide field of view is constant. The following deformable mirrors $DM_{25\text{ km}}$ and $DM_{8\text{ km}}$, which are located at the subscripted conjugate distance, are parallel to each other. Thanks to this parallelism and the constant footprint, it would be possible to track the turbulent layers as the telescope elevates in order to follow the Sun without dismissing effective actuators. (However, doing so is an action item for the adolescence of MCAO, which just started to learn walking.) Finally, the camera mirror M_{19} collimates the pupil and produces the actual science focus F_{science} which is fed into different instruments by the pivot-mounted flat M_{20} . The image scales in F_3 and in F_{science} are identical in the AO and in the MCAO configuration and is about 3.6''/mm, corresponding to an effective focal length of 57.3 m. In order to minimize astigmatism that is due to inclined illumination of curved mirrors, M_{12} and M_{19} feature biconic shapes. M_{15} and M_{16} are spherical mirrors because they have much less optical powers and steeper illumination angles. Optical data of the MCAO optics is listed in table A.1.

The placement of $DM_{25\text{ km}}$ ahead of $DM_{8\text{ km}}$ violates the ideally required order of compensa-

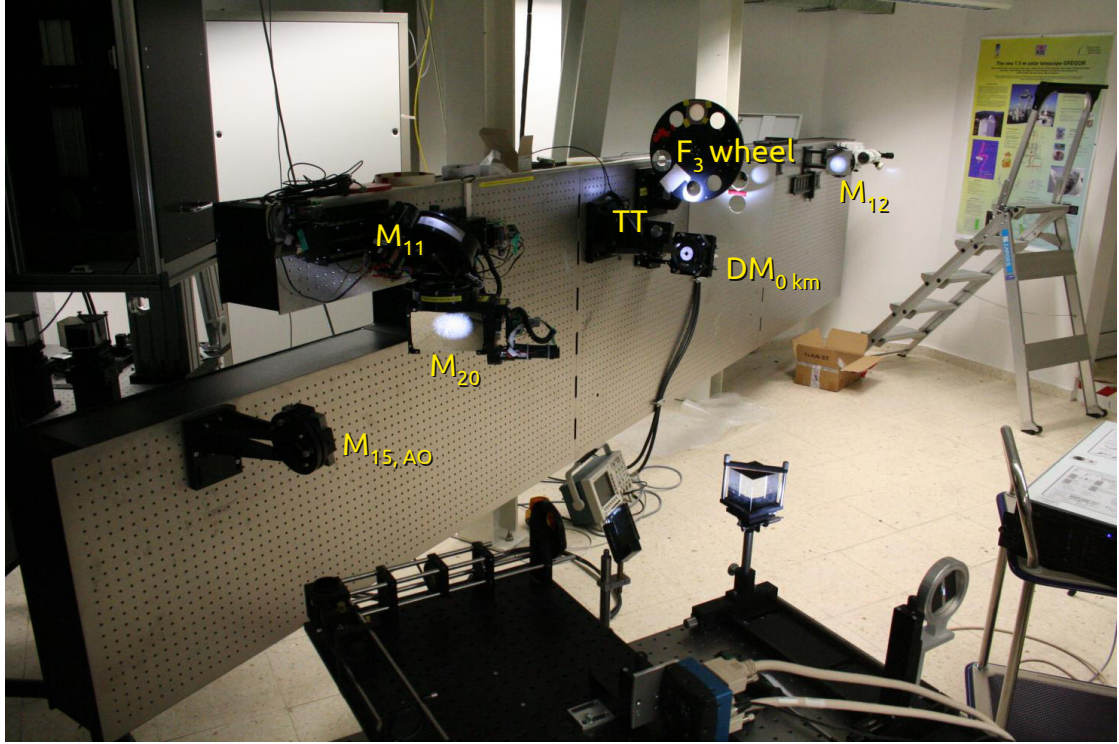


Figure 3.4: The optical bench in GREGOR holding the first-light adaptive optics in 2011. GREGOR MCAO will be mounted on this bench which measures 5.1×1.0 meters.

tion which would be the other way round, as explained in section 2.1.1.3. However, Berkefeld et al. (2006) do not expect negative effects of this configuration due to the weak turbulence in the high altitudes. To meet the ideal order of compensating high altitude turbulence, additional imaging optics would be required. The advantage of the current configuration is the saving of space, photons and stray light.

3.3 Key components of GREGOR's MCAO

3.3.1 Adaptive mirrors

3.3.1.1 High-altitude deformable mirrors

The deformable mirrors $DM_{8\text{ km}}$ and $DM_{25\text{ km}}$ make the heart of GREGOR's MCAO. The compromise between performance and cost lead to 69 actuators on each mirror which is less than the originally foreseen 85 actuators. The mirrors, which are identical, were made by the Dutch company Flexible Optical B.V. (also known as OKO Tech) and delivered in December 2008. They are referred to as *OKO PDM69* or *OKO PDM* in this document. The technical data of the mirrors is printed in table A.2 and a picture is shown in figure 3.5. The actuator spacing corresponds to 46 cm in 8 km distance and to 108 cm in 25 km distance from the

3 The Multi-conjugate Adaptive Optics System of GREGOR

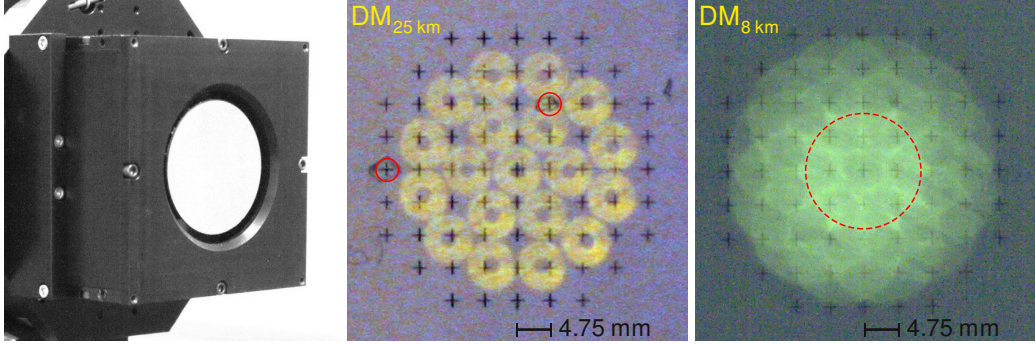


Figure 3.5: *Left:* Picture of an OKO PDM69 deformable mirror used as DM_{8 km} and DM_{25 km}. *Center and right:* The 69 actuators of this mirror are arranged on a square grid as printed on the paper screens shown in the center and right pictures. The bright areas are the footprint of the 19 guide directions on DM_{25 km} and DM_{8 km}. The two red circles on the DM_{25 km} screen mark the broken actuators of this device. The dashed circle marks the footprint of a single direction in DM_{8 km}. About 5 actuators across on DM_{8 km} and about 3 on DM_{25 km} are covered by a single footprint, which therefore account for pupil distortion (sect. 3.4.1).

telescope on the optical axis. Because we expect the turbulence being much stronger in the lower than in the upper layer, buying two identical mirrors was reasonable and cost effective. Additionally, the device in the 25 km conjugate can serve as a spare for DM_{8 km} if that one fails.

The OKO PDMs are made of a thin, reflectively coated glass plate (≈ 1 mm) which is bonded to an array of about 50 mm long piezo actuator slats. The actuator slats stand upright on a printed circuit board, to which they are also bonded, which routes the voltage to them (see also fig. 6.7). The edge of the reflective plate of the OKO PDMs is not fixed, so extending all actuators by the same amount just moves the plate up and does not change its shape (except of minor effects due to uneven actuator response). The initial shape of the OKO PDMs is a sphere with about 60–80 meters radius of curvature which is influenced by temperature, humidity and aging. The spherical shape is a consequence of the protective mirror coating which induces a mechanical stress that bends the thin glass plate[†]. Although it would be possible to produce a flat surface by means of the actuators, a lot of their stroke would be waisted and would not be available for compensation of atmospheric aberrations. Hence, the OKO PDMs are used with their initial spherical surface, and the optical configuration was adapted such that the imaging magnification of 1 from the coudé focus F₃ to science focus F_{science} is preserved (table A.1).

The OKO-PDMs are unipolar with an allowed voltage range from 0 V to +400 V. We limit the maximum voltage to 300 V and we bias the actuators with 150 V to cope with bipolar modes. Two actuators of one OKO PDM69 device have an electric break-through. One actuator is close to the edge and was cut by the manufacturer in order to release it from the mirror plate. The other actuator cannot be removed and the device will be replaced from the manufacturer in late 2012.

[†]The OKO PDMs cannot be polished to a flat surface after assembly of the device because of its thin glass plate and delicate actuator slats. The backside of the glass plate is not coated, which would allow to compensate the stress, due to the lack of appropriate non-conductive coatings (manufacturer information).

3.3.1.2 Pupil-conjugate deformable mirrors

Three deformable mirror devices were used as the pupil-conjugate mirror $DM_{0\text{ km}}$ along this thesis. The device that will be used for GREGOR MCAO at the telescope features 256 actuators. It is in use at GREGOR since January 2012 for the conventional adaptive optics system, which is referred to as *GAOS.256* in this document. A mirror device with 80 actuators was used for GREGOR's first light adaptive optics and until its installation at the telescope it was operated and tested in the MCAO testbed. A similar device with 68 actuators replaced this mirror in the MCAO testbed and was used for all MCAO test runs reported in this document (chapter 6). The latter two mirrors were also used earlier in MCAO experiments at the VTT(von der Lühe et al., 2005).

80-actuator $DM_{0\text{ km}}$ The 80-actuator bimorph mirror was designed for GREGOR's first light adaptive optics system that featured 78 15-cm hexagonal subapertures in the on-axis wavefront sensor(Berkefeld et al., 2006). This mirror was delivered by the Russian company *Night N* in July 2006 and was used in the testbed in Freiburg until July 2009. It is designated *Night DM2-55-80 #00042*. A picture and the actuator pattern are shown in figure 3.6 and the technical data is listed in table A.3. The housing features "free-edge fixation" with a soft clamp to hold the bimorph plate in place. However, the actuator pattern was designed for a true fixed edge. Thus, the outer actuators are not effective inside GREGOR's 48 mm pupil image and only about 60 wavefront modes were controllable (see section 5.3.2.2)

256-actuator $DM_{0\text{ km}}$ The 256-actuator mirror that is the heart of *GAOS.256* with 156 10-cm square subapertures (Berkefeld et al., 2012) was made by the French company *CILAS* and delivered in August 2011. It is shown in figure 3.7 and the technical data is printed in table A.4. Like the OKO PDMs, it features discrete actuators on a rectangular grid. However, the CILAS exploits the longitudinal piezo effect and the mirror is thus made of stacked actuators that are more pillar-like than the thin transversal slats in the OKO PDMs. The mirror substrate of the CILAS mirror is thicker than the substrate of the OKO PDMs and it was polished after assembly, providing a very flat initial surface. The CILAS Stack-Array-Mirrors allow bipolar voltages from -400 to $+400$ V which is beneficial for its lifetime because of the zero mean-voltage. The voltage range used in GREGOR is limited to ± 300 V.

68-actuator $DM_{0\text{ km}}$ The 68-actuator mirror is a bimorph mirror made by *Night N*. It looks similar to the 80-actuator mirror and is labeled *Night DM2-51-69 #0018*. The 68-actuator mirror has probably the same design issue as the 80-actuator version because only about 35 modes are controllable with the 78-subaperture on-axis wavefront sensor. This mirror was reported by Berkefeld after the operation at the VTT to have only little stroke. However, the 68-actuator device was not specifically analyzed in the scope of this thesis and just used as it is, because it was not planned to use it at the telescopes yet another time.

3 The Multi-conjugate Adaptive Optics System of GREGOR

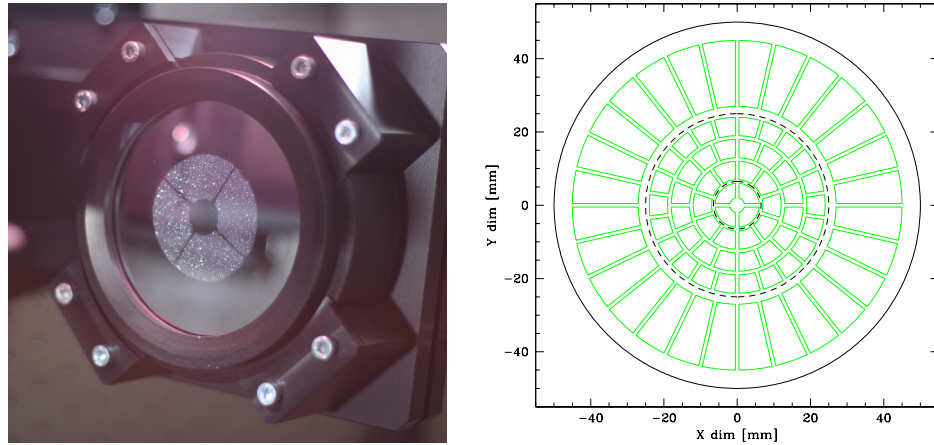


Figure 3.6: The first-generation DM_0_{km} with 80 actuators made by Night N (left). This picture shows the mirror mounted in GREGOR during commissioning phase in 2011. The illuminated pupil and the shadow of the secondary mirror are visible in the center. The bimorph actuator pattern is shown on the right (Drawing courtesy of O. von der Lühe). The dashed circles indicate the illuminated area.

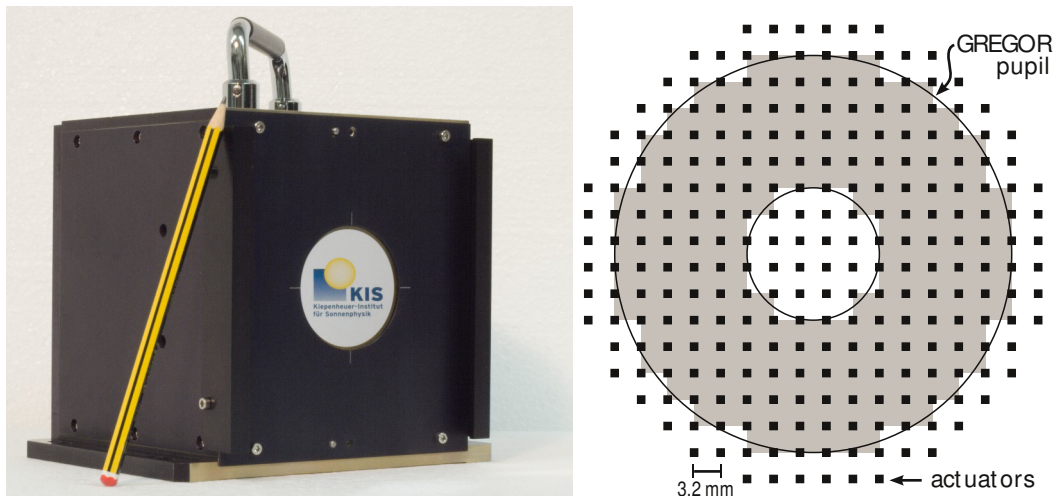


Figure 3.7: The second-generation DM_0_{km} with 256 actuators made by CILAS (left) and its actuator pattern (right). Actuator size is not to scale. The gray area marks the used subapertures.

3.3.1.3 High-voltage electronics and interfacing

All deformable mirrors presented in the previous sections are driven by a digital high-voltage amplifier system which was developed and built by the electronics lab staff of the Kiepenheuer-Institut and verified in the scope of this thesis. One of the three existing systems is shown in figure 3.9. This system, which in principle can be used to control any voltage driven deformable mirror, provides a 32-bit parallel RS-422 interface for real-time control of the mirrors and an Ethernet interface for testing and service. The RS-422 interface can be connected to a compatible daughter board in the control computer. The clock frequency is 10 MHz. The 32-bit wide word that is transmitted in each clock cycle includes the whole data to control a single actuator. 11 bits hold the address of the actuator, 16 bits hold the actuator value and 5 bits are used for control purposes or unassigned. One bit transmits a heartbeat signal, which is generated by the control software, that is used to shut down the high voltage output in order to pause and protect the mirrors when the control software is not active. Multiple interfaces could be used to overcome the 2048-actuator limit due to the 11 address bits. More technical details are listed in table A.5.

Operation with the originally planned *General Standards HPDI32A* RS-422 PCI-Express interface board, which was used for a long time in the MCAO testbed, often suffered from versatile problems as reported in section 5.3.2.4 and was replaced by a *EDT PCIe8 DV Camera Link Simulator* Camera Link transmitter PCI-Express board. This board outputs multiple streams of serialized bits on low-voltage differential signals (LVDS) conforming to the *Channel Link* standard rather than purely parallel RS-422 signals. In order to use the Channel Link signals with the high-voltage system, a board which deserializes the bits and converts them into the parallel RS-422 signals was developed in corporation with F. Heidecke (KIS), who was in charge of the electronic design, in Spring 2012. This board, which is shown in figure 3.8, is mainly made of two *National Semiconductor DS90CR288A* chips that deserialize the Channel Link input into parallel low-voltage TTL signals and eight transmitter chips that convert the TTL signals into RS-422 for data output. The converter board features a single MDR26 Camera Link connector which is fed by the *full-mode* output connector of the EDT Camera Link simulator board. The KAOS control software was adapted to output the mirror commands in the appropriate format via Camera Link image data through the *EDT* simulator board. The logical wiring of the board and the bit assignment is printed in tables A.6 and A.7. After verification in the MCAO testbed, the Channel Link interfacing

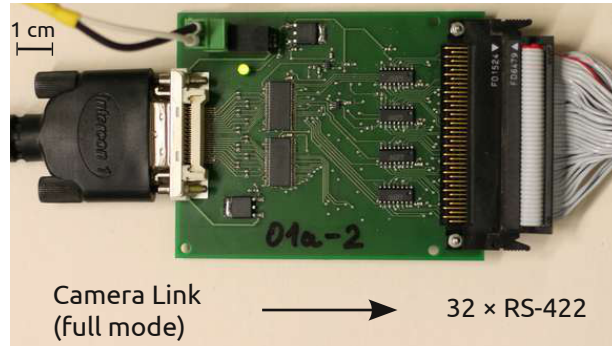


Figure 3.8: The converter board for the KIS-M-Link communication with the high-voltage amplifier system to command the adaptive mirrors. The MDR26 cable on the left side receives the Channel Link signals from the EDT Camera Link simulator that is plugged into the control computer. The IDC cable on the right side carries the RS-422 signals to the amplifier system.

Figure 3.9: The 19-inch chassis of the complete high-voltage amplifier electronics for the deformable mirrors and the tip-tilt mirror. Each slide-in module of the top three aluminum colored chassis features 16 channels (DACs and high-voltage amplifiers). The slim white devices are the high-voltage power-supplies for the deformable mirror channels. The blueish chassis contains the amplifier of the Physikinstrumente tip-tilt mirror and the chassis on the bottom includes the amplifier for the KIS tip-tilt mirror.



solution that shall be named *KIS-M-Link* was brought on-line in GAOS.256 at GREGOR in July 2012. The effective actuator data rate that is currently used is 10 MHz (with the Channel Link LVDS clock running at 20 MHz). 20 MHz actuator rate was also reached, however, this is borderline due to the RS-422 subsystem in the high-voltage system which was never designed for such high frequencies and hence is the bottle neck of the communication. The EDT simulator board and the Channel Link deserializers would allow for total data rate of up to 680 MB/s at 85 MHz LVDS clock in full Camera Link mode. Using Camera Link to transfer mirror command was inspired by a controller box advertised by the company *Boston Micromachines* for their deformable mirrors that features a Camera Link connector. However, *KIS-M-Link* was an entirely independent development. In particular the data format is most likely not compatible.

3.3.1.4 Tip-tilt mirrors

GREGOR's AO/MCAO system uses a separate tip-tilt mirror which relieves $DM_{0\text{ km}}$ from the task of image stabilization for greater dynamic range of compensating non-linear wavefront aberrations. The tip-tilt mirror might also be used for scanning small fields of view. When starting with the setup of the testbed in 2006, a tip-tilt stage was used that was made by the Kiepenheuer institute several years ago. Technical data from construction are no more available and the results of the recent characterization is listed in table A.8. A second tip-tilt stage was needed to have one tip-tilt mirror for GREGOR's commissioning and one

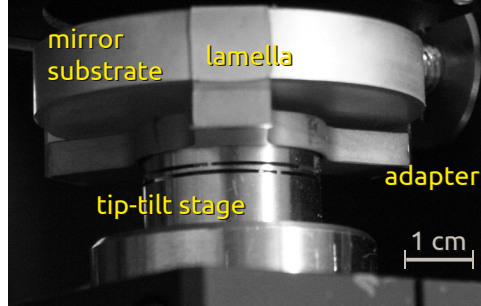


Figure 3.10: Fixture of the mirror substrate to the Physikinstrumente tip-tilt stage with lamellas bonded to the beveled rim.

in the MCAO testbed in Freiburg at the same time. A tip-tilt platform was delivered by the German company *Physikinstrumente* in Spring 2009 and was characterized in the testbed. Both mirrors perform comparably and we decided to install the Physikinstrumente device in GREGOR in July 2011 because it could be replaced easily by an identical copy in the case of failure. Refer to table A.8 for details on this mirror.

Both tip-tilt mirrors are driven by individual high-voltage amplifiers which were made by KIS and Physikinstrumente, respectively. The low-voltage input of the amplifiers is generated by additional digital-analog converters that are integrated into the high-voltage system of the deformable mirrors. The digital-analog conversion factor was adjusted individually for each of the two tip-tilt systems such that 14 bits cover a range of $\pm 10''$ on sky in order to avoid oscillations due to low steering resolution, which occurred prior to that. This angle is the maximum range of the tip-tilt mirrors for use in GREGOR's AO/MCAO, although in particular the Physikinstrumente device offers a larger range by its construction.

The ZERODUR[‡] mirror substrate is supported on its rim with three ZERODUR lamellas that are bonded to an adapter made of Invar[§] that on its part is bonded to the tip-tilt stage as shown in figure 3.10. This kind of fixing has been used for the tip-tilt mirror of the VTT for many years now. The fixture of the tip-tilt mirror substrate was an important design issue for the *Sunrise* balloon-borne solar telescope mission in 2009, for which KIS contributed the image stabilizing system CWS(Berkefeld et al., 2011). Experimental analysis made by KIS for this project showed that the introduced fixture is very robust and involves least mechanical stress caused by hardening adhesives, i. e. mirror warp is minimal(Feger, 2009). Another advantage of fixing the mirror at the rim with lamellas is attenuating the impact of the diverse thermal expansion of the ZERODUR mirror substrate and the Invar interface. The penalty of this joint is its greater moment of inertia, slowing down the speed of the mirror and requiring greater acceleration forces.

[‡]ZERODUR is the registered trademark of a lithium aluminosilicate glass-ceramic product line of SCHOTT AG (Germany) which is known for its ultra low coefficient of thermal expansion of $\alpha = (0.02 \text{ to } 0.1) \cdot 10^{-6} \text{ K}^{-1}$.

[§]Invar is the registered trademark of ArcelorMittal S.A. (Luxembourg) for a machinable iron nickel alloy (FeNi36) which has a coefficient of thermal expansion below $\alpha = 2 \cdot 10^{-6} \text{ K}^{-1}$. This is about 10-20 times less than of other machinable metals like aluminum, copper or steel.

3.3.2 Wavefront sensors

3.3.2.1 Opto-mechanical design

GREGOR's MCAO uses two wavefront sensor units—an on-axis and a multi-direction wavefront sensor (multi-dir-WFS, MD-WFS)—for wavefront tomography. The functional principles of these sensors are described in section 2.6. The on-axis sensor used in the testbed in conjunction with the 80- and 68-actuator DM_0 km features a hexagonal subapertures with 15 cm inscribed diameter. This totals to 78 subapertures (in consideration of the central obstruction). The subapertures of the on-axis sensor that is used in conjunction with the 256-actuator DM_0 km at the telescope are squarish with 10 cm edge length, yielding 156 usable subapertures. More technical data about these sensors is printed in table A.10.

The wavefront sensor assemblies are built of the *LINOS Microbench* system. The optical scheme of the multi-dir sensor is shown in figure 3.11. The on-axis wavefront sensor assemblies look similar. A wheel in the entrance focus accommodates

- a field stop for normal adaptive optics control mode,
- a single pinhole in the case of the on-axis WFS or a 19-pinhole asterism, representing the guide directions in the case of the multi-dir WFS for referencing the ideal wavefront,
- a large field stop for calibration of the control system
- and a dark stop.

This wheel is referred to as *focus unit* of the wavefront sensor. A combination of two positive doublet lenses L_1 and L_2 form the image of the pupil on the microlens array (MLA). Two lenses are used to ease fine tuning of the magnification. The beam in between the lenses is not collimated. The microlens array is mounted in a two-axis translation stage which allows for precise lateral alignment with respect to the pupil. The focus of the microlens array is reimaged by another two lenses L_3 and L_4 in the appropriate scale onto the wavefront sensor camera. Using two lenses for this task allows for convenient imaging of the microlens array onto the camera to ease aligning the microlens array with respect to the pupil. Only the lens L_3 array has to be shifted axially by the microlenses' focal length towards it in order to focus the camera to the microlens array. The other elements and especially the camera do not need to be moved.

The wavefront sensors of GAOS.256 and the MCAO were designed with the use of the optical simulation software *OpTaliX*^I and with the help of the CAD programm *QCAD/LibreCAD*^{II} in the scope of this thesis based on the original model from D. Soltau (KIS) who introduced the LINOS Microbench system for KIS wavefront sensors. For easy operation at GREGOR and remote service, the focus unit and L_3 are motorized. A motorized MLA translation stage is under construction. A motorized filter wheel that is holding ten neutral density filters is placed in front of the wavefront sensors in GREGOR. The motorized stages were constructed and built in-house and verified in the MCAO testbed.

^I<http://www.optenso.com>

^{II}<http://www.qcad.org> and <http://www.librecad.org>

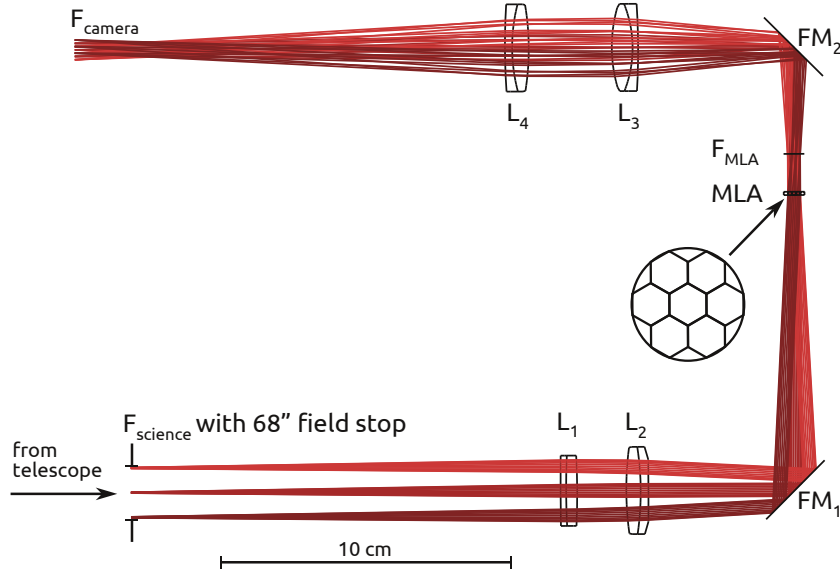


Figure 3.11: Optical layout of the multi-direction wavefront sensor. A circular field stop in the telescope focus F_4 limits the field of view to $68''$. The pupil is imaged onto a microlens array (MLA) with a cascade of two lenses (L_1 and L_2). The MLA divides the pupil into 7 subapertures (the central subaperture is obstructed). The microlens focus F_{MLA} is magnified and reimaged to the plane F_{camera} by additional optics (L_3 and L_4). A camera (not shown) in this plane records the subaperture images. Folding mirrors (FM_1 and FM_2) are used to reduce the length of the assembly. By moving lens L_3 towards FM_2 , the pupil plane can be imaged onto the camera when aligning the MLA with respect to the pupil.

3.3.2.2 Wavefront sensor cameras and frame grabbers

Each wavefront sensor unit is equipped with a *Mikrotron EoSens CL MC1362* camera. This camera features a fast CMOS sensor and a *full Camera Link* interface. Technical data and configurations in use is printed in table A.9. Each camera is read out with an *EDT PCIe8 DV* Camera Link frame grabber, which is a PCI-Express daughter board added to the control computer. The image data is passed into the host computer's main memory via DMA (direct memory access) without being buffered on the frame grabber. The next exposure can take place while the previous image is transferred.

Camera exposure synchronization It is important that the cameras of the on-axis and the multi-dir wavefront sensor expose synchronously, i. e. with same frequency and phase, in order that both sensors sample the atmospheric turbulence and the status of the adaptive mirrors in the same time frame. In order to ensure this, the strobe-out signal of the multi-dir camera is fed into the frame grabber that is connected to the on-axis camera. This frame grabber triggers the on-axis camera via the CC1 control signal of Camera Link. The multi-dir wavefront sensor camera is used as master—and not vice versa—because its exposure time is shorter due to the larger subapertures in this sensor. Because the strobe-out signal is high during exposure, using the on-axis camera as master would cause the multi-dir EoSens camera to re-expose before it was read-out completely. A signal converter, made by KIS electronics lab staff, converts the 3.3 V LVTTL strobe-out signal of the multi-dir camera to a 5 V TTL signal that is needed to drive the frame grabbers trigger input. The delay of the on-axis camera exposure start was measured to be less than 2 μs which is negligible since this is a very small fraction of the correlation time of atmospheric turbulence and of the control loop period.

3.3.3 Control computer

The computer that runs the control software *KAOS Evo 2* and accommodates the frame grabber devices as well as the digital output board for GREGOR's MCAO is a standard Intel x86-64 computer. The features of the computer that is used in the testbed and of the one that is in use for GAOS.256 at GREGOR and that will also be used for MCAO at the telescope are listed in table A.11. The control computers are housed in 19-inch chassis which are four units high to accommodate the PCI-Express extension boards.

Debian Squeeze (amd64) with Linux kernel was chosen as operating system. Only minor customizations were made to improve the real-time performance. A number of CPU cores is reserved for the KAOS control software with cpusets. All (maskable) interrupt requests are assigned to a separate, fixed CPU core by writing appropriate masks to the files `/proc/irq/X/smp_affinity`, where X is the number of the interrupt. Both means are necessary to reduce the number of context switches and cache misses of the CPU cores dedicated to the control loop processes. In conjunction with setting the scheduling parameter `PRIO_PROCESS` (the *nice* level) of control software processes to -19 , this is sufficient to accomplish a good real-time performance with a root-mean-square jitter of $2\text{-}3 \mu\text{s}$. The real-time scheduling policy `SCHED_FIFO`, which was used earlier for time-critical tasks of KAOS Evo 2 at the cost of GUI responsiveness, is currently not set. **

The driver software from EDT for the frame grabber boards currently (version 5.3.3.7) lacks complete 64-bit support and it is necessary to limit the active main memory (RAM) with the Linux boot parameter "mem" to less than 4 GB for the way the driver is used in KAOS Evo 2.

3.4 Position of the On-axis wavefront sensor in GREGOR MCAO

At the beginning of this thesis, it was planned to place both the multi-direction wavefront sensor and the on-axis sensor behind all deformable mirrors. This section explains why we decided to move the on-axis wavefront sensor upstream such that this sensor does not see the high-altitude deformable mirrors $\text{DM}_{8 \text{ km}}$ and $\text{DM}_{25 \text{ km}}$, but only $\text{DM}_0 \text{ km}$.

3.4.1 Dynamic misregistration caused by high-altitude DMs

Actuator positions of $\text{DM}_0 \text{ km}$ and the subaperture layout of the on-axis Hartmann-Shack WFS need to be matched for most effective wavefront control. For example in the Fried geometry, the position of actuators correspond to the corners of square subapertures (figures 2.22 and 3.7). The lateral misalignment of this configuration should not exceed 10 to 15% of the grid

**Real-time patches for the Linux kernel were tried but did not yield any performance gain but involved major complications like frequent dead-locks and driver availability issues. The Debian standard Linux kernel is compiled with `CONFIG_PREEMPT_VOLUNTARY=y` since Debian Squeeze. Activating `CONFIG_PREEMPT` (for low latency desktop), like other Linux vendors (used to) do, lead to increased temporal jitter and missed loop cycles. The best option for KAOS control computers was found to be `CONFIG_PREEMPT_NONE=y`. However, Debian's new standard is okay, too. The best real-time strategy for adaptive optics control systems based on CPUs seems to be avoiding context switches on all possible levels, thereby eliminating the need for low-latency or even true real-time operating systems.

spacing, as it is typically agreed with in the adaptive optics community. Wavefront control degrades with larger misalignments and the control loop might even become unstable. However, this limit is expressed for alignment errors that are static or very slowly changing with respect to the control loop period. The tolerance for fast and very non-uniform distortions of the pupil image may be larger. This still needs to be studied. This section concentrates on the consequence of pupil distortion on the reconstruction model in principle and gives an estimate of the magnitude of the distortion.

The on-axis WFS was located before the high-altitude DMs in solar MCAO experiments with effective turbulence compensation over a wider field of view (Langlois et al., 2004; Berkefeld et al., 2006; Rimmele et al., 2010). This configuration was initially used because it was simpler to integrate only the multi-direction WFS unit while using the on-axis WFS of the existing classical AO systems as it was. However, placing all wavefront sensors behind all adaptive mirrors had been assumed to be ideal. Up to now, we do not know of any effective and stable MCAO control pointed at the Sun that featured at least one wavefront sensor with small subapertures behind all deformable mirrors; although it was tried at the Dunn Solar Telescope in 2008 and 2009 for example. We contemplate dynamic pupil distortion caused by high-altitude DMs as the reason for this, because it yields a misregistration of $DM_0 \text{ km}$ in an on-axis WFS that features small subapertures. The multi-direction WFS is less prone to this effect because of its larger subapertures.

Deformable mirrors conjugate to high altitudes distort the pupil, as a side effect, when they compensate for anisoplanatic turbulence. Thus, they break the matching between actuators of $DM_0 \text{ km}$ and subapertures, and dynamically with the timescale of the turbulence. The effect of pupil distortion is visualized in figure 3.12 and was also found to be the cause of "flying shadows" in an MCAO compensated image plane(von der Lühe, 2004). The pupil distortion looks similar to the surface gradient of the high-altitude mirror within the penetrated area (see also fig. 3.5). The questions that arise in this context are:

1. do deformations calibrate out in a linear control system and hence do not degrade the turbulence compensation performance as a matter of principle?
2. how strong are these deformations?

3.4.2 Non-linear interaction

The first question is answered by calculating the wavefront slopes registered in an one-dimensional Hartmann-Shack sensor with four subapertures that is shifted against an imagined $DM_0 \text{ km}$ as shown in figure 3.14. In the unshifted arrangement, the slope in the j^{th} subaperture is given by the difference in deflection of the two adjacent actuators, that is

$$s_j = a_{j+1} - a_j. \quad (3.1)$$

The distance of the actuators is 1 in this example. If the subapertures are shifted versus the actuators by Δ , with $0 \leq \Delta < 1$, the average shift s'_i in subaperture i becomes

$$s'_i = s_i [1 - \Delta] + s_{i+1} \Delta = [a_{i+1} - a_i] [1 - \Delta] [a_{i+2} - a_{i+1}] \Delta. \quad (3.2)$$

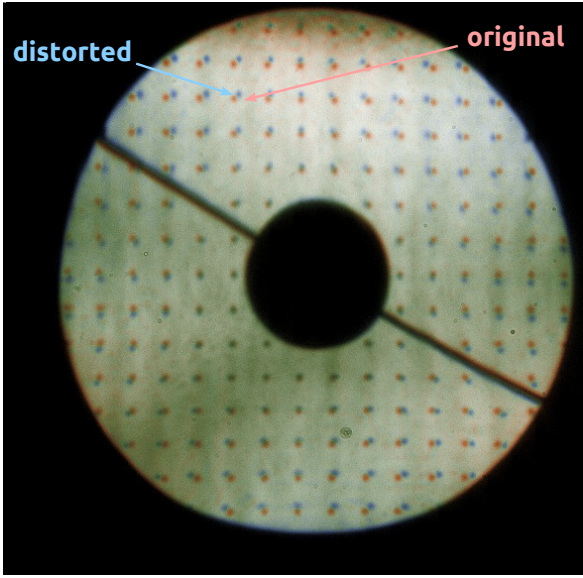


Figure 3.12: Photographic illustration of pupil distortion. A dot grid pattern corresponding to 10 cm subapertures was placed in the pupil mockup stop in the MCAO testbed (fig. 5.3) in front of $\text{DM}_{0 \text{ km}}$. The picture is made of two digitally superimposed images taken of a pupil image following the high-altitude DMs. One component of the image shows the initial position (red) of the dots and the other one the distorted positions (blue) while applying a certain shape to $\text{DM}_{8 \text{ km}}$.

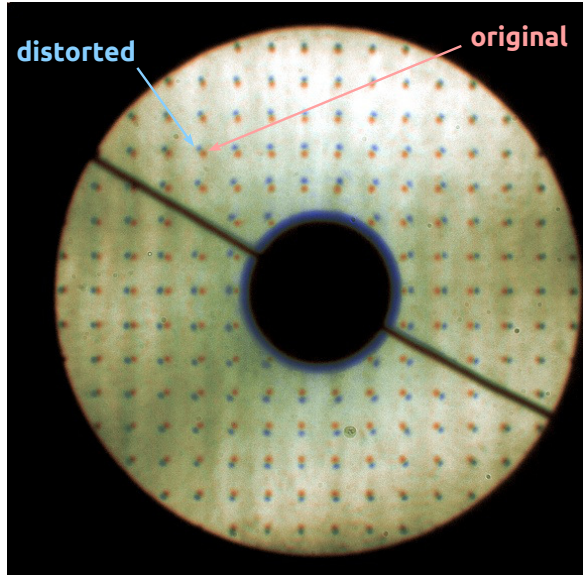


Figure 3.13: Photographic illustration of pupil distortion. The same grid pattern with the central actuator on $\text{DM}_{8 \text{ km}}$ extended by 0.4 μm . Distortion around the central obstruction is about 10% of grid spacing.

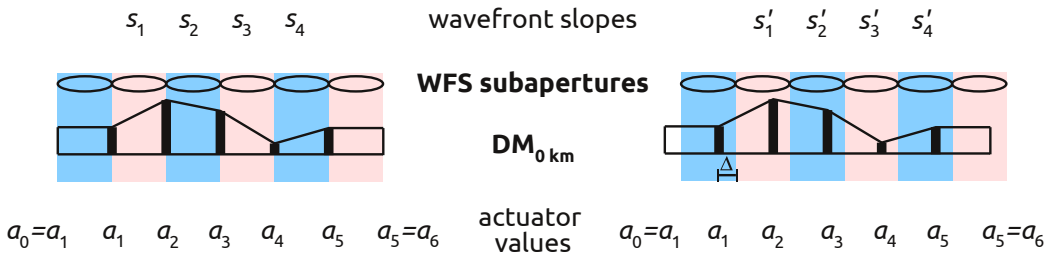


Figure 3.14: Illustration of linear misregistration. A perfectly aligned Fried geometry (left) between WFS subapertures and the deformable mirror, and the WFS shifted slightly by the amount Δ (right). a_j indicates the deflection of actuator j , and s_j represents the average slope in subaperture j . The shape of the mirror surface is assumed to be linear between two actuators for sake of simplicity. The mirror surface sections averaged by the subapertures are colored.

Two virtual actuators with deflections $a_0 = a_1$ and $a_6 = a_5$ need to be added at each side for correct averaging. For the combination of all actuators and subapertures, equation (3.2) can be written in matrix notation as

$$\begin{aligned} \begin{pmatrix} s'_1 \\ s'_2 \\ s'_3 \\ s'_4 \end{pmatrix} &= \begin{pmatrix} \Delta - 1 & 1 - 2\Delta & \Delta & 0 & 0 \\ 0 & \Delta - 1 & 1 - 2\Delta & \Delta & 0 \\ 0 & 0 & \Delta - 1 & 1 - 2\Delta & \Delta \\ 0 & 0 & 0 & \Delta - 1 & 1 - \Delta \end{pmatrix} \begin{pmatrix} a_1 \\ a_2 \\ a_3 \\ a_4 \\ a_5 \end{pmatrix} \quad (3.3) \\ &= \left[\begin{pmatrix} 1 & -2 & 1 & 0 & 0 \\ 0 & 1 & -2 & 1 & 0 \\ 0 & 0 & 1 & -2 & 1 \\ 0 & 0 & 0 & 1 & -1 \end{pmatrix} \Delta + \begin{pmatrix} -1 & 1 & 0 & 0 & 0 \\ 0 & -1 & 1 & 0 & 0 \\ 0 & 0 & -1 & 1 & 0 \\ 0 & 0 & 0 & 1 & -1 \end{pmatrix} \right] \begin{pmatrix} a_1 \\ a_2 \\ a_3 \\ a_4 \\ a_5 \end{pmatrix}. \quad (3.4) \end{aligned}$$

The shift Δ shall be introduced by another deformable mirror (not drawn in fig. 3.14) in between $DM_{0\text{ km}}$ and the wavefront sensor. Thus, the shift Δ can be represented by the difference $\Delta = A_2 - A_1$ of two actuators of the intermediate mirror without loss of generality. Hence, the slopes $\{s_j\}$ measured in the subapertures are no longer given by a set of linear equations with respect to the actuators of both deformable mirrors, but they depend on the product of two actuators $A_j a_i$, e.g.

$$s'_1 = [A_2 - A_1] a_1 - 2 [A_2 - A_1] a_2 + [A_2 - A_1] a_3 - a_1 + a_2 - A_1 + A_2. \quad (3.5)$$

A sign-function enters equation (3.5) if Δ is bipolar. For arbitrary distortions, actuator products of higher degrees occur. This means, the wavefront slopes $\vec{s} = (s'_1, \dots, s'_4)^T$ that are registered by the wavefront sensor and the actuator voltages $\vec{v} \propto (a_1, \dots, a_4, A_1, A_2)^T$ cannot be modeled by a set of linear equations. However, the possibility to connect wavefront sensing and wavefront compensation in a linear fashion is the foundation of most adaptive optics control loops. For this reason, the on-axis WFS was placed before the high-altitude DMs in the testbed. However, we consider retrying the other configuration with a more sophisticated reconstruction in the testbed or at the telescope later.

3.4.3 Atmospheric power of pupil distortion

The atmospheric power of the pupil deformation can be estimated from the average difference of the level of two neighboring actuators as given by the phase-structure function (section 2.3.1.2)

$$D_\phi(r) = 6.88 \left(\frac{r}{r_0} \right)^{5/3} \text{ rad}^2. \quad (3.6)$$

If we assume a fair Fried parameter of $r_0 = 20$ cm and an actuator spacing of $r = 42$ cm in the metapupil in 8 km distance, the average actuator difference is $0.2 \mu\text{m}$, which is half of the value shown in figure 3.13. The pupil distortion scales linearly with the actuator level. Thus, atmospheric turbulence frequently causes deformations of several 10%.

4 The Kiepenheuer-Institute Adaptive Optics System – KAOS Evo 2

«Jedes Computer-Programm
hat mindestens einen Fehler.»

(Prof. Michael Stix)

4.1 Introduction

KAOS (Kiepenheuer-Institute Adaptive Optics System) is the name of the adaptive optics control software that is developed at the Kiepenheuer-Institute since 2001. It was originally written by T. Berkefeld and it is in everyday use for observations at the VTT since 2002(von der Lühe et al., 2003). KAOS was also used for the first MCAO demonstrations at the VTT(Berkefeld et al., 2005) as well as for image stabilization and active optics control in the Sunrise balloon telescope mission in 2009(Berkefeld et al., 2011).

The source code of the original version grew over time as the algorithms ripened and it became difficult to maintain the program and to continuously include the experiences of the first decade of operating a solar AO system. T. Berkefeld and the author of this thesis developed a new program—referred to as *KAOS Evo 2* in this document—taking the experiences gained from the first software version into account and rethinking approaches and implementations. The new version implements a modal reconstruction approach. Direct reconstruction was not carried over. We consider the modal approach—especially for MCAO—to be implemented easier and less prone to pitfalls and it also feels more "natural". KAOS Evo 2 is used in the MCAO testbed and since July 2011 also at GREGOR. KAOS Evo 2 follows the philosophy and design goals of the original KAOS that are:

- **Formidable benefit** The use of AO must provide significant advantages with minimal drawbacks such that astronomers like and desire to use it. In particular, AO must perform with the omnipresent low-contrast solar granulation pattern.
- **Ease of use** Astronomers shall be able to use AO on their own without the need for highly trained AO operators.
- **Robustness** The AO system must be tolerant to incorrect use and must offer remote serviceability.
- **Ease of development** The application of techniques that require rarely available specialized experts shall be avoided and widely-used hardware shall be preferred to exclusive, special-purpose hardware.
- **High flexibility** Algorithms should be easily modifiable to try out new ideas with little extra efforts.
- **High portability** The AO control software shall be quickly adaptable to new demands and possibilities in terms of hard- and software as well as telescopes.

The compromise of these aspects resulted in the architectural foundation that should be made of general purpose computers running unixoid operating systems and the programming language C for the original software and C++ for KAOS Evo 2. All computations should be performed by the computer’s CPUs.* Additional hardware such as cameras, frame-grabber devices and interfaces for commanding of the adaptive mirrors should be selected from off-the-shelf product ranges in order to avoid costly development efforts.

KAOS Evo 2 uses specialized third-party software libraries, namely the FFTW for efficient Fourier transforms, the BLAS interface to optimized matrix-vector-multiplications, as well as LAPACK for singular-value decomposition (SVD).† The user interface is based on Qt (fig. 4.1). All these libraries are used by a large number of software developers and they are available for wide range of operating systems and hardware architectures. The libraries are available with various licenses that allow for both proprietary and open licensing of KAOS Evo 2.

KAOS Evo 2 offers generic code for all functions. For some sections that are not well optimized and vectorized by the compilers, SIMD (*single instruction, multiple data*) code specific to x86-64 CPUs is also included in KAOS Evo 2. This code can be easily adapted to other instructions if runtime-performance needs to be improved for other CPU families. Only a few lines of code in KAOS Evo 2 make use of Linux system calls. They are mainly related to process scheduling and timing issues for that no appropriate POSIX interface is available. The corresponding code lines can be quickly adapted to system calls specific to other operating systems, if needed. KAOS Evo 2 makes use of multiple CPU cores of the computer for parallel processing of the wavefront sensor data and matrix multiplies. Parallelization is managed through the Unix System V shared memory interface.

KAOS Evo 2 is designed for Hartmann-Shack wavefront sensors. However, thanks to the modal wavefront reconstruction approach, it may be extended to use other (non-zonal) wavefront sensor types such as the Optical-Differentiation WFS(von der Lühe, 1988; Schmidt and von der Lühe, 2007) which is interesting for layer-oriented solar adaptive optics. Modal reconstruction feels natural for MCAO because wavefront gradients are first converted into wavefront modes that are assigned to the conjugate layers of the deformable mirrors with tomography. Then, the modes are converted into actuator commands of the corresponding mirror. The modal basis used by KAOS Evo 2 is defined in configuration files read at runtime. Arbitrary bases can be used. However, we usually use Karhunen–Loève functions or individually optimized orthogonal modes described by Lai et al. (2000) (see sec. 2.7.2).

*The use of graphics processing units (GPU), which entered scientific computing in the last years, for image data processing seems not to be appropriate to us for the present application. To our knowledge, the additional latency involved to transfer the image data from host computer RAM to the GPU RAM would be greater than the savings because relatively few processing operations are to be executed. We do not know of any solution to transfer image data from the frame grabber directly to the GPU RAM, bypassing the host RAM and the CPU. We did not study the utilization of GPUs in detail for this reason.

†The BLAS (Basic Linear Algebra Subprograms) interface (Lawson et al., 1979) is offered by numerous specialized implementations among which the most prominent are ATLAS (Automatically Tuned Linear Algebra Software) Whaley and Dongarra (1999), OpenBLAS (formerly GotoBLAS) Goto and van de Geijn (2008) and the Intel Math Kernel Library Intel Corporation (2012). The latter also offers an FFTW-compatible FFT library. LAPACK (Linear Algebra Package) Anderson et al. (1999) is normally used in conjunction with an optimized BLAS implementation such as the ones mentioned previously. FFTW (Fastest Fourier Transform in the West) (Frigo and Johnson, 2005). The KAOS Evo 2 GUI depends on Qt (Blanchette and Summerfield, 2008) and Qwt (QWidgets for Technical Applications) (Rathmann and Wilgen, 2012).

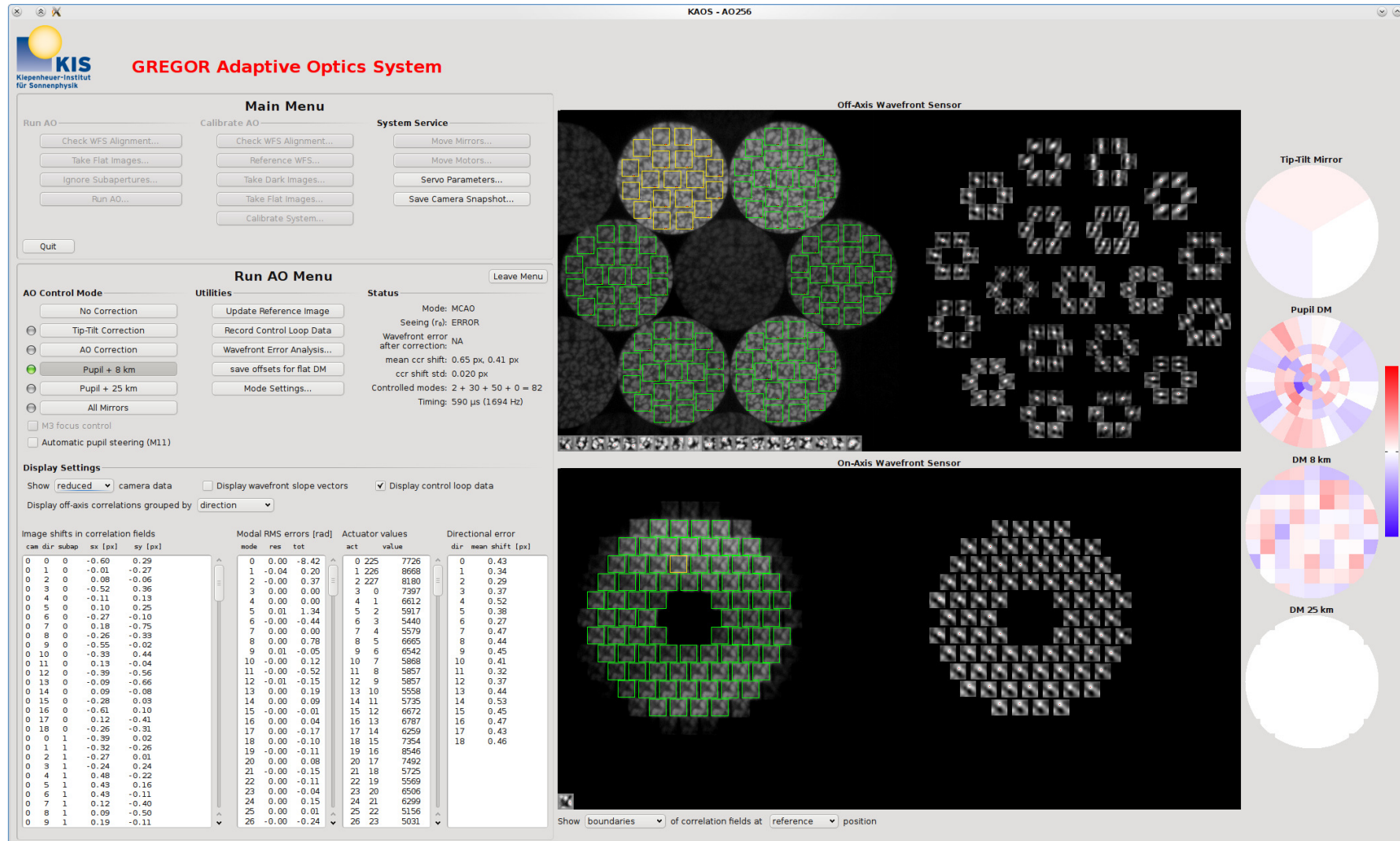


Figure 4.1: Screenshot of the main interface window of KAOS Evo 2 while running in MCAO control mode (Pupil + DM_{8 km}). In the left half of the upper black panel, live images of the multi-dir (off-axis) WFS camera are displayed. The right half displays the computed cross-correlation functions ordered by guide directions (refer to figs. 2.25 and 2.26 for explanation). The lower panel shows the same for the on-axis WFS. Green and yellow boxes mark the correlation fields. Yellow boxes indicate the fields that provide the reference images for the correlations. The current reference images are displayed at the bottom of the black panels. The instantaneous actuator values of the adaptive mirrors are displayed on the right-hand side.

4.2 The essentials of KAOS Evo 2

The control loop, in which the output commands for the adaptive mirrors are computed from the input measurements of the wavefront sensors, and the procedure to calibrate this loop are the essential modules of KAOS. Calibrating the system is very easy and essentially done with one mouse click. At the telescope, the motorized stages are moved automatically, inserting the appropriate objects into the light path. The involved calculations to build the matrices are performed in the background without user interaction. The possibility to have the system calibrated remotely or by normal observers is superior to other solar AO systems.

4.2.1 The KAOS control loop

The sequence of a control loop cycle is shown in figure 4.2 and discussed on the following pages.

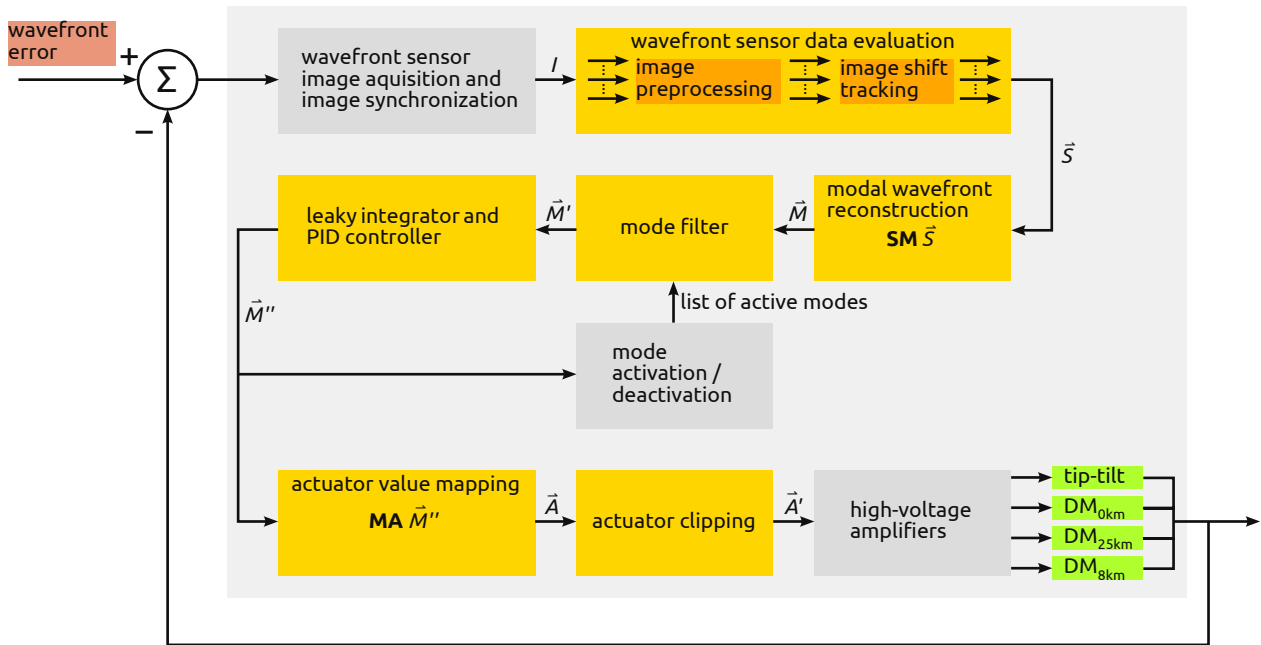


Figure 4.2: Flow diagram of the KAOS control loop. Yellow boxes indicate parallelized tasks and dark gray boxes indicate serial procedures.

4.2.1.1 Prerequisites

Wavefront sensor referencing For the estimation of the wavefront gradients in the Hartmann-Shack sensors from the wavefront-sensor camera images, three steps are necessary before entering the control loop. A dark image and a flat field image are recorded which are needed for the image preprocessing. Next, the points of origin for the shift estimation in wavefront sensors' correlation fields are defined. In the case of the on-axis WFS, a single pinhole is placed into its entrance focus. The pinhole is imaged multiple times onto the wavefront sensor camera according the subaperture layout of the microlens array of the sensor. The positions, identified with a 3×3 -pixel parabolic fit, of the pinhole images are defined as the points of origin of the shift estimation (fig. 4.3). The correlation fields are then centered to the points of origin to pixel precision. The position \vec{f} of the pinhole image in the correlation field is the reference for the wavefront control, i. e. this is considered the image position for a flat, unaberrated wavefront. Referencing of the multi-dir WFS is similar but a pinhole asterism that represents and defines the guide directions is placed into the entrance focus instead of a single pinhole.

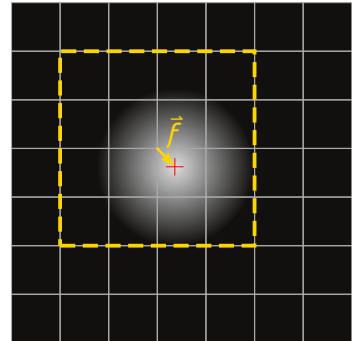


Figure 4.3: Referencing of a correlation field. Tiled background: camera pixels. Cross: pinhole image position to sub-pixel precision. Dashed line: correlation field (actually 24×24 pixels wide).
 \vec{f} : pinhole image position in correlation-field coordinates.

Camera image synchronization Synchronizing the captured images is indispensable for MCAO with two wavefront sensor cameras. In order to prevent trailing image data processing of one camera, which would result in misinterpretation of wavefront information, it must be ensured that the images being evaluated in each loop cycle represent the wavefront of the same point in time. The exposures of both cameras are synchronized by hardware as explained in section 3.3.2.2 in the case of GREGOR's MCAO. The image counter that is provided by the cameras is analyzed by KAOS Evo 2 in order to identify temporally matching images. The incorporated Mikrotron EoSens cameras are configured to store a 32-bit counter in the first four pixels of each image taken. (If the cameras wouldn't offer this feature, the counter could also be generated by the EDT frame grabbers.). The difference of the counters is registered at startup of KAOS Evo 2 by processing the following sequence:

1. set the frame rate of the clocking multi-dir camera to 1 Hz
2. grab an image from the multi-dir camera (blocking function)
3. grab an image from the on-axis camera directly after this
4. calculate: $\text{counter}_{\text{multi-dir}} - \text{counter}_{\text{on-axis}} + 1$
5. set the frame rate of the clocking multi-dir camera to the control loop frequency

The "+1" in step 4 is required due to fact that the image grabbing function is blocking, i. e. the image grabbed from the on-axis camera in step 3 was not exposed in the same cycle as the image from the multi-dir camera in step 2, but in the next cycle. (The image exposed by the on-axis camera during step 2 is missed.) The frame rate is set to 1 Hz in the first step in order to ensure that no exposure is lost between steps 2 and 3. A ring buffer with the size of four image frames is used to have data transferred from the frame grabber into the main memory (RAM) via DMA (direct memory access). The number of four is recommended by EDT for each frame grabber. At the beginning of a control loop cycle, the buffers of the leading multi-dir camera are searched for the greatest image counter (the first four pixels of each buffer) that is larger than in the last cycle. Next, the image with the counter difference from above is searched in the buffers of the on-axis camera. Looking for the greatest image count rather than for the next count ensures that the loop does not lag behind permanently (and unnoticed) if frames were lost to what ever reason (which may happen rarely). As soon as the searched image counts are found, the processing of the image data in order to compute the wavefront gradients is being started. At this moment, the corresponding image frames have not yet been completely stored into ring buffers but transfer is going on. This image synchronization method is in new in KAOS Evo 2 and eliminates disordered image processing.

4.2.1.2 Zonal wavefront gradient computation

The image shifts in the correlation fields of the Hartmann-Shack sensors are registered and interpreted as wavefront gradients in the same way as it is done in the original KAOS version(Berkefeld et al., 2010). In order to lower the latency by not waiting until a complete image has been transferred into the ring buffers, processing of a correlation field starts as soon as it is filled with new data and a CPU core is available. For this purpose, four of the last pixels of each correlation field are used as "trigger pixels" which indicate whether this field needs to be or was already processed in the current control loop cycle. After processing of the correlation field data, the trigger pixels are filled with a bit pattern that cannot occur naturally in the exposed images. During the next exposure the trigger pixels are reset with natural image data, thus indicating new data that requires for processing.

Image preprocessing The following image processing is performed on the correlation fields individually, i. e. independently of the image data in the other correlation fields, by the next available CPU core once the trigger pixels have been reset:

1. The raw image data gets corrected for dark image and flat field artifacts by computing

$$I'_{i,j} = \frac{I_{i,j} - D_{i,j}}{F_{i,j} - D_{i,j}}, \quad (4.1)$$

where $I_{i,j}$ is the raw image data of the correlation in the pixel at the position (i, j) , F is the flat field image and D is the dark image. [‡]

[†]Dark- and flat correction is well known in digital processing of image data with low contrast or signal-to-noise

2. The intensity gradient of the corrected image I' is removed, yielding I'' , in order to prevent the upcoming correlation tracking from getting stuck on patterns larger than the correlation field size that might otherwise be more significant than the small scale structures which shall be the essential structures for tracking.
3. A two-dimensional fractional *Hamming* window is applied in order to attenuate frequency leakage (ringing) in the upcoming discrete Fourier transform. The window is defined[§] by

$$w_i = \begin{cases} a + [a - 1] \cdot \cos(2\pi i / p) & , \text{ for } i = 1, \dots, p/2 \\ 1 & , \text{ for } i = p/2 + 1, \dots, N - p/2 \\ a + [a - 1] \cdot \cos(-2\pi i / p) & , \text{ for } i = N - p/2 + 1, \dots, N \end{cases} \quad (4.2)$$

$$W_{i,j} = w_i \cdot w_j, \quad (4.3)$$

with $a = 0.53836$ and $p = 10$. N is the number of rows of the square correlation field and is 24 in the case of the wavefront sensors in the MCAO testbed. The window is applied by computing

$$I'''_{i,j} = \left[\left[I''_{i,j} - \langle I'' \rangle \right] W_{i,j} \right] + \langle I'' \rangle. \quad (4.4)$$

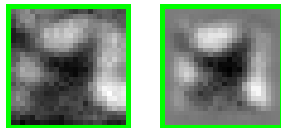


Figure 4.4: Windowing of correlation field image data.
Left: A raw image I . Right: The windowed image I''' .

4. The image data I''' is normalized such that the mean is one, yielding \hat{I} , in order to remove slight mean intensity variations that can occur despite the flat field correction as the telescope spider rotates, continuously shadowing the subapertures differently, or when pronounced structures are shifted (partially) in or out of the correlation field as a consequence of the corresponding instantaneous wavefront slope. In conjunction with the gradient removal in the second step, this adds up to data detrending that is widely performed before discrete Fourier transforms in order to avoid that lots of spectral power is being attributed to the uninteresting lowest frequencies.

This image processing sequence was re-implemented for KAOS Evo 2 basing upon the SSE2 instruction set introduced by Intel for the x86 processor architecture. The new implementation is about twice as fast as the old generic implementation even though the latter is auto-vectorized by the compiler.

ratio. The dark image accounts for read-out noise and dark current which is different for all pixels. The flat field represents the static intensity pattern superimposed to the actual image data, being dust on the detector, stray light or uneven pixel sensitivity.

[§]The fractional *Hamming* window is very similar to the *Tukey* window that seems to be more widely referred in the literature and could likely be used as well. The critical aspect of windowing the correlation field is the width of the unattenuated area. A classical Hamming window falls off too fast, effectively removing too much information from the very narrow 24×24-pixel data, ending up in a less distinct peak of the cross correlation and hence in a more insensitive shift estimation.

Image registration and shift estimation As explained in section 2.5.1, the shift of an image \hat{I} in an arbitrary correlation field is determined with respect to a reference image \hat{R} . The reference image is defined to be the image in a certain correlation field (see fig. 4.1) at a fixed point in time and is updated regularly because of the continuous evolution of the structure on the Sun's surface.⁴ The shift is estimated following equation (2.63) by computing the cross correlation

$$X = \text{IFFT} \left(\text{FFT}(\hat{I}) \text{ conj} \left(\text{FFT}(\hat{R}) \right) \right) \quad (4.5)$$

and by finding the maximum $\vec{m} = \max(X)$ with a 3×3 -pixel parabolic fit. The maximum \vec{m} refers to the coordinate system of the correlation field. In order to get the actual deviation from the ideal wavefront, the position \vec{f} of the referencing pinhole (fig. 4.3) needs to be considered. In order to keep track with the tip-tilt error, the shift of the current reference image with respect to the initial reference image needs to be taken into account as well. For this reason, the wavefront gradients that are used for the upcoming wavefront reconstruction are computed by

$$\vec{g}_k = \vec{m}_k - \vec{f}_k + \vec{t}_{\text{ref}} + \vec{f}_{\text{ref}}, \quad (4.6)$$

where \vec{m}_k is the position of the correlation maximum in the k^{th} correlation field and $\vec{m}_k - \vec{f}_k$ is its deviation from the ideal position. \vec{t}_{ref} is the tip-tilt error of the current reference image with respect to the initial reference image. \vec{f}_{ref} is added in equation (4.6) in order to cancel \vec{f}_k if k is the correlation field that was selected to provide the reference image, i. e. for " $k = \text{ref}$ ". The proportionality factor that translates the image shift into a physical wavefront gradient is omitted in equation (4.6) because it cancels during the calibration procedure of the adaptive mirrors and the wavefront sensors. Therefore image shift is used synonymously to wavefront gradient in this context. The individual wavefront gradients of the s correlation-field shifts are stored in the *shifts-vector*

$$\vec{s} = (\vec{g}_1, \dots, \vec{g}_s)^T. \quad (4.7)$$

This vector is the error signal for the control loop.

Multiple CPU cores (seven in the case of the MCAO testbed) run this task in parallel going through all correlation fields. It is verified in KAOS Evo 2 that the correlation field data being processed originate from the same camera image frame by checking the camera's image counter. If this condition is failed, e. g. as a consequence of rare delays (it is not a 100% real-time system), the current cycle is discarded.

Correlation reference, absolute tip-tilt error and image distortion As explained in the footnote on page 47, a correlating Hartmann-Shack sensor per se does not allow for absolute identification

⁴The reference image is updated several times a minute as follows: The preprocessed image, with the most contrast in a certain time interval is selected to be the new reference image. The shift of the new reference image with respect to the old one is registered and added to the shift of the old reference image, yielding \vec{t}_{ref} .

of the tip-tilt error. The initial reference image that is the baseline of \vec{t}_{ref} is a simple snapshot in the current implementation of KAOS Evo 2. Thus, the tip-tilt error in KAOS refers to this instantaneous, random and undefined tip-tilt error of the initial reference snapshot. The absolute referencing problem affects the wavefront control in two matters. The first and less severe effect is that the image gets a little bit out of place randomly when entering the tip-tilt control loop. For MCAO, the random correlation reference is more critical since it does not allow to identify the tip-tilt error in the guide directions, i. e. the image distortion. Thus, the current implementation of KAOS introduces a random but fixed image distortion when running in MCAO control mode. To overcome this issue, using a temporally averaged image, which voids random fluctuations, as correlation reference could be worthwhile. Such a feature was implemented in the original KAOS version, which was used in the test runs at the VTT in 2004–2006, and accounted for the temporal evolution of the solar structure, which would otherwise have caused the MCAO trying to counteract that evolution. However, static image distortion introduced by the telescope optics cannot not be deduced from the temporally averaged image of the Sun.

4.2.1.3 The modal wavefront reconstruction and control scheme

After the computation of the shifts vector \vec{S} , the modal wavefront reconstruction is performed and the actuator commands are sent to the high-voltage amplifier system following the sequence whose steps are explained on the next pages:

1. reconstruction of the *modes-vector* $\vec{M} = \mathbf{SM}\vec{S}$ from the Hartmann-Shack wavefront sensor shifts-vector \vec{S}
2. online mode filtering yielding \vec{M}'
3. applying a digital PID controller on the mode coefficients M'_i yielding \vec{M}''
4. mapping the modes to the *actuators-vector* $\vec{A} = \mathbf{MA}\vec{M}''$
5. clipping the actuator values A_i to the operating range yielding \vec{A}' and output to the high-voltage amplifiers

Wavefront reconstruction Wavefront reconstruction and control in KAOS Evo 2 involves the following vectors and matrices^{||}:

- The shifts-vector $\vec{S} = \left(g_1^{(x)}, g_1^{(y)}, \dots, g_s^{(x)}, g_s^{(y)} \right)^T$ contains the x and y image shifts of the s correlations fields (subapertures and subfields) of all wavefronts sensors (eq. (4.7)).
- The modes-vector $\vec{M} = (M_1, \dots, M_m)^T$ assembles the coefficients of the wavefront modes of all adaptive mirrors in the system.

^{||}Lots of confusing names (interaction-, reconstruction-, command-matrix, etc.) appear in the AO community for all this matrices, some of them are even ambiguous and depend on the very context they are referring to. The descriptive names in brackets are used in this document to clarify the meanings and functions of the matrices.

- The $m \times 2s$ matrix **SM** (*shifts-to-modes matrix*) converts the measured shifts \vec{S} into the modes \vec{M} .
- The actuators-vector $\vec{A} = (A_1, \dots, A_a)^T$ contains the control values of the actuators of all adaptive mirrors.
- The $a \times m$ matrix **MA** (*modes-to-actuators matrix*) maps the modes vector into the actuator space.
- The $2s \times a$ matrix **AS** (*actuators-to-shifts matrix*) converts the actuator values into correlation field image shifts. This matrix is automatically set up by the one-click calibration procedure of KAOS as explained in section 4.2.2.

The wavefront modes used in KAOS Evo 2 can be either defined on the mirrors or on the wavefront sensors.

In the first case, the modes-to-actuators matrix **MA** is modeled by decomposing a set of wavefront modes into actuator values through modeled or interferometrically measured influence functions. The shifts-to-modes matrix **SM** is assembled from the calibration measurements by

$$\mathbf{SM} = \begin{pmatrix} \text{pinv}(\mathbf{MS}_{\text{TT}, \text{MD-WFS}}) & 0 \\ \text{pinv} \left(\begin{pmatrix} \mathbf{MS}_{\text{DM}_0 \text{ km}, \text{MD-WFS}} \\ \mathbf{MS}_{\text{DM}_8 \text{ km}, \text{MD-WFS}} \\ \mathbf{MS}_{\text{DM}_{25} \text{ km}, \text{MD-WFS}} \end{pmatrix}_{\text{DM}_0^{\text{low}}} \right) & \begin{pmatrix} \text{pinv} \left(\mathbf{MS}_{\text{DM}_0 \text{ km}, \text{OA-WFS}} \right)_{\text{DM}_0^{\text{high}}} \\ 0 \\ 0 \end{pmatrix} \end{pmatrix}, \quad (4.8)$$

where, for example, $\mathbf{MS}_{\text{DM}_0 \text{ km}, \text{OA-WFS}} = \mathbf{AS}_{\text{DM}_0 \text{ km}, \text{OA-WFS}} \mathbf{MA}_{\text{DM}_0 \text{ km}}$ denotes the modes-to-shifts matrix for $\text{DM}_0 \text{ km}$ with respect to the on-axis wavefront sensor. The subscript DM_0^{low} shall express, that only the lowest K modes of $\text{DM}_0 \text{ km}$ enter the inversion and that the higher modes in the inverse matrix are padded with zeros to restore it with full size. $\text{DM}_0^{\text{high}}$ means that modes higher than K are used while padding the lowest modes after inversion. Thus, the tip-tilt mirror and the lowest K modes of $\text{DM}_0 \text{ km}$ are controlled by the multi-dir WFS. At least focus and astigmatism are included in K for the current 6 subapertures, and probably more modes if 18 subapertures are available in the multi-dir WFS in the future. The on-axis WFS is used to control the higher modes of $\text{DM}_0 \text{ km}$. Thanks to this delegation scheme of mirror modes, non-common path aberrations are minimized because the multi-dir WFS is next to the science focus whereas the on-axis WFS is located upstream (fig. 3.3). In particular, tip-tilt and focus are referenced by the multi-dir sensor, which may be different from the on-axis WFS's perspective, due to misalignment, lab seeing and vibrations. The reconstruction scheme in equation (4.8) means moreover that the lowest K modes of $\text{DM}_0 \text{ km}$ do not reflect the on-axis wavefront error but the average error of all guide directions. The pseudo-inversions (pinv) are computed using SVD and singular value clipping. Modes that shall never be used for reconstruction (e.g. badly seen, aliased modes, or tip-tilt on $\text{DM}_8 \text{ km}$ and $\text{DM}_{25} \text{ km}$) do not enter the inversion. An additional matrix that removes the mean image shift of the correlation fields of each wavefront sensor can be multiplied optionally with the $\text{pinv}(\cdot)_{\text{DM}}$ -matrices of the deformable mirrors in equation (4.8) for additional regularization of the inversion problem.

When using wavefront sensor modes, the modes-to-shifts matrix \mathbf{MS} is modeled from the wavefront sensors' geometries and the modes-to-actuator matrix is obtained from

$$\mathbf{MA} = \text{pinv}(\mathbf{AS}) \mathbf{MS}. \quad (4.9)$$

For MCAO control, only the mirror-based approach is available in KAOS Evo 2 at this time. For classical AO, both approaches can already be used. The sensor-based approach allows for precise absolute measurement of the residual wavefront error, since only the fixed WFS optics and the camera detector is needed for the model. The mirror-based approach suffers from time-varying effects on actuator length, like creeping etc, that might have appeared since last calibration as well as from hysteresis. These effects lower the knowledge of the actual mirror deflection. However, we do not expect any additional negative effects from the mirror-based modes within this context in closed-loop operation.

The temporal sequence as well as the power spectrum of the reconstructed modes can be displayed in real-time by the user interface of KAOS Evo 2 as shown in figure 4.5.

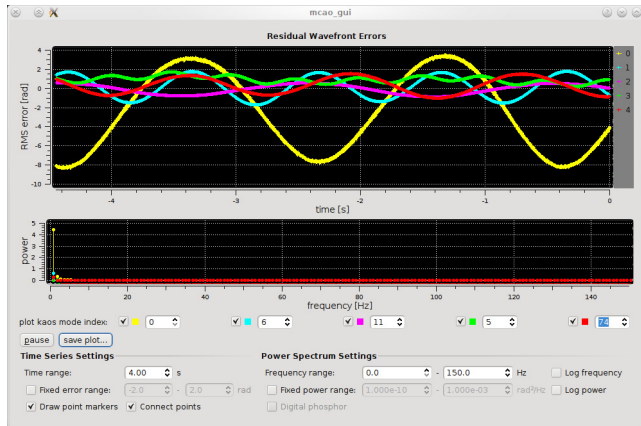


Figure 4.5: Screenshot of the time sequence and power spectrum display window of KAOS Evo 2. The residual error (i.e. the element of the modes-vector \vec{M}) of up to five arbitrary modes can be displayed.

Modal filtering and control The gain of the individual mode coefficients is set, yielding \vec{M}' . At present, no statistical or whatsoever weighting is implemented but it may be in future. The gain is just set to one for modes that shall be controlled at the moment or it is set to zero for modes that shall momentarily be inactive (the step after the next). A leaky integrator ensures that badly seen modes of the deformable mirrors do not windup. A digital proportional–integral–derivative controller (PID controller) is applied individually on the coefficients of the filtered modes-vector \vec{M}' yielding \vec{M}'' . All modes of a deformable mirror share the same PID parameter set. The parameter sets are manually tuned for each adaptive mirror and are not changed in the control loop. The derivative term of the controller is normally set to zero for deformable mirrors.

Output of the actuator values The modes-vectors \vec{M}'' that was calculated by the PID controller is translated into actuator values of the adaptive mirrors with the modes-to-actuators matrix \mathbf{MA} . In order to ensure that the actuator values stay within the allowed operating range,

the values are clipped accordingly, yielding the final actuators-vector \vec{A}' that is sent to the high-voltage amplifier system.

Adjustment of the number of controlled modes In order to switch on the control loop softly and to keep it stable when seeing degrades temporary, the number of actively controlled modes is adjusted by setting the gain of higher modes to either zero or one. (The new gain is considered in the step "modal filtering and control" in the next loop cycle.) When switching on the control loop, only the lowest mode is active and higher modes are activated successively. When seeing degrades higher modes are deactivated top-down. Re-activation when seeing improves is carried out again bottom-up. At present, this is accomplished by basically considering the actuator value variance that a mode would add and activating or deactivating the mode if the variance would be in or out of a given limit. However, this approach can cause the control loop to stuck with half the actuators on the upper limit and the others at the lower limit in some strange situations and needs to changed. Considering the peak-to-valley difference instead of the variance could be a better solution.

4.2.2 Calibration

Calibration refers to the procedure of teaching the control loop the quasi-static actions and reactions of the adaptive mirrors (including the high-voltage amplifiers) and the wavefront sensors, that is measuring the actuators-to-shifts matrix **AS**. Latencies (e. g. settling times) and transient oscillations are not considered. In principle, the digital value of each actuator of an adaptive mirror is ramped up (slowly enough to avoid oscillations) while the image shift in all correlation fields of the relevant wavefront sensors is recorded. A fit is applied in order to estimate the linear relation of the each correlation field shifts and the value of the actuator. The slope of each fit is stored in the matrix **AS** that converts the actuator values into correlation field shifts. Actually, and because it is not essential for the understanding of this chapter it is not explained in to much detail, the actuators are not ramped one by one but altogether with a set various patterns in order to increase the signal-to-noise ratio by avoiding correlation fields with little or no image shift. This set of actuator value patterns is sometimes referred to as *poke matrix*. An additional matrix is involved to remap the shifts effected by the poke matrix patterns to single actuators. KAOS normally incorporates *Hadamard* matrices for poke patterns as proposed by Kasper et al. (2004). Each of the Hadamard poke patterns pushes 50% of the actuators equally while pulling the other 50% by the same amount, leaving no actuator at rest.

In order not to confuse the calibration by atmospheric seeing, not a structure on the Sun is tracked but an artificial object that is placed in an intermediate telescope focus upstream of the adaptive mirrors (F_3 in the case of GREGOR). This object can be a pinhole or an extended (solar-like) structure. The possibility to calibrate the control system with extended targets is new in KAOS Evo 2. The original calibration procedure was based on centroid tracking and hence was only applicable for pinholes. Two optional correlation tracking methods were added to the calibration routine. The first method of image tracking is exactly the same

as executed in the control loop, i. e. correlation fields share a constant reference image. The second method uses the image of the previous ramp step—individually for each field—as correlation tracking reference. Both methods can be used with extended structures as well as with pinholes. Calibrating with extended objects is interesting for the high-altitude mirrors of an MCAO system. Actuators of these mirror do not simply shift the image in a correlation field (like those of $DM_0 \text{ km}$ would) but also slightly distort the image as depicted in figure 4.6. Thus tracking a very narrow section of the correlation field, as it would be the case with a pinhole, also accounts for the distortion within the field. This is not desirable because an extended structure is to be tracked in the control loop. The advantage of the individual, moving reference of the second method is that large actuator strokes can be tracked because the structure does not escape from the reference. In addition, the measured shift of consecutive ramp steps is always small, which is beneficial because the employed cross-correlation tracking in the Fourier domain «systematically underestimates large shifts»(Löfdahl, 2010). This method is moreover less prone to "miscalcorrelation" as a consequence of the mentioned distortion.

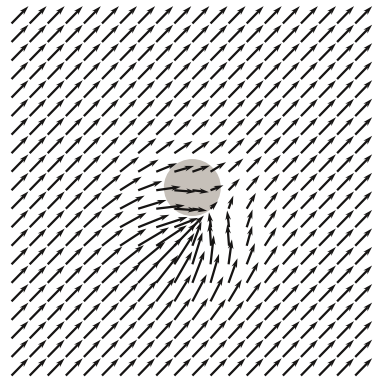


Figure 4.6: Image shift and distortion in a correlation field due to a high-altitude DM and the area of a pinhole image.

5 The Testbed of GREGOR's MCAO system

Control is nothing without power.

*(Extension of Pirelli's claim
"Power is nothing without control")*

5.1 Introductory remarks

The testbed of GREGOR's MCAO system was set up in the optics lab of the Kiepenheuer Institute in Freiburg. It began with GREGOR's classical AO system GAOS.80 in 2007. This system was extended to the multi-conjugate system in January 2009. The 80-actuator $DM_0\text{ km}$ was replaced by a 68-actuator mirror in July 2009 because GAOS.80 was installed at the telescope. The testbed is mostly made of the original hardware (optics, mechanics, electronics) that will be installed in the GREGOR telescope. Only $DM_0\text{ km}$ and the control computer have become obsolete. These parts will be superseded by the 256-actuator mirror and the more powerful computer that have been installed at GREGOR in 2012.

The control computer, the wavefront sensor cameras and the interface boards are critical for the feasibility of GREGOR's MCAO system. Although being off-the-shelf products, they were cutting-edge at the time of their purchase and we were among the very first customers. Virtually every electronic device, except the computer screen, the keyboard and the mouse as well as the illumination lamp, was the source of severe problems at least once. All our suppliers and manufacturers proved to be very corporative and did a great job in supporting us and improving their products. The devices work properly together now and—if any—only minor issues are known.

In May 2010, one of the OKO PDM69 mirrors had an electrical break-through between a couple of actuators and ground, resulting in a creeping mirror which was not able to keep its shape. This mirror was replaced on warranty in September 2010. In January 2012, another break-through was noticed in the other OKO PDM69 mirror of the first batch. This actuator, which was located at the edge, was removed by the manufacturer. However, another actuator of this mirror failed shortly thereafter. It was not possible to have this actuator removed because it is not at the edge and therefore not accessible. For this reason, the MCAO testbed was used in 2012 only with two deformable mirrors, namely $DM_0\text{ km}$ and $DM_{8\text{ km}}$, for most of the time. $DM_{25\text{ km}}$ was replaced by a flat mirror. The defective mirror will be kindly replaced at the manufacturer's expense.

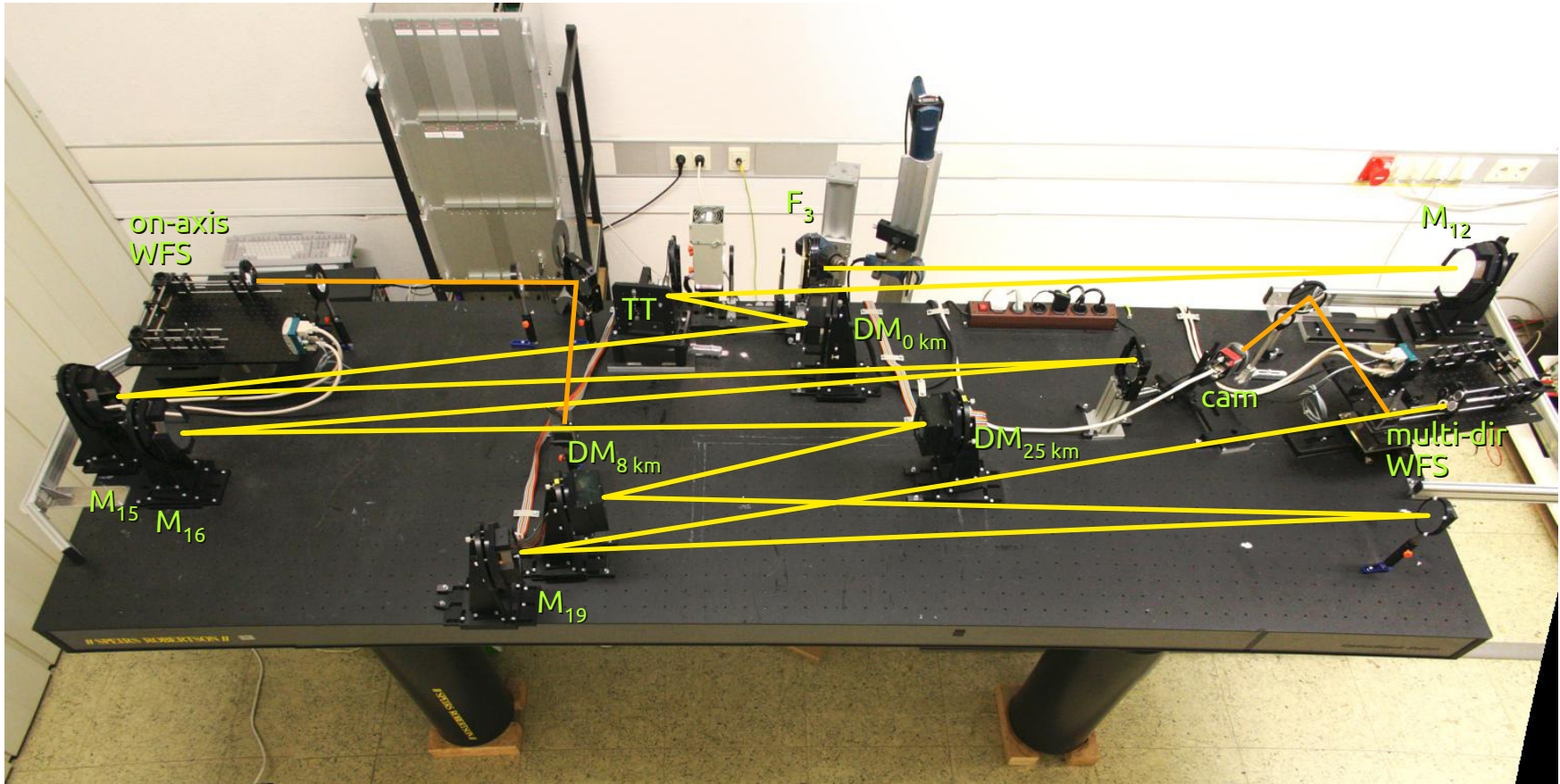


Figure 5.1: The testbed of the MCAO for GREGOR as set up in Freiburg. The setup starts with a target in the imitate of the telescope's focus F_3 (top center of the bench) which is illuminated with a halogen light. Between the tip-tilt mirror (TT) and $DM_{0\text{ km}}$, a pupil mock-up stop is placed (not shown, see fig. 5.3). Light for the on-axis WFS is split of before $DM_{25\text{ km}}$. A science camera (cam) records the MCAO corrected images in a duplicated focus. The rack in the back accommodates the DM drive electronics. The optical bench measures 3.6×1.2 meters.

5.2 Configuration of the MCAO testbed

The MCAO testbed was to be build up on a 3.6×1.2 -meters wide optical bench (*Speirs Robertson LiteLine*) that was present in the optics lab of the Kiepenheuer-Institut. The setup is shown in figure 5.1 and starts with an illuminated mock-up of GREGOR's tertiary focus F_3 that is realized by a revolving wheel accommodating various image structures (pinholes, asterisms, granulation slides etc.) which are used as observation targets. Two additional flat mirrors are used to fold the light beam according to the bench dimensions. A cooktop is used to generate turbulence. An additional imaging camera represents the scientific instrument and is used to rate the performance of the control loop.

5.2.1 Illumination

GREGOR's MCAO testbed is illuminated with a halogen light bulb in a *Linos Lamphouse* (G6.35 socket). Bulbs with either 150 W or 250 W at 24 V are used. The bulb's filament is about 6 mm wide and about 2.5 mm high. The lamphouse features a reflector mirror that is used to image the backside of filament adjacent to the filament itself. In this way, the luminous area effective for the illumination of the testbed is doubled. The light emitted by the filament is collected by a condenser lens that—along with the collimating mirror M_{12} —images the filament into the pupil plane as shown in figure 5.2. The aperture stop shown in figure 5.3 imitates the telescope pupil. The image of the filament and its reflected backside fill the aperture stop. This illumination scheme is very similar to the illumination in classical slide projectors, which is made for even illumination of the image plane and efficient use of the filament light. However, due to the low etendue of GREGOR's MCAO train, most of the light emitted by the bulb in the lamphouse is actually lost and does not find its way to the cameras. The condenser lens in the testbed features an f-number of about $f/10$ whereas the original condenser of the lamphouse, or as it is usually found in slide projectors, is a strongly aspheric $f/1.2$ lens. A stop with 13 mm diameter has been attached to lamphouse. This stop transmits just enough light to illuminate an area of about 20 mm in F_3 such that the lamp cannot dazzle people in the room. Due to the filament's thready nature, the pupil is not illuminated evenly. By moving the condenser out of focus, the filament image could be blurred for even pupil illumination. In this way, however, a blurred image of the filament would occur in the image planes of F_3 . Artifacts of the filament in the image plane are particularly bad because they are not static but very rapidly changing as a consequence of the vast turbulence in the lamphouse. The moving artifacts may interfere with low-contrast objects put in F_3 , and the wavefront sensing would be degraded since it is based on image tracking. The uneven illumination of the pupil was accepted for this reason and was not a matter of problems. A heat-absorbing glass and a yellow glass* are located next to the 13 mm stop in order to prevent the escape of ultra-violet radiation that is emitted by the halogen bulb. The heat-absorber is necessary to protect the yellow glass from the thermal load.

Other light sources such as ultra-high-pressure (UHP) mercury gas discharge lamps as used in

*The yellow glass (GG435) was selected in consideration of a liquid crystal display that was temporarily used in F_3 and which suffers from UV load.

5 The Testbed of GREGOR's MCAO system

modern video projectors or lasers where considered. The halogen bulb was chosen because it was the most feasible option and provides enough light (i.e. radiant density). Today's high-power LEDs might also be an option for illuminating such a testbed.

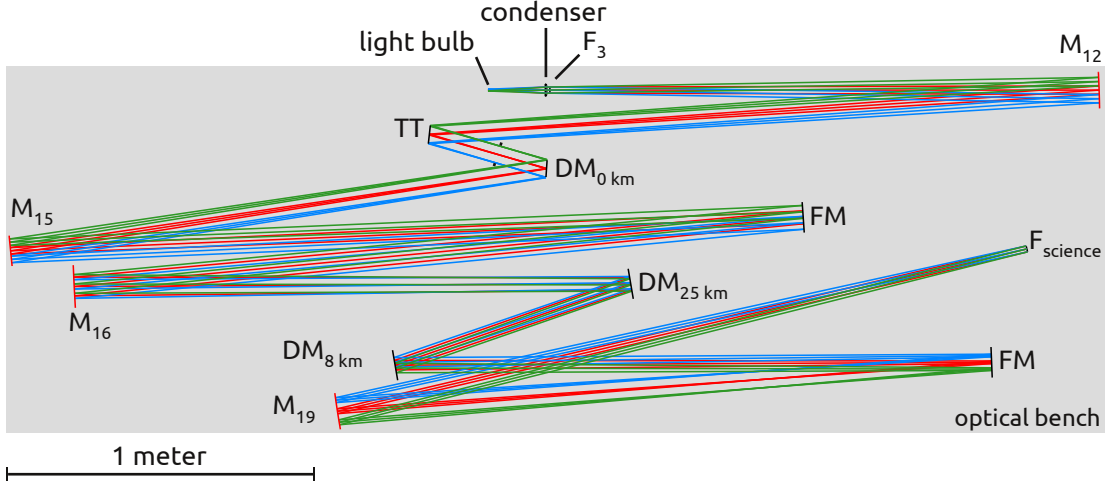


Figure 5.2: Optical configuration and illumination scheme of the MCAO testbed. A halogen light bulb and condenser lens illuminate the F_3 mock-up. An aperture stop between the tip-tilt mirror (TT) and $DM_{0\text{ km}}$ forms the pupil of the setup. The image of the light bulb filament fills this stop. The traced rays originate in the center of the light bulb (red) or at its ends (green/blue). An intermediate focus is located about halfway between M_{16} and $DM_{25\text{ km}}$. A pupil image is formed in between M_{19} and the prior folding mirror FM. Wavefront sensors and science camera are not shown. Red-drawn mirrors are curved, all others are flat. Distances of the components on the optical axis are the same as in figure 3.3.

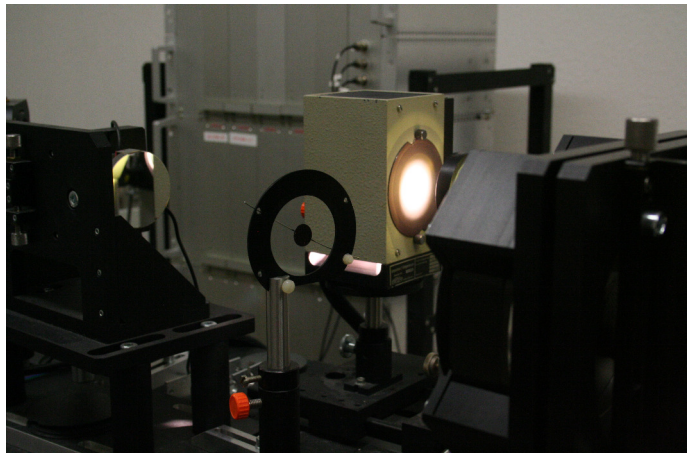


Figure 5.3: The mock-up stop (center) of the telescope pupil with secondary mirror shadow between the tip-tilt mirror (left) and $DM_{0\text{ km}}$ (right). The diameter is 48 mm. The lamphouse is in the background (the bright spot is light reflected from the heat-absorbing and yellow glasses, not shown).

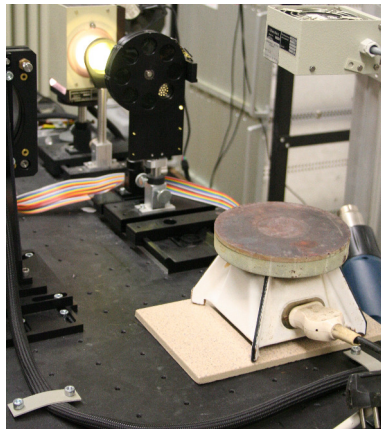
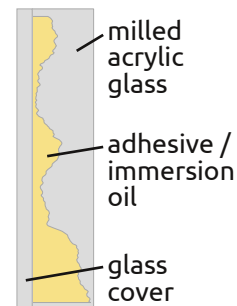


Figure 5.4: The cooktop used to generate turbulence. It is located downstream of the revolving wheel in F_3 . A fan is mounted above the cooktop to optionally suck on air from the cooktop. The lamphouse is in the background and $DM_{0\text{ km}}$ at the left edge of the picture.

5.2.2 Turbulence generation

For the test runs reported in chapter 6, optical turbulence was produced with a cooktop that was located approximately 30 cm downstream of F_3 as shown in figure 5.4. This location spans the conjugate volume between $DM_{8\text{ km}}$ and $DM_{25\text{ km}}$. A cooktop temperature of 200–300 °C produces "reasonable" seeing. Additional fans were sometimes used to modify the turbulence. Hot air blowers were also used, however, the turbulence they produced did not "feel as good" as the cooktop turbulence even though lots of configurations to shape the air flow were tried. Rotating phase plates which would be penetrated by the light beam in a small section were also considered. It was tried to reproduce phase plates based on nearly matching the refractive indices on two sides of a topographic surface. An atmospheric wavefront profile was CNC-milled into acrylic glass therefor. The profile was filled with either optical adhesives or optical oils and closed with glass plate on top. The refractive index of the filling differed only slightly from the acrylic glass in order to attenuate the optical effect of the profile height to the proper strength. Similar phase plates are commercially available from Lexitek Inc.[†] but they did not meet the required specifications. However, the wavefront error, which was measured interferometrically, of the phase plates produced in the KIS workshop was dominated by large structures of unknown origins which were not present in the unmachined acrylic glass. These structures could be the result of tensions inside the acrylic glass that relieved unevenly during machining. However, the use of rotating phase plates was never preferred by the author of this document: Due to their rotating nature, the generated wavefront repeats fast and one does not really know how long the loop can run with random turbulence and towards what one is optimizing the control system.

The cooktop turbulence is certainly not a very good representation of atmospheric turbulence in terms of Kolmogorov statistics. However, it was not intended to have a perfectly realistic turbulence because this could probably be the content of a thesis on its own. The turbulence



[†]Lexitek Inc., Wellesley, Massachusetts, USA, <http://www.lexitek.com>

5 The Testbed of GREGOR's MCAO system

for the MCAO testbed should only allow to reach the limit of the control system in terms of strength as well as speed and should somehow "feel good".

Digital turbulence In order to test the wavefront reconstruction and control, digital turbulence, which can be activated on demand, was implemented in KAOS Evo 2. Digital turbulence means that additional actuator values, which were computed in advance, are superimposed to the actuators values that are output by the control loop. The control loop perceives this modification only by the wavefront sensor measurements. Perfect wavefront reconstruction and control would end up in constant actuator voltages at the end of the line. This feature is very useful even though it is not a complete test because the on-axis wavefront sensor does not see the digital turbulence of DM_{8 km} and DM_{25 km}. Digital turbulence is not intended to test any temporal characteristics. Because of the latencies of the modification and the feedback control, the bandwidth of the digital turbulence should be below about 10 Hz to be potentially eliminated by the control loop.

5.2.3 Science focus camera

The camera in the duplicated science focus, which is used to record the MCAO corrected images, is a DALSA 1M150. This camera offers 1024×1024 pixels which are 10.6×10.6 μm wide and it is read out with 143 frames per second. Additional relay optics (they were changed since the photograph in fig. 5.1 was taken) magnify F_{science} by factor 0.5 in order to fit a sufficient large field of view onto the camera detector. The image on the detector is equivalent to a 81.92 arcseconds wide field in the real focus of GREGOR.

5.3 System tests

5.3.1 Tip-tilt systems

In order to verify and characterize the time response of the tip-tilt systems, their step responses were recorded. The step response was measured with a laser beam that was directed onto the tip-tilt mirror as sketched in figure 5.5. The reflected beam was attenuated by a linearly variable density filter parallel to the deflection of the reflected laser beam. A collecting lens focused the laser beam on a photo diode. (Without this lens, the deflected beam would escape the photo diode.) In this way, the photo diode current is related linearly to the deflection angle of the tip-tilt mirror. The photo diode current, the low-voltage step that was input to the high-voltage amplifier as well as the high-voltage output, i. e. the actuator voltage, were measured with a digital oscilloscope. The resonance frequency was identified additionally. The relation of the step response and the resonance frequency is specified by Physik Instrumente GmbH & Co. KG (2012): «A piezo actuator can reach its nominal displacement in approximately 1/3 of the period of the resonant frequency, provided the controller can deliver the necessary current.»

Two holders for the tip-tilt stages were available, a lighter and a more massive version, which are similar apart from the material thickness.

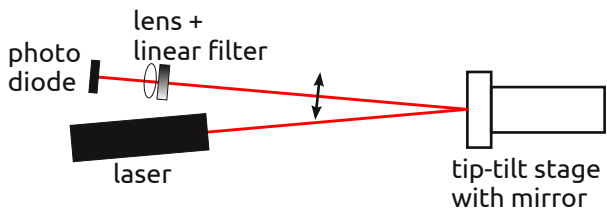


Figure 5.5: Schematic setup (not to scale) used to measure the step response and the resonance frequency of the tip-tilt mirrors. The laser beam is attenuated by a linear density filter depending on the deflection angle. The photo diode current is a linear measure of the mirror's tilt angle.

Table 5.1: Step response of the Physik Instrumente tip-tilt system.

high-voltage step	2 V	5 V	10 V	20 V	30 V	50 V	read. error
HV-out rise time 0-90% [μs]	100	100	104	104	104	132	4
HV-out rise time 0-100% rise [μs]	130	130	150	150	160	152	40
photo-diode rise-time to nominal [μs]	440	432	432	448	448	488	8
photo-diode peak-time [μs]	696	696	696	712	720	768	< 24
photo-diode overshooting [%]	69	63	62	67	65	55	

5.3.1.1 Physik Instrumente tip-tilt mirror system

The step response of the Physik Instrumente (PI) tip-tilt mirror system is shown in figure 5.6, and the measurements for steps from 2–50 V are listed in table 5.1. The rise time is constant up to at least 30 V steps, i. e. the amplifier behaves linearly within this range. The PI tip-tilt stage was mounted in the massive holder when the step response was measured. The frequency response of the PI tip-tilt system was measured automatically with a HP35665A analyzer and is shown in figure 5.7. There is no further resonance peak up to 2 kHz. It seems that the massive holder suppresses the resonance peak that occurs with the light holder at 812 Hz. However, the characteristics of the frequency response of the massive holder is not understood. The resonance peak at about 752 Hz would correspond to a rise time of

$$\frac{1}{3 \cdot 752 \text{ Hz}} \approx 443 \text{ μs}, \quad (5.1)$$

according to the rule of PI. This conforms with the values in the order of 440 μs given in table 5.1. Exercising this calculation for the resonance at 812 Hz, which was observed when the tip-tilt stage was mounted in the lighter holder, yields a rise time of about 410 μs. The PI tip-tilt stage was mounted with the massive holder in GREGOR because of attenuated gain at 812 Hz.

5.3.1.2 KIS tip-tilt mirror system

The step response of the KIS tip-tilt mirror system is shown in figure 5.8. The rise-time to the nominal deflection is about 350 μs which is 100 μs faster than response of the Physik Instrumente system. The resonance frequency of the KIS tip-tilt mirror was found by increasing the excitation frequency manually while registering the mirror's deflection amplitude with an oscilloscope. The resonance peak was at about 955 Hz (fig. 5.9). Calculating $1/(3 \cdot 955 \text{ Hz}) \approx 349 \text{ μs}$ also agrees with the rule of Physik Instrumente.

5 The Testbed of GREGOR's MCAO system

Figure 5.6: Response of the undamped PI tip-tilt system to 10 V step.
 Yellow (channel 1): Low-voltage input.
 Cyan (channel 2): High-voltage (HV) output.
 Magenta (channel 3): Photo diode current (i. e. mirror deflection).
 Rise times of HV (0-90%) and of photo diode (nominal and peak) are indicated.
 0-100% rise time of HV output is about 150 μ s.
 Oscillation frequency is about 830 Hz.
 Overshoot is about 60%.
 (Picture shows an oscilloscope screenshot with three separate cursor gauges overlaid on the same data.)

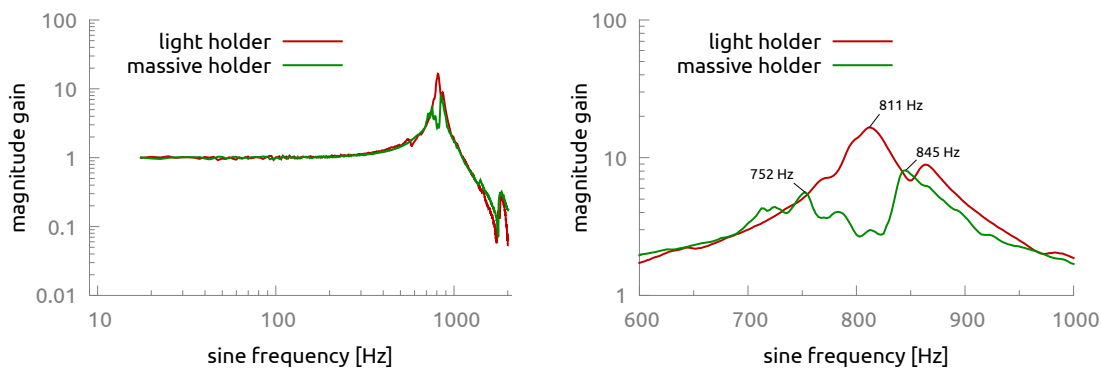
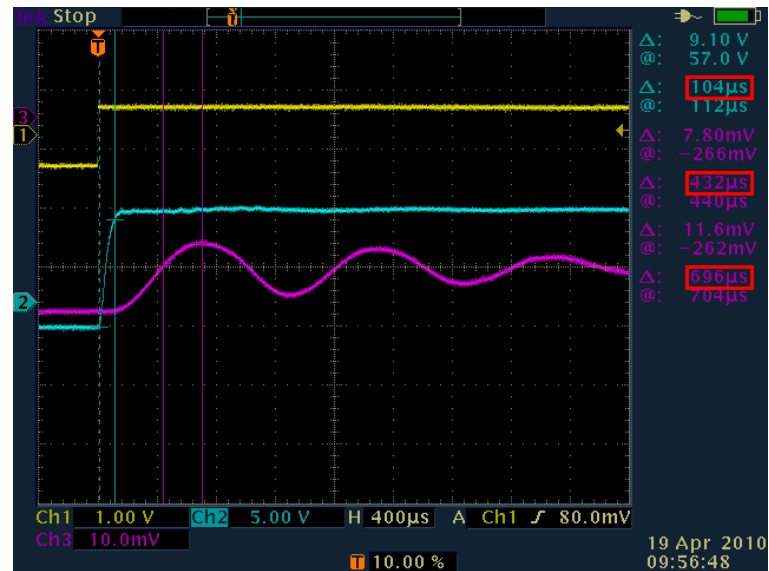
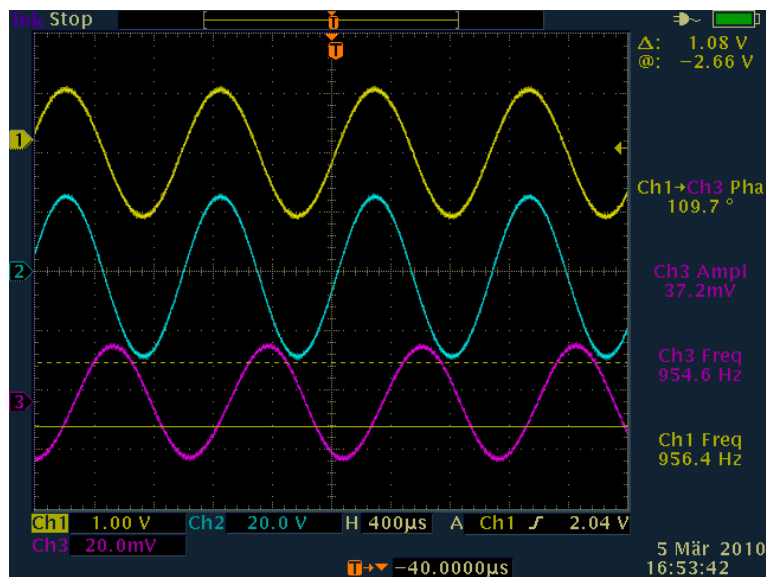
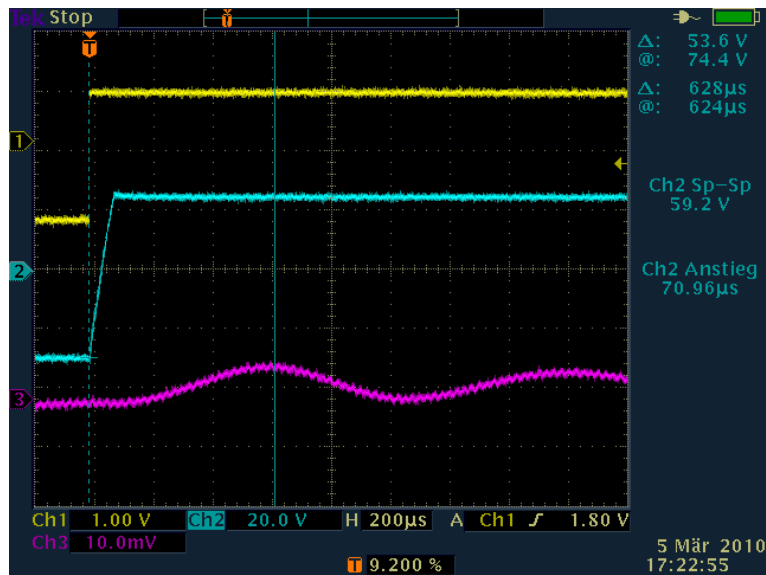


Figure 5.7: Frequency response function of the Physik Instrumente tip-tilt system. The mirror deflection was measured with a photo diode (fig. 5.5). The sinus oscillation with increasing frequency but constant amplitude was generated by the spectrum analyzer and input to the PI high-voltage amplifier. The tip-tilt stage was mounted in two different holders for testing.



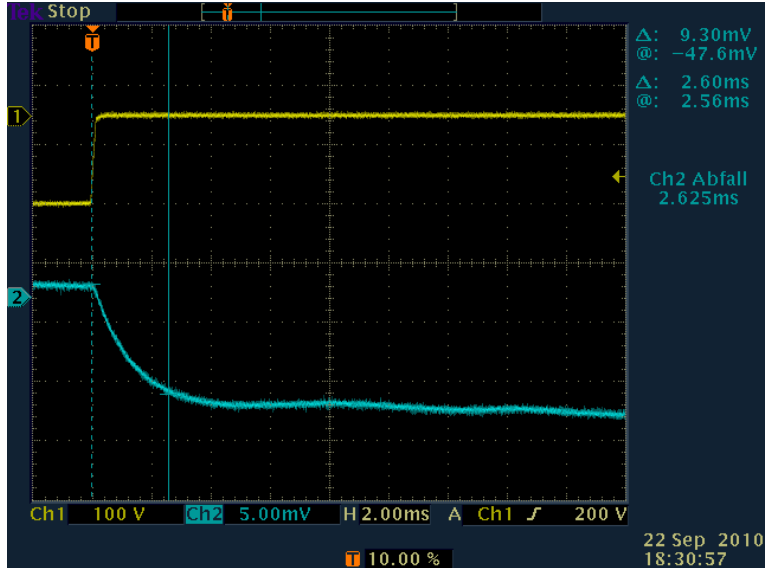


Figure 5.10: Response of the undamped OKO PDM69 KIS3 to 150 V step applied to the central actuator.

Yellow (channel 1): High-voltage output.
Cyan (channel 2): Photo diode current (i.e. mirror deflection).

The measurement setup was similar to fig. 5.5. The laser was pointed onto the tested actuator.

0-100% rise time of HV output is about 200 μs , 0-90% is about 160 μs .
Rise time of photo diode is about 4 ms.

5.3.2 Deformable mirrors

5.3.2.1 OKO PDM69 – the high-altitude mirrors

Step response In order to identify the latency of the OKO PDM69 mirrors, the step response was measured for the central actuator of OKO PDM69 KIS3. The step response was measured in a similar fashion as it was for the tip-tilt mirrors. The laser was pointed onto the central actuator which deflected the beam. The step response is shown in figure 5.10. The actuator rise time to 90% is about 2.6 ms and about 4 ms to 100%.

Flatness The surface profile of OKO PDM69 KIS3 when the bias voltage of 150 V is applied to all actuators is shown in figure 5.11. This profile changes as the mirror ages. The spherical shape of the mirror was removed in the figure by subtracting a fitted parabola. The radius of curvature varies between about 33 and 42 meters depending on the ambient temperature. The mirror was flattened (figure 5.12) with the use of interferometrically measured influence functions of all actuators and by iteratively projecting them with a linear least-squares fit onto the measured surface error. It was not possible to remove the actuator print-through, not even by manually tweaking the actuator voltages. The reason for this is shown in figure 5.13. The print-through bumps are not located at the positions of the actuators but in between. See section 6.3.1.2 for additional comments on the potential origin of this effect.

5.3.2.2 Night DM2-55-80 #00042 – the 80 actuators $\text{DM}_{0\text{ km}}$

$\text{DM}_{0\text{ km}}$ of the GREGOR's first generation system GAOS.80 is a bimorph mirror and was manufactured by Night Opt N. It is labeled *DM2-55-80 #00042*. When this mirror was operated in closed loop in the AO testbed in the lab in Freiburg in 2007 (no MCAO at this time), it was only possible to control about 44 modes. However, the combination of this

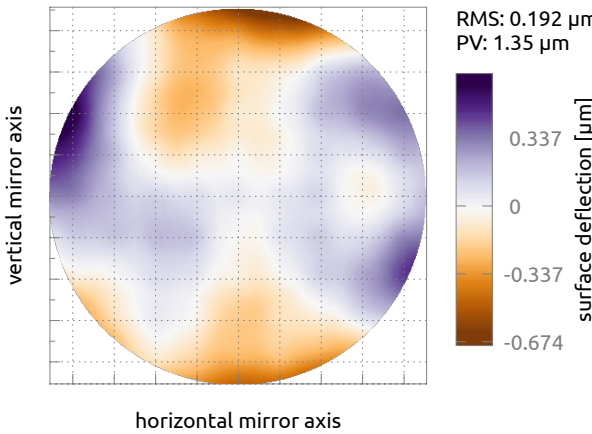


Figure 5.11: Surface profile of OKO PDM69 KIS3 when 150 V applied to all actuators in 01/2012, measured interferometrically. Parabolic portion is subtracted. Grid lines represent the actuator grid. Shown diameter is 43 mm.

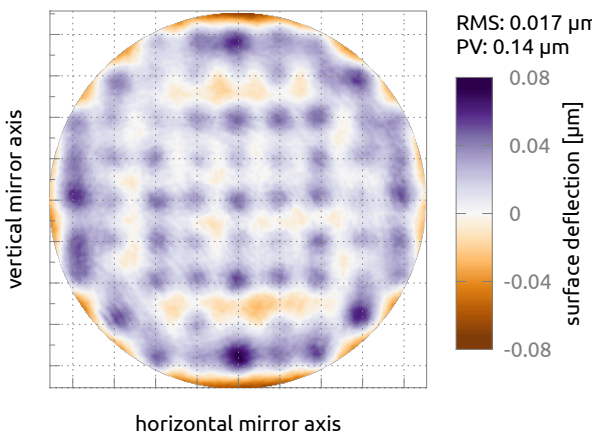


Figure 5.12: Surface profile of OKO PDM69 KIS3 after flattening in 01/2012, measured interferometrically. The incorporated actuator offset values are plotted in fig. 5.14. Parabolic portion is subtracted. Grid lines represent the actuator grid. Actuator print-through is present. Shown diameter is 43 mm.

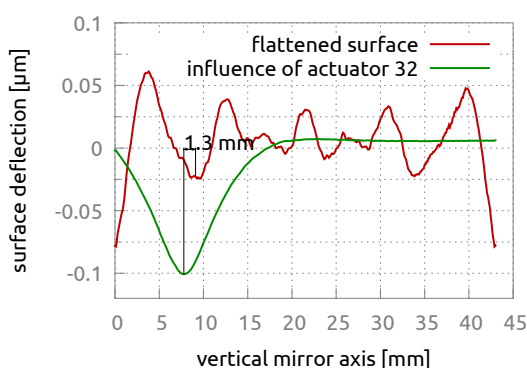


Figure 5.13: Bottom-up cross-section through the center of the flat profile in fig. 5.12 and through the influence function of the 2nd the actuator from the bottom (vertically scaled to fit in the plot). The extrema of the actuator print-through are not located at the position of the of the actuators. Print-through is about 80 nm peak-to-valley.

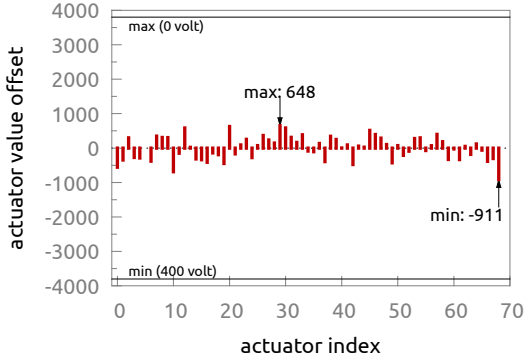


Figure 5.14: Actuator offset values of the flat profile in fig. 5.12.

mirror with 80 actuators and the used on-axis wavefront sensor should had yield 60–70 controllable modes. Also, the calibration method of the KAOS control software using on Hadamard matrix actuator patterns didn't work. This mirror was analyzed by the author of this thesis(Schmidt, 2007) in order to find the reasons thereof. The most important result of this report is repeated in the following.

The influence functions of the mirror's actuators were measured with a *Fisba μPhase* interferometer. The reason for the low number of controllable modes was found to be the outer ring with 28 actuators that does not affect the mirror shape within the used diameter of 48 mm as intended. The outer ring had been designed for a face sheet edge that is fixed in the mirror housing, i. e. the outer actuators are radially much more extended than the actuators of the inner rings. However, the manufacturer used a «free-edge fixation» with a soft clamp to hold the bimorph plate in its place without significant constraints on the surface gradients at the edge. That this kind of fixation is used was not clear when the mirror was designed and specified. It was first revealed during the close inspection of the mirror. Figure 5.15 shows the interferometrically measured influence functions of four actuators in the outer and second-outer ring. Although the interferometer was slightly decentered horizontally during the measurement, it can be clearly seen that boundary of the 50 mm aperture of the interferometer is completely covered by the actuators of the second outer ring and that the actuators of the outer ring have no great additional effect within that area.

These measurements show that the outer 28 actuators are not as effective as needed within the used aperture and therefore do not contribute to the number of compensated modes of the KAOS. According to Kudryashov (2007), it is possible to fix the mirror edge more tightly by replacing the foamed fixation rings with rubber rings. However, this was never tried.

5.3.2.3 CILAS SAM256 – the 256 actuators $DM_0\text{ km}$

The rise-time of the step response of the $DM_0\text{ km}$ for GAOS.256 is about 400 to 500 μs . (It was measured slightly differently that for the other mirrors). The surface error of this mirror after flattening was 8 nm RMS and less than 5% of the full actuator voltage range was needed therefor.

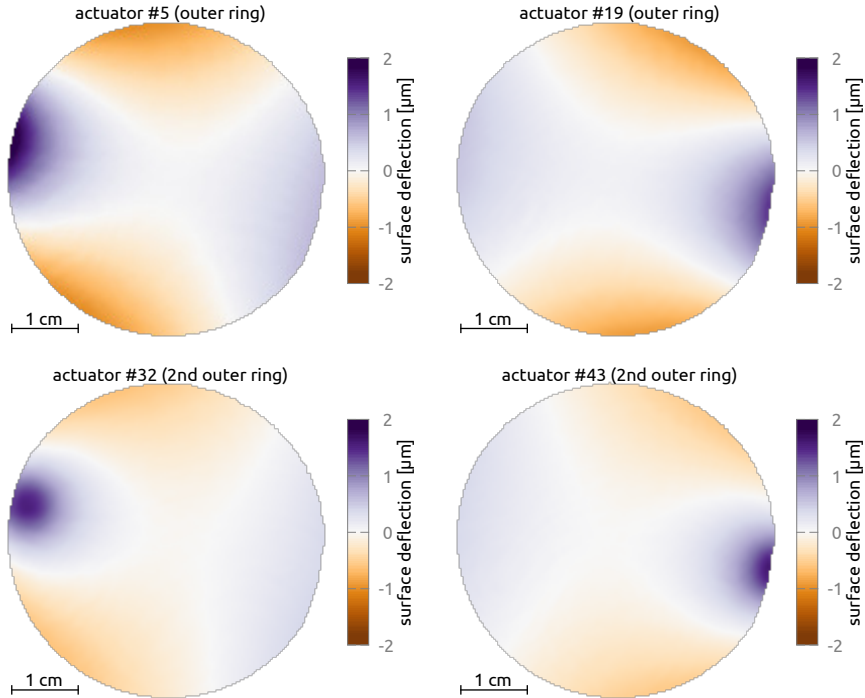


Figure 5.15: Interferometric influence functions of 4 actuators in the two outer rings of *Night* DM2-55-80 #00042 at +300 V. Note the slight decentering of interferometer to the left, perceivable by asymmetric detail in the left and center columns. The aperture of the measurement is approximately 50 mm in diameter. The used diameter of this mirror in the GREGOR telescope and in the (MC)AO testbed is 48 mm.

5.3.2.4 High-voltage amplifier system

Bandlimit To verify the bandlimit of the high-voltage amplifiers, the frequency response was measured for a single channel. The digital high-voltage drive electronics system for the deformable mirrors does not offer an easily accessible analog input. For this reason, the sinusoidal oscillation to measure the frequency response was generated digitally with the control computer for discrete frequencies. The high-voltage output was measured with an oscilloscope and is plotted in figure 5.16. The 3-dB cut-off frequency is about 1900 Hz

Old digital interface The operation with the originally planned RS422 PCI Express interface board (*General Standards HPDI32A*) that was used for a long time in the MCAO testbed often suffered from versatile problems. The most severe issue was a randomly freezing address bit that screw up the mirror commanding. It was not possible to solve this problem although great effort was spent. Thus, one of the unassigned bits had been re-routed and used as replacement. Another flawed bit was found in Spring 2012 in one of the least significant bits of the actuator value. This unswitchable bit provoked resonance of the 68-actuator DM_0 km in the testbed because of relatively large, ever-hammering voltage steps if controller parameters had been set fast enough to compensate for hot-air turbulence. For this reason, it was needed

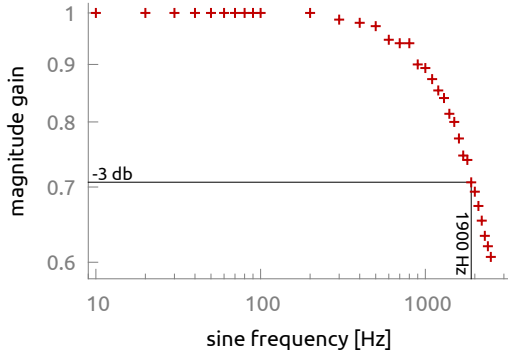


Figure 5.16: Frequency response function of channel 183 of the high-voltage amplifier. Mirror was not connected. Excitation amplitude was 150 V. 3-dB-bandwidth is about 1900 Hz.

to revise the interfacing to the high-voltage amplifier system. The General Standards board was replaced by a CameraLink transmitter PCI Express board (*EDT PCIe8 DV CameraLink Simulator*) that outputs *ChannelLink* signals. In order to use this, a board which converts the ChannelLink signals to the required RS422 signal was developed in corporation with F. Heidecke (KIS) towards the end of this thesis.

5.3.3 Frame grabbers and camera synchronization

The synchronization of the exposures of the two wavefront sensor cameras is shown in figure 5.17. The strobe-out signal of the multi-dir camera is used to trigger the on-axis camera. The delay of the on-axis camera exposure, caused by the signal amplifier and the trigger logic in the on-axis camera's frame grabber, is less than 2 μ s and is negligible short.

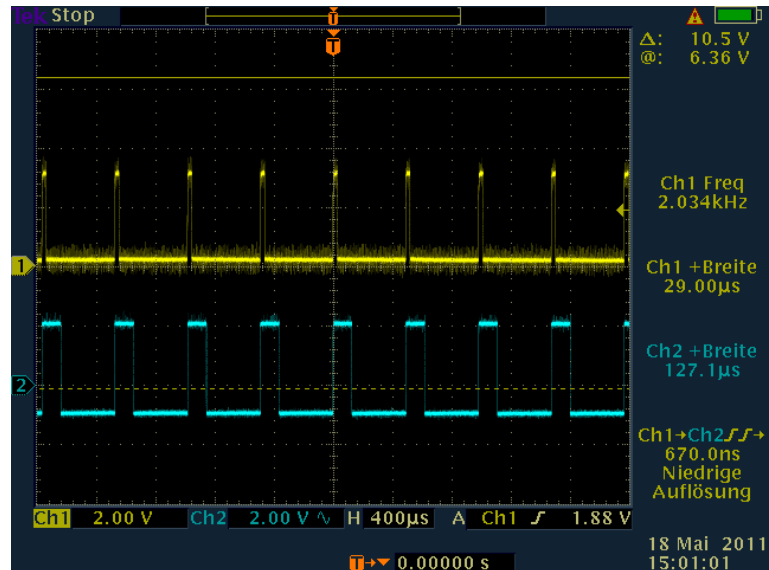


Figure 5.17: Exposure synchronization of the on-axis and the multi-dir WFS cameras. Yellow (ch 1): exposure of multi-dir camera. Cyan (ch 2): exposure of on-axis camera. Measured were the strobe-out signals of the Mikrotron EoSens cameras. This signal is high during exposure. Exposure times were 28 and 128 μ s. The delay of the on-axis camera exposure is less than 2 μ s (read from other measurement).

5.3.4 Control loop timing

The measured computing times and latencies are summarized in figure 5.18. To compute the image shift (from data preprocessing to peak fitting) in a single correlation field, a CPU core of the control computer needs about 10–11 μs . The temporal root-mean-square jitter of the control loop is about 2–3 μs . This was measured with a digital oscilloscope at the digital input of the high-voltage system. The overall latency from processing in the control computer and until the adaptive mirrors reach their nominal position (within the linear range) is about 900 μs for the KIS tip-tilt mirror and about 4.5 ms for the OKO PDM69 mirrors. For both the CILAS mirror and the Physik Instrumente tip-tilt mirror that are already installed in GREGOR, the latency is about 1000 μs . To estimate the overall latency of the wavefront control, half of the exposure time has to be added because this is the average age of the camera image that is processed. The exposure time at the telescope is in the order of 100 μs .

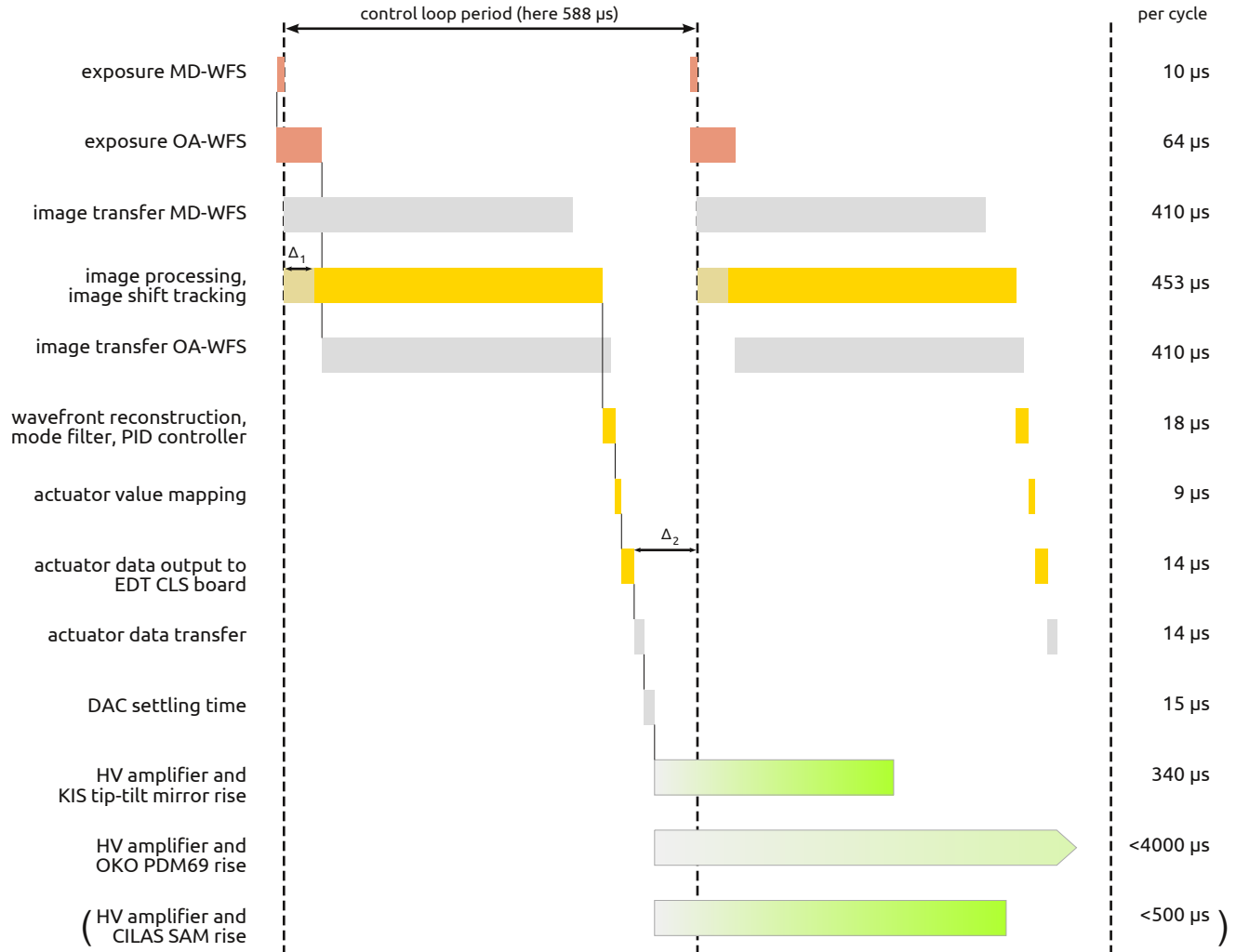


Figure 5.18: Timing diagram of the MCAO tested control loop. The given timings refer to MCAO control with TT, $DM_{0\text{ km}}$ and $DM_{8\text{ km}}$, i. e. 140 actuators and 192 correlation fields. The given exposure times were used in the test runs reported in chapter 6. Image processing and tracking includes the time Δ_1 that is needed until the first correlation field has been transferred completely (≥ 24 lines) and which depends on the exact position of this field. Here $\Delta_1 = 43\mu\text{s}$. Residual processing time is $453\mu\text{s} - 43\mu\text{s} = 410\mu\text{s}$. This corresponds to the image transfer time. Actual processing time is about $300\mu\text{s}$, however image data is not transferred fast enough. Thus, image transfer is the bottleneck and about $110\mu\text{s}$ are idled. Δ_2 is the CPU idle time at the end of a cycle according to the loop frequency. Rise time of the adaptive mirrors depend on the step size. Yellow indicates CPU processing.

6 MCAO Testruns

«Achtung! Jetzt gibt es nur zwei Möglichkeiten:
Entweder es funktioniert oder es funktioniert nicht.»

(aus Michael Endes
"Jim Knopf und Lukas der Lokomotivführer")

6.1 General remarks on the test runs

6.1.1 Failure of deformable mirrors

Because of the failure of one OKO PDM69 mirror, most of the tests that are reported in this chapter were made with only two deformable mirrors, namely $DM_{0\text{ km}}$ and $DM_{8\text{ km}}$, as well as the tip-tilt mirror. It was preferred to replace $DM_{25\text{ km}}$ by a flat mirror and to use the remaining OKO PDM device for $DM_{8\text{ km}}$ because $DM_{8\text{ km}}$ is more important due to the stronger turbulence in its conjugate plane at the telescope site. Furthermore, the footprint of a guide direction is larger on $DM_{8\text{ km}}$, i. e. it covers more actuators (see fig. 3.5), which allows for better compensation of image blurring aberrations. Because of the small guide direction foot print on $DM_{25\text{ km}}$, the scope of this mirror is rather compensation of image distortion than compensation of image blurring aberrations. Towards the end of the test runs, the broken device was reintegrated into the testbed as $DM_{25\text{ km}}$ for a few experiments.

6.1.2 Unstable optical alignment due to thermal expansion

The MCAO testbed was set up in the optics lab in *Haus 3* of the Kiepenheuer-Institut. This lab is equipped with a cooling system that can control the ambient temperature by flushing the room with cold air every few minutes. It also dehumidifies the air. However, it is not a true lab air-conditioning system which would constantly control the temperature to the set point accurately by dripping sensitively pre-tempered air into the room. Although the mean room temperature is kept sufficiently accurate by the lab cooling system, the air that is pumped into the room is several centigrades cooler than ambient, accompanying a significant amount of lab seeing. In order to calibrate the MCAO system, the cooling system must be turned off. It was also turned off during all control loop measurements reported in this chapter in order not to pollute the turbulence generated with the cooktop.

However, the lab temperature changes significantly (either with or without cooktop powered on) during the day without the cooling by several centigrades. The significance is given by thermal bending of the optics table which misaligns the optics. The vertical displacement of

the light beam can be greater than 1 cm whereas the alignment in horizontal direction is pretty stable. The image of the pupil stop between the tip-tilt mirror and $DM_0 \text{ km}$ (see fig. 5.3) can move by more than a subaperture in the on-axis wavefront sensor, hence screwing up the calibration. Thus, the optics needed to be realigned several times a day. (Recalibrating the system after realignment is not necessary but advisable if time is available.)

The thermal bending and the need for frequent realignment make it nearly impossible to elaborate the significance of parameter changes in the test runs when they only cause small effects, besides being very annoying and time consuming. Test runs cannot be repeated several times with constant conditions. Thus, it is hard to tell whether small features are the effect of changed parameters or of misalignment.

The table, a *Speirs Robertson LiteLine*, is 3.6 m long, 1.2 m wide and 11 cm thick. Its top and bottom steel plates are press-bonded to 10 cm thick non-metallic honey comb structure material that is named *NORMALEX* in (Speirs Robertson Ltd, 2004). The idea to explain the misalignment is as follows: The air on the top side and on the bottom side of the table changes temperature unequally fast. The consequence is an unequal thermal expansion of both table sides which curves the table severely (due its humble thickness). The thermal conductivity of the honey comb structure inside the table is assumed to be too low to equalize the temperature difference fast. Detailed measurements were performed (by the author of this document and not specified herein) in 2010. The beam of a laser at one table end was reflected by a mirror at the other table end. The displacement of the reflected beam was registered next to the laser with a camera. The temperature of the air and at multiple points on and below the table was recorded. A clear correlation of the temperature and the laser displacement was observed. This was interpreted as a curvature of the table which inclines the laser and the mirror. An elementary finite element analysis of the table performed by A. Fischer (KIS) agreed to the observed deflections. However, the corresponding notes were not archived.

Luckily, it was possible to attribute the frequent misalignment mostly to the *Speirs Robertson* optics table and not to the mounts of the optics that will be moved to GREGOR. The optical table that will carry the MCAO at GREGOR is mounted vertically, i. e. it is actually an optical wall hanging in the room (see fig. 3.4). The GREGOR team expects the temperature differences on the two sides of this table to be less because of the vertical arrangement and the decent air-conditioning system in GREGOR. Furthermore, this table, which is manufactured by *Newport*, is about twice as thick as the *Speirs Robertson LiteLine* table and hence should be less prone to thermal bending.

6.2 Evaluation tools and measures of the MCAO effectivity

In order to rate the effectivity of the MCAO control loop, I recorded time sequences (movies) of short-exposed images of the science focus while logging the control loop data of the KAOS software at the same time. The control loop data included the image shifts in all subapertures and guide directions (i. e. in all correlation fields), the residual wavefront error assigned to each wavefront mode, the number of controlled modes, and the actuator values. A *DALSA 1M150* camera was used to capture the science focus images. The image scale was

0.08 arcsecond equivalents (ase)^{*} per pixel. 5000 images were recorded in most cases which took approximately 35 seconds. The control loop frequency was 1700 Hz if not expressed elsewhere and hence 59500 samples of control loop data were recorded during 35 seconds. To give a quantitative impression of the effectivity of the MCAO control, I use the kinds of visualizations and numbers explained in the following.

6.2.1 Plain images in the science focus

The most obvious and convincing representation of the MCAO's effectivity would of course be a side-by-side comparison of an uncompensated and a compensated long-exposed image (or the temporal mean of the movies). The effect of MCAO is clearly visible in the movies on a computer screen. However, the difference in still mean images is hardly visible and it is probably even harder visible if the images are printed onto paper. For this reason, I concentrate on the following physical figures of merit.

6.2.2 Image distortion in the science focus

The movies recorded with the science focus camera were used to evaluate the temporal evolution of image distortion, i. e. local image motion. After perfect compensation of turbulence, no such image motion would remain. The term *agile image distortion* will be used as a synonym for local image motion in this document.

6.2.2.1 Evaluation procedure

After dark image and flat field image correction (see eq. (4.1)) of the recorded images, hot pixels were reconstructed with a local 3×3 px median filter. These steps are inevitable to prevent the tracking algorithm from sticking on fixed patterns of the image sensor and dust thereon. After this pre-processing, the image sequences of the movies were sliced into stacks of subfields. The two-dimensional shift of the image structure in each subfield with respect to the first picture was determined throughout the stack. The image shift was computed with GNU Octave and the FFT-based cross-correlation method explained in section 2.5.1. A fractional Hamming window was used. The gradient was not removed from the images because it did not prove to make any difference for the used image structures but doubled the computation time.[†] The location of the cross-correlation's maximum was estimated to sub-pixel precision by fitting a parabola in a 5×5 px field. The side length of the subfields was 115 px, which translates to 9.2 ase. As shown in figure 6.1, the subfields overlap by 80 % such that 36 subfields cover 920 px or 73.6 ase, that is their pitch is 23 px.

^{*}The term *equivalents* is used because this angle refers to the on-sky angle in the GREGOR telescope and not to a real angle in the testbed.

[†]The (single-threaded) shift computation of the 36×36 subfields of 115×115 pixels took about 4 to 5 hours for a sequence 5000 frames with the computers at hand.

6 MCAO Testruns

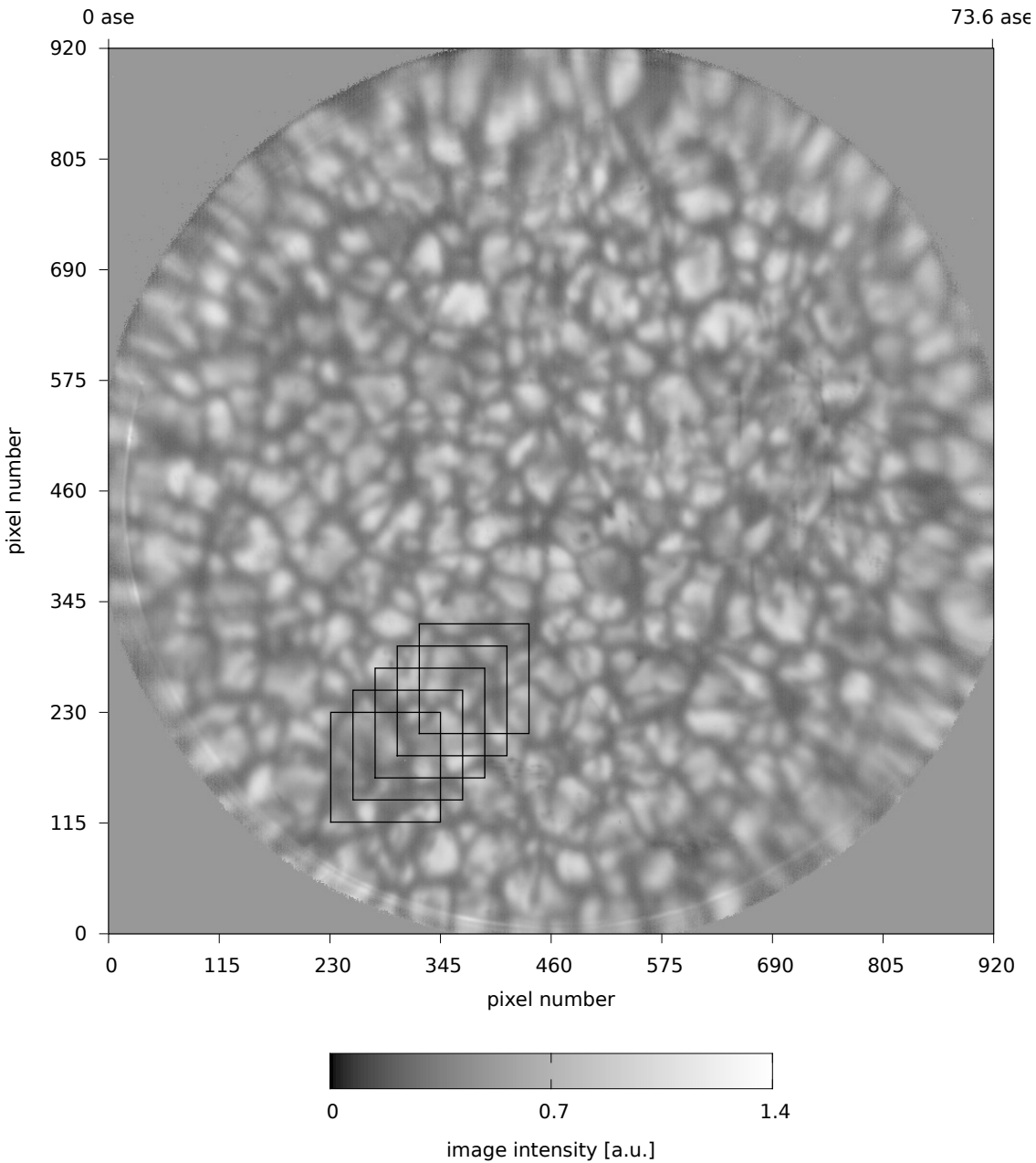


Figure 6.1: Example snapshot of a granulation slide located in the F_3 mockup that was captured in the science focus of the MCAO testbed. Dark image and flat field image correction was applied, and the circular field stop was masked with the value 0.5. The black squares exemplify five subfields in that the image shift is tracked. Blurred and stretched areas in the outer regions are the consequence of static aberrations. Non-granulation like structures in this image are dirt and scratches on the slide (may not be visible on printed paper at all). The image size is equivalent to a 73.6 arcseconds wide field in the real F_3 focus of GREGOR. (The image scale of the granulation slide is not true to the original.)

6.2.2.2 Informative value

A significant figure of merit of the MCAO performance is the set of the temporal standard deviation of the image shift (distortion) in all subfields which is given by

$$d_{\text{SDEV}}^{(s)} = \sqrt{\frac{1}{N-1} \sum_{k=1}^N \left[d_k^{(s)} - \sum_{k'=1}^N d_{k'}^{(s)} \right]^2}, \quad \text{with } s = 1, \dots, S. \quad (6.1)$$

$d_k^{(s)}$ is the two-dimensional image shift length in subfield number s at the time index k with respect to the first image of the time series. S is the total number subfields. $d_{\text{SDEV}}^{(s)}$ is visualized in circle diagrams as shown and explained in figure 6.2.

Because of the lack of an absolute reference, the described image distortion evaluation cannot be used to rate the overall benefit of the MCAO but only gives informations about how good time variant distortions (caused by turbulence on large spacial scales) are compensated but not how well the images actually look.

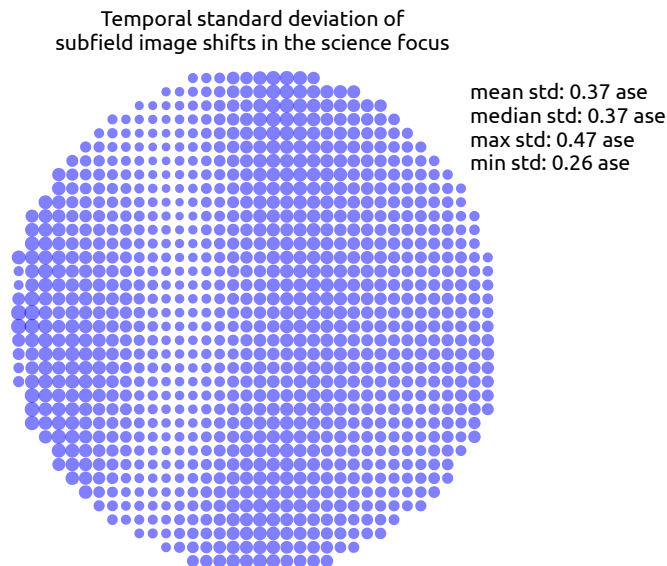


Figure 6.2: Example of a circle diagram showing the agile image distortion in the science focus. The circles mark the centers of the tracking subfields on a 36×36 grid within the circular field of view. The diameters of the circles represent the temporal standard deviation of the two-dimensional shift length in the corresponding subfield $d_{\text{SDEV}}^{(s)}$ computed from equation (6.1). This kind of graph does not allow to distinguish overall image shift (global tilt) fluctuations from local motions (distortion). Both can contribute homogeneously to the sizes of all circles. If not expressed explicitly, the global tilt has not been removed from the data plotted in this diagrams. The scale of the circles with respect to the grid spacing is preserved throughout this document. The statistical numbers given in the graph refer to the ensemble of subfields, i. e. to the circle sizes in this plot. This example shows the typical situation of uncompensated cooktop turbulence. The vertical predominant direction is probably the result of plumes above the cooktop which seem to form frequently.

In particular, neither the mean distortion nor its standard deviation express how much detail the images show and how well small scale aberrations are compensated which do not distort the image but cause local blur. To answer this question, I analyzed the wavefront as explained in the next subsection.

6.2.3 Wavefront modes in the guide directions and wavefront slopes

The accumulated wavefront error and its modal composition in the guide directions of the multi-direction wavefront sensor (MD-WFS) are used to rate the imaging quality without considering image distortion.

6.2.3.1 Evaluation procedure

The wavefront modes in the guide directions can be reconstructed from the subaperture and subfield image shifts logged by KAOS. The MD-WFS unit in the MCAO testbed features six subapertures with 19 subfields (the guide directions) yielding a total of 114 two-dimensional image shifts and hence wavefront slope measurements per control loop cycle. As explained in section 2.6.3, these 114 shifts can be separated into 19 individual Hartmann-Shack wavefront sensors (HS-WFS) with six subapertures each. I modeled the interaction matrix that converts Karhunen-Loëve wavefront modes into subaperture wavefront slopes of a HS-WFS with six hexagonal subapertures (see fig. 3.11) with GNU Octave and a little program written by Markus Kasper (then MPIA). The first five columns (i. e. modes) of this matrix were inverted using the `pinv` function of Octave yielding the 12×5 reconstruction matrix **SM** which converts the subaperture slopes into the coefficients of the first five Karhunen-Loëve modes. These five modes are x -tilt, y -tilt, focus and both astigmatism modes. These modes exhibit a central obstruction of 30% as it the case for the pupil of GREGOR. Orders higher than astigmatism cannot be reconstructed with six subapertures. For each logged control loop cycle, the wavefront in the i^{th} guide direction was then computed with Octave from

$$\vec{m}^{(i)}(t) = \mathbf{SM} \vec{s}^{(i)}(t) \quad (6.2)$$

in reference to the wavelength $\lambda = 500$ nm. The vector $\vec{s}^{(i)}(t) = \left\{ s_x^{(1)}, s_y^{(1)}, \dots, s_x^{(6)}, s_y^{(6)} \right\}_i^T(t)$ contains the six two-dimensional subaperture slopes associated with the i^{th} guide direction (see fig. 2.25 and 2.26) at the time index t . The vector $\vec{m}^{(i)}(t) = \left\{ m_1^{(i)}, \dots, m_5^{(i)} \right\}^T(t)$ contains the five Karhunen-Loëve coefficients at the time index t reconstructed in the i^{th} guide direction. The modes are normalized such that the coefficient m_j is equal to the root-mean-square error attributed to mode number j .

6.2.3.2 Informative value

The mode coefficients computed from equation (6.2) can be used to estimate the temporal mean square wavefront error in the i^{th} guide direction expressed by

$$w_i^2 := \frac{1}{N} \sum_{t=1}^N \left[\sum_{j=3}^5 [m_j^{(i)}(t)]^2 \right], \quad (6.3)$$

where N is the number of recorded control loop cycles. I start the summation at $j = 3$ because the zero point of the tip-tilt error, i. e. m_1 and m_2 , computed from equation (6.2) is not well defined since KAOS currently lacks an absolute reference of guide direction tip-tilt error (i. e. image distortion reference) as explained in section 4.2.1.2. Hence, w_i^2 only accounts for wavefront modes that instantaneously blur the image in the guide directions whereas image distortion over the field is dismissed. This error is also visualized in a circle diagram as exemplified in figure 6.3.

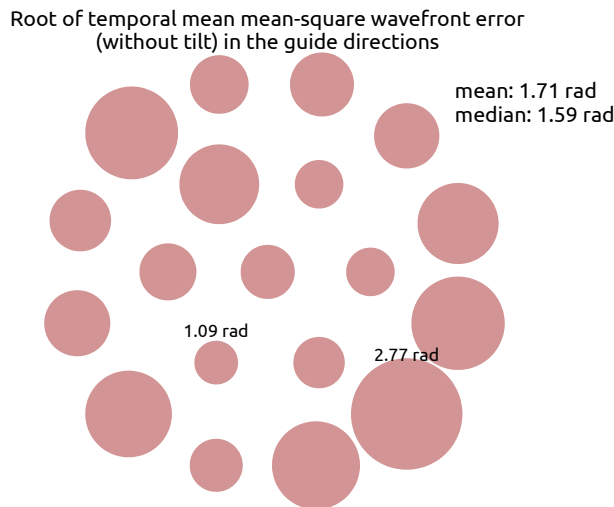


Figure 6.3: Example of a circle diagram showing the temporal mean image degradation in the guide regions of the multi-dir wavefront sensor. The circles mark the directions of the 19 guide regions. The diameters of the circles represent the root-mean-square error of focus and astigmatism w_i computed from equation (6.3). The scale of the circles with respect to the grid spacing is preserved throughout this document. The guide regions with the least and greatest temporal errors are tagged and the mean and median of all guide direction errors is referred.

The example shows the typical situation of uncompensated errors. The increasing errors in outer directions represent static aberrations that are also visible in figure 6.1.

The contribution of mode j to the error in the i^{th} guide direction can be expressed by the root-mean-square

$$m_j^{(i)}_{\text{RMS}} := \sqrt{\frac{1}{N} \sum_{t=1}^N [m_j^{(i)}(t)]^2}. \quad (6.4)$$

Figure 6.4 shows an example diagram of this measure for uncompensated turbulence and the residual error when KAOS's tip-tilt control mode and MCAO control mode is active. Although the root-mean-square is the measure that describes the wavefront error that is relevant for the image quality, it hides information of the effect of the MCAO. This is because the root-mean-square of a random number x with arithmetic mean \bar{x} and standard deviation σ_x is given by

$$x_{\text{RMS}} = \sqrt{\bar{x}^2 + \sigma_x^2}. \quad (6.5)$$

In this context, \bar{x}^2 represents the static aberration of the optics, and σ_x^2 represents the turbulent air. Thus, the root-mean-square would not reflect if, for any reason, the MCAO does not decrease a large static error but compensates well for the weaker turbulence. On this account, I also use the standard deviation of the guide direction modes

$$m_j^{(i)}_{\text{SDEV}} := \sqrt{\frac{1}{N-1} \sum_{t=1}^N \left[m_j^{(i)}(t) - \sum_{t'=1}^N m_j^{(i)}(t') \right]^2} \quad (6.6)$$

to rate the effect of the MCAO control. Figure 6.5 shows an example plot of the standard deviation similar to figure 6.4. The tip-tilt modes are included in this plot, because the lack of their absolute reference is not relevant for the standard deviation.

The standard deviation of the subaperture and subfield image shifts in the multi-dir wavefront sensor (and thus wavefront slopes) can also be used to rate the effectiveness of the MCAO control. Let $s_x^{(l)}(t)$ be the value of the l^{th} x -shift variable at time index t , then

$$r^{(l)}(t) := \sqrt{[s_x^{(l)}(t)]^2 + [s_y^{(l)}(t)]^2} \quad (6.7)$$

is the two-dimensional shift length at that time. The standard deviation thereof is

$$r_{\text{SDEV}}^{(l)} := \sqrt{\frac{1}{N-1} \sum_{t=1}^N \left[r^{(l)}(t) - \sum_{t'=1}^N r^{(l)}(t') \right]^2}. \quad (6.8)$$

Although $r_{\text{SDEV}}^{(l)}$ is of limited meaning for physical imaging error analysis, it is evident that smaller standard deviations imply better compensation of wavefront fluctuations. Figure 6.6 shows an example graph visualizing this quantity for all subapertures and subfields.

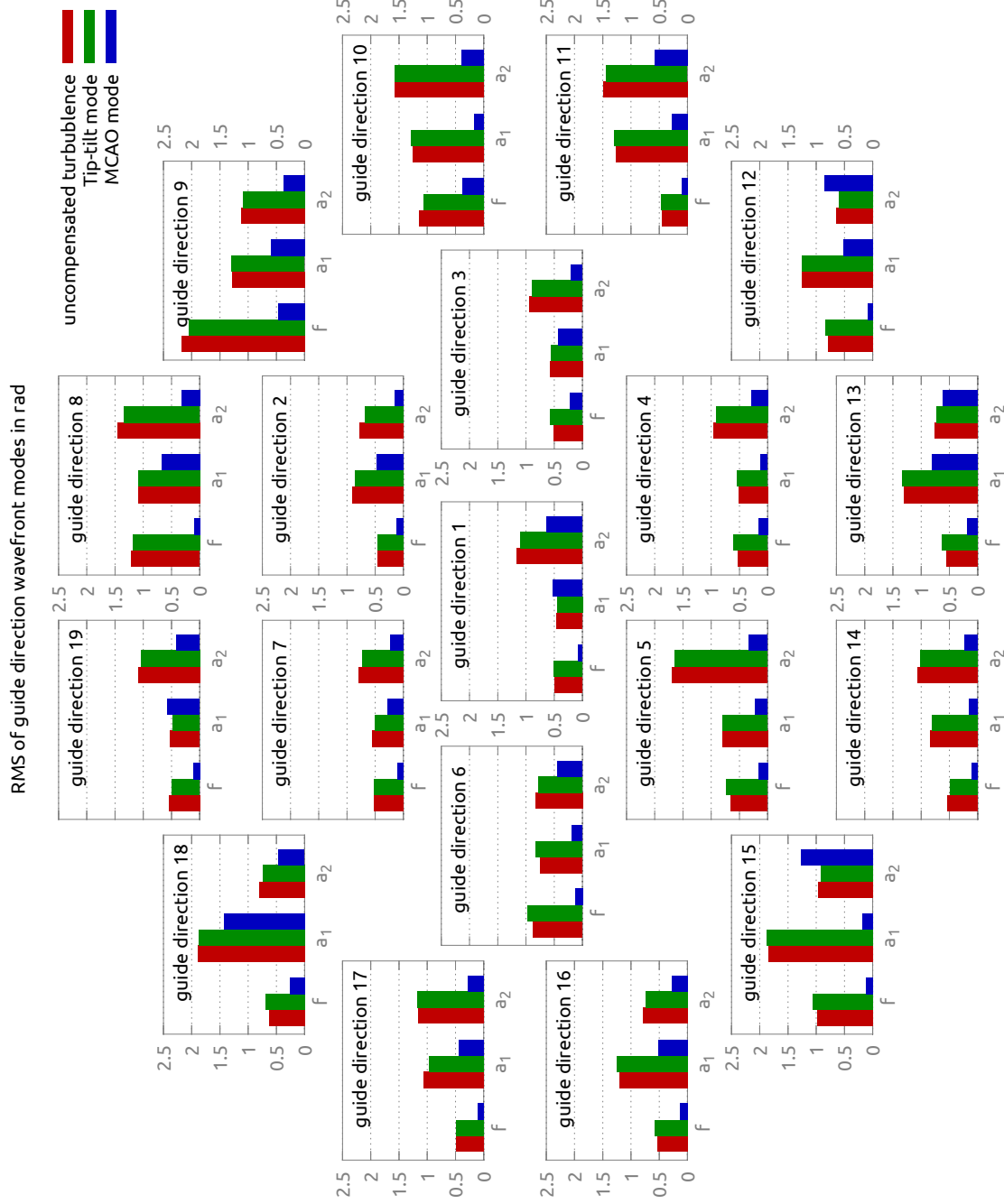


Figure 6.4: Example diagram showing the modal composition of the wavefront error in the guide directions. Each of the 19 bar plots represents a guide direction. They plot $m_j^{(i)}_{\text{RMS}}$ in radians from equation (6.4) versus the mode j . The label f stands for focus and a_1 as well as a_2 stand for the astigmatism modes. Because of the undefined offset of the reconstructed tip-tilt modes, their RMS is not plotted. In this example, three datasets are plotted which are designated by different colors.

This example shows the frequent effect of the MCAO, that clearly reduces the modal RMS in most guide directions but might fail to reduce astigmatism in a few directions (e.g. guide directions 15 and 12).

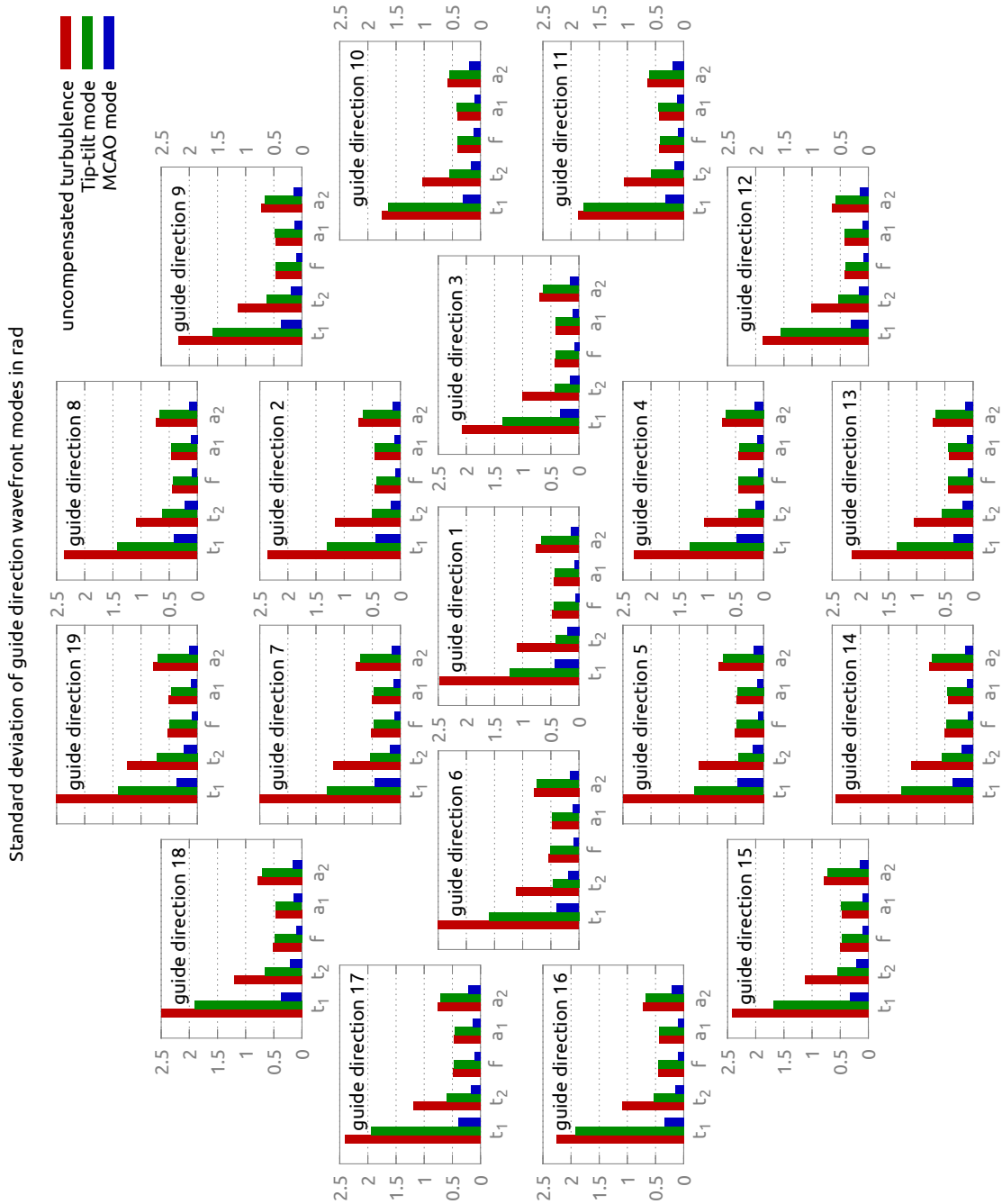


Figure 6.5: Example diagram showing the modal wavefront fluctuations in the guide directions. The diagram is designed similar to figure 6.4. Here, $m_j^{(i)}_{\text{SDEV}}$ in radians from equation (6.6) is plotted versus the mode j . Additionally, the fluctuations of the tip-tilt modes are included in this diagram. The labels t_1 and t_2 refer to them.

This typical example shows that the fluctuations are well suppressed by the MCAO throughout all modes and guide directions, in contrast to the root-mean-square in figure 6.4 guide directions 15 and 12. Both figures source the same datasets.

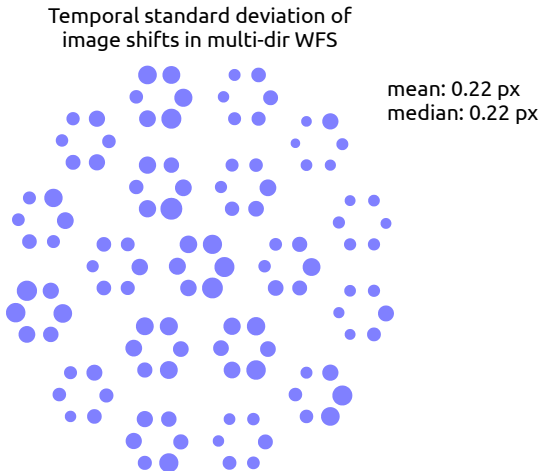


Figure 6.6: Example of a circle diagram showing the fluctuations of image shifts in the correlation fields the multi-dir wavefront sensor. The circles mark the correlation fields. They are arranged such that each six subapertures refer to one guide direction (see figs. 6.3, and 2.25). The diameters of the circles represent the temporal standard deviation of the two-dimensional image shift length in the corresponding correlation field from equation (6.8). The scale of the circles with respect to the spacing is preserved throughout this document. This diagram does not contain any information about the modal composition of the wavefront error and the image quality except that “the smaller the better”.

6.2.4 Wavefront error reconstructed by the KAOS software

The data that was recorded with the KAOS software included the coefficients of all reconstructed modes of the residual wavefront. The data also contained an estimate of the total error, i. e. the residual error plus the estimated state of the deformable mirrors. But this feature of the software is not well tested yet and I did not consider the total error in my analysis at all. The residual modal errors computed by KAOS, however, also involve potential pitfalls because they are the result of tomographical wavefront reconstruction that might have unknown problems. The term *KAOS modes* will be used in this document to discriminate these modes from the guide direction modes of section 6.2.3, which were reconstructed in the established way. Although I do not use them as a measure of the image quality, I show time series of the KAOS modes since this is the quantity that is controlled by KAOS. In particular, I use KAOS modes to compute temporal power spectra of the residual error and the bandwidth of the control. The temporal bandwidth of the control can be analyzed on the basis of KAOS modes as well as on guide direction modes, even if the tomographical reconstruction would not assign the modes correctly, because the reconstruction process is time-invariant. Analyzing the power spectrum by means of KAOS modes requires less coding and computation and was preferred for this reason. The science focus camera recorded the images referred to in section 6.2.2 at a frequency of about 143 Hz, which is too low to gain an adequate understanding of the power spectrum. Thus, the recordings by KAOS were the best database available.

6.3 Tested scenarios and results

6.3.1 MCAO control with $DM_{0\text{km}}$ and $DM_{8\text{km}}$

Recordings from June 26th, 2012 are used to analyze the effect of MCAO control using $DM_{0\text{ km}}$ and $DM_{8\text{ km}}$ in this section. 13 datasets of KAOS logs and science focus movies were recorded. Six recordings deal with MCAO mode, four deal with pupil AO (PAO) mode, two deal with tip-tilt mode, and one recording was dedicated to uncompensated turbulence. The PID controller parameters were set for the control frequency of 1700 Hz according to the Tyreus-Leuben method (see section 2.7.1) with manual fine-tuning with respect to the step response of the controller, which can be displayed by KAOS Evo 2. Fine-tuning was made such that the step function rose quickly, the overshoot was less than 20% and oscillations decayed fast. The used controller parameter set is printed in table 6.1. The Lai modes (see section 2.7.2) were used as KAOS modes for $DM_{8\text{ km}}$. 30 modes were controlled on $DM_{0\text{ km}}$ and 50 modes on $DM_{8\text{ km}}$. The data was processed as described in section 6.2. The results are visualized in figures 6.8 to 6.11 and summarized in tables 6.2 and 6.3.

Table 6.1: Controller parameters used for the test runs.

	P	I	D
TT	0.85	22	0
$DM_{0\text{ km}}$	0.45	20	0
$DM_{8\text{ km}}$	0.6	10^{10}	0

6.3.1.1 Agile image distortion

The mean local image motion in the science focus was reduced in MCAO control mode to 0.016 ase, whereas this error was about 0.07 ase in the case of uncompensated cooktop turbulence and about 0.05 ase in tip-tilt control mode, which removes the total field average of the subfield image motion. Accordingly, the MCAO control mode compensated agile image distortion by almost 70 %. In pupil AO control mode, the local motion was 0.042 ase. The fluctuations were distributed inhomogeneously after removing the field average motion, as visible in the first row of figure 6.8. There is no lock-point (i. e. a small area with very little circles in the diagrams) visible in the pupil AO mode as it would be if a conventional AO control had been used. The absence of a lock-point is a consequence of the fact that the tip-tilt error is defined over the total field in the GREGOR MCAO system rather than in a single guide direction. MCAO mode clearly suppressed agile image distortion over the whole field. However, the suppression was worse at one edge of the field from 15:40:44 onwards. The cause of this asymmetry is not known. It is possibly the consequence of a degrading registration of $DM_{8\text{km}}$ in the MD-WFS due to the thermal bending of the optics bench.

6.3.1.2 Guide direction wavefront error

The average temporal RMS wavefront error of all guide directions ascribed to focus and astigmatism was decreased in MCAO control mode by 47 % to 0.9 rad. However, there were 3–4 guide directions with considerably larger errors (3rd and 4th row in figure 6.9). Because these errors increased with time, I assume that this is also an effect of changing temperature of either the optics bench or the deformable mirror (next paragraph).

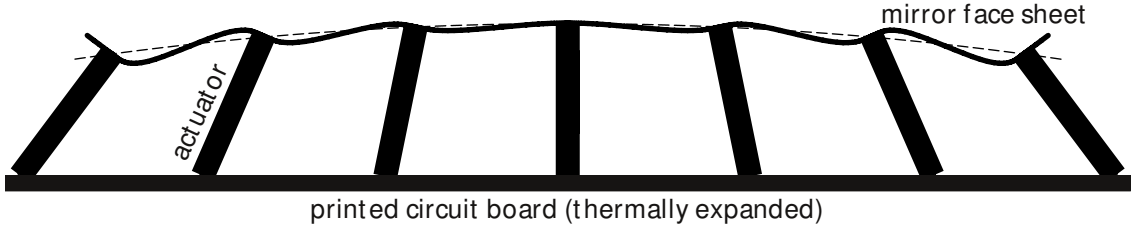


Figure 6.7: Schematic sketch of the imagined effect of thermal expansion in the OKO PDM69 deformable mirrors. The actuators are glued between the mirror face sheet and the printed circuit board. The circuit board expands with respect to the mirror face sheet because of different coefficients of thermal expansion. The vertical expansion of the actuators is of no meaning since they are equally long. The actuators incline due to the expansion. The actuators and the printed circuit board are much stiffer than the mirror face sheet. Consequently, the face sheet is pulled down (dashed line) in the first place and curved rather than stretching the actuators. Furthermore, the actuators of the OKO PDM are extended and glued to the face sheet on the full contact area. Consequently, local torque is generated that buckles the face sheet. These buckles cannot be eliminated by driving the actuators without changing the face sheet curvature. (The effects in the actuators' contact points with the circuit board are not shown because I assume that they do not affect the face sheet contact fundamentally.)

The modal analysis of the guide direction error fluctuations is shown in figure 6.10. Most of the wavefront error generated by the cooktop turbulence is attributed to local tip-tilt, i. e. local image motion. This error was below 0.5 rad in MCAO control mode in all guide directions. The tip-tilt modes were not equally strong. This is possibly the effect of the asymmetric turbulence that was generated with the cooktop below the light beam. The averaged fluctuations of the guide direction modes are listed in table 6.4. This table tells that the fluctuations of the first five Karhunen-Loëve modes dropped by 70–80 % in MCAO mode. The modal analysis of the root-mean-square errors, which contains both the fluctuations and the static aberrations, in the guide directions is depicted in figure 6.11. The averaged root-mean-squares of the guide region modes are listed in table 6.5. They were reduced to 40–50 % in MCAO mode. However, the great variations of the root-mean-squares (tab. 6.5) and the little variations of the standard deviations (tab. 6.4) reflect that static aberrations were not equally well compensated in all guide directions. These tables also tell that a significant amount of static aberration remains in MCAO control mode, while fluctuations due to turbulence were compensated more effectively.

Thermal buckling of DM_{8 km} The great difference in the root-mean-squares in some guide directions of the MCAO recordings of 15:37:04 and 16:08:45 may be the consequence of another temperature effect of the OKO PDM. I assume that the thermal expansions of the printed circuit board on that the actuators are fixed and the expansion of the mirror substrate that is glued to the other end of the actuators are different. Then, as sketched in figure 6.7, changing temperature would cause local torque that produces buckles in the mirror face sheet that the actuators cannot cancel. This is just an idea which is not strengthened by a profound, quantitative analysis. However, this idea complies with the observed increase of the initial radius of curvature of the OKO PDM mirrors with temperature as given in table A.2.

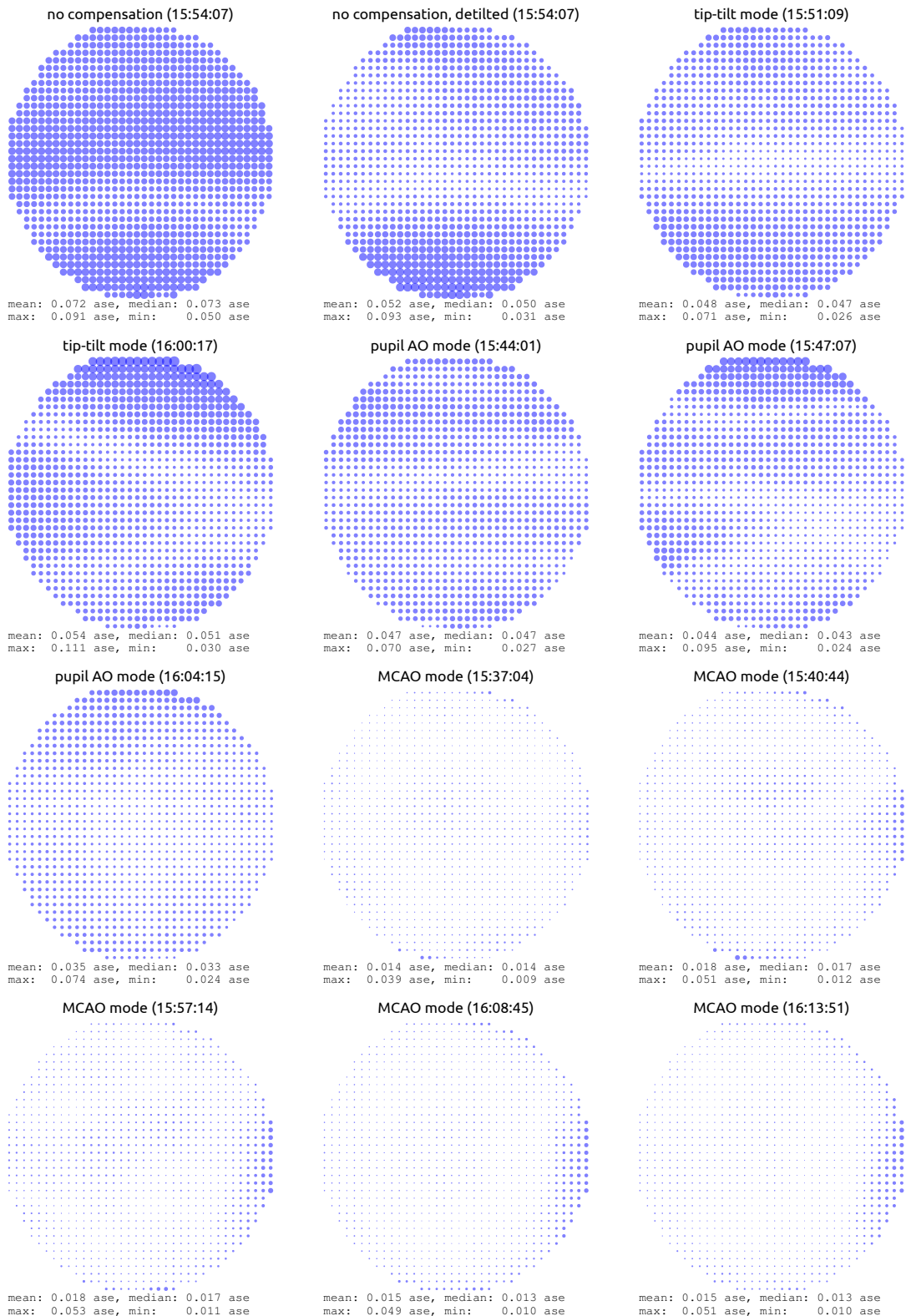


Figure 6.8: Temporal standard deviation of subfield image shift in the science focus with various AO control modes compensating for cooktop turbulence. In the second graph, which is labeled “no compensation, detilted”, the overall image shift (wavefront tilt) has been subtracted from the images (=post-facto, digital tip-tilt compensation) before computing the standard deviation in the subfields.

6.3 Tested scenarios and results

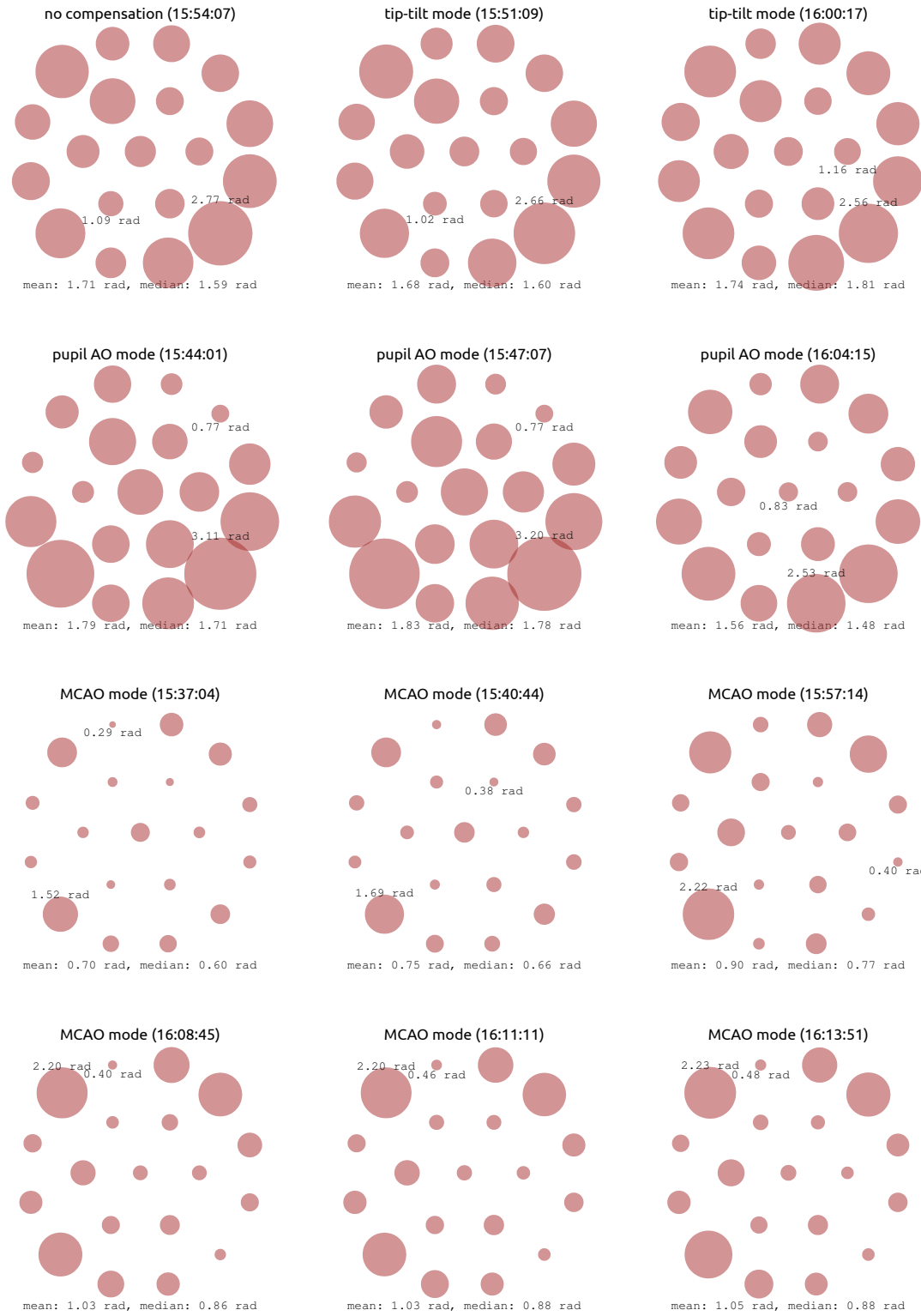


Figure 6.9: Temporal root-mean-square error of focus and astigmatism in the guide directions of the multi-dir wavefront sensor with various AO control modes compensating for cooktop turbulence.

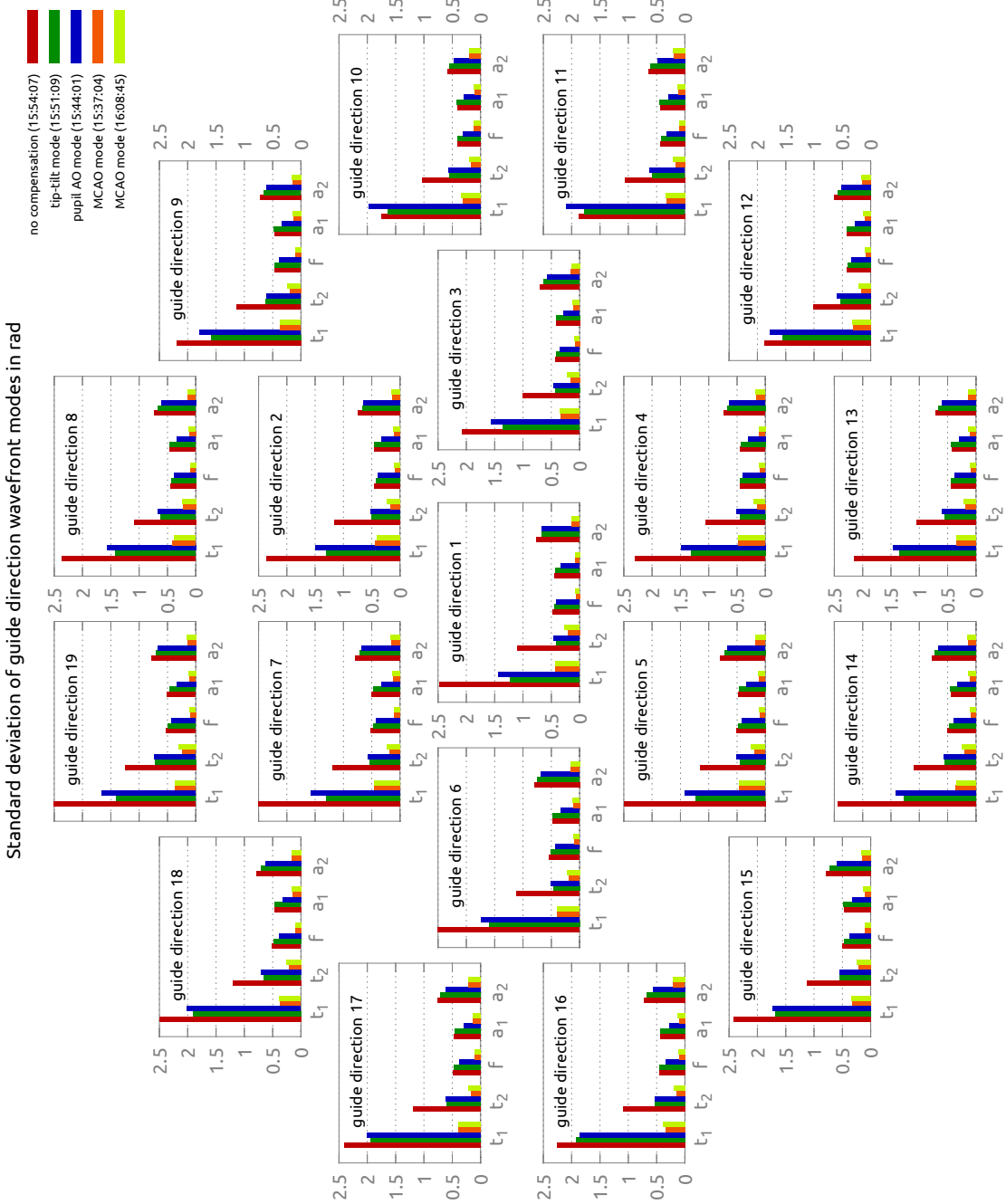


Figure 6.10: Temporal standard deviation of tip-tilt, focus and astigmatism in the guide directions of the multi-dir wavefront sensor with various AO control modes compensating for cooktop turbulence.

6.3 Tested scenarios and results

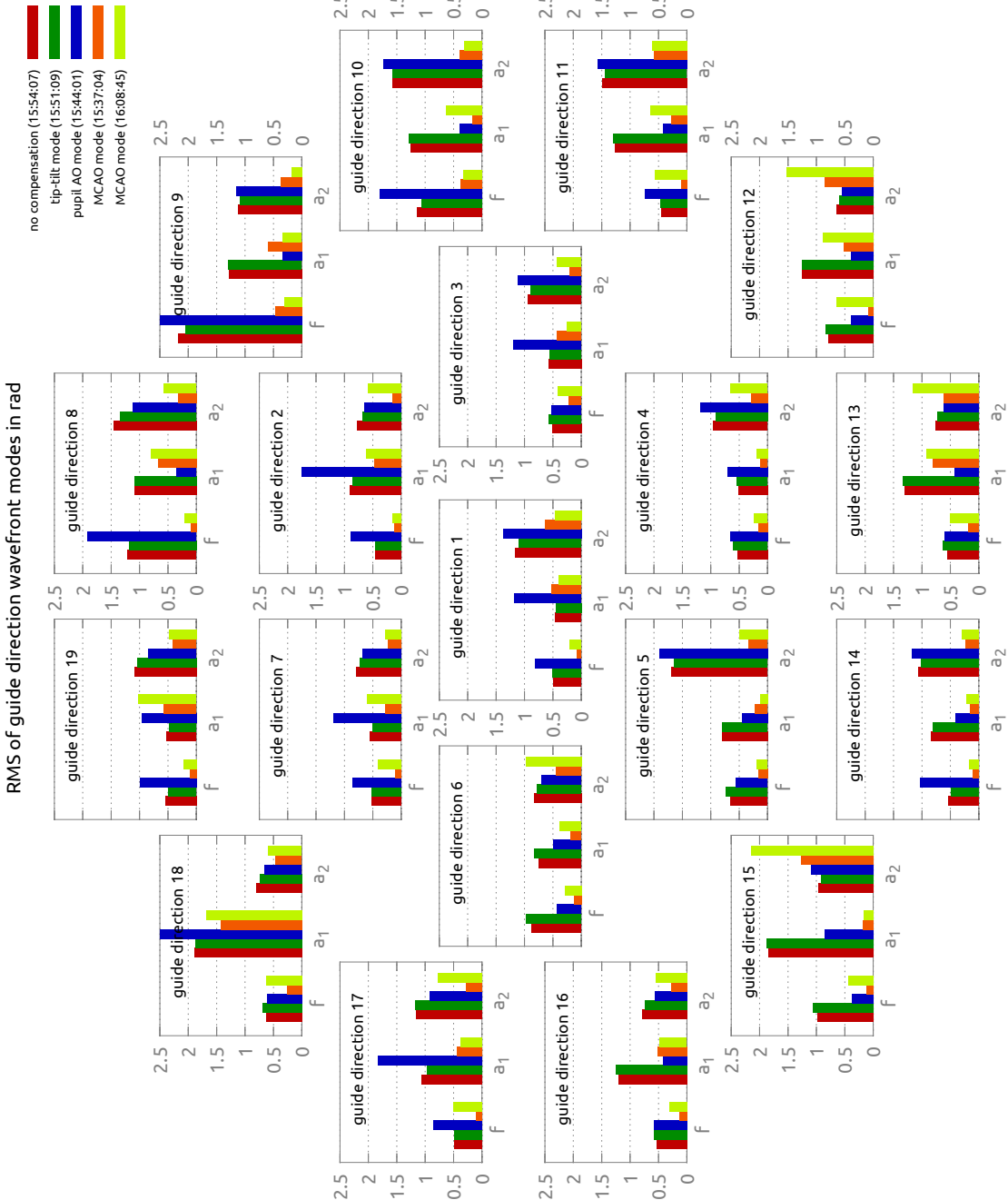


Figure 6.11: Temporal root-mean-square error of focus and astigmatism in the guide directions of the multi-dir wavefront sensor with various AO control modes compensating for cooktop turbulence.

6 MCAO Testruns

Table 6.2: Performance indicators of the test runs with DM_{0km} and DM_{8 km} on June 26th, 2012

mode	time	$\langle d_{\text{SDEV}}^{(s)} \rangle_s$ agile image distortion	$\langle w_i \rangle_i$ guide direc- tion error	min w_i	max w_i	$\langle r_{\text{SDEV}}^{(l)} \rangle_l$ MD-WFS shifts	cooktop temp.	control freq.
MCAO	15:34:04	0.014 ase	0.69 rad	0.28 rad	1.52 rad	0.06 px	255 °C	1400 Hz
MCAO	15:40:44	0.018 ase	0.75 rad	0.38 rad	1.69 rad	0.08 px	265 °C	1400 Hz
MCAO	15:57:14	0.018 ase	0.90 rad	0.40 rad	2.20 rad	0.08 px	280 °C	1400 Hz
MCAO	16:08:45	0.015 ase	1.03 rad	0.40 rad	2.23 rad	0.07 px	280 °C	1700 Hz
MCAO	16:13:51	0.015 ase	1.05 rad	0.48 rad	2.23 rad	0.07 px	280 °C	1700 Hz
MCAO	16:11:11	–	1.03 rad	0.46 rad	2.20 rad	0.07 px	280 °C	1700 Hz
PAO	15:44:01	0.047 ase	1.79 rad	0.77 rad	3.11 rad	0.18 px	275 °C	1400 Hz
PAO	15:47:07	0.045 ase	1.83 rad	0.77 rad	3.20 rad	0.17 px	275 °C	1400 Hz
PAO	16:04:15	0.035 ase	1.56 rad	0.83 rad	2.53 rad	0.14 px	280 °C	1400 Hz
PAO	16:16:11	–	1.53 rad	0.66 rad	2.82 rad	0.12 px	280 °C	1700 Hz
tip-tilt	15:51:09	0.048 ase	1.68 rad	1.02 rad	2.66 rad	0.17 px	275 °C	1400 Hz
tip-tilt	16:00:17	0.054 ase	1.74 rad	1.16 rad	2.56 rad	0.18 px	280 °C	1400 Hz
No AO	15:54:07	0.072 ase	1.71 rad	1.09 rad	2.77 rad	0.22 px	275 °C	1400 Hz

Table 6.3: Residual errors averaged over the recordings of the AO modes.

	MCAO	PAO	tip-tilt	No AO
$\langle d_{\text{SDEV}}^{(s)} \rangle_s$	(0.016±0.002) ase	(0.042±0.006) ase	0.051 ase	0.072 ase
$\langle w_i \rangle_i$	(0.91±0.16) rad	(1.68±0.15) rad	1.72 rad	1.71 rad
min w_i	(0.40±0.07) rad	(0.76±0.07) rad	1.09 rad	1.09 rad
max w_i	(2.0±0.3) rad	(2.9±0.3) rad	2.6 rad	2.8 rad
$\langle r_{\text{SDEV}}^{(l)} \rangle_l$	(0.071±0.007) px	(0.15±0.03) px	0.18 px	0.22 px

Table 6.4: Standard deviations of the guide direction errors shown in figure 6.10 averaged over the 19 guide directions.

wavefront mode	no compensation (15:54:07)	MCAO mode (16:08:45)	drop in MCAO mode
t ₁	(2.3±0.3) rad	(0.38±0.04) rad	83 %
t ₂	(1.1±0.1) rad	(0.23±0.03) rad	79 %
f	(0.47±0.04) rad	(0.10±0.01) rad	78 %
a ₁	(0.45±0.03) rad	(0.13±0.02) rad	71 %
a ₂	(0.73±0.06) rad	(0.17±0.03) rad	77 %

Table 6.5: Root-mean-squares of the guide direction errors shown in figure 6.11 averaged over the 19 guide directions.

wavefront mode	no compensation (15:54:07)	MCAO mode (16:08:45)	drop in MCAO mode
f	(0.7±0.4) rad	(0.35±0.16) rad	53 %
a ₁	(1.0±0.4) rad	(0.56±0.38) rad	44 %
a ₂	(1.1±0.3) rad	(0.69±0.48) rad	37 %

6.3.1.3 Power spectra

Tip-tilt control The power spectra of the tip-tilt wavefront error of uncompensated cooktop turbulence, in tip-tilt control mode and in MCAO control mode are plotted in figure 6.12. The tip-tilt error of the cooktop turbulence was about 5–10 times greater in vertical direction than in horizontal direction. This is presumably the consequence of the hot air bubbling up from the cooktop.

The 0-dB-bandwidth of the tip-tilt control mode was about 100 Hz in horizontal direction and about 140 Hz in vertical direction. In MCAO control mode the 0-dB-bandwidth was about 40 Hz and 45 Hz, respectively. In terms of damping of the tip-tilt error, the tip-tilt control mode was on par with MCAO control mode up to about 15–20 Hz. Tip-tilt control mode performed about a magnitude better than MCAO control mode at higher frequencies up to the band limit. The power spectra show an elevation around about 120 Hz in both control modes. This could be oscillations of the controller and might be eliminated by tuning the PID parameters in a better way. The power spectra of the tip-tilt error in tip-tilt control mode with a loop frequencies of 1400 and 1700 Hz are compared in figure 6.13. The damping was better with the faster control loop up to about 40 Hz but the peak at about 120 Hz was higher.

The origin of the slower tip-tilt compensation in MCAO control mode is not yet known. An error in the wavefront reconstruction seems to be unlikely because I cannot imagine how this could depend on the frequency. Possible, however, would be that some of the KAOS modes of the deformable mirrors produce an unnoticed tip-tilt. This would be counteracted in the control loop by the tip-tilt mirror at low frequencies whereas higher frequencies could build up, degrading the bandwidth. Another possibility could be a penalty of clipping the actuator values at the stroke limit. As a consequence of this clipping, fast small deviations from the zero-overall-gradient of the mirror surface could be introduced.

DM_{0 km} control The power spectrum of the focus wavefront error, which is compensated by DM_{0 km}, in MCAO control mode is shown in figure 6.14, and the power spectrum of mode 20 of DM_{0 km} in figure 6.15. These spectra do not show a bump at about 120 Hz as it is the case for the tip-tilt error (figs. 6.12 and 6.13). The 0-dB-bandwidth of the focus control was about 35 Hz and about 100 Hz for mode 20. The bandwidth is about 100 Hz for all modes from trefoil upwards whose power spectra are not especially shown in this document.

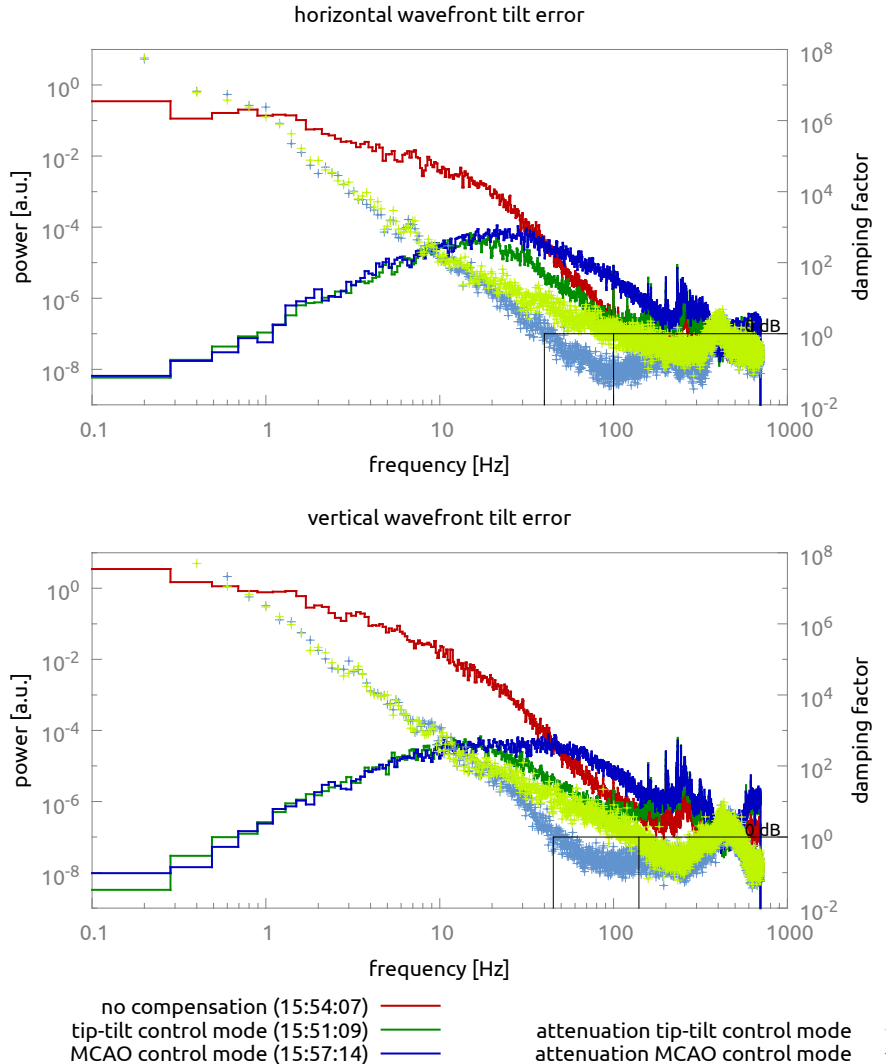


Figure 6.12: Power spectra of tip-tilt wavefront error of uncompensated cooktop turbulence and in MCAO control mode. 0 dB lines of the attenuation is emphasized. Temperature of the cooktop was 275–280 °C and the control loop frequency was 1400 Hz. (The vertical descent at the end of the spectra curves is part of the step plotting style.)

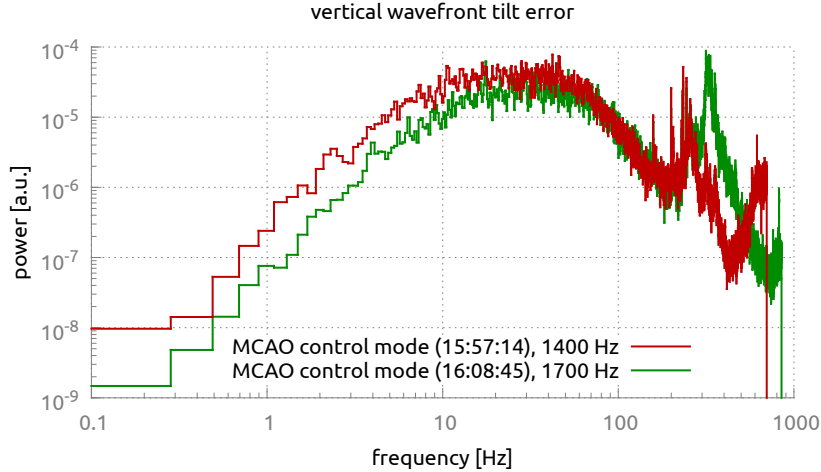


Figure 6.13: Power spectra of vertical tip-tilt wavefront error in MCAO control mode with 1400 Hz and 1700 Hz control loop frequency. Controller parameters were tuned for 1700 Hz and were not modified for 1400 Hz. Temperature of the cooktop was about 280 °C.

The power spectra of the focus error as well as modes 7 and 20 of $DM_{0\text{ km}}$ look the same in the MCAO control mode recording from 15:57:14 and in the PAO control mode recording from 16:04:15 (not shown). For this reason, the lower control bandwidth for lower wavefront modes of $DM_{0\text{ km}}$ cannot be induced by the additional actuation of $DM_{8\text{ km}}$ in MCAO mode. Notably, however, is that fact that in the control loop, the $DM_{0\text{ km}}$ modes below 7 were reconstructed from the MD-WFS camera whereas modes ≥ 7 were computed from the on-axis WFS camera image. The bandwidth of the $DM_{8\text{ km}}$ control, which exclusively considers MD-WFS images, is about 130 Hz (next paragraph). On account of this, it seems to be unlikely that the images of both cameras were not synchronized and that the MD-WFS image lagged behind (see also image synchronization procedure in section 4.2.1.1). Another reason of the low control bandwidth of the lower modes that is not excluded could be attributed the harmonic oscillations of the "freely fixed" bimorph plate. The lower wavefront modes could be related to the first harmonic oscillation mode whereas higher wavefront modes would then be related to higher harmonics (overtones), which have a shorter oscillation period. Resonance tests of the mirror *Night DM2-51-69 #0018* that was used as $DM_{0\text{ km}}$ were not performed in the scope of this thesis and it is unknown at what frequencies the harmonics of this mirror occur.

DM_{8 km} control The power spectrum of the parabola mode of DM_{8 km} is shown in figure 6.16. The 0-db-bandwidth was about 130 Hz and also no elevation (e.g. controller oscillations) was present at higher frequencies.

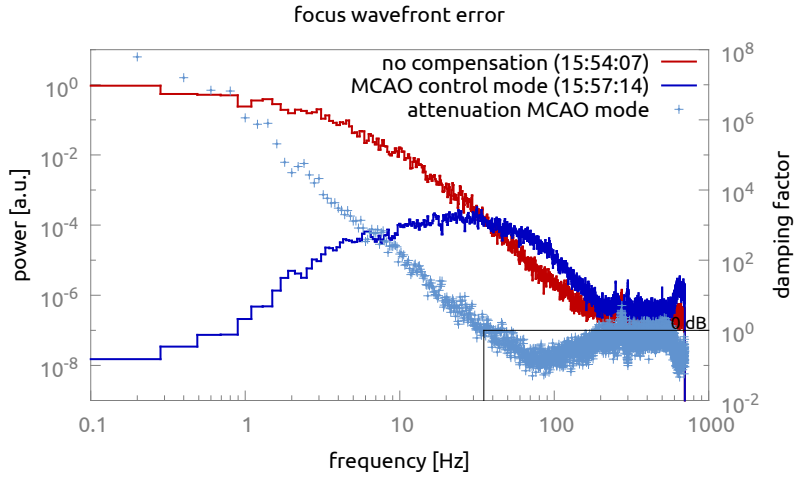


Figure 6.14: Power spectra of focus wavefront error of uncompensated cooktop turbulence and in MCAO control mode. 0-dB-bandwidth was about 35 Hz and 3-dB-bandwidth was about 30 Hz. Temperature of the cooktop was about 280 °C and the control loop frequency was 1400 Hz.

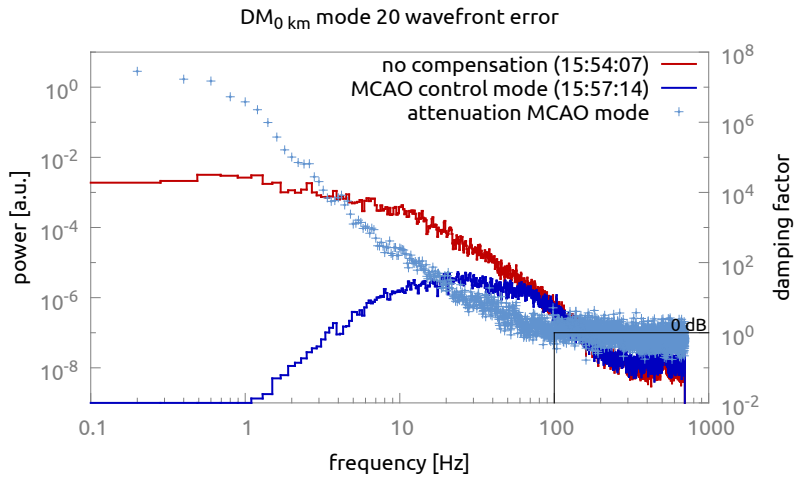


Figure 6.15: Power spectra of wavefront error mode 20 of DM_0_{km} of uncompensated cooktop turbulence and in MCAO control mode. 0-dB-bandwidth was about 100 Hz and 3-dB-bandwidth was about 60 Hz. Temperature of the cooktop was about 280 °C and the control loop frequency was 1400 Hz.

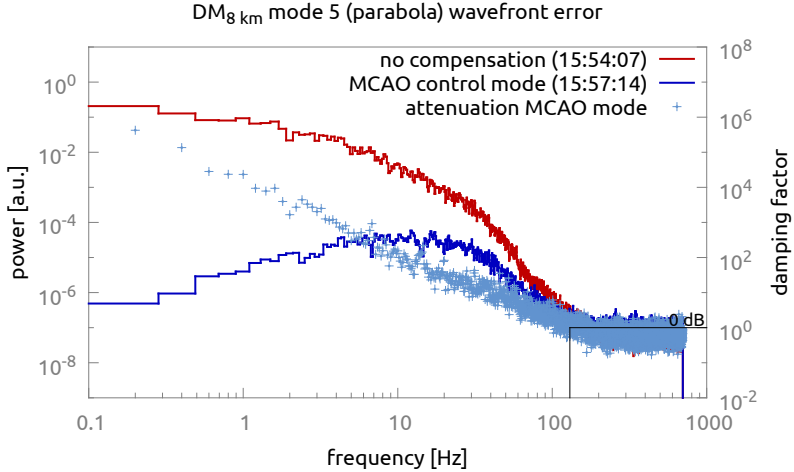


Figure 6.16: Power spectra of wavefront error mode 5 (parabola) of $DM_{8\text{ km}}$ of uncompensated cooktop turbulence and in MCAO control mode. 0-dB-bandwidth was about 130 Hz and 3-dB-bandwidth was about 90 Hz. Temperature of the cooktop was about 280 °C and the control loop frequency was 1400 Hz.

6.3.2 Comparison of Karhunen-Loève modes and Lai modes

I used three different mode sets, Karhunen-Loève modes, Lai modes and modified Lai modes, for $DM_{8\text{km}}$ to investigate their impact on the MCAO control performance.

6.3.2.1 Computation of modes

The modal set used in KAOS is defined by the matrix **MA** (see sec. 4.2.1.3) that converts a vector \vec{m} of mode coefficients into a vector \vec{a} representing the actuator values, i. e.

$$\vec{a} = \mathbf{MA} \vec{m}. \quad (6.9)$$

This matrix was modeled for each of the three modal sets on the basis of the influence functions of the OKO PDM69 that had been measured with a *Fisba μPhase 2 HR* interferometer. To set up the matrix **MA** for the Karhunen-Loève modes, first the Karhunen-Loève modes had been computed in Octave with a program written by Markus Kasper (then MPIA) such that they cover 43 mm in diameter on the interferometric measurements of the mirror surface. Then these modes were projected onto the influence functions. The actuator value patterns used to form Karhunen-Loève modes with $DM_{8\text{ km}}$ are shown in figures B.1 and B.2. The matrix **MA** for the Lai modes was set up with the use of an IDL program provided by O. Lai. I translated this program, which models the modes and projects them onto the influence functions, to Octave. Also 43 mm of the mirror surface were used. The actuator patterns for Lai modes are shown in figures B.3 and B.4. A peculiarity of the Lai modes computed this way is that the outer actuators are slightly short in the low order modes. This can be seen for example by comparing the actuator patterns of modes 1 and 2 in figure B.3 to the ones in figure B.1. To avoid this effect, I modified the computation of the Lai modes by replacing

projections implemented in the form of

$$m_{f,g} = \sum_{x,y} f(x,y) g(x,y) \quad (6.10)$$

by an ordinary least squares fit using the `ols` function of Octave. The modified Lai modes are shown in figures B.3 and B.4.

6.3.2.2 Tests and results

The basis of this subsection are 13 datasets of science camera movies and KAOS logs that were recorded on July 30th. 12 recordings deal with MCAO control mode with DM_{8 km} and one recording was made without any wavefront control, i. e. plain cooktop turbulence. The modal sets were alternated between the recordings in order to mitigate the impact of variable conditions like room temperature and sagging of the optics table. The temperature of the cooktop was 220–230 °C.

Figure 6.17 shows the diagrams of one of the best recordings of MCAO control mode and figure 6.18 refers to uncompensated turbulence. Table 6.6 lists some statistical numbers of the performance of the three different KAOS modes sets. The guide direction wavefront errors were reduced in MCAO mode to about $\langle w_i \rangle_l = 0.7$ rad and agile image distortion to $\langle d_{\text{SDEV}}^{(s)} \rangle_s = 0.07$ ase. The image shifts in the correlation fields of the multi-dir WFS were mitigated to $\langle r_{\text{SDEV}}^{(l)} \rangle_l = 0.07$ px. All these numbers correspond to an improvement of 50 to 60 % compared to the recording with no wavefront control.

One of the recordings with the least guide direction wavefront error was made in MCAO mode with the Lai modes. However, as implied by the large variation in table 6.6, the Lai modes did not perform as reliable as the Karhunen-Loève and the modified Lai modes, and test runs with greater residuals were frequent. I conclude from these tests that the Karhunen-Loève or the modified Lai modes should be used as KAOS modesets for the present testbed setup. The modified Lai modes tend to perform little better than the Karhunen-Loève modes. However, more data needs to be taken to strengthen the empirical impression and to prove this statistically.

Table 6.6: Residual errors in MCAO control mode with three different KAOS modesets for DM_{8km}.

modeset	MCAO, modified Lai	MCAO, Karhunen-Loève	MCAO, Lai	No AO
$\langle d_{\text{SDEV}}^{(s)} \rangle_s$	(0.07±0.02) ase	(0.07±0.02) ase	(0.10±0.01) ase	0.25 ase (0.15 ase*)
$\langle w_i \rangle_l$	(0.69±0.04) rad	(0.71±0.03) rad	(0.75±0.12) rad	1.54 rad
min w_i	(1.26±0.13) rad	(1.41±0.09) rad	(1.57±0.21) rad	2.74 rad
max w_i	(0.27±0.06) rad	(0.32±0.04) rad	(0.36±0.12) rad	0.73 rad
$\langle r_{\text{SDEV}}^{(l)} \rangle_l$	(0.07±0.02) px	(0.07±0.02) px	(0.10±0.02) px	0.18 px

*) overall image shift (tip-tilt) subtracted

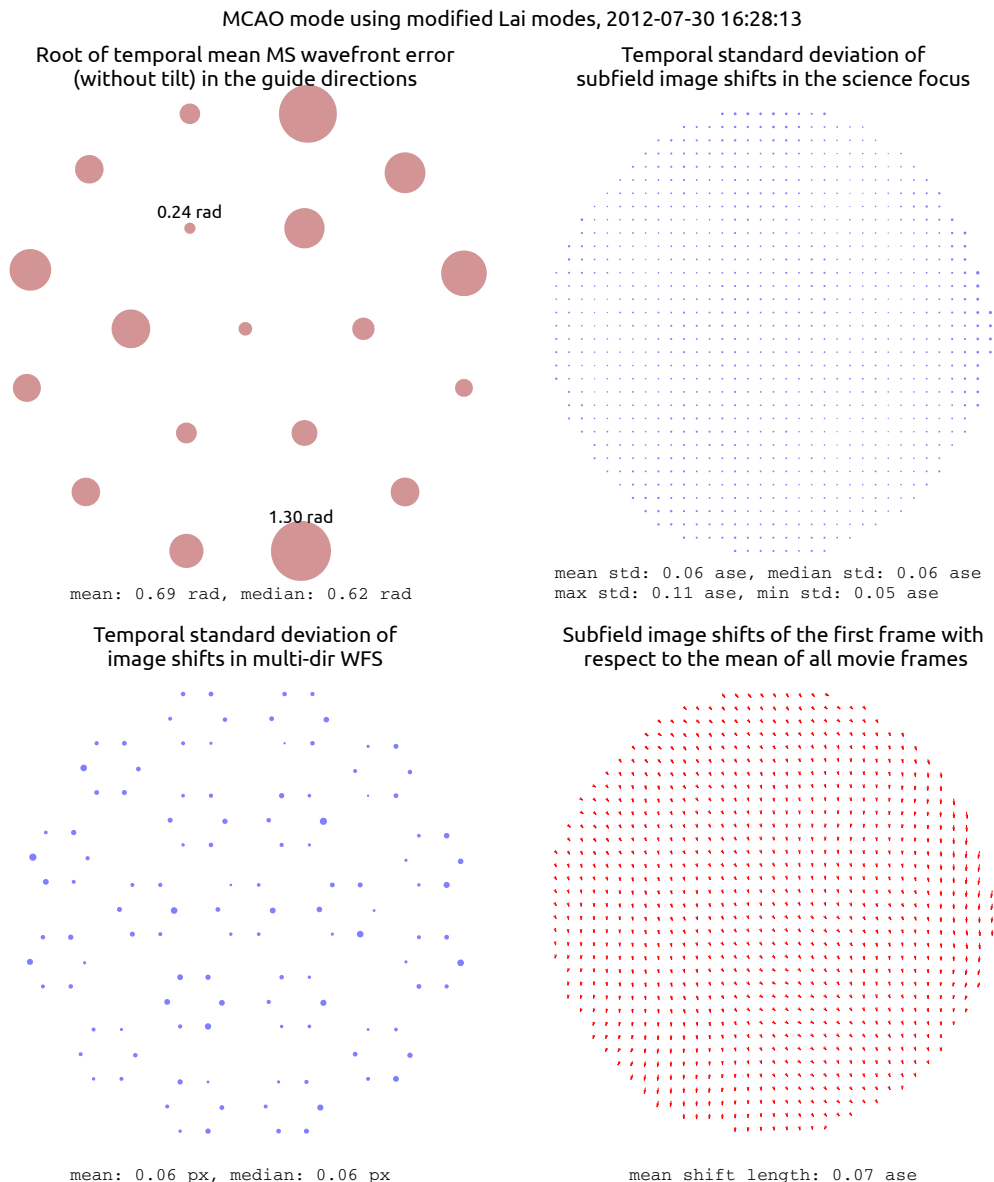


Figure 6.17: Diagrams showing the residuals of MCAO control mode with modified Lai modes.

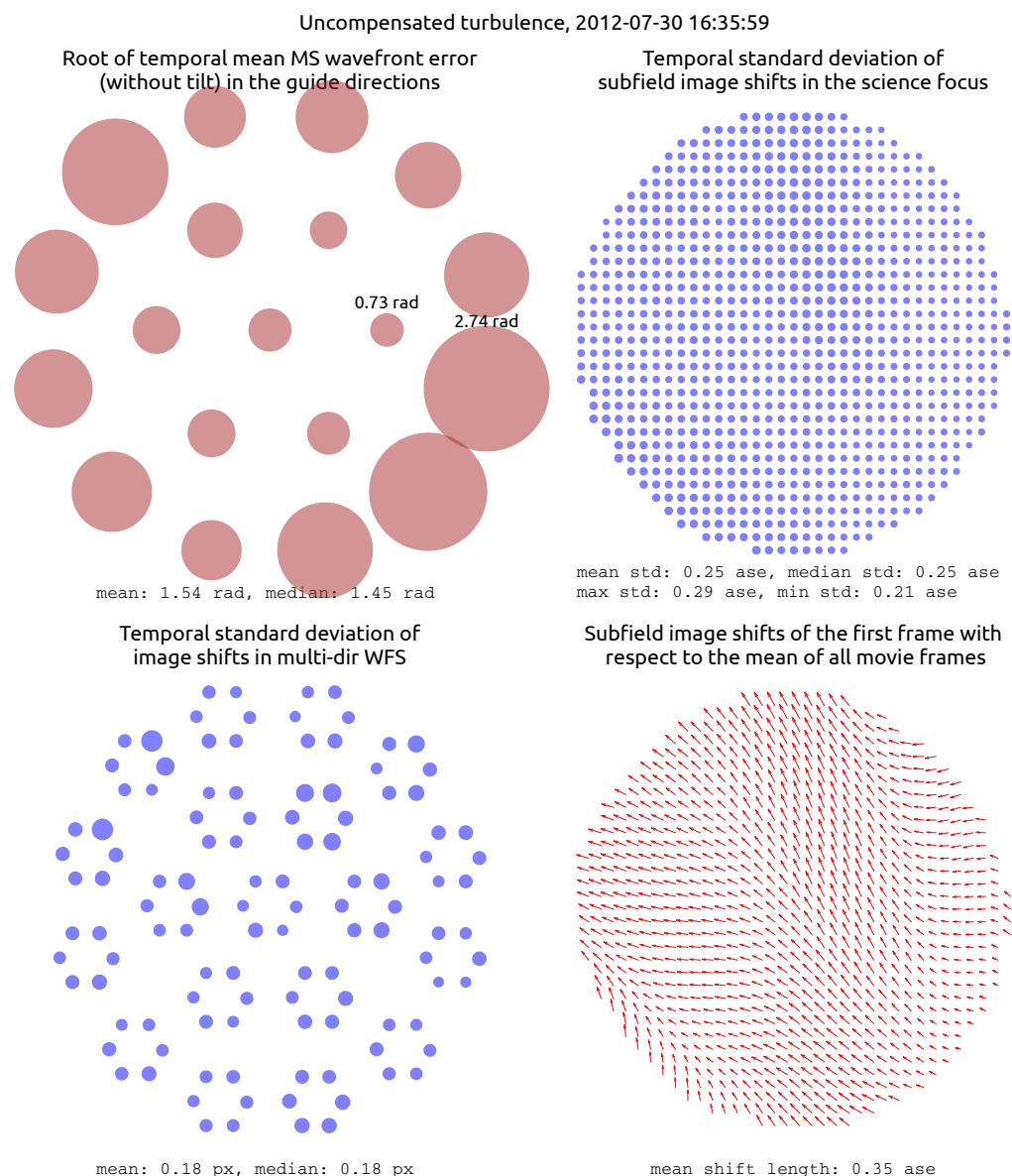


Figure 6.18: Diagrams showing the residuals of uncompensated turbulence for comparison with figure 6.17.

6.3.3 MCAO control with $DM_0\text{ km}$, $DM_8\text{ km}$ and $DM_{25}\text{ km}$

In spite of the broken actuators of one deformable mirror, I tried to use all three mirrors in the control loop. The mirror device *OKO PDM69 KIS1* that has two actuators broken was chosen to act as $DM_{25}\text{ km}$ because the guide direction footprint is smaller on this mirror than on $DM_8\text{ km}$ (fig. 3.5). The broken actuators had greater penalty on image distortion than on local blur this way.

Karhunen-Loëve modes were used as KAOS modes for $DM_8\text{ km}$ and $DM_{25}\text{ km}$. 30 modes were controlled on $DM_0\text{ km}$, 50 modes on $DM_8\text{ km}$ and 25 modes $DM_{25}\text{ km}$. Although KAOS Evo 2 should allow to specify actuators to be ignored in the control loop, this feature did not work at the time when the presented tests were conducted. The number of controlled modes on $DM_{25}\text{ km}$ was limited to the rather low number of 25 in order to avoid the commanding of modes with smaller spatial scales that would have driven the values of the unignored broken actuators into saturation, rendering the control unstable[‡].

The cooktop was heated to about 290 °C and the turbulence was so strong that it was hard to get recordings of 35 seconds length during that the control loop was running stable. The results are visualized in figures 6.20 to 6.23 and summarized in tables 6.7 and 6.8.

6.3.3.1 Agile image distortion

The mean local image motion in the science focus was reduced in MCAO control mode to approximately 0.015 ase from about 0.06 ase without compensation and in tip-tilt control mode. That is, 75 % of the agile image distortion was suppressed. The agile distortion of the recordings are shown in figure 6.20. Removing the global image motion (either with tip-tilt control or by subtraction from the evaluated subfield motions) reduced the agile distortion by about 0.010 ase. The reduction was less in the tip-tilt mode recording of 18:05:31 compared to 18:07:55 which means that the control loop performed poorly at that time. In the MCAO control mode recordings of 17:47:41 and 17:56:25, strong image motion is visible on two edges of the field of view in figure 6.20. The agile distortion in average is still well controlled whereas a weak wave-like pattern remained in distribution of the distortion. This pattern is emphasized in figure 6.19 and is possibly the residue of the strong turbulence at 290 °C. The predominant direction is given by the air bubbling up from the cooktop (plumes). The value of (0.015 ± 0.003) ase in MCAO control mode with all three deformable mirrors is on par with (0.016 ± 0.002) ase that was achieved with two deformable mirrors as reported in section 6.3.1, table 6.3.

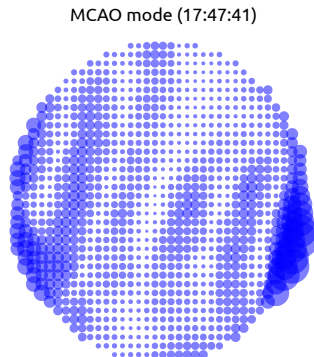


Figure 6.19: Agile image distortion in MCAO mode (circle scale is magnified compared to the other diagrams).

[‡]35 modes were controlled on $DM_{25}\text{ km}$ in earlier test runs with all actuators functional, but they were not recorded for analysis.

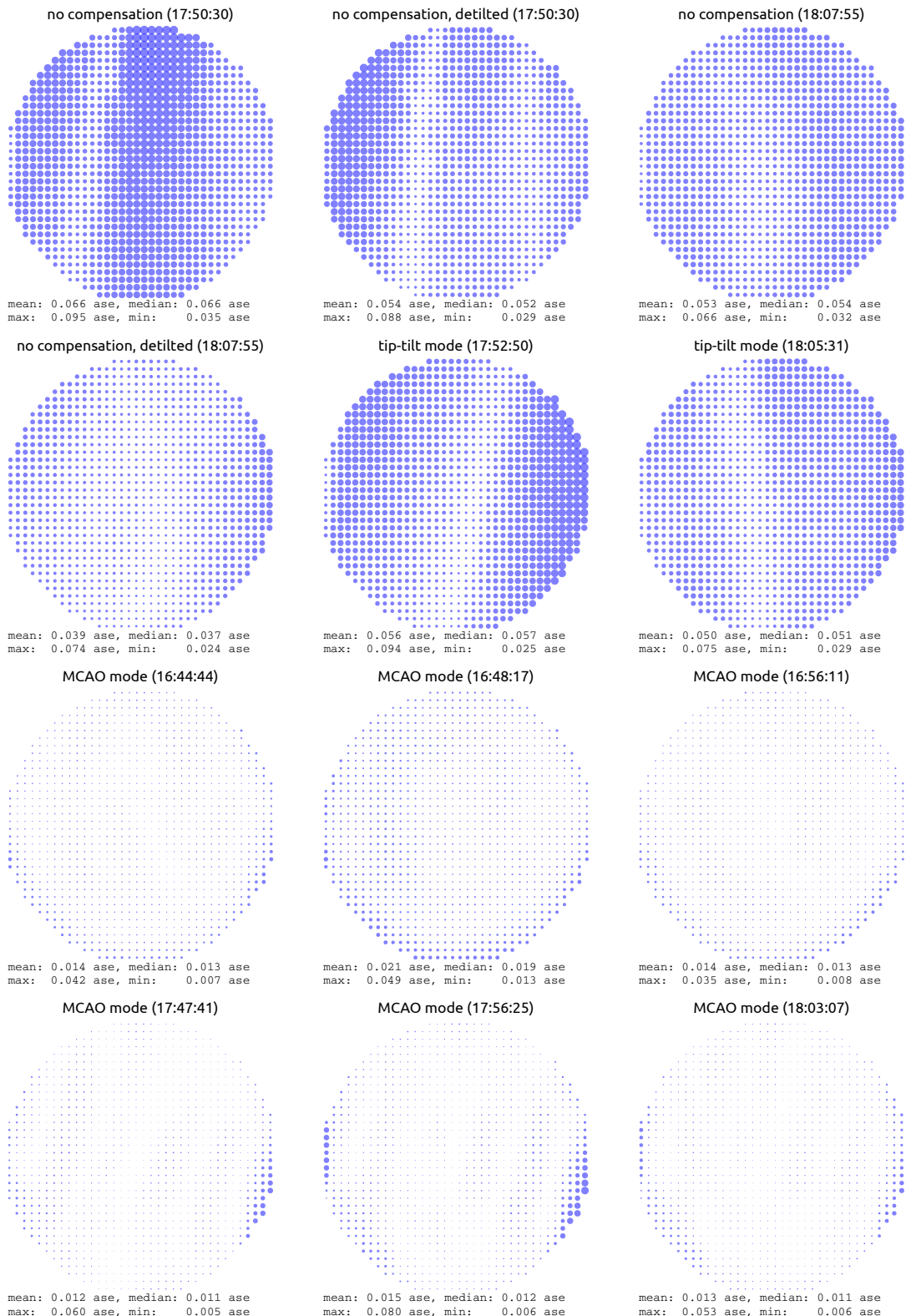


Figure 6.20: Temporal standard deviation of subfield image shift in the science focus with various AO control modes compensating for cooktop turbulence. In the 2nd and 4th graphs, which are labeled “no compensation, detilted”, the overall image shift (wavefront tilt) was subtracted before computing the standard deviation, with the effect of tip-tilt mode by post-processing.

6.3.3.2 Guide direction wavefront error

The average temporal root-mean-square (RMS) wavefront error of all guide directions ascribed to focus and astigmatism was decreased in MCAO control mode to 0.67 rad from about 1.65 rad without control or with tip-tilt control only. This error was approximately 0.9 rad in the case of MCAO control with only $DM_{0\text{ km}}$ and $DM_{8\text{ km}}$ (table 6.3). That is, MCAO with three deformable mirrors lowered the average RMS guide direction wavefront error by another 25 %. The minimum and maximum RMS guide direction errors were about 40 % less with three deformable mirrors than with two.

The modal analysis of the fluctuations and the root-mean-square of the guide direction errors are shown in figure 6.22 and 6.23. The errors due to the two broken actuators of $DM_{25\text{ km}}$, which were located somewhere between guide directions 7 and 19 as well as between 10 and 11, cannot be clearly identified, neither in recordings with MCAO control nor without. Although strong errors were present in that regions, there were also regions far away from the broken actuators that featured comparably large RMS errors (see also fig. 6.21). Actuator number 67 of $DM_{25\text{ km}}$, which was located between guide directions 10 and 11, had been completely removed by the manufacturer and the corresponding region is now controlled by the remaining neighbors. Actuator number 24, in between guide directions 7 and 17, was not removed. For this reason, this actuator pulls the face sheet as soon as the bias voltage is applied to the actuators, yielding a strong permanent depression of several micrometers. In consideration of this, it was surprising that the wavefront fluctuations were equally well compensated in all guide directions as represented in figure 6.22.

Table 6.7: Performance indicators of the test runs with $DM_{0\text{ km}}$, $DM_{8\text{ km}}$ and $DM_{25\text{ km}}$ on August 13th, 2012

mode	time	$\langle d_{\text{SDEV}}^{(s)} \rangle_s$ agile image distortion	$\langle w_i \rangle_i$ guide direc- tion error	min w_i	max w_i	$\langle r_{\text{SDEV}}^{(l)} \rangle_l$ MD-WFS shifts
MCAO	16:39:37	-	0.68 rad	0.17 rad	1.08 rad	0.08 px
MCAO	16:44:44	0.014 ase	0.74 rad	0.26 rad	1.16 rad	0.08 px
MCAO	16:48:17	0.021 ase	-	-	-	-
MCAO	16:56:11	0.014 ase	-	-	-	-
MCAO	17:47:41	0.013 ase	0.67 rad	0.22 rad	1.48 rad	0.07 px
MCAO	17:56:25	0.014 ase	0.63 rad	0.27 rad	1.09 rad	0.07 px
MCAO	18:03:07	0.013 ase	0.62 rad	0.24 rad	0.99 rad	0.07 px
tip-tilt	17:52:50	0.056 ase	1.73 rad	0.79 rad	2.95 rad	0.15 px
tip-tilt	18:05:31	0.050 ase	1.65 rad	0.97 rad	2.57 rad	0.16 px
No AO	17:50:53	0.066 ase	1.73 rad	0.87 rad	2.81 rad	0.17 px
No AO	18:07:53	0.053 ase	1.56 rad	0.80 rad	2.55 rad	0.16 px

Cooktop temperature was 290 °C during all recordings and the control frequency was 1700 Hz.

Table 6.8: Average performance indicators of table 6.7

MCAO	tip-tilt	No AO
$\langle d_{\text{SDEV}}^{(s)} \rangle_s$	(0.015±0.003) ase	0.053 ase
$\langle w_i \rangle_i$	(0.67±0.05) rad	1.69 rad
min w_i	(0.23±0.04) rad	0.88 rad
max w_i	(1.2±0.2) rad	2.74 rad
$\langle r_{\text{SDEV}}^{(l)} \rangle_l$	(0.074±0.005) px	0.16 px
		0.17 px

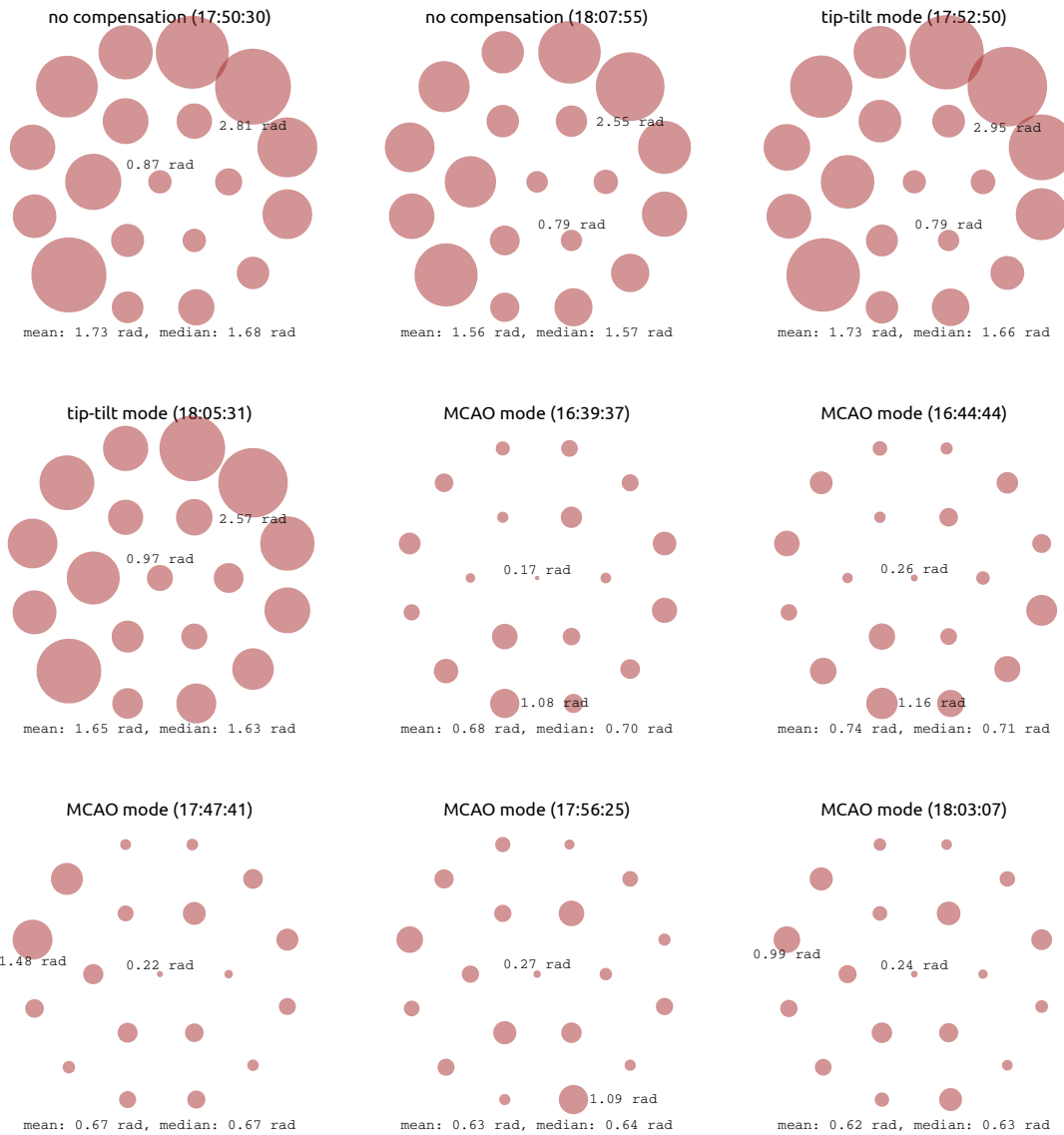


Figure 6.21: Temporal root-mean-square error of focus and astigmatism in the guide directions of the multi-dir wavefront sensor with various AO control modes compensating for cooktop turbulence.

6.3 Tested scenarios and results

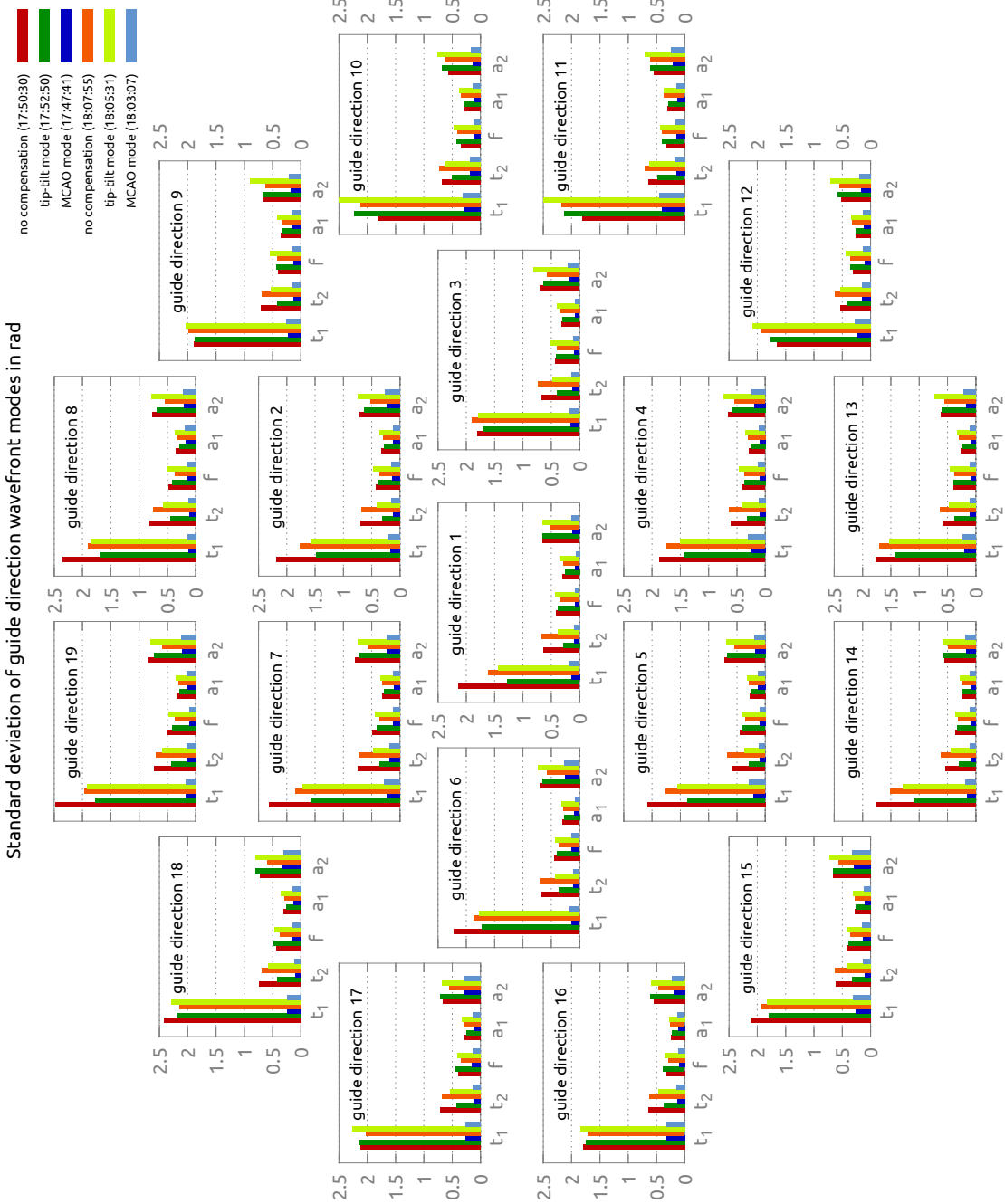


Figure 6.22: Temporal standard deviation of tip-tilt, focus and astigmatism in the guide directions of the multi-dir wavefront sensor with various AO control modes compensating for cooktop turbulence.

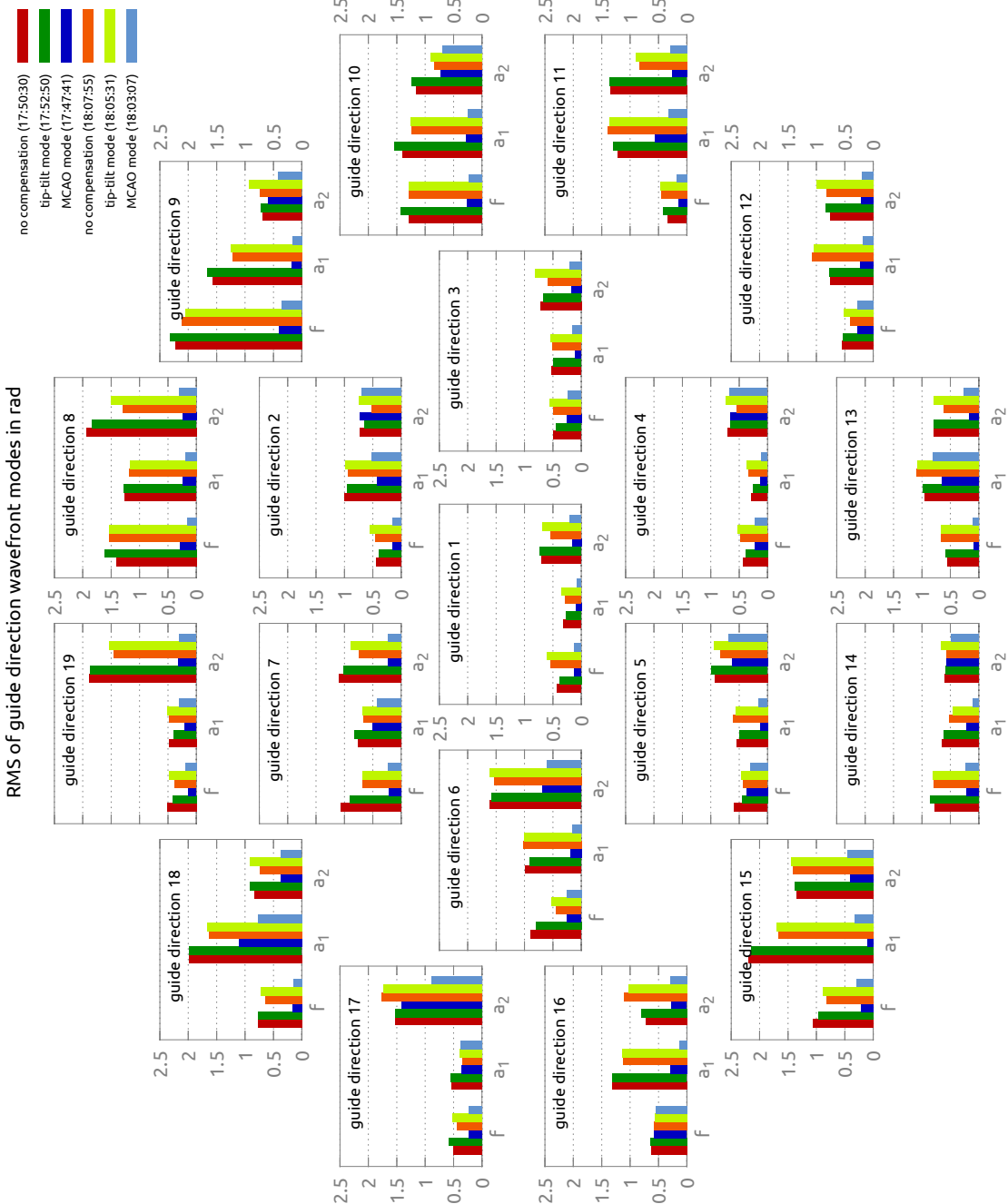


Figure 6.23: The temporal root-mean-square error of focus and astigmatism in the guide directions of the multi-dir wavefront sensor with various AO control modes compensating for cooktop turbulence.

6.3.3.3 Badly disentangled modes of $DM_{8\text{ km}}$ and $DM_{25\text{ km}}$

The time series of the KAOS modes of $DM_{8\text{ km}}$ and $DM_{25\text{ km}}$ generally feature striking similarities in certain modes. An arbitrary 0.588 seconds long time series cut from the recording of 17:50:30 (no AO control) is shown in figures 6.24 and 6.25 and scatter plotted in figures 6.26 and 6.27. 16 modes exhibit a linear correlation coefficient greater than 0.85. Although the MCAO control loop runs stable without winding up, it sometimes happens that $DM_{8\text{ km}}$ and $DM_{25\text{ km}}$ work against each other (slowly), degrading the effectiveness of the wavefront error compensation. It was not possible to investigate this issue in greater experimental detail because of the actuator failures of one OKO PDM69 device.

The statistical correlation of the used Karhunen-Loève modes for the cooktop turbulence is not known and not assumed to follow Kolmogorov's model necessarily. Hence, the question arose whether the strong temporal correlation of some modes is a weird feature of the cooktop turbulence, whether the reconstruction is badly solved, whether there is a bug in the KAOS software or if even the MD-WFS is insensitive to the plane in which those modes are introduced. In order to find out whether the MD-WFS is the source of the problem, I analyzed its modes-to-shifts matrix **MS** which is gained from the calibration procedure of KAOS. The idea is: if a certain mode would induce the same shifts no matter if it is embossed to $DM_{8\text{ km}}$ or $DM_{25\text{ km}}$, it would not be possible from the MD-WFS point of view to assign this mode to one mirror (i. e. conjugate plane on the optical axis) rather than to the other. Figure 6.28 shows the correlation matrix of the shift vectors (the tuple of 2-d image shifts in all correlation fields, referred to as *signature* in the following) registered in the MD-WFS if the KAOS modes are embossed on $DM_{8\text{ km}}$ or $DM_{25\text{ km}}$ individually. This matrix is mostly diagonal with strong elements in the first ten rows. The correlation of 1 for the tip-tilt modes (first two lines) is of course not surprising because this wavefront error cannot be attributed to a certain distance with a Hartmann-Shack type MD-WFS. However, the great similarity of the signatures of the modes 3–5 with respect to the two DMs was not imagined previously. To understand this effect, I modeled the response of MD-WFS for Karhunen-Loève modes in the metapupils in 8 and 25 km distance numerically with GNU Octave.[§] The correlation matrix of the modeled signatures is also shown in figure 6.28. Additionally, the modeled correlation matrices of MD-WFSs with 18 and 78 subapertures is shown in this figure. The matrix of six-subaperture model looks very similar to the matrix computed from the real KAOS calibration data. The deviations at higher modes are assumed to be the consequence of using synthetic mirror surface shapes instead of real ones in the simulations. The correlation coefficients of the first 12 modes of the simulation and the KAOS calibration data are very similar. The signatures of modes 3–5 (parabola and metapupil astigmatism) feature a correlation greater than 0.9. Following the idea of this analysis, neither an MD-WFS with 18 nor with 78 subapertures would allow per se for better assignment of the low order wavefront modes to $DM_{8\text{ km}}$ or $DM_{25\text{ km}}$. What magnitude of the correlation coefficient

[§]The model was very simple and purely geometric. The appropriate sections for the guide directions and subapertures were cut from the metapupils' Karhunen-Loève modes and summed up. The average slopes thereof were taken as the MD-WFS's image shifts. Neither imaging through microlenses nor measurement errors were modeled. The Karhunen-Loève modes were synthetic and not real, measured mirror surface shapes that were actually generated by the corresponding actuator command patterns.

impacts the reconstruction severely was not elaborated. How to perform the 3d-wavefront reconstruction inversion of very similar, though not equal, wavefront sensor signatures needs to be analyzed in the future. Maybe it is useful to include additional information about the (instantaneous) turbulence profile in the reconstruction in order to weight the mode assignment to the mirrors. It could be also worthwhile to subtract average shift of each subaperture image from the corresponding MD-WFS shifts as is was done for other reasons in the old KAOS software, that is—for example for the horizontal shift—calculating

$$\tilde{s}_x^{(i,j)} = s_x^{(i,j)} - \langle s_x^{(i,j)} \rangle_i, \quad (6.11)$$

where $s_x^{(i,j)}$ is the originally computed image shift in the correlation field of the i^{th} guide direction in the j^{th} subaperture of the MD-WFS and $\langle \dots \rangle_i$ means averaging over the guide directions. This would add up to a two-step reconstruction in which the subaperture averages

$$\left\{ \langle s_x^{(i,1)} \rangle_i, \langle s_y^{(i,1)} \rangle_i, \dots, \langle s_x^{(i,6)} \rangle_i, \langle s_y^{(i,6)} \rangle_i \right\}$$

(in the case of 6 subapertures) would be used to reconstruct the field independent defocus and astigmatism which are delegate to $\text{DM}_{0 \text{ km}}$ whereas the shifts from equation (6.11) would be used to reconstruct the $\text{DM}_{8 \text{ km}}$ and $\text{DM}_{25 \text{ km}}$ modes only. This could hopefully help the numerical SVD inversion to be sensitive to smaller differences in the shift signatures of $\text{DM}_{8 \text{ km}}$ and $\text{DM}_{25 \text{ km}}$.

6.3.4 Unperformed tests

Some test scenarios which seem to be interesting were not performed. No obvious impact of the three different calibration methods (see sec. 4.2.2) was noticed when watching the control loop. Because of the mentioned repeatability problem, this was not analyzed in detail. Experience that will be gained at the telescope will probably reveal the best method for a stable and well performing control loop. Asymmetric distribution of the guide directions was not tested because the trigger pixels of one correlation field can fall in an other correlation field nearby in the current implementation of KAOS Evo 2, hence corrupting the raw image data. Therefore, the positioning of the trigger pixels needs to be rearranged. Operating the testbed with the on-axis wavefront sensor downstream of the high-altitude deformable mirrors was skipped because of the limited time. This is certainly a matter that should be attempted in the future and in particular at the telescope.

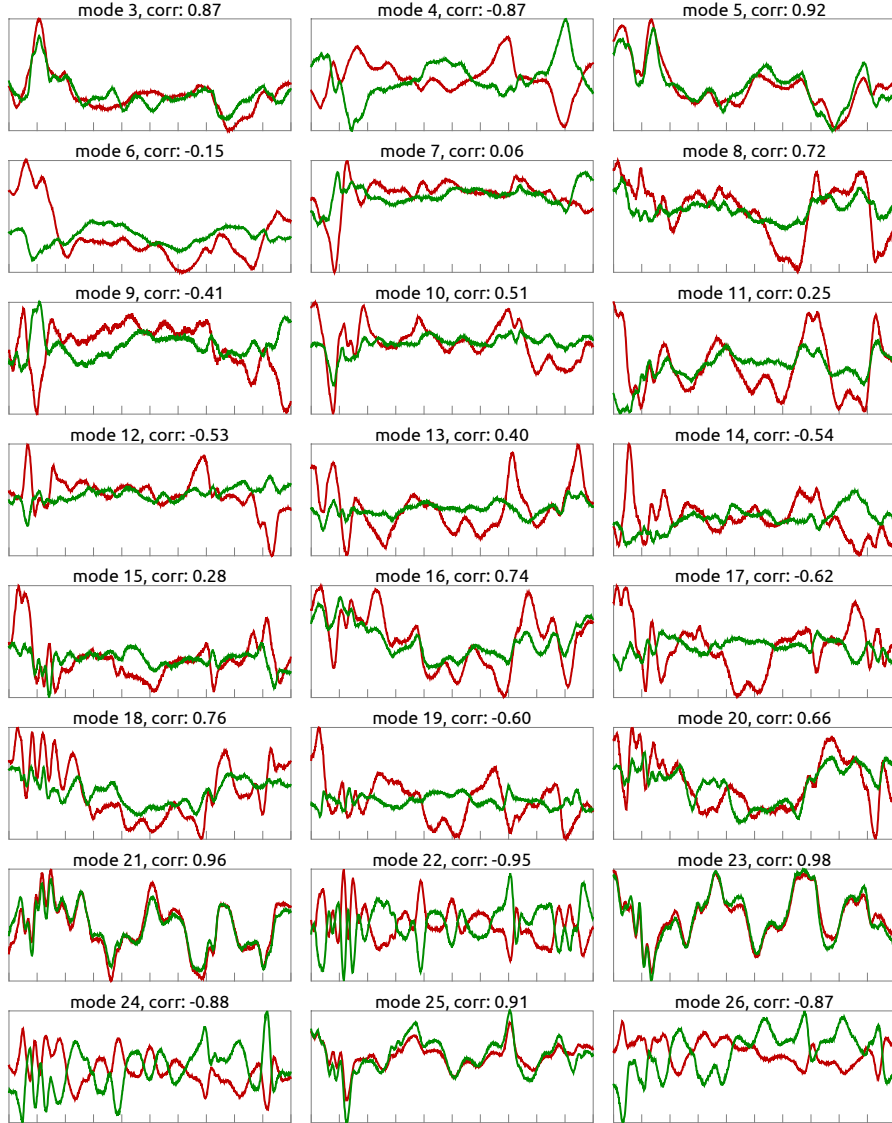


Figure 6.24: Time series of KAOS modes 3-26 of $\text{DM}_{8 \text{ km}}$ and $\text{DM}_{25 \text{ km}}$. In each panel, the mode coefficients of $\text{DM}_{8 \text{ km}}$ (red) and $\text{DM}_{25 \text{ km}}$ (green) are plotted vs. time. The mode number is given in the title as well as the linear correlation coefficient of both curves. The mean value was subtracted from the curves for clearer plotting. Time series span 1000 control loop cycles corresponding to 0.588 s. The scale of the y-axis is not constant throughout the panels. The scale is not given because this figure shall emphasize the mode correlation. The actuator patterns corresponding to the Karhunen-Loëve modes, which were used by KAOS in this case, are shown in fig. B.1 and B.2. The time series of modes 26-59 are shown in the next figure.

6 MCAO Testruns

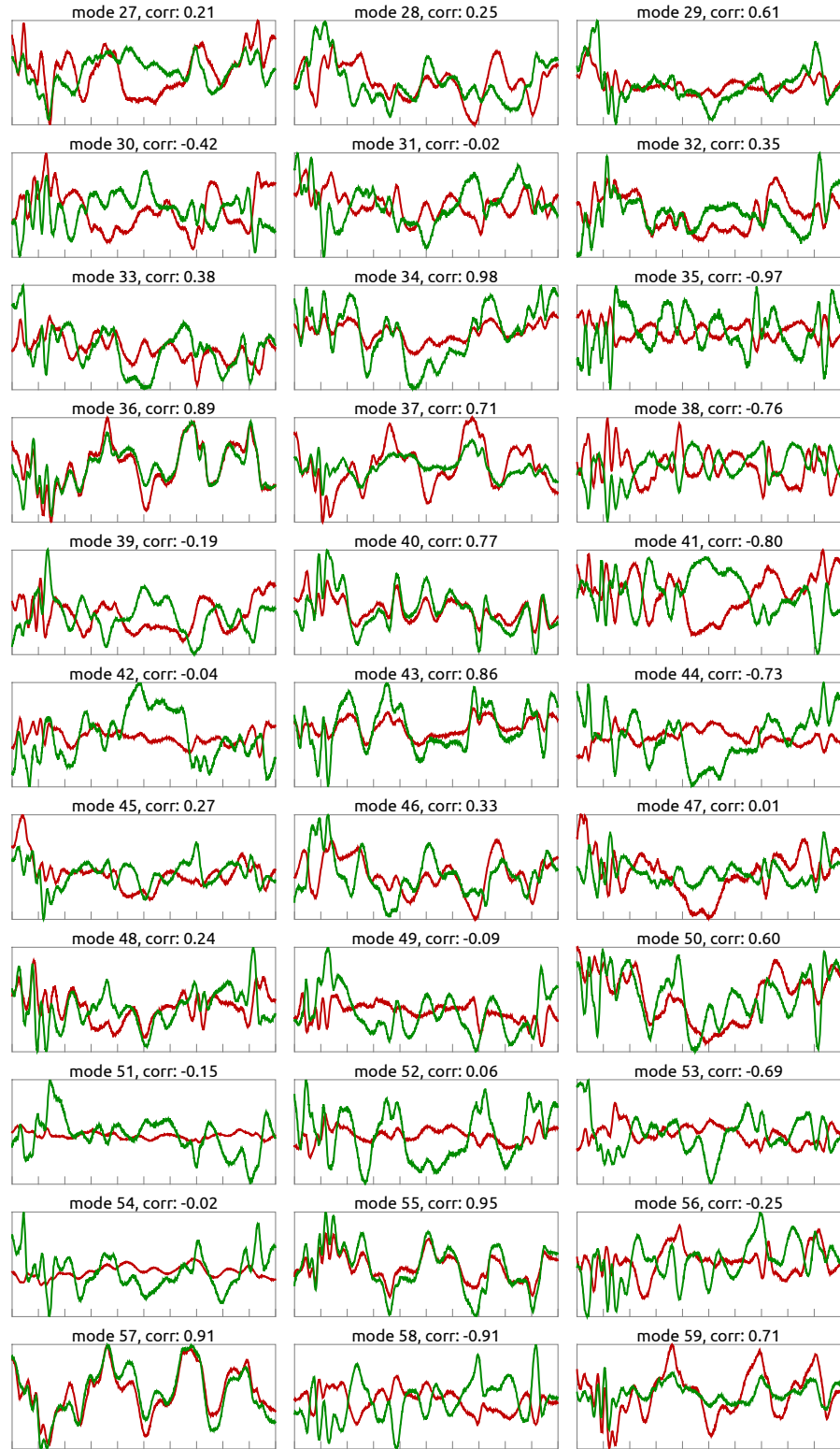


Figure 6.25: Time series of KAOS modes 27-59 of $DM_{8\text{ km}}$ and $DM_{25\text{ km}}$. Refer to fig. 6.24 for explanation.

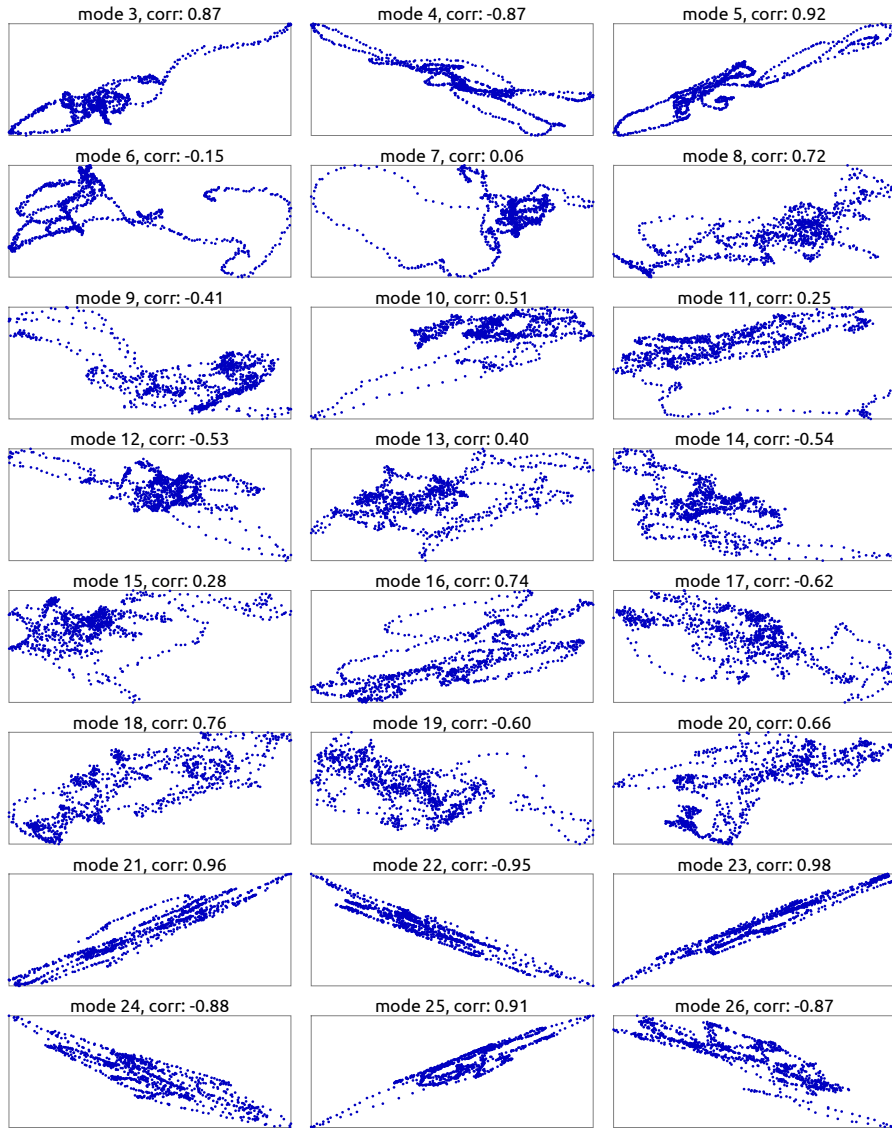


Figure 6.26: Scatter graphs of the time series in fig. 6.24. In each panel, the mode coefficient of $DM_{8\text{ km}}$ is plotted vs. the same coefficient of $DM_{25\text{ km}}$. The mode number is given in the title as well as the linear correlation coefficient of both variables. Axis scales are linear but of no quantitative relevance and therefore omitted.

6 MCAO Testruns

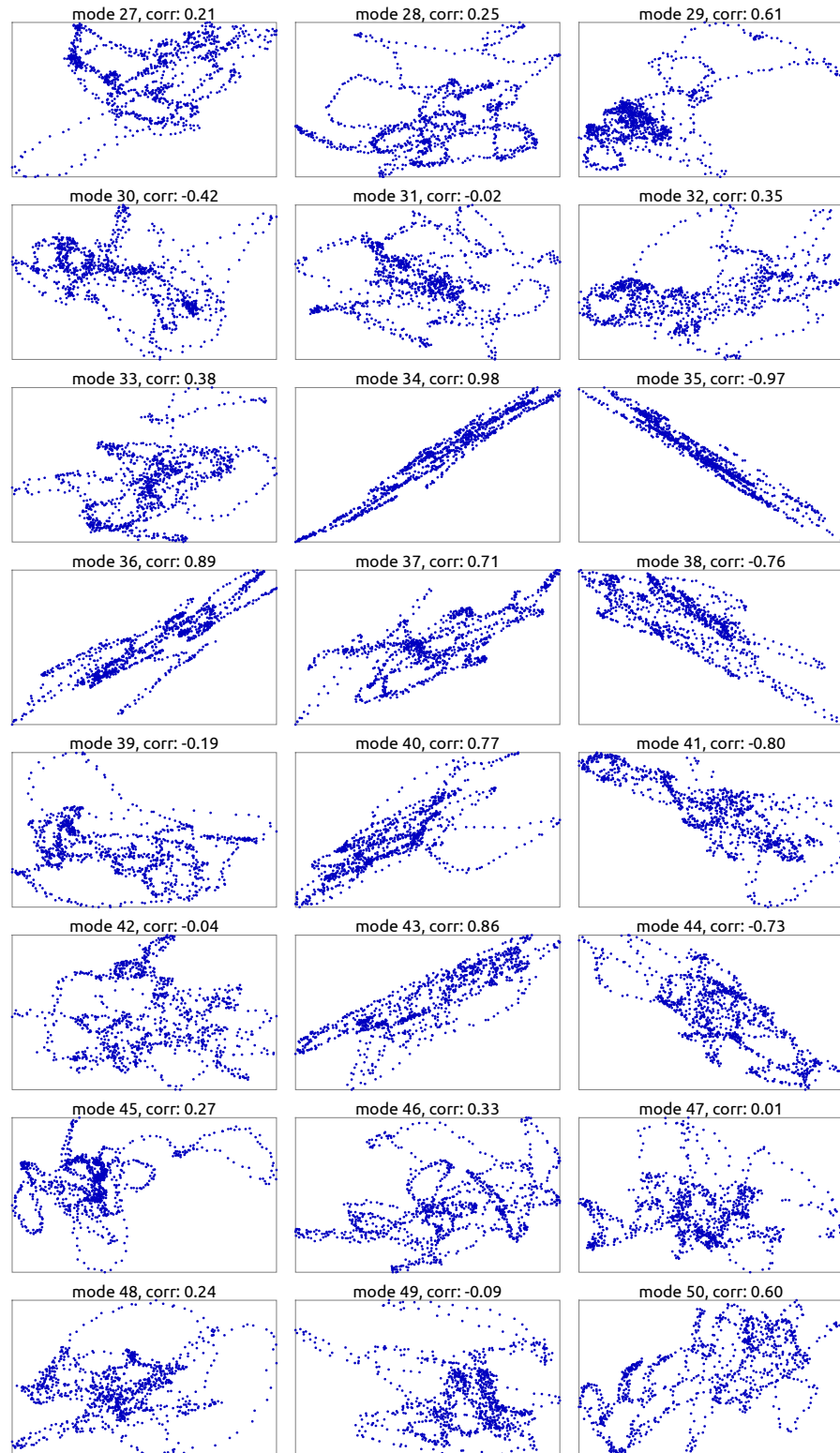


Figure 6.27: Scatter graphs of the time series in fig. 6.25. Refer to fig. 6.26 for explanation.

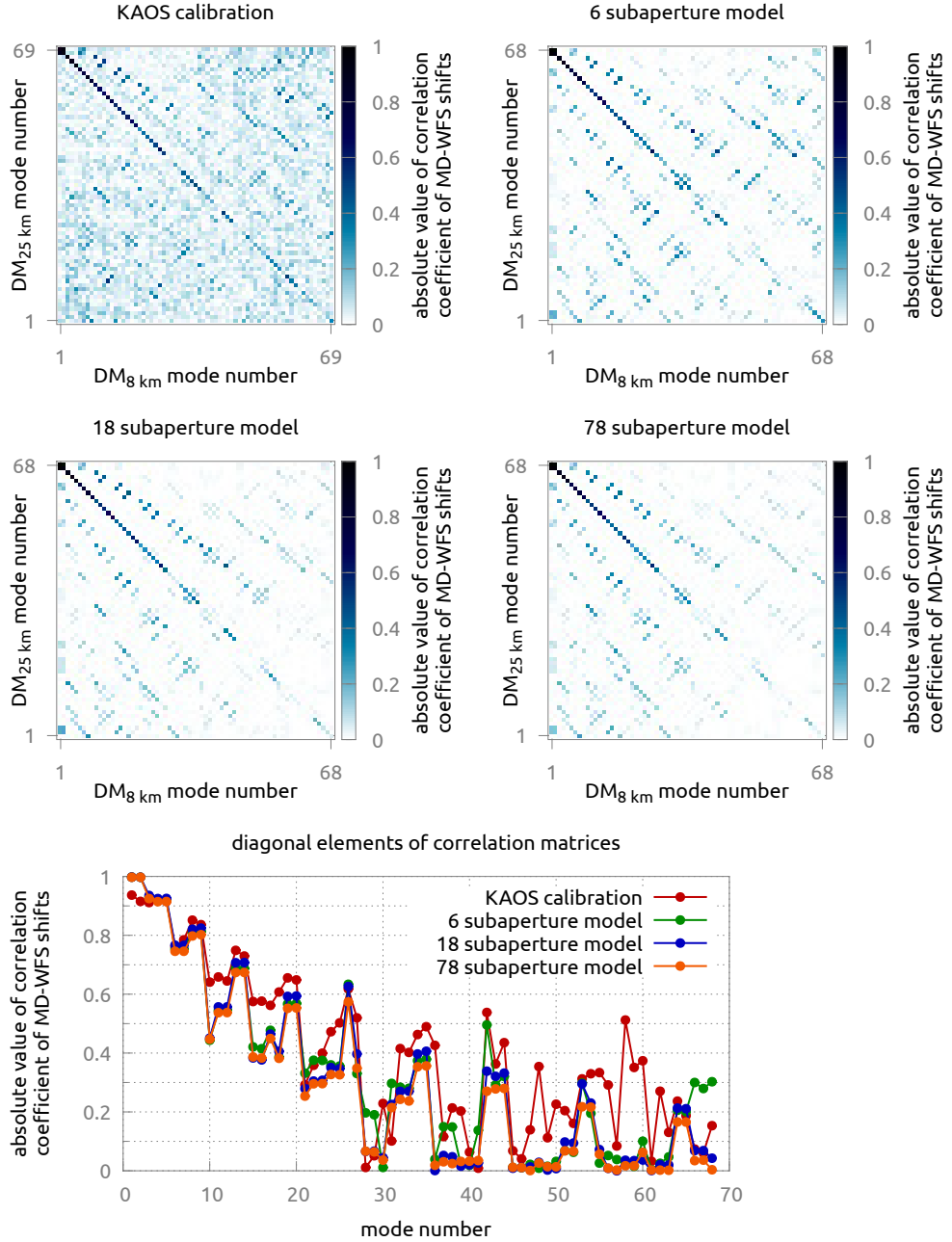


Figure 6.28: Correlation matrices of the MD-WFS signatures of DM_{8 km} and DM_{25 km} (top four panels). The elements of the matrix represent the linear correlation coefficient $c_{i,j} = \text{corr}(\vec{s}_{8 \text{ km},i}, \vec{s}_{25 \text{ km},j})$ of the shift vectors $\vec{s}_{8 \text{ km},i}$ and $\vec{s}_{25 \text{ km},j}$ in the MD-WFS induced by mode number i embossed on DM_{8 km} and mode number j on DM_{25 km}. The absolute value of $c_{i,j}$ is plotted to emphasize the strength of correlations. KAOS calibration refers to the actually measured signatures in the real MD-WFS with 6 subapertures. The other three panels show the result numerically modeled MD-WFS with the given number of subapertures. The diagonals of the matrices are plotted below for quantitative comparison.

7 Summary

«All good things come to an end.»

(Nelly Furtado, "All good things")

7.1 GREGOR MCAO system and the testbed

The MCAO system of GREGOR was set up in the optics lab of the Kiepenheuer-Institut in Freiburg. Its subsystems were tested and verified. The setup was used for the development of a new control software and wavefront control algorithms. The system's performance was characterized with the use of turbulence generated by a cooktop.

GREGOR's MCAO system features three deformable mirrors (DM) in planes conjugate 0 km, 8 km and 25 km distance on the optical axis, and a tip-tilt mirror. Wavefront sensing is performed with two wavefront sensor units: the on-axis wavefront sensor with 78 subapertures and about 10 arcseconds field of view, and the multi-direction wavefront sensor with 6 subapertures and 19 guide directions which are distributed over a field of view of one arcminute. The on-axis wavefront registers the actuations of the tip-tilt mirror and of $DM_{0\text{ km}}$, whereas the multi-direction sensor registers the actuations of all four mirrors.

The GREGOR MCAO testbed demonstrates that a real-time MCAO system for a solar telescope with more than 200 subapertures can be realized with off-the-shelf computer hardware and industry-grade computer vision cameras.

7.2 MCAO Performance

The MCAO control mode was able to suppress the cooktop turbulence significantly and very uniformly over the field of view. 30 modes were controlled with $DM_{0\text{ km}}$, 50 modes with $DM_{8\text{ km}}$ and 25 modes with $DM_{25\text{ km}}$. The rather low number of 25 is the consequence of broken actuators of $DM_{25\text{ km}}$. 35 modes were controlled earlier with this mirror.

MCAO with the tip-tilt mirror, $DM_{0\text{ km}}$ and $DM_{8\text{ km}}$ (two DMs) decreased the average subfield image motion to about 0.016 arcsecond equivalents (ase) of the GREGOR focus. MCAO with tip-tilt mirror, $DM_{0\text{ km}}$, $DM_{8\text{ km}}$ and $DM_{25\text{ km}}$ (three DMs) reached the same value. The average subfield image motion of uncompensated turbulence was about 0.07 ase and about 0.05 ase when the field-average motion (global tip-tilt) was removed. Hence, MCAO suppressed field-dependent image motion ("agile image motion", distortion) from 0.05 to 0.016 ase by about 70 %.

The root-mean-square wavefront-error in the guide directions on account of focus and astigmatism was reduced with two DMs by about 47 % to approximately 0.9 rad (Strehl-ratio

7 Summary

calculated from this: $S = 0.44$) in average of all guide directions. By using three DMs, this value was lowered to 0.67 rad ($S = 0.64$). The minimal root-mean-square guide-direction wavefront-error on account of focus and astigmatism was about 0.2 rad ($S = 0.96$) and the maximum error was round about 1 rad ($S = 0.37$).

The standard deviation of the guide-direction wavefront-error including tip-tilt was reduced from about 2.7 rad ($S \approx 0$) by about 80 % to 0.5 rad ($S = 0.78$) in average of all guide directions. There is no striking difference between two DMs and three DMs with respect to this error.

A significant amount of root-mean-square error was not well removed in some guide directions whereas the standard deviation, i. e. the error fluctuations, were compensated much more uniformly over the field. This means that some static aberrations remained. The root-mean-square surface-error of the $\text{DM}_{8\text{ km}}$ device with respect to the complete surface was about 0.42 rad ($S = 0.84$) (reflected wavefront) after manual flattening. This error is attributed to actuator print-through and the root-mean-square error is higher in certain subregions of the surface. For this reason, at least a great portion of the remaining field-dependent static aberrations can be attributed to $\text{DM}_{8\text{ km}}$ and $\text{DM}_{25\text{ km}}$. For comparison: the root-mean-square wavefront error of the manually flattened CILAS mirror with 256 actuators used as $\text{DM}_{0\text{ km}}$ in GREGOR is less than half of the value above.

The 0-dB-bandwidth of the MCAO control loop was approximately: 45 Hz for tip-tilt compensation, 35 Hz for the lowest six modes of $\text{DM}_{0\text{ km}}$, 100 Hz for higher modes of $\text{DM}_{0\text{ km}}$, and 130 Hz for all modes of $\text{DM}_{8\text{ km}}$. The tip-tilt control bandwidth was above 100 Hz when only tip-tilt was controlled. In consideration of this, it seems to be likely that $\text{DM}_{8\text{ km}}$ introduced an unnoticed tip-tilt action which counteracted the tip-tilt mirror. The low bandwidth of the low modes of $\text{DM}_{0\text{ km}}$ is assumed to be the consequence of the harmonic oscillations (overtones) of the bimorph plate which have longer periods for lower orders. However, this device will not be used at GREGOR and its bandwidth is irrelevant for this reason.

Low order modes, such as parabola mode and metapupil astigmatism, cannot be ascribed well to $\text{DM}_{8\text{ km}}$ or $\text{DM}_{25\text{ km}}$ from the perspective of the multi-direction wavefront sensor. The reason thereof is the signature of the modes in the wavefront sensor which are very similar for both mirrors. A numerical model showed that this problem is not relaxed with a greater number of subapertures in the multi-direction wavefront sensor.

7.3 Outlook

Besides yet unknown effects that will welcome the MCAO system at the telescope, there are a few known issues that need to be addressed in the near future, some of which before the installation at GREGOR. A reference of image distortion needs to be implemented in the KAOS control software and tested. The tip-tilt control bandwidth in MCAO control mode must be increased. A method to separate low order modes of $\text{DM}_{8\text{ km}}$ from the modes of $\text{DM}_{25\text{ km}}$ better should be found. A more elaborate algorithm to automatically set the number of controlled modes of the high-altitude mirrors should be conceived and implemented. The new algorithm could take the turbulence profile and the efficiency of the individual modes with respect to actuator stroke into account. Placing the on-axis wavefront sensor behind all

deformable mirrors should be tried again and theoretical analyses should be deepened in order to find out whether dynamic misregistration is in fact a real problem and constitutes a limiting factor of subaperture size and hence of the number of degrees of freedom in an MCAO system.

A Technical data of GREGOR's adaptive optics systems

A.1 Optical design of the MCAO

element	radius of curvature	distance to next element
F_3	-	1800 mm
M_{12}	3605.09 mm, 3594.73 mm	2200 mm
TT	∞	400 mm
$DM_{0 \text{ km}}$	∞	1777 mm
M_{15}	13961.51 mm	5000 mm
M_{16}	6290.91 mm	1824 mm
$DM_{25 \text{ km}}$	∞ (80 m)	817 mm
$DM_{8 \text{ km}}$	∞ (80 m)	4105 mm (4248 mm)
M_{19}	3254.62 mm, 3227.10 mm	990 mm (951 mm)
M_{20}	∞	1331 mm
F_{science}	-	-

Table A.1: The optical geometry of GREGOR MCAO. Focal lengths of M_{12} , M_{15} , M_{16} and M_{19} were measured by their manufacturers. The distances from $DM_{8 \text{ km}}$ to M_{19} and from M_{19} to M_{20} need to be set to the values in brackets to preserve F_3 's image scale in F_{science} because the device used as $DM_{8 \text{ km}}$ and $DM_{25 \text{ km}}$ actually feature a radius of curvature of typically 80 m (see sec. 3.3.1.1).

A.2 Deformable mirrors

Table A.2: Technical key data of the deformable mirrors that are used as DM_{8 km} and DM_{25 km}

	DM _{8 km} and DM _{25 km}
manufacturer	Flexible Optical B.V. (OKO Tech), Delft, The Netherlands, http://www.okotech.com
designation serial numbers	PDM69 KIS1 (delivery 12/2008, broken 01/2012, to be replaced in Q4/2012), KIS2 (delivery 12/2008, broken 05/2010, replaced by KIS3), KIS3 (delivery 09/2010)
type	continuous faceplate with discrete actuators using the transversal piezoelectric effect, custom made
number of actuators	69
actuator layout	square grid (9×9 without 3 actuators in each corner, see fig. 3.5)
actuator spacing	4.75 mm (\cong 46 cm @ 8 km, and 108 cm @ 25 km)
reflective surface diameter	50 mm
illuminated diameter	43 mm
voltage range [†]	0 to +400 V
single actuator stroke*	> $\pm 1.5 \mu\text{m}$ (from 150 to 0 and 300 V)
maximum stroke*	> 10 μm (overall-tilt within 38 mm Ø from 0 to 300 V)
influence function FWHM*	(8.2 \pm 0.2) mm (best Gauss in 20 mm Ø around actuators)
frequency range [†]	0 to 2 kHz
resonance frequency*	\approx 1.9–2.0 kHz (measured for a 109-actuator DM, dominated by faceplate and hence applicable for 69 actuators DM)
step response rise time*, ⁺	<4 ms (no overshoot) (see fig. 5.10)
actuator capacitance *	(5.3 \pm 0.2) nF
initial surface	spherical
initial focal length*	\approx 33–41 m (varies with ambient temperature)
hysteresis*	10 % at 0 to 350 V (measured for a 109 actuators DM, dominated by actuators piezo material and hence applicable for 69 actuators DM)
reflective coating	protected aluminum

^{*}) own measurements, see chapter 5

[†]) manufacturer information

⁺) inconjunction with the KIS high-voltage amplifier system

Table A.3: Technical key data of the deformable mirror made by Night that is used as $DM_{0 \text{ km}}$.

	GAOS.80 $DM_{0 \text{ km}}$
manufacturer	Night N, Moscow, Russia, http://www.nightn.ru
type	continuous faceplate with bimorph actuators, free-edge fixation
number of actuators	80 (+1 focus actuator, not used)
actuator layout	keystone (see fig. 3.6)
illuminated diameter	48 mm
voltage range [†]	-240 to +300 V
maximum stroke*	radius of curvature > ± 10 m
frequency range [†]	0 to 1.8 kHz
first resonance frequency [†]	2.43 kHz
hysteresis*	19 % at -240 to +300 V
reflective coating	protected aluminum

^{*}) own measurements, see chapter 5[†]) manufacturer information

Table A.4: Technical key data of deformable mirrors.

	GAOS.256 $DM_{0 \text{ km}}$
manufacturer	Compagnie Industrielle des Lasers (CILAS), Orléans, France, http://www.cilas.com
type	continuous faceplate with discrete actuators using the longitudinal piezoelectric effect (stacked piezos)
number of actuators	256
actuator layout	rectangular grid (18×18 without 17 actuators in each corner, see fig. 3.7)
actuator spacing	3.27 mm, and 3.16 mm ($\cong 10$ cm @ 0 km)
illuminated diameter	48 mm
voltage range [†]	-400 to +400 V
max. slew rate [†]	100 V/ms
single actuator stroke [†]	$\pm 1.4 \mu\text{m}$
maximum stroke*	$8.6 \mu\text{m}$ (overall-tilt from -395 to +395 V)
first resonance frequency [†]	>2 kHz
actuator capacitance [†]	$(3.4 \pm 0.5) \text{nF}$
initial surface	flat
hysteresis [†]	3.5 % at -400 to +400 V
reflective coating	protected aluminum

^{*}) own measurements, see chapter 5[†]) manufacturer information

A.3 High-voltage electronics system

Table A.5: Technical data of the KIS High-voltage amplifier system used in GREGOR's AO/MCAO.

type interfaces	voltage-driven 32-bit parallel RS422 for realtime control, CoSM field bus via Ethernet for service
RS422 PC-interface daughter board	EDT PCIe8 DV CLS with KIS-M-LINK converter
actuator data transfer rate	10 MHz
maximum high-voltage output range	–500 to + 500 V
actual high-voltage output range	reduced to the range of the connected mirrors
3-dB bandwidth*	≈ 1900 Hz (see fig. 5.16)
actuator address width	11 bit
actuator value width	16 bit
actuator value analog conversion	14 bit
digital-analog conversion factor (HV out)	≈ 53 mV/LSB
settling time of DACs	15 µs

Table A.6: Pin connections and bit assignment of KIS-M-LINK

	MDR26 Pin Sender	MDR26 Pin Empfänger	Camera-Link- Signal	DS90CR288A Eingang Pin-Name	DS90CR288A Eingang TSSOP Pin
Kabel 1	18	9	XCLK+	X RxCLKIN+	X 18
	5	22	XCLK-	X RxCLKIN-	X 17
	19	8	X3+	X RxIN3+	X 20
	6	21	X3-	X RxIN3-	X 19
	17	10	X2+	X RxIN2+	X 16
	4	23	X2-	X RxIN2-	X 15
	16	11	X1+	X RxIN1+	X 12
	3	24	X1-	X RxIN1-	X 11
	15	12	X0+	X RxIN0+	X 10
	2	25	X0-	X RxIN0-	X 9
	1	1	GND		
	13	13	GND		
	14	14	GND		
	26	26	GND		
	21	6	SERTFG+	--	
	8	19	SERTFG-	--	
	7	20	SERTC+	--	
	20	7	SERTC-	--	
	12	15	CC4+	--	
	25	2	CC4-	--	
	24	3	CC3+	--	
	11	16	CC3-	--	
	10	17	CC2+	--	
	23	4	CC2-	--	
	22	5	CC1+	--	
	9	18	CC1-	--	
Kabel 2	24	3	ZCLK+	Z RxCLKIN+	Z 18
	11	16	ZCLK-	Z RxCLKIN-	Z 17
	25	2	Z3+	Z RxIN3+	Z 20
	12	15	Z3-	Z RxIN3-	Z 19
	23	4	Z2+	Z RxIN2+	Z 16
	10	17	Z2-	Z RxIN2-	Z 15
	22	5	Z1+	Z RxIN1+	Z 12
	9	18	Z1-	Z RxIN1-	Z 11
	21	6	Z0+	Z RxIN0+	Z 10
	8	19	Z0-	Z RxIN0-	Z 19
	18	9	YCLK+	Y RxCLKIN+	Y 18
	5	22	YCLK-	Y RxCLKIN-	Y 17
	19	8	Y3+	Y RxIN3+	Y 20
	6	21	Y3-	Y RxIN3-	Y 19
	17	10	Y2+	Y RxIN2+	Y 16
	4	23	Y2-	Y RxIN2-	Y 15
	16	11	Y1+	Y RxIN1+	Y 12
	3	24	Y1-	Y RxIN1-	Y 11
	15	12	Y0+	Y RxIN0+	Y 10
	2	25	Y0-	Y RxIN0-	Y 9
	1	1	GND		
	13	13	GND		
	14	14	GND		
	26	26	GND		
	7	20	100 Ohm Term	--	1x Abschluß!
	20	7	100 Ohm Term	--	

Table A.7: Pin connections and bit assignment of KIS-M-LINK

DS90CR288A Ausgang Pin-Name	DS90CR288A Ausgang TSSOP Pin	Camera-Link- Bit (8x8)	KAOS-Bit	DS90CR288A Ausgang Pin-Name	DS90CR288A Ausgang TSSOP Pin	Camera-Link- Bit (8x8)	KAOS-Bit
X RxOUT0	X 27	D0		Y RxOUT0	Y 27	D24	
X RxOUT1	X 29	D1		Y RxOUT1	Y 29	D25	
X RxOUT2	X 30	D2		Y RxOUT2	Y 30	D26	
X RxOUT3	X 32	D3		Y RxOUT3	Y 32	D27	
X RxOUT4	X 33	D4		Y RxOUT4	Y 33	D28	
X RxOUT5	X 34	D7		Y RxOUT5	Y 34	D31	
X RxOUT6	X 35	D5		Y RxOUT6	Y 35	D29	
X RxOUT7	X 37	D8		Y RxOUT7	Y 37	D32	AO_TRIGGER
X RxOUT8	X 38	D9		Y RxOUT8	Y 38	D33	LDAC
X RxOUT9	X 39	D10		Y RxOUT9	Y 39	D34	AO_EN
X RxOUT10	X 41	D14		Y RxOUT10	Y 41	D38	A2
X RxOUT11	X 42	D15		Y RxOUT11	Y 42	D39	A3
X RxOUT12	X 43	D11		Y RxOUT12	Y 43	D35	RES
X RxOUT13	X 45	D12		Y RxOUT13	Y 45	D36	A0
X RxOUT14	X 46	D13		Y RxOUT14	Y 46	D37	A1
X RxOUT15	X 47	D16		Y RxOUT15	Y 47	D40	A4
X RxOUT16	X 49	D22		Y RxOUT16	Y 49	D46	A10
X RxOUT17	X 50	D23		Y RxOUT17	Y 50	D47	D0
X RxOUT18	X 51	D17		Y RxOUT18	Y 51	D41	A5
X RxOUT19	X 53	D18		Y RxOUT19	Y 53	D42	A6
X RxOUT20	X 54	D19		Y RxOUT20	Y 54	D43	A7
X RxOUT21	X 55	D20		Y RxOUT21	Y 55	D44	A8
X RxOUT22	X 1	D21		Y RxOUT22	Y 1	D45	A9
X RxOUT23	X 2	SPARE/HIGH		Y RxOUT23	Y 2	SPARE/HIGH	
X RxOUT24	X 3	LVAL		Y RxOUT24	Y 3	LVAL	
X RxOUT25	X 5	FVAL		Y RxOUT25	Y 5	FVAL	
X RxOUT26	X 6	DVAL		Y RxOUT26	Y 6	DVAL	
X RxOUT27	X 7	D6		Y RxOUT27	Y 7	D30	
X RxCLK OUT	X 26			Y RxCLK OUT	Y 26		CLOCK
Z RxOUT0	Z 27	D48	D1	Z RxOUT1	Z 29	D49	D2
Z RxOUT1	Z 29	D49		Z RxOUT2	Z 30	D50	D3
Z RxOUT2	Z 30	D50		Z RxOUT3	Z 32	D51	D4
Z RxOUT3	Z 32	D51		Z RxOUT4	Z 33	D52	D5
Z RxOUT4	Z 33	D52		Z RxOUT5	Z 34	D55	D8
Z RxOUT5	Z 34	D55		Z RxOUT6	Z 35	D53	D6
Z RxOUT6	Z 35	D53		Z RxOUT7	Z 37	D56	D9
Z RxOUT7	Z 37	D56		Z RxOUT8	Z 38	D57	D10
Z RxOUT8	Z 38	D57		Z RxOUT9	Z 39	D58	D11
Z RxOUT9	Z 39	D58		Z RxOUT10	Z 41	D62	D15
Z RxOUT10	Z 41	D62		Z RxOUT11	Z 42	D63	
Z RxOUT11	Z 42	D63		Z RxOUT12	Z 43	D59	D12
Z RxOUT12	Z 43	D59		Z RxOUT13	Z 45	D60	D13
Z RxOUT13	Z 45	D60		Z RxOUT14	Z 46	D61	D14
Z RxOUT14	Z 46	D61		Z RxOUT15	Z 47	- / LOW	
Z RxOUT15	Z 47	- / LOW		Z RxOUT16	Z 49	- / LOW	
Z RxOUT16	Z 49	- / LOW		Z RxOUT17	Z 50	- / LOW	
Z RxOUT17	Z 50	- / LOW		Z RxOUT18	Z 51	- / LOW	
Z RxOUT18	Z 51	- / LOW		Z RxOUT19	Z 53	- / LOW	
Z RxOUT19	Z 53	- / LOW		Z RxOUT20	Z 54	- / LOW	
Z RxOUT20	Z 54	- / LOW		Z RxOUT21	Z 55	- / LOW	
Z RxOUT21	Z 55	- / LOW		Z RxOUT22	Z 1	- / LOW	
Z RxOUT22	Z 1	- / LOW		Z RxOUT23	Z 2	SPARE/HIGH	
Z RxOUT23	Z 2	SPARE/HIGH		Z RxOUT24	Z 3	LVAL	
Z RxOUT24	Z 3	LVAL		Z RxOUT25	Z 5	FVAL	
Z RxOUT25	Z 5	FVAL		Z RxOUT26	Z 6	DVAL	
Z RxOUT26	Z 6	DVAL		Z RxOUT27	Z 7	D54	D7
Z RxCLK OUT	Z 26						

A.4 Tip-tilt mirrors

Table A.8: Technical key data of the tip-tilt stages and the attached mirrors used in GREGOR and in the testbed.

	KIS TT	PI TT
manufacturer of tip-tilt stage	KIS	Physikinstrumente Karlsruhe, Germany, http://www.pi.ws
model	-	S-330.4SD with E505
type	piezo electric actuators using the longitudinal piezoelectric effect (stacked piezos)	dito
number of axes	3	2
low-voltage input range	1.7 to 8.3 V	3.3 to 6.7 V
zero-tilt input voltage	5 V	5 V
high-voltage output range	-250 to + 250 V	0 to 100 V
digital resolution	14 bit	14 bit
digital-analog conversion factor	403 μ V/LSB	207.5 μ V/LSB
illuminated diameter	48 mm	48 mm
used tilt range (on sky)*	$\pm 10''$	$\pm 10''$
full tilt range of device (on sky)*	$\pm 15.2''$	$\pm 29.4''$
first resonance frequency*	≈ 960 Hz	≈ 812 Hz
Eigenfrequency*	≈ 990 Hz	≈ 830 Hz
rise time of HV amp (0-90 %) *	≈ 80 μ s	≈ 100 μ s
rise time HV + mirror (to nominal)*	≈ 340 μ s	≈ 440 μ s
actuator capacitance */†	43 nF	6 μ F \pm 20 %
mirror substrate material	ZERODUR	ZERODUR
dimensions of substrate	55 mm \varnothing , 10 mm	60 mm \varnothing , 10 mm
reflective coating	aluminum	aluminum
RMS surface error*	9 nm	13 nm
RMS wavefront error (500 nm)*	0.04 λ	0.05 λ

*) own measurements, see chapter 5

†) manufacturer information.

A.5 Wavefront sensors

Table A.9: Technical data and used configurations of the wavefront sensor cameras of GREGOR.

	Mikrotron EoSens CL MC1362
sensor type	area scan, CMOS, monochrome
sensor chip	Cypress Semiconductor LUPA-1300-2
sensor lid	D263 glass, \approx 90 % transmission, no IR blocker
shutter type	electronic, global
sensor size	1280 \times 1024 px
pixel size	14 μm \times 14 μm
QE \times FF	35 % (average 400-720 nm)
full-well capacity	30000 e $^-$
digitization	8, and 10 bit
min. exposure time	1 μs
internal dynamic	50 dB
digital interface	CameraLink (base, medium, and full mode)
used configuration	
read-out window	512 \times 512 px
max. frame rate	2026 Hz @ 512 \times 512 px
CameraLink mode	full mode, 8 taps
digitization	8 bit
pixel clock	80 MHz
sensor clock	41 kHz
frame transfer time	409.6 μs (to frame grabber, calculated from settings)
data rate	500 MiB/s @ 2000 Hz framerate
frame counter	32 bit (stored in first 4 pixels of every image)
exposure control	internal clock (MCAO on-axis WFS, and GPFI / GRIS AO on-axis WFS), external trigger through CameraLink CC1 (MCAO on-axis WFS), individually set exposure time (all cameras)
firmware versions	#00250-B2.02-V1.24-F1.17 (MCAO multi-dir WFS), #00212-B2.02-V1.21-F1.13 (MCAO on-axis WFS), #00620-B2.02-V1.22-F1.14 (GPFI / GRIS AO on-axis WFS)
hot or dead pixels	none observed in three camera exemplars after 3 years in use
exposure delay on-axis	< 2 μs
to multi-dir camera	

Table A.10: Technical key data of wavefront sensors in the testbed.

	on-axis wavefront sensor*	multi-dir wavefront sensor
type	correlating Hartmann-Shack	correlating Hartmann-Shack
subaperture size in pupil plane	15 cm	50 cm
number of used subapertures	78	6 (with 19 subfields each)
subaperture arrangement	hexagonal	hexagonal
R_{ML}^2/f_{ML}	$2.87 \cdot 10^{-6}$ m	$5.24 \cdot 10^{-5}$ m
microlens manufacturer	Smart Microoptical Solutions Walldorf, Germany, http://www.smos-microoptics.de	Advanced Microoptics Systems Saarbrücken, Germany, http://www.amus.de
microlens technology	GRIN by ion exchange	"machining" by photolithography
light, wavelength at GREGOR	90% of 10 nm band at 500 nm	10% of 10 nm band at 500 nm
light, wavelength in testbed	50% of white light	25% white light
field of view	9.6'' \times 9.6''	68'' \varnothing (with 9.6'' \times 9.6'' subfields)
pixel scale	0.4''/Pixel	0.4''/Pixel
camera	Mikrotron EoSens CL 1362 (512 \times 512 px ROI)	Mikrotron EoSens CL 1362 (512 \times 512 px ROI)

*) On-axis sensor of GAOS.256 features 156 square 10 cm subapertures with 16'' field

A.6 Control computer

Table A.11: Technical data of the control computers in the MCAO testbed in Freiburg and at GREGOR on Tenerife.

	MCAO testbed computer	GAOS.256 computer
CPUs	2 \times Intel Xeon X5570 (2.93 GHz, 4 cores)	2 \times Intel Xeon E5-2690 (2.90 GHz, 8 cores)
mainboard	Supermicro X8DTH-iF	Supermicro X9DR3-F
RAM configuration	6 \times 2 GB, (3 GB seen by operating system)	8 \times 4 GB (2 GB seen by operating system)
extension slots	7 \times PCIe x8 (2.0)	3 \times PCIe x8 (3.0) 3 \times PCIe x16 (3.0)
chassis	19 inch, 4U	dito
operating system	Debian Squeeze (amd64)	dito
Linux kernel	Debian 2.6.32-5-amd64	dito
control loop jitter	2 to 3 μ s at digital output	dito
shift compute time per 24 \times 24 px field	\approx 10–11 μ s/core	\approx 9–10 μ s/core

B Wavefront modes used for OKO PDMs

B Wavefront modes used for OKO PDMs

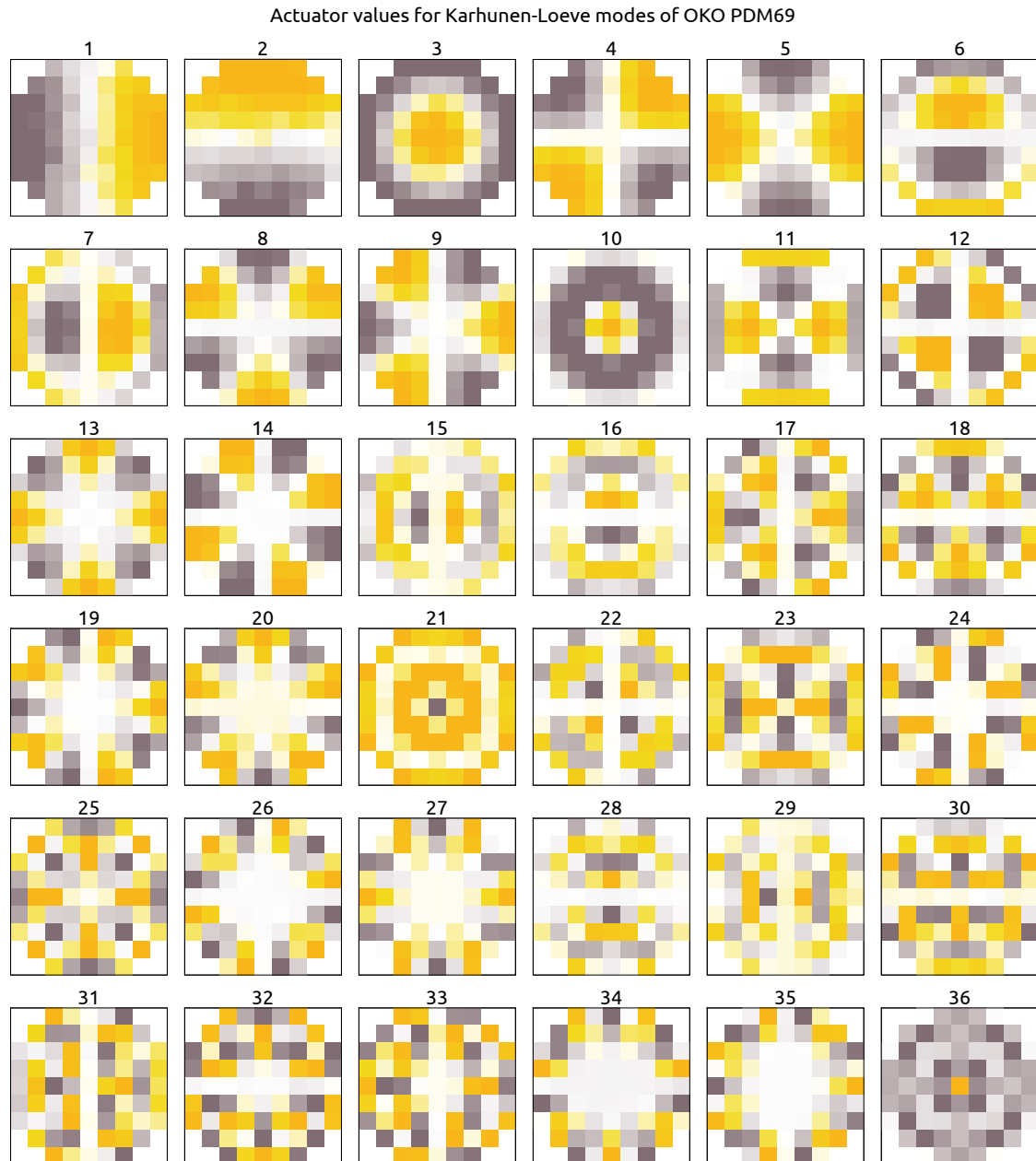


Figure B.1: Actuator value patterns that were used to form the first 36 Karhunen-Loeve modes with the OKO PDM69 mirrors. Each box represents one mode, the mode index is given in the superscription. The colored squares represent the positions and the values of the actuators. Modes 37 to 69 are shown in figure B.2.

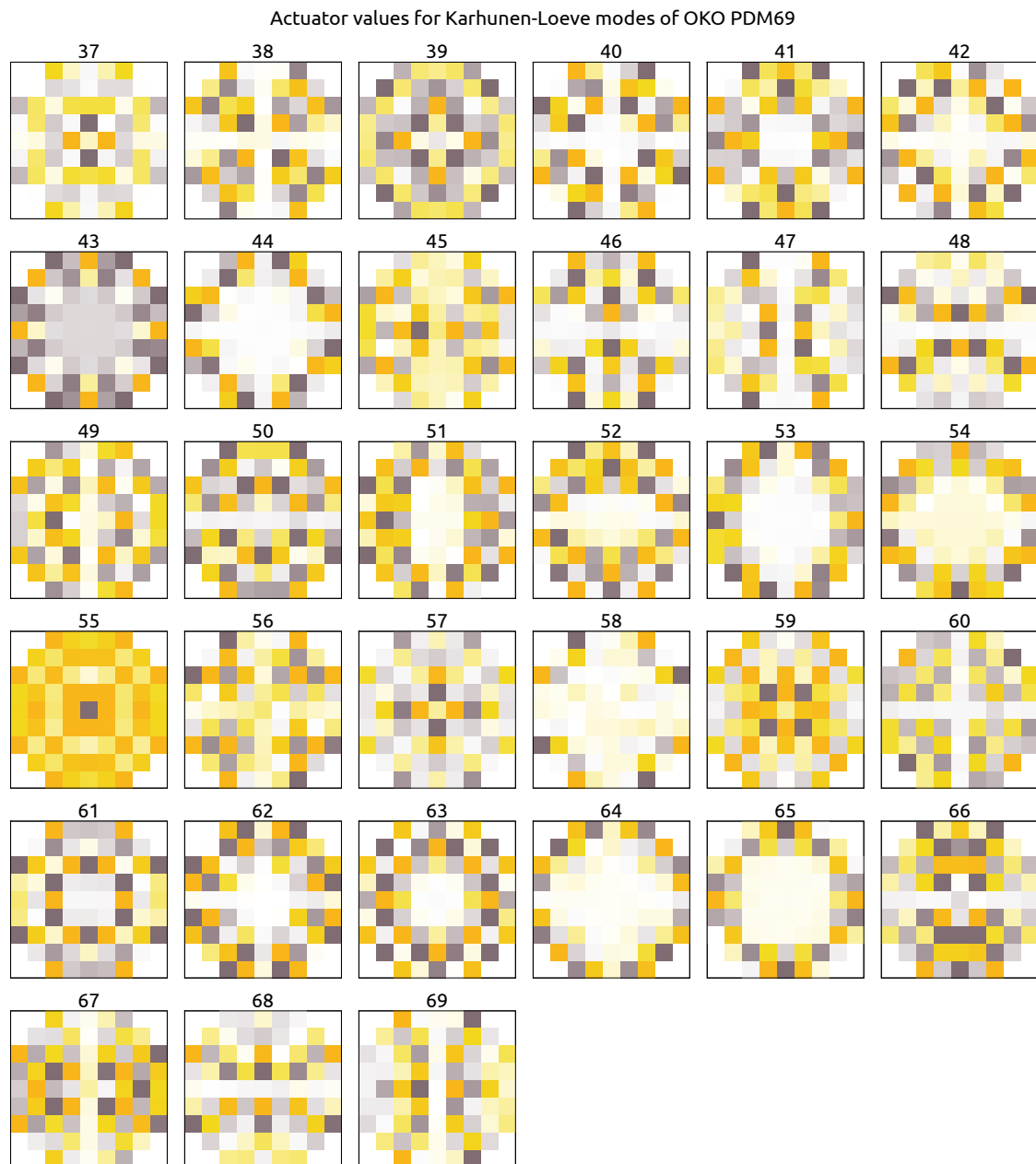


Figure B.2: Actuator value patterns that were used to form Karhunen-Loeve modes 37 to 69 with the OKO PDM69 mirrors. Refer to figure B.1 for explanation.

B Wavefront modes used for OKO PDMs

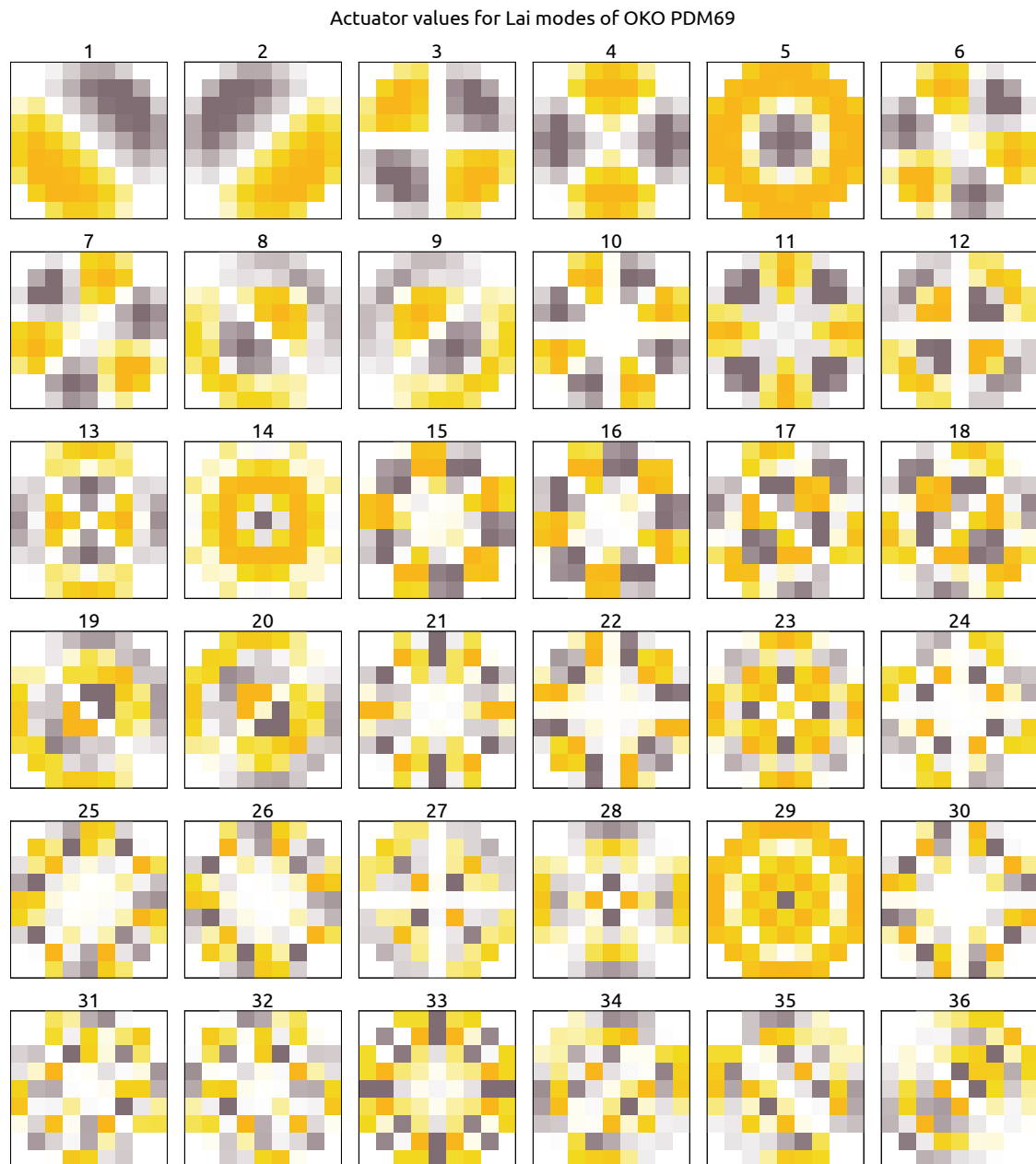


Figure B.3: Actuator value patterns that were used to form the first 36 Lai modes with the OKO PDM69 mirrors. Refer to figure B.1 for explanation. Modes 37 to 68 are shown in figure B.4.

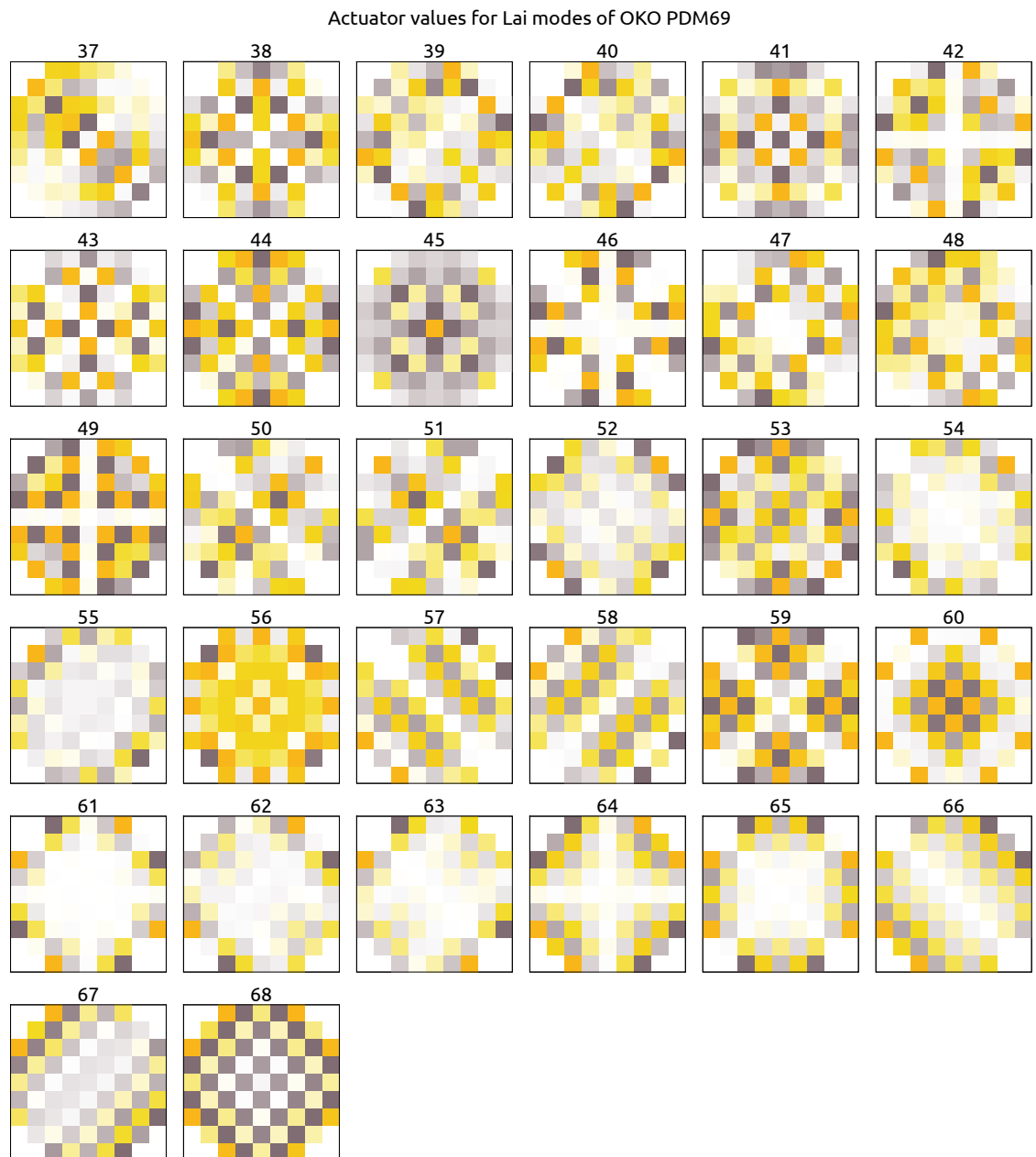


Figure B.4: Actuator value patterns that were used to form Lai modes 37 to 68 with the OKO PDM69 mirrors. Refer to figure B.1 for explanation.

B Wavefront modes used for OKO PDMs

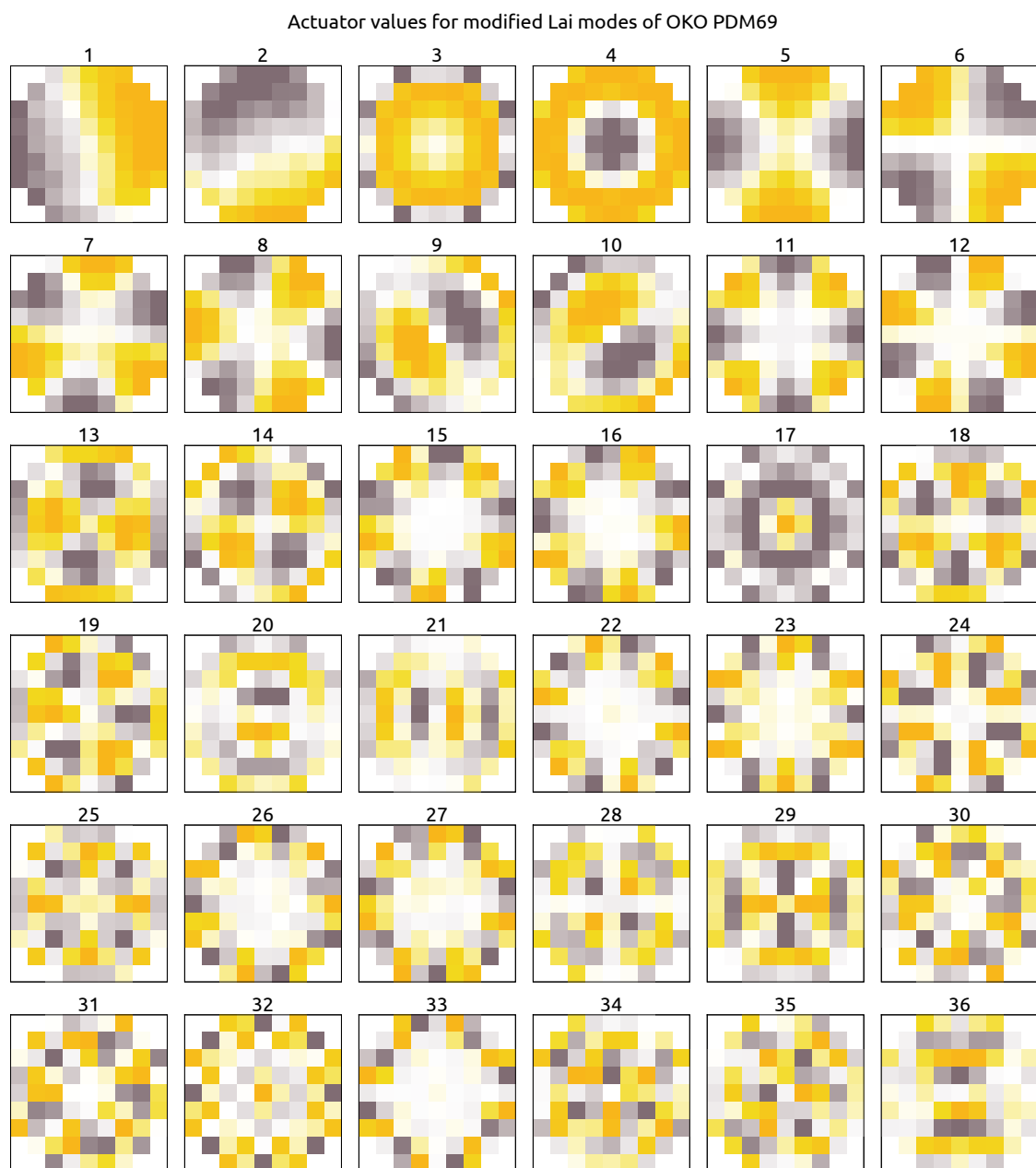


Figure B.5: Actuator value patterns that were used to form the first 36 modified Lai modes with the OKO PDM69 mirrors. Refer to figure B.1 for explanation. Modes 37 to 68 are shown in figure B.6.

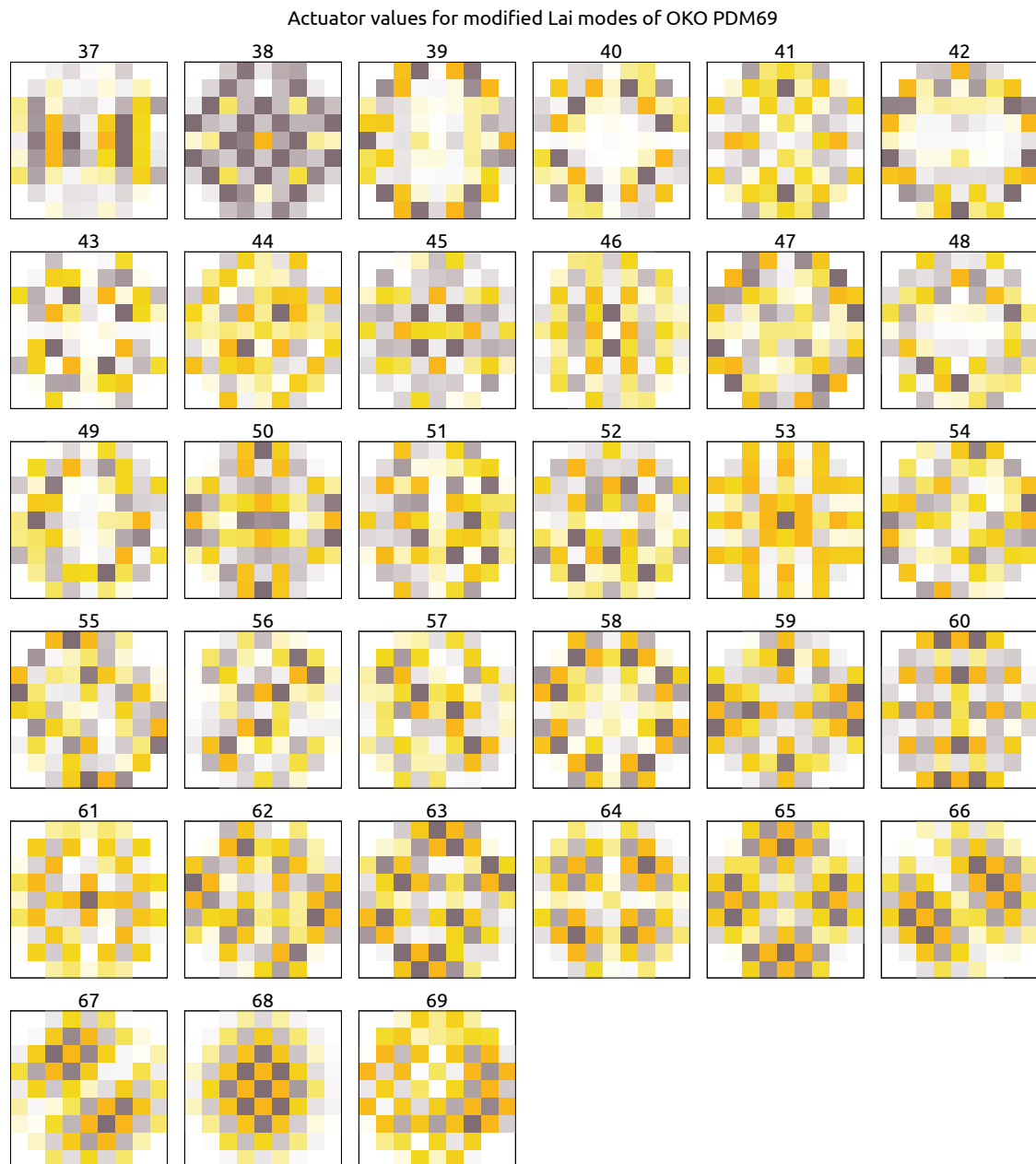


Figure B.6: Actuator value patterns that were used to form modified Lai modes 37 to 69 with the OKO PDM69 mirrors. Refer to figure B.1 for explanation.

C Design tips for Hartmann-Shack Wavefront Sensors for extended fields

The microlens array of a Hartmann-Shack sensor is placed into an image of the telescope pupil. Usually, the pupil image is formed with a lens that collimates the telescope's focal plane (image-space telecentric system). Once the telescope diameter, the geometry of the subapertures relative to the pupil and the sensor's field of view are fixed, a general property of the needed microlens array is implied. In paraxial optics, a microlens array is fully specified by the size a_{ML} of a microlens and its focal length f_{ML} . In this section it is derived that the ratio $a_{\text{ML}}^2/f_{\text{ML}}$ is constant for a given set of the previously mentioned features. This constant—or requirement—is very useful when contacting microlens manufacturers because it opens up a wide set of parameters ($f_{\text{ML}} = \text{const. } a_{\text{ML}}^2$ for reasonable sized microlenses) on which they can (or not) produce an adequate array. Depending on the manufacturer and the employed technique, it is possible to save thousands of Euros by fitting the magnification of pupil size to microlens size rather than the other way round. Adapting the pupil magnification can be generally done with two off-the-shelf lenses.

Derivation of the microlens requirement

Since an image-space telecentric system is considered, the diameter of the pupil image is given by

$$P = D f_c / f_t, \quad (\text{C.1})$$

where D is the telescope diameter, f_t its focal length and f_c the focal length of the collimator. Neighboring subaperture images must not overlap; this is the most important requirement on the design of a microlens array for a correlating Hartmann-Shack sensor. Subapertures and thus microlenses are usually shaped hexagonal or quadratic. First, consider the pupil diameter as a multiple of a microlens side length a_{ML} , i. e.

$$P = c_1 \cdot a_{\text{ML}} \quad (\text{C.2})$$

like exemplified in figure C.1. In the case of quadratic microlenses, preventing neighboring subaperture images from overlapping means that the images may not be larger than the

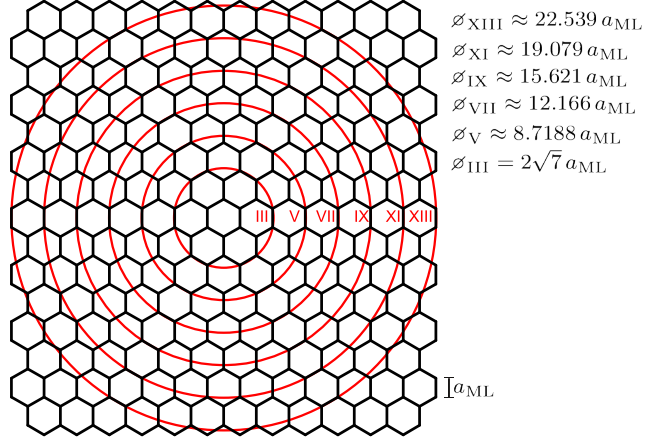


Figure C.1: Circles in a 2d hexagon array as typically used in subaperture layouts.

subapertures itself. Generally, the images do not overlap if the image size $b < c_2 a_{\text{ML}}$, where

$$c_2 = \begin{cases} 1 & , \text{for quadratic microlenses} \\ \sqrt{3} & , \text{for hexagonal microlenses with round field of view} \\ 3/2 & , \text{for hexagonal microlenses with square field of view} \end{cases} \quad (\text{C.3})$$

Refer to figure C.2 for explanation. To get a clear separation of the images it is practical to make the images little smaller than the maximum size, i. e.

$$c_3 b = c_2 a_{\text{ML}} \quad \text{with } c_3 \geq 1. \quad (\text{C.4})$$

Subaperture images have been relayed from the telescope focus and magnified by the collimator and the microlens. The image size in the microlens focus is

$$b = \frac{f_{\text{ML}}}{f_c} f_t \alpha, \quad (\text{C.5})$$

where α is the angular field of view in radians, and the f_i denote the focal lengths of the telescope, the collimator, and the microlens, respectively. This is all that is needed to find the constant expression for $a_{\text{ML}}^2/f_{\text{ML}}$. Combining equations (C.1) and (C.2) yields:

$$a_{\text{ML}} = \frac{D f_c}{c_1 f_t} \quad (\text{C.6})$$

Equations (C.4) and (C.5) deliver:

$$f_{\text{ML}} = \frac{c_2}{c_1 c_3} D \frac{f_c^2}{f_t^2 \alpha} \quad (\text{C.7})$$

Finally, it is:

$$\frac{a_{\text{ML}}^2}{f_{\text{ML}}} = \frac{c_3}{c_1 c_2} D \alpha \quad (\text{C.8})$$

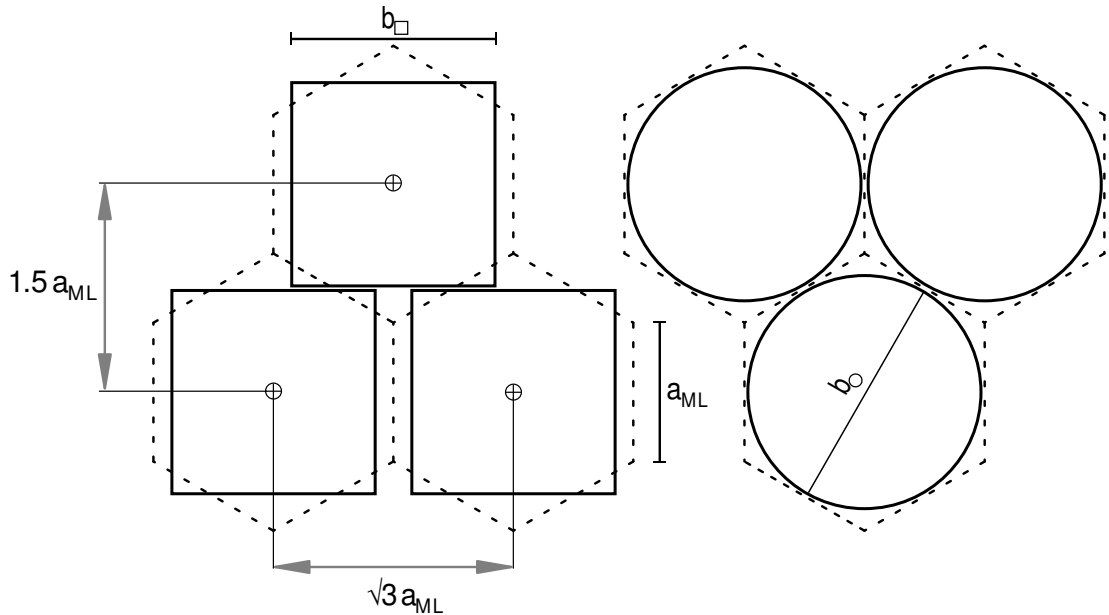


Figure C.2: Non-overlapping square and circular images of neighboring subapertures.

Scaling the components

Pupil magnification For a given microlens size, the collimator's focal length needs to measure

$$f_c = c_1 a_{ML} \frac{f_t}{D} \quad (C.9)$$

according to equation (C.6). If there is no lens with f_c available, it is possible to replace it with two lenses with focal lengths f_1 and f_2 separated by

$$d = f_1 + f_2 - \frac{f_1 f_2}{f_c}. \quad (C.10)$$

Imaging to wavefront sensor camera The focal plane of the microlens array needs to be scaled to the wavefront sensor camera. Given the pixel scale (angular field per length) s of the wavefront sensor camera, the required magnification for imaging the microlens focus onto the camera is

$$m = \frac{f_c}{f_{ML} f_t} \frac{1}{s} \quad (C.11)$$

$$= \frac{c_1 c_3}{c_2} \frac{f_t}{D} \frac{\alpha}{s f_c}. \quad (C.12)$$

Microlenses and diffraction

The derived microlens requirement for $a_{\text{ML}}^2/f_{\text{ML}}$ looks similar but is not connected to the Fresnel number which is defined as $FN := a_{\text{ML}}^2/(\lambda f_{\text{ML}})$ using the introduced identifiers, and the light's wavelength λ . The Fresnel number is known in diffraction optics because it separates the Fresnel diffraction ($FN \gg 1$) from the Fraunhofer diffraction ($FN \ll 1$). Propagation of light through a microlens with a low Fresnel number is more dominated by diffraction at its aperture than by refraction at its surface profiles. Wavefront sensors for solar observations typically require microlenses with Fresnel number well beyond 1, so that they can be modeled with the means of geometrical optics without considering effects of diffraction like focus shifting.

List of Figures

1.1	Daytime and nighttime views of the sky above the Teide volcano on Tenerife.	13
1.2	Electro-magnetic transmittance of Earth's atmosphere.	14
1.3	Earth's atmosphere blurring the image of the Sun.	14
1.4	The Sun in the visible light regime.	15
2.1	Graphical explanation of the term <i>wavefront error</i> .	18
2.2	Wavefront flattening with a deformable mirror.	18
2.3	Scheme of a generic astronomical adaptive optics system.	19
2.4	Illustration of anisoplanatism in Earth's atmosphere.	20
2.5	Illustration of wavefront conjugation in conjugate planes.	21
2.6	Single conjugate adaptive optics scheme.	21
2.7	Multi-object adaptive optics scheme.	22
2.8	Multi-conjugate adaptive optics scheme.	24
2.9	Example of anisoplanatic imaging.	28
2.10	Airy disc.	29
2.11	Illustration of the Rayleigh criterion.	29
2.12	Example of a discrete $C_n^2(h)$ profile estimation.	32
2.13	Wavefronts of four basic optical aberrations.	33
2.14	Variance of Zernike coefficients of atmospheric wavefronts.	36
2.15	Zernike polynomial mean temporal power spectra.	39
2.16	Angular correlation of Zernike coefficients of atmospheric wavefronts.	40
2.17	Exemplary plot of Strehl ratio vs. field angle.	41
2.18	Cross-section of piezo actuators.	42
2.19	Cross-section of a deformable mirror with discrete piezo actuators.	43
2.20	Cross-section of a bimorph mirror.	43
2.21	Principle of a Hartmann-Shack wavefront sensor.	45
2.22	Top view of the Fried geometry.	49
2.23	Waffle mode.	49
2.24	Wavefront tomography.	52
2.25	Illustration of multi-direction wavefront sensing in GREGOR's MCAO.	54
2.26	Principle of a wide-field Hartmann-Shack sensor for multi-direction wavefront sensing.	55
2.27	Block diagram of a simplified adaptive optics control loop.	56
3.1	The GREGOR telescope pointing at the Sun.	61
3.2	The <i>New Solar Telescope</i> in Big Bear Lake.	62

List of Figures

3.3	Optical layout of the GREGOR telescope including AO and MCAO paths.	63
3.4	The optical bench in GREGOR holding first-light adaptive optics in 2011.	65
3.5	Picture of DM _{8 km}	66
3.6	The first-generation DM _{0 km}	68
3.7	The second-generation DM _{0 km}	68
3.8	The converter board for the KIS-M-Link communication.	69
3.9	High-voltage driver electronics.	70
3.10	Fixture of the tip-tilt mirror substrate.	71
3.11	Optical layout of the multi-direction wavefront sensor.	73
3.12	Photographic illustration of pupil distortion.	76
3.14	Illustration of linear misregistration.	76
4.1	Screenshot of the KAOS Evo 2 user interface.	81
4.2	Flow diagram of the KAOS control loop.	82
4.3	Referencing of a correlation field.	83
4.4	Windowing of correlation field image data.	85
4.5	Screenshot of the time sequence and power spectrum display of KAOS Evo 2. .	89
4.6	Image shift and distortion in a correlation field due to a high-altitude DM .	91
5.1	The testbed of the MCAO for GREGOR.	94
5.2	Optical configuration and illumination scheme of the MCAO testbed.	96
5.3	Pupil mock-up stop.	96
5.4	The cooktop used to generate turbulence.	97
5.5	Tip-tilt mirror step response measurement setup.	99
5.6	Step response of the PI tip-tilt system.	100
5.7	Frequency response function of the Physik Instrumente tip-tilt system.	100
5.8	Step response of the KIS tip-tilt system.	101
5.9	Resonace frequency of the KIS tip-tilt system.	101
5.10	Response of the undamped OKO PDM69 KIS3 to 150 V step.	102
5.11	Surface profile of OKO PDM69 KIS3.	103
5.12	Surface profile of OKO PDM69 KIS3 after flattening.	103
5.13	Bottom-up cross-section trough the center of the flat profile in fig. 5.12. .	103
5.14	Actuator offset values of the flat profile in fig. 5.12.	104
5.15	Influence functions of the outer actuator ring of Night DM2-55-80 #00042. .	105
5.16	Frequency response function of the high-voltage amplifier.	106
5.17	Exposure synchronization of the on-axis and the multi-dir WFS cameras. .	106
5.18	Control loop timing.	108
6.1	Example snapshot of a granulation slide located in the F ₃ mockup.	112
6.2	Example of a circle diagram showing the agile image distortion in science focus.	113
6.3	Example of a circle diagram showing the temporal mean image degradation in the guide regions.	115
6.4	Example diagram showing the modal composition of the wavefront error in the guide directions.	117

6.5 Example diagram showing the modal wavefront fluctuations in the guide directions	118
6.6 Example of a circle diagram showing the fluctuations of image shifts in the correlation fields the multi-dir wavefront sensor	119
6.7 Schematic sketch of the imagined effect of thermal expansion in the OKO PDM69 deformable mirrors.	121
6.8 Temporal standard deviation of subfield image shift in the science focus with various AO control modes compensating for cooktop turbulence.	122
6.9 Temporal root-mean-square error of focus and astigmatism in the guide directions of the multi-dir wavefront sensor with various AO control modes compensating for cooktop turbulence.	123
6.10 Temporal standard deviation of tip-tilt, focus and astigmatism in the guide directions of the multi-dir wavefront sensor with various AO control modes compensating for cooktop turbulence.	124
6.11 Temporal root-mean-square error of focus and astigmatism in the guide directions of the multi-dir wavefront sensor with various AO control modes compensating for cooktop turbulence.	125
6.12 Power spectra of tip-tilt wavefront error of uncompensated cooktop turbulence and in MCAO control mode.	128
6.13 Power spectra of vertical tip-tilt wavefront error in MCAO control mode with 1400 Hz and 1700 Hz control loop frequency.	129
6.14 Power spectra of focus wavefront error of uncompensated cooktop turbulence and in MCAO control mode.	130
6.15 Power spectra of wavefront error mode 20 of $DM_{0\text{ km}}$ of uncompensated cooktop turbulence and in MCAO control mode.	130
6.16 Power spectra of wavefront error mode 5 (parabola) of $DM_{8\text{ km}}$ of uncompensated cooktop turbulence and in MCAO control mode.	131
6.17 Diagrams showing the residuals of MCAO control mode with modified Lai modes.	133
6.18 Diagrams showing the residuals of uncompensated turbulence for comparison with figure 6.17.	134
6.19 Agile image distortion in MCAO mode.	135
6.20 Temporal standard deviation of subfield image shift in the science focus with various AO control modes compensating for cooktop turbulence.	136
6.21 Temporal root-mean-square error of focus and astigmatism in the guide directions of the multi-dir wavefront sensor with various AO control modes compensating for cooktop turbulence.	138
6.22 Temporal standard deviation of tip-tilt, focus and astigmatism in the guide directions of the multi-dir wavefront sensor with various AO control modes compensating for cooktop turbulence.	139
6.23 The temporal root-mean-square error of focus and astigmatism in the guide directions of the multi-dir wavefront sensor with various AO control modes compensating for cooktop turbulence.	140
6.24 Time series of KAOS modes 3-26 of $DM_{8\text{ km}}$ and $DM_{25\text{ km}}$	143

List of Figures

6.25 Time series of KAOS modes 27-59 of $DM_{8\text{ km}}$ and $DM_{25\text{ km}}$	144
6.26 Scatter graphs of the time series in fig. 6.24.	145
6.27 Scatter graphs of the time series in fig. 6.25.	146
6.28 Correlation matrices of the MD-WFS signatures of $DM_{8\text{ km}}$ and $DM_{25\text{ km}}$	147
B.1 Actuator value patterns of OKO PDM69 for the first 36 Karhunen-Loeve modes	164
B.2 Actuator value patterns of OKO PDM69 for Karhunen-Loeve modes 37–69 . .	165
B.3 Actuator value patterns that were used to form the first 36 Lai modes with the OKO PDM69 mirrors.	166
B.4 Actuator value patterns that were used to form Lai modes 37 to 68 with the OKO PDM69 mirrors.	167
B.5 Actuator value patterns that were used to form the first 36 modified Lai modes with the OKO PDM69 mirrors.	168
B.6 Actuator value patterns that were used to form modified Lai modes 37 to 69 with the OKO PDM69 mirrors.	169
C.1 Circles in a 2d hexagon array as typically used in subaperture layouts.	172
C.2 Non-overlapping square and circular images of neighboring subapertures. . .	173

List of Tables

2.1	The first 11 Zernike polynomials.	35
2.2	Examples of angle of arrival fluctuations.	37
2.3	Tyreus-Leuben PI(D) control parameter tuning.	58
5.1	Step response of the Physik Instrumente tip-tilt system.	99
6.1	Controller parameters used for the test runs.	120
6.2	Performance indicators of the test runs with $DM_{0\text{km}}$ and $DM_{8\text{ km}}$ on June 26 th , 2012	126
6.3	Residual errors averaged over the recordings of the AO modes.	126
6.4	Standard deviations of the guide direction errors shown in figure 6.10 averaged over the 19 guide directions.	126
6.5	Root-mean-squares of the guide direction errors shown in figure 6.11 averaged over the 19 guide directions.	127
6.6	Residual errors in MCAO control mode with three different KAOS modesets for $DM_{8\text{km}}$	132
6.7	Performance indicators of the test runs with $DM_0\text{ km}$, $DM_{8\text{ km}}$ and $DM_{25\text{ km}}$ on August 13 th , 2012	137
6.8	Average performance indicators of table 6.7	138
A.1	The optical geometry of GREGOR MCAO.	153
A.2	Technical key data of $DM_{8\text{ km}}$ and $DM_{25\text{ km}}$	154
A.3	Technical key data of the deformable mirror made by Night that is used as $DM_0\text{ km}$	155
A.4	Technical key data of deformable mirrors.	155
A.5	Technical data of the KIS High-voltage amplifier system used in GREGOR's AO/MCAO.	156
A.6	Pin connections and bit assignment of KIS-M-LINK	157
A.7	Pin connections and bit assignment of KIS-M-LINK	158
A.8	Technical key data of the tip-tilt stages and the attached mirrors used in GREGOR and in the testbed.	159
A.9	Technical data and used configurations of the wavefront sensor cameras of GREGOR.	160
A.10	Technical key data of wavefront sensors in the testbed.	161
A.11	Technical data of the control computers in the MCAO testbed in Freiburg and at GREGOR on Tenerife.	161

Bibliography

- E. Anderson, Z. Bai, C. Bischof, S. Blackford, J. Demmel, J. Dongarra, J. Du Croz, A. Greenbaum, S. Hammarling, A. McKenney, and D. Sorensen. *LAPACK Users' Guide*. Society for Industrial and Applied Mathematics, Philadelphia, PA, third edition, 1999. ISBN 0-89871-447-8 (paperback). The LAPACK reference implementation is available for free download at <http://www.netlib.org/lapack>. Commerical use allowed. 80
- H. W. Babcock. The Possibility of Compensating Astronomical Seeing. *Publ. Astron. Soc. Pac.*, 65:229, October 1953. doi:10.1086/126606. URL <http://adsabs.harvard.edu/abs/1953PASP...65..229B>. 18
- J. M. Beckers. Increasing the Size of the Isoplanatic Patch with Multiconjugate Adaptive Optics. In *European Southern Observatory Conference and Workshop Proceedings*, volume 30 of *ESO Proc.*, page 693, 1988a. 23
- J. M. Beckers. Increasing the size of the isoplanatic patch with multiconjugate adaptive optics. In *Very Large Telescopes and their Instrumentation, Vol. 2*, volume 2, pages 693–703, October 1988b. 23
- T. Berkefeld. *Untersuchungen zur Messung und Korrektur einzelner Schichten in der Erdatmosphäre*. PhD thesis, Ruprecht-Karls-Universität Heidelberg, 1998. 40
- T. Berkefeld, D. Soltau, and O. von der Lühe. Results of the multi-conjugate adaptive optics system at the German solar telescope, Tenerife. In *Astronomical Adaptive Optics Systems and Applications II*, volume 5903 of *Proceedings of SPIE*, pages 219–226, August 2005. doi:10.1117/12.619132. 23, 79
- T. Berkefeld, D. Soltau, and O. von der Lühe. Multi-conjugate solar adaptive optics with the VTT and GREGOR. In *Advances in Adaptive Optics II*, volume 6272 of *Proceedings of SPIE*, July 2006. doi:10.1117/12.671718. 23, 64, 65, 67, 75
- T. Berkefeld, D. Soltau, D. Schmidt, and O. von der Lühe. Adaptive optics development at the German solar telescopes. *Appl. Opt.*, 49:G155, September 2010. doi:10.1364/AO.49.00G155. 84
- T. Berkefeld, W. Schmidt, D. Soltau, A. Bell, H. P. Doerr, B. Feger, R. Friedlein, K. Gerber, F. Heidecke, T. Kentischer, O. von der Lühe, M. Sigwarth, E. Wälde, P. Barthol, W. Deutsch, A. Gandorfer, D. Germerott, B. Grauf, R. Meller, A. Álvarez-Herrero, M. Knölker, V. Martínez Pillet, S. K. Solanki, and A. M. Title. The Wave-Front Correction System for the Sunrise Balloon-Borne Solar Observatory. *Solar Physics*, 268:103–123, January 2011. doi:10.1007/s11207-010-9676-3. 71, 79

Bibliography

- T. Berkefeld, D. Schmidt, D. Soltau, O. von der Lühe, and F. Heidecke. The GREGOR Adaptive Optics System. *Astronomische Nachrichten*, 333:863, November 2012. doi:10.1002/asna.201211739. 62, 67
- J. Blanchette and M. Summerfield. *C++ GUI Programming with Qt 4 (2nd Edition) - The official C++/Qt book*. Prentice Hall, 2008. ISBN 978-0132354165. Qt, licensed under the LGPL, is available for free download at <http://qt-project.org>. 80
- R. C. Cannon. Optimal bases for wave-front simulation and reconstruction on annular apertures. *J. Opt. Soc. Am. A*, 13:862–867, April 1996. doi:10.1364/JOSAA.13.000862. 59
- M. Collados, A. Calcines, J. J. Díaz, E. Hernández, R. López, and E. Páez. A high-resolution spectrograph for the solar telescope GREGOR. In *Society of Photo-Optical Instrumentation Engineers (SPIE) Conference Series*, volume 7014 of *Proceedings of SPIE*, August 2008. doi:10.1117/12.790060. 62
- J.-M. Conan, G. Rousset, and P.-Y. Madec. Wave-front temporal spectra in high-resolution imaging through turbulence. *J. Opt. Soc. Am. A*, 12:1559–1570, July 1995. doi:10.1364/JOSAA.12.001559. 39
- B. Feger, 2009. Personal communication. 71
- D. L. Fried. Statistics of a Geometric Representation of Wavefront Distortion. *J. Opt. Soc. Am.*, 55:1427, November 1965. doi:10.1364/JOSA.55.001427. 32
- D. L. Fried. Time-delay-induced mean-square error in adaptive optics. *J. Opt. Soc. Am. A*, 7: 1224–1227, July 1990. doi:10.1364/JOSAA.7.001224. 38
- M. Frigo and S. G. Johnson. The design and implementation of FFTW3. *Proc. IEEE*, 93(2): 216–231, 2005. FFTW is available for free download at <http://www.fftw.org>. GPL and commerical licensing. 47, 80
- J. J. Fuensalida, S. Chueca, J. M. Delgado, B. García-Lorenzo, J. M. Rodríguez-González, C. K. Hoegemann, E. G. Mendizabal, M. Reyes, M. Verde, and J. Vernin. Vertical structure of the turbulence above the observatories of the Canary Islands: parameters and statistics for adaptive optics. In *Advancements in Adaptive Optics*, volume 5490 of *Proceedings of SPIE*, pages 749–757, October 2004. doi:10.1117/12.552031. 64
- J. D. Gaskill. *Linear Systems, Fourier Transforms and Optics*. John Wiley & Sons, New York, 1978. ISBN 0471292885. 25
- K. Goto and R. A. van de Geijn. Anatomy of high-performance matrix multiplication. *ACM Trans. Math. Softw.*, 34(3):12:1–12:25, May 2008. ISSN 0098-3500. doi:10.1145/1356052.1356053. GotoBLAS was discontinued by the original author and is now distributed under the name OpenBLAS. OpenBLAS is licensed under the BSD license and is available for free download at <http://xianyi.github.com/OpenBLAS>. 80
- D. P. Greenwood. Bandwidth specification for adaptive optics systems. *J. Opt. Soc. Am.*, 67: 390–393, March 1977. doi:10.1364/JOSA.67.000390. 38

Bibliography

- J. W. Hardy. *Adaptive Optics for Astronomical Telescopes*. Number 16 in Oxford Series in Optical and Imaging Sciences. Oxford University Press, 1998. ISBN 0-19-509019-5. 17
- Intel Corporation. Intel Math Kernel Library. <http://software.intel.com/en-us/intel-mkl>, 2012. The Intel Math Kernel Library is available under a proprietary license. 80
- M. Kasper, E. Fedrigo, D. P. Looze, H. Bonnet, L. Ivanescu, and S. Oberti. Fast calibration of high-order adaptive optics systems. *J. Opt. Soc. Am. A*, 21:1004–1008, June 2004. doi:10.1364/JOSAA.21.001004. 90
- A Kudryashov, 10 2007. E-mail communication. 104
- O. Lai. Modal control: A primer. Keck Adaptive Optics Notes 164, Keck, 07 1998. 60
- O. Lai, P. J. Stomski, and E. Gendron. MANO: the modal analysis and noise optimization program for the W.M. Keck Observatory adaptive optics system. In *Adaptive Optical Systems Technology*, volume 4007 of *Proceedings of SPIE*, pages 620–631, July 2000. doi:10.1117/12.390357. 60, 80
- R. G. Lane and M. Tallon. Wave-front reconstruction using a Shack-Hartmann sensor. *Appl. Opt.*, 31:6902–6908, November 1992. doi:10.1364/AO.31.006902. 59
- M. Langlois, G. Moretto, K. Richards, S. Hegwer, and T. R. Rimmele. Solar multiconjugate adaptive optics at the Dunn Solar Telescope: preliminary results. In *Advancements in Adaptive Optics*, volume 5490 of *Proceedings of SPIE*, pages 59–66, October 2004. doi:10.1117/12.548929. 23, 75
- C. L. Lawson, R. J. Hanson, D. R. Kincaid, and F. T. Krogh. Basic linear algebra subprograms for fortran usage. *ACM Trans. Math. Softw.*, 5(3):308–323, September 1979. ISSN 0098-3500. doi:10.1145/355841.355847. 80
- M. G. Löfdahl. Evaluation of image-shift measurement algorithms for solar Shack-Hartmann wavefront sensors. *Astron. Astrophys.*, 524:A90, December 2010. doi:10.1051/0004-6361/201015331. 47, 91
- P-Y. Madec. Overview of deformable mirror technologies for adaptive optics and astronomy. In *Adaptive Optics Systems III*, volume 8447 of *Proceedings of SPIE*, pages 844705–844705–18, 2012. doi:10.1117/12.924892. 42
- E. Marchetti, R. Brast, B. Delabre, R. Donaldson, E. Fedrigo, C. Frank, N. Hubin, J. Kolb, J.-L. Lizon, M. Marchesi, S. Oberti, R. Reiss, J. Santos, C. Soenke, S. Tordo, A. Baruffolo, P. Bagnara, and CAMCAO Consortium. On-sky Testing of the Multi-Conjugate Adaptive Optics Demonstrator. *The Messenger*, 129:8–13, September 2007. 23
- V. Michau, G. Rousset, and J. C. Fontanella. Wavefront Sensing from Extended Sources. In *Real Time and Post Facto Solar Image Correction*, NSO/SP Summer Workshop Series No. 13, pages 124–128, 1992. 47

Bibliography

- N. M. Milton, M. Lloyd-Hart, A. Cheng, J. A. Georges, III, and J. R. P. Angel. Design and expected performance of an MCAO system for the Giant Magellan Telescope. In *Astronomical Adaptive Optics Systems and Applications*, volume 5169 of *Proceedings of SPIE*, pages 238–249, December 2003. doi:10.1117/12.511742. 32
- R. J. Noll. Zernike polynomials and atmospheric turbulence. *J. Opt. Soc. Am.*, 66:207–211, March 1976. doi:10.1364/JOSA.66.000207. 34, 35, 59
- Physik Instrumente GmbH & Co. KG. Piezo-university, dynamic operation fundamentals, 10 2012. URL <http://www.physikinstrumente.com/en/products/prdetail.php?sortnr=400600.60>. Accessed: 05/10/2012. 98
- K. G. Puschmann, H. Balthasar, S.-M. Bauer, T. Hahn, E. Popow, T. Seelemann, R. Volkmer, M. Woche, and C. Denker. The GREGOR Fabry-Perot Interferometer - A New Instrument for High-Resolution Spectropolarimetric Solar Observations. *ArXiv e-prints*, November 2011. 62
- R. Ragazzoni, E. Marchetti, and F. Rigaut. Modal tomography for adaptive optics. *Astron. Astrophys.*, 342:L53–L56, February 1999. 52
- U. Rathmann and J. Wilgen. QWidgets for Technical Applications (Qwt), 2012. Qwt is licensed under an extended LGPL and is available for free download at <http://qwt.sourceforge.net>. 80
- F. Rigaut. Ground Conjugate Wide Field Adaptive Optics for the ELTs. In *European Southern Observatory Conference and Workshop Proceedings*, volume 58 of *ESO Proc.*, page 11, 2002. 23
- F. Rigaut, B. Neichel, M. Boccas, C. d'Orgeville, G. Arriagada, V. Fesquet, S. J. Diggs, C. Marchant, G. Gausach, W. N. Rambold, J. Luhrs, S. Walker, E. R. Carrasco-Damele, M. L. Edwards, P. Pessev, R. L. Galvez, T. B. Vucina, C. Araya, A. Gutierrez, A. W. Ebbers, A. Serio, C. Moreno, C. Urrutia, R. Rogers, R. Rojas, C. Trujillo, B. Miller, D. A. Simons, A. Lopez, V. Montes, H. Diaz, F. Daruich, F. Colazo, M. Bec, G. Tranco, M. Sheehan, P. McGregor, P. J. Young, M. C. Doolan, J. van Harmelen, B. L. Ellerbroek, D. Gratadour, and A. Garcia-Rissmann. GeMS: first on-sky results. In *Adaptive Optics Systems III*, volume 8447 of *Proceedings of SPIE*, pages 84470I–84470I–15, 2012. doi:10.1117/12.927061. 23
- T. Rimmele and J. Marino. Solar adaptive optics. *Living Reviews in Solar Physics*, 8(2), 2011. URL <http://www.livingreviews.org/lrsp-2011-2>. 17, 32, 46
- T. Rimmele, K. Richards, J. M. Roche, S. L. Hegwer, R. P. Hubbard, E. R. Hansen, B. Goodrich, and R. S. Upton. The wavefront correction system for the Advanced Technology Solar Telescope. In *Advances in Adaptive Optics II*, volume 6272 of *Proceedings of SPIE*, July 2006. doi:10.1117/12.672330. 32
- T. R. Rimmele, F. Woeger, J. Marino, K. Richards, S. Hegwer, T. Berkefeld, D. Soltau, D. Schmidt, and T. Waldmann. Solar multiconjugate adaptive optics at the Dunn Solar

- Telescope. In *Adaptive Optics Systems II*, volume 7736 of *Proceedings of SPIE*, July 2010. doi:10.1117/12.857485. 23, 75
- F. Roddier. *Adaptive Optics in Astronomy*. Cambridge University Press, November 2004. ISBN 0521612144. 17
- D. Schmidt. Test of deformable mirror Night N DM2-55-80 #00042. Technical Report GRE-KIS-TRE-0009, Kiepenheuer-Institut für Sonnenphysik, 09 2007. 104
- D. Schmidt and O. von der Lühe. Optical wavefront differentiation: wavefront sensing for solar adaptive optics based on a LCD. In *Adaptive Optics for Laser Systems and Other Applications*, volume 6584 of *Proceedings of SPIE*, May 2007. doi:10.1117/12.722640. 80
- UK Speirs Robertson Ltd. Optical tables, bread boards & vibration isolation systems, June 2004. URL http://www.speirsrobertson.com/acatalog/optical_tables.pdf. product brochure. 110
- V. I. Tatarski. *Wave Propagation in a Turbulent Medium*. McGraw-Hill Book, 1961. 32
- A. Tokovinin, M. Le Louarn, E. Viard, N. Hubin, and R. Conan. Optimized modal tomography in adaptive optics. *Astron. Astrophys.*, 378:710–721, November 2001. doi:10.1051/0004-6361:20011213. 22
- Bjorn D. Tyreus and William L. Luyben. Tuning pi controllers for integrator/dead time processes. *Industrial & Engineering Chemistry Research*, 31(11):2625–2628, 1992. doi:10.1021/ie00011a029. 58
- R. K. Tyson. *Principles of Adaptive Optics*. Academic Press, 1991. ISBN 0-12-705900-8. 17
- O. von der Lühe. A study of a correlation tracking method to improve imaging quality of ground-based solar telescopes. *Astron. Astrophys.*, 119:85–94, March 1983. 47
- O. von der Lühe. Wavefront error measurement technique using extended, incoherent light sources. *Opt. Eng.*, 27:1078–1087, December 1988. 80
- O. von der Lühe. Photometric stability of multiconjugate adaptive optics. In *Society of Photo-Optical Instrumentation Engineers (SPIE) Conference Series*, volume 5490 of *Proceedings of SPIE*, pages 617–624, October 2004. doi:10.1117/12.553053. 75
- O. von der Lühe. Broad band imager. Technical report, KIS, 2011. 62
- O. von der Lühe, D. Soltau, T. Berkefeld, and T. Schelenz. KAOS: Adaptive optics system for the Vacuum Tower Telescope at Teide Observatory. In *Innovative Telescopes and Instrumentation for Solar Astrophysics*, volume 4853 of *Proceedings of SPIE*, pages 187–193, February 2003. doi:10.1117/12.498659. 79
- O. von der Lühe, T. Berkefeld, and D. Soltau. Multi-conjugate solar adaptive optics at the Vacuum Tower Telescope on Tenerife. *Comptes Rendus Physique*, 6:1139–1147, December 2005. doi:10.1016/j.crhy.2005.09.007. 67

Bibliography

- J. Y. Wang and J. K. Markey. Modal compensation of atmospheric turbulence phase distortion. *J. Opt. Soc. Am.*, 68:78–87, January 1978. doi:10.1364/JOSA.68.000078. 59
- R. C. Whaley and J. Dongarra. Automatically Tuned Linear Algebra Software. In *Ninth SIAM Conference on Parallel Processing for Scientific Computing*, 1999. ATLAS is licensed under the BSD license and is available for free download at <http://math-atlas.sourceforge.net>. 80
- F. Wöger and T. Rimmele. Effect of anisoplanatism on the measurement accuracy of an extended-source Hartmann-Shack wavefront sensor. *Appl. Opt.*, 48:35, 2009. doi:10.1364/AO.48.000A35. 48
- J. G. Ziegler and N. B. Nichols. Optimum settings for automatic controllers. *Transactions of ASME*, 64:759–768, 1942. 58

*«Twenty years from now
you will be more disappointed
by the things that you didn't do
than by the ones you did do.
So throw off the bowlines.
Sail away from the safe harbor.
Catch the trade winds in your sails.
Explore. Dream. Discover.»*

(Mark Twain)